**UNIVERSITÀ DEGLI STUDI DI PAVIA**
Dipartimento di Biologia e Biotecnologie L. Spallanzani

# High-resolution epigenetic analysis of the cell nucleus

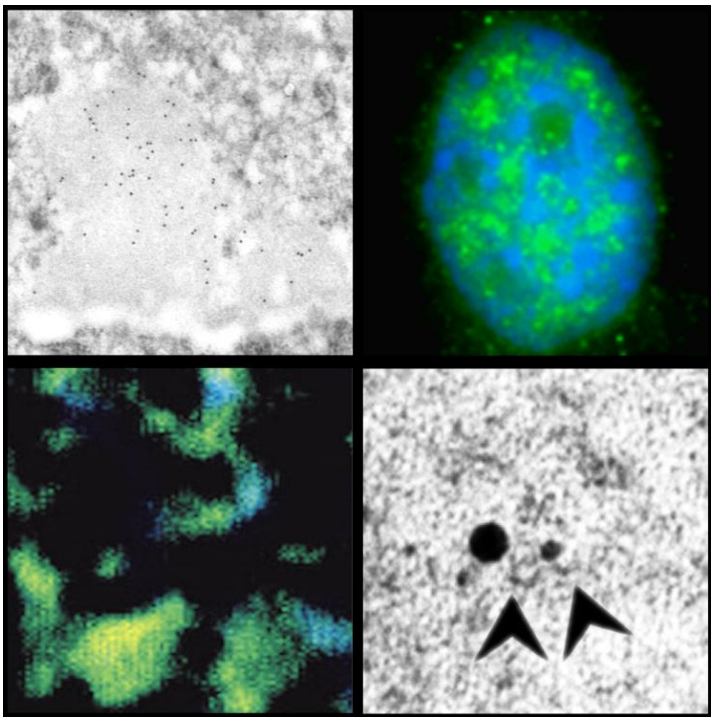

***Irene Masiello***

Dottorato di Ricerca in
Genetica, Biologia Molecolare e Cellulare
Ciclo XXX – 2014-2017

**UNIVERSITÀ DEGLI STUDI DI PAVIA**
Dipartimento di Biologia e Biotecnologie L. Spallanzani

# High-resolution epigenetic analysis of the cell nucleus

**PhD Student:** Irene Masiello
**Advisor:** Prof. M. Biggiogera

PhD Program in
Genetics, Molecular and Cellular Biology
XXX Cycle – 2014-2017

*Ai miei genitori,*

*A Matteo*

# ACKNOWLEDGEMENTS

First of all, I would like to sincerely thank my advisor Prof. Marco Biggiogera for embracing me in this laboratory three years ago, for his continuous scientific support and for believing in me. However, I am also glad to have shared funny moments with him.

Thanks to Prof. Carlo Pellicciari and Prof. Maria Grazia Bottone likewise for the help and useful suggestions. Thanks also to Ms Gloria Milanesi, Ms Francine Flach and Ms Paola Veneroni for their technical support.

I am very grateful to my colleagues, Valentina, Beatrice, Silvia, Sara, Laura, Stella, Erica and all the other met during my PhD, to have shared with me laboratory life. A special thanks to Violetta and Caterina not only to have faced with me scientific problems but also for their friendship. I would like to extend my thanks to all the people I met during my experience in Mainz, especially Dr. J. Y. Roignant.
In particular, my warm thanks are addressed to all my students, Claudio, Marzia, Monah, Valentina B and Valentina T, for their hard work without which this PhD thesis would be different.

By now, I would like to thank my family, in particular my sweet mum, for their support during this “adventure” and for making feel their love always, even miles away when I needed them most.
Thanks to my friends, even the ones present only in my heart, for simply being my friends.
Thanks Matteo to have understood my choice, for your patience and sacrifices and for making me stronger but loved!

Finally, thanks to me for my determination and perseverance which allowed me to never give up and go back home!

# CONTENTS

ABSTRACT ..... 1
ABBREVIATIONS ..... 3
1. REVIEW OF THE LITERATURE ..... 7
*1. THE STRUCTURE OF CHROMATIN* ..... 7
*2. REGULATION OF CHROMATIN STRUCTURE AND GENE EXPRESSION* ..... 13
*2.1. The epigenetic modifications* ..... 14
2.1.1. DNA methylation ..... 14
2.1.2. Histone modifications ..... 18
*2.2. The chromatin remodeling* ..... 23
*2.3. The role of ions* ..... 24
2.3.1. Ca and Mg effect on epigenetic modifications ..... 27
*2.4. Other processes* ..... 28
*3. THE STRUCTURE OF RNA AND ITS MODIFICATIONS* ..... 30
*4. TECHNICAL APPROACHES TO STUDY EPIGENETIC MODIFICATIONS* ..... 38
2. AIM OF RESEARCH ..... 43
3. MATERIALS AND METHODS ..... 45
*1. CELLS, TISSUES AND TREATMENTS* ..... 45
*1.1. Cells in vitro* ..... 45
1.1.1. Cells for EM immunocytochemistry ..... 45
1.1.2. Cells for EM morphological analysis ..... 46
1.1.3. Cells for fluorescence immunocytochemistry ..... 46
*1.1. Tissues* ..... 47
*1.2. Treatments* ..... 47
1.2.1. Fluorouridine incubation ..... 47
1.2.2. Incubation with different concentrations of divalent cations ..... 47
1.2.3. Heat shock ..... 49
*2. EM ANALYSIS* ..... 49
*2.1. EM immunocytochemistry* ..... 49
*2.2. EM in situ hybridization* ..... 51
*2.3. Staining procedures* ..... 51
*3. FLUORESCENCE IMMUNOCYTOCHEMISTRY* ..... 52
*4. ELECTRON SPECTROSCOPIC IMAGING* ..... 53
*5. STATISTICAL ANALYSIS* ..... 55
*5.1. Analysis of the optical density* ..... 57
*6. ANALYSIS OF NOVEL COMPONENTS OF m6A-METHYLTRANSFERASE COMPLEX* ..... 58

*6.1. Drosophila stocks and cell line* ....58
*6.2. Quantification of transcript level* ....59
6.2.1. RNA isolation and cDNA synthesis ....59
6.2.2. qPCR ....59
*6.3 Detection of protein localization* ....60
6.3.1. Cloning ....60
6.3.2. Transfection ....61
6.3.3. Immunolabelling ....61
*6.3. Characterization of interacting proteins* ....63
4. RESULTS ....65
*1. REGULATION OF CHROMATIN STRUCTURE – I PART* ....65
*1.1. DNA methylation analysis* ....65
*1.2. EM analysis of histone modifications* ....68
*2. REGULATION OF CHROMATIN STRUCTURE – II PART* ....71
*2.1. Ionic environment, epigenetic modifications and chromatin condensation* ....71
2.1.1. DNA methylation analysis ....71
2.1.2. Histone modification analysis ....78
2.1.3. ESI analysis ....80
*2.2. Heat shock, epigenetic modifications and chromatin condensation* ....83
*2.3. Epigenetic modifications during erythropoiesis* ....86
2.3.1. DNA methylation changes during erythropoiesis ....87
2.3.2. Variation of histone modifications during erythropoiesis ....88
*3. RNA METHYLATION* ....89
*3.1. 5mC detection on RNA fibrils and RNA-containing granules* ....90
3.1.1. DNMT3A localization on RNA fibrils and granules ....92
*3.2. Nucleolar distribution of 5mC* ....92
*3.3. m6A localization at EM* ....93
*4. HAKAI AND CG7358 CHARACTERIZATION IN Drosophila melanogaster* ....97
5. DISCUSSION ....101
6. CONCLUSIONS AND PERSPECTIVES ....109
7. REFERENCES ....111
LIST OF ORIGINAL MANUSCRIPTS ....123
CONGRESS COMMUNICATIONS ....125

# ABSTRACT

In the eukaryotic interphase nucleus, DNA is necessarily organized around the histone core and, then, in higher order structures. At the electron microscope, dispersed euchromatin fibers and dark heterochromatin regions can be distinguished. The latter is divided in constitutive heterochromatin, reasonably localized nearby the nuclear envelope and far from the perichromatin region where transcription occurs, and facultative heterochromatin, containing the genes undergoing silencing and activation (regulated genes) on the surface facing the perichromatin region. Chromatin structure affects numerous and fundamental genetic processes and, therefore, it is strictly regulated by different mechanisms. DNA methylation prevents the binding of transcriptional factors and recruits transcriptional repressor complexes, thus forming compact and inactive chromatin, although recent studies show 5-methylcytosine to reduce nucleosome stability. 5-methylcytosine was also found in the 3' untranslated regions to probably influence mRNA stability. Histone post-transcriptional modifications can lead both to a more compact or relaxed chromatin structure by inducing nucleosome repositioning: for instance, H3K9me3 is known as a marker of constitutive heterochromatin while H3K27me3 or H4K20me3 label facultative heterochromatin. The ionic environment is also known to profoundly affect chromatin organization: an increase of calcium or magnesium results in different types of chromatin conformations with different stability.

Until now, DNA or RNA methylation, as well as histone modifications, was studied through biomolecular approaches. Here, we propose an alternative epigenetic analysis at ultrastructural level, using mouse hepatocytes to describe the distribution of 5-methylcytosine and histone modified residues

on condensed chromatin regions and HeLa cells in order to detect epigenetic modifications on RNA fibrils. Treatments known to induce chromatin compaction (modification of cation concentration or heat shock) were also chosen to deeply investigate chromatin structure regulation. Therefore, cells and tissues were prepared principally for the cytochemical analysis, combining numerous immunocytochemical reactions with specific staining methods.

Although the regulation of chromatin organization is a complex process and more variables have to be considered, our results suggest that the main function of DNA methylation and histone modifications is the gene switching-on and -off, which occurs on chromatin surface. However, these modifications do not seem necessarily involved in the maintaining of chromatin condensation status, probably preserved by other mechanisms to be further investigated. As for RNA, our data indicate that cytosine methylation is a very precocious event, probably confirming its involvement in mRNA stability, and DNMT3A is unexpectedly involved in this modification.

Additional studies will be carried out to understand the processes regulating chromatin structure and the role of mRNA methylation. The influence of the ionic environment on both chromatin structure and the epigenetic modifications should be further studied.

# ABBREVIATIONS

**5caC:** 5-carboxylcytosine
**5fC:** 5-methylcytosine
**5hmC:** 5-hydroxymethylcytosine
**5mC:** 5-methylcytosine
**7mG:** 7-methylguanosine
**A:** adenine
**ALKBH5:** alkylation repair homolog 5
**ALYREF:** Aly/R export factor
**AM:** active modification
**AR:** active restoration
**ATF4:** mammalian activating transcription factor 4
**Aza-IP:** 5-azacytidine mediated RNA immunoprecipitation
**BER:** base excision repair
**BSA:** bovine serum albumin
**btz:** barentsz
**C:** cytosine
**CA:** calcium-concentrated solution/sample
**CAMK:** calcium-calmodulin kinase
**ChIP:** chromatin immunoprecipitation
**CoIP:** co-immunoprecipitation
**CTR:** control sample
**dCTP:** deoxycytidine triphosphate
**DFC:** dense fibrillar component
**DGS:** donkey goat serum
**DMEM:** Dulbecco’s minimal essential medium
**dMettl14:** Drosophila methyltransferase-like 14
**DNA:** deoxyribonucleic acid
**DNMTs:** DNA methyltransferases
**DTT:** dithiothreitol
**EDTA:** ethylenediaminetetraacetic acid
**Egta:** calcium- and magnesium-free solution/sample
**EGTA:** ethylene glycol-bis(β-aminoethyl ether)-N,N,N',N'-tetraacetic acid
**EM:** electron microscope
**EMISH:** electron microscopy in situ hybridization

**ESI:** electron spectroscopic imaging
**F:** forward oligonucleotide
**FBS:** foetal bovine serum
**FC:** fibrillar center
**Fl(2)d:** female lethal d
**FRAXA:** fragile X syndrome
**FTO:** fat mass and obesity associated protein
**FU:** fluoro-uridine
**G:** guanosine
**GC:** granular component
**GFP:** green fluorescence protein
**Gt:** glutaraldehyde
**HA:** human influenza hemagglutinin
**HAP:** hnRNP A1 associated protein
**HATs:** histone acetyltransferases
**HDACs:** histone deacetylases
**Hepes:** 4-(2-hydroxyethyl)-1-piperazineethanesulfonic acid
**HKMTs:** histone lysine methyltransferases
**HMTs:** histone methyltransferases
**HP1:** heterochromatin protein 1
**hpf:** hours post-fertilization
**HPLC:** high-performance liquid chromatography
**HRP:** horseradish peroxidase
**HS:** heat shocked sample
**HSF1:** heat shock transcription factor 1
**IG:** interchromatin granules
**Ime4:** inducer of meiosis 4
**KIAA1429:** vir-like m6A methyltransferase associated protein
**LC-MS:** liquid chromatography and mass spectrometry
**LDS:** lithium dodecyl sulfate
**m6A:** 6-methyladenosine
**MBDs:** methyl CpG binding proteins
**MeCP2:** methyl CpG binding protein 2
**MeFISH:** methylation-specific fluorescence in situ hybridization
**METTL3/14:** methyltransferase-like 3/14
**MG:** magnesium-concentrated solution/sample

**miCLIP:** methylation individual nucleotide resolution crosslinking immunoprecipitation
**MS:** mass spectrometry
**MTases:** methyltransferases
**NGS:** normal goat serum
**nito:** spenito
**nito:** spenito
**NP-40:** nonyl-phenoxypolyethoxylethanol
**OA:** osmium ammine-B
**OD:** optical density
**Oligo:** oligonucleotides
**ON:** overnight
**PBS:** phosphate buffered saline
**PBT:** PBS-Tween20
**PBTB:** PBS-Tween20-BSA
**PBTX:** PBS and Triton X
**PCR:** polymerase chain reaction
**PD:** passive dilution
**PF:** perichromatin fibrils
**PFA:** paraformaldehyde
**PG:** perichromatin granules
**PK:** proteinase K
**PMSF:** phenylmethylsulfonyl fluoride
**Pol II:** RNA polymerase II
**$PP_i$:** pyrophosphate
**PR:** perichromatin region
**PRMTs:** protein arginine methyltransferases
**PTMs:** post-transcriptional modifications
**PWS:** Prader-Willi syndrome
**qPCR:** quantitative polymerase chain reaction
**R:** reverse oligonucleotide
**RIP:** RNA immunoprecipitation
**RISC:** RNA inducing silencing complex
**RNA:** ribonucleic acid
**RNP:** ribonucleoprotein
**RT:** room temperature
**S2R+:** Drosophila Schneider 2 cells

**SAH:** S-adenosylhomocysteine
**SAM:** S-adenosyl-L-methionine
**SLE:** systemic lupus erythematosus
**SSC:** saline sodium citrate
**SWI/SNF:** switch/sucrose non-fermentable
**T:** thymine
**T:** tween20
**TDG:** thymidine DNA glycosylase
**TEM:** transmission electron microscope
**TETs:** ten-eleven translocation enzymes
**TLC:** thin layer chromatography
**TRIS:** 2-Amino-2-(hydroxymethyl)-1,3-propanediol
**U:** uracil
**UTRs:** untranslated regions
**vir:** virilizer
**WTAP:** Wilms tumour 1-associated protein
**α-KG:** α-ketoglutarate
**ΔE:** energy loss

# 1. REVIEW OF THE LITERATURE

## 1. *THE STRUCTURE OF CHROMATIN*

The deoxyribonucleic acid (DNA) is formed by two interwound strands. Each strand is a polymer of repeating subunits, called nucleotides. One nucleotide is composed of a phosphate group, a deoxyribose (a five-carbon sugar) and a nitrogenous base – the chemical structures of these basic components are shown in **Fig. 1.1**.

Each DNA filament is formed in three steps. First, the base is chemically linked to one molecule of sugar at the 1′-carbon, forming a nucleoside; when a phosphate group is also attached to the 5′-carbon of the same sugar, the nucleoside becomes a nucleotide. Finally, nucleotides are joined to form a DNA chain by a 5′ → 3′ phosphodiester bond (**Fig. 1.2**). Each DNA strand shows a chemical polarity, indicated by referring to the ends as 5′ or 3′ end. Thermodynamically stable hydrogen bonds form

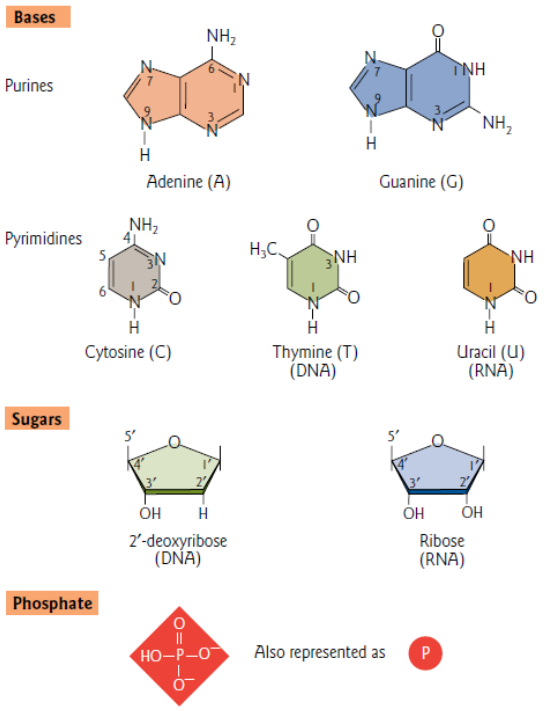


**Figure 1.1. Components of nucleic acids.** Bases are divided into purines and pyrimidines; primes are used to number the sugars, differentiating them from bases; phosphate groups are negatively charged.

(*Allison 2007*)

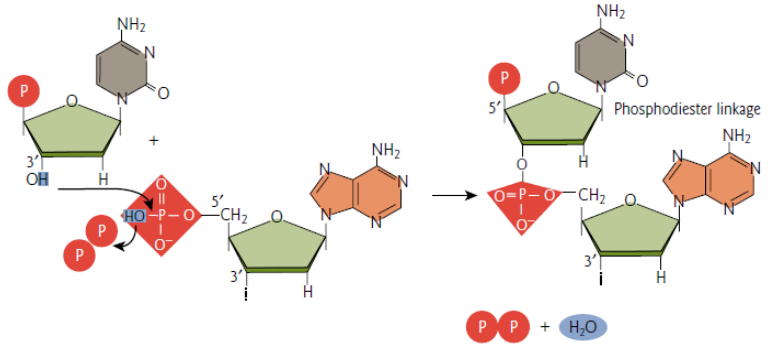


**Figure 1.2. Formation of a nucleic acid chain.** Two adjacent nucleotides are linked by 5′→3′ phosphodiester bond. The condensation reaction occurs between the 3′ OH of the sugar and the 5′ P of the second nucleotide involving the removal of a $H_2O$ molecule and a pyrophosphate.

(*Allison 2007*)

between the nitrogenous bases on the two DNA chains, which are antiparallel, namely the polarity of one strand is opposite oriented to that of the other strand (**Fig. 1.3**). The hydrogen bonding is referred to "Watson–Crick" or "complementary" base pairing. This occurs between adenine (A) and thymine (T) by two hydrogen bonds or guanine (G) and cytosine (C) by three hydrogen bonds (**Fig. 1.3**). The paired and relatively flat bases stack on top of one another, eliminating any gaps between the bases and excluding the maximum amount of water from the interior of the double helix. Therefore, a double-stranded DNA molecule has a hydrophobic core and a hydrophilic backbone due to sugars and phosphates oriented towards the outside of the polymer, where the charged phosphate groups can interact with the polar environment. The sugar-phosphate backbone is not equally spaced resulting in the major and minor DNA grooves (**Fig. 1.3**): the major groove has a significant role in sequence specific DNA-protein interactions whereas the minor groove is less informative. Therefore, DNA is simply a long and regular sequence of base pairs organized into a ladder-like and double-helical structure.

Three fundamental types of DNA double helix are known: B-, A- and Z-DNA (**Table 1.1**). Since the cell environment is mostly water with relatively low salt concentration, the predominant form in vivo is B-DNA. Moreover, unusual secondary structures, such as slipped structures, cruciforms and triple helix DNA, exist and are generally sequence-specific.

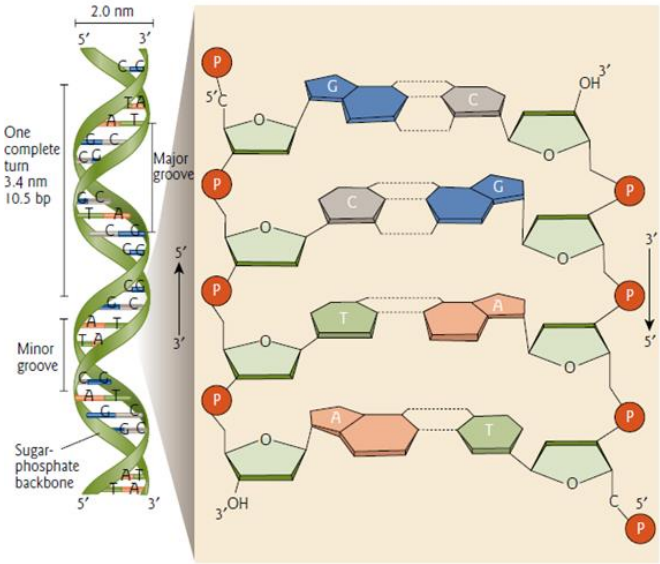


**Figure 1.3. DNA double helix.** Watson and Crick pairs occur between adenine and thymine by two hydrogen bonds or between guanine and cytosine by three hydrogen bonds. The two DNA chains are antiparallel. The internal bases are stacked perpendicularly to the helix axis while minor and major grooves are visible on the sugar-phosphate backbone on the helix outside.

(*Allison 2007*)

| | A-DNA | B-DNA | Z-DNA |
|---|---|---|---|
| **Orientation** | Right-handed | Right-handed | Left-handed |
| **Major groove** | Deep and narrow | Moderate depth, wide | Very shallow, virtually nonexistent, sometimes called a "single groove" |
| **Minor groove** | Shallow and broad (superficial) | Moderate depth, narrow | Very deep and narrow |
| **Bases/turn** | 11 | 10.5 | 12 |
| **Conditions** | Low humidity (75%), high salt | High humidity (95%), low salt | High $MgCl_2$ (> 3 M), NaCl, or ethanol In the presence of methylated cytosine: high humidity and low salt |

**Table 1.1. Parameters of the alternative forms of the DNA double helix.**

(*Allison 2007*)

Eukaryotic cells contain approximately 2 m of DNA into the spherical nucleus, which shows less than 10 µm diameter. Therefore, linear DNA molecules must be packed: each molecule is first coiled around a histone complex constituting a chromatin fiber, which forms a zig-zag string folded into loop domains and, finally, metaphase chromosomes (**Fig. 1.4**).

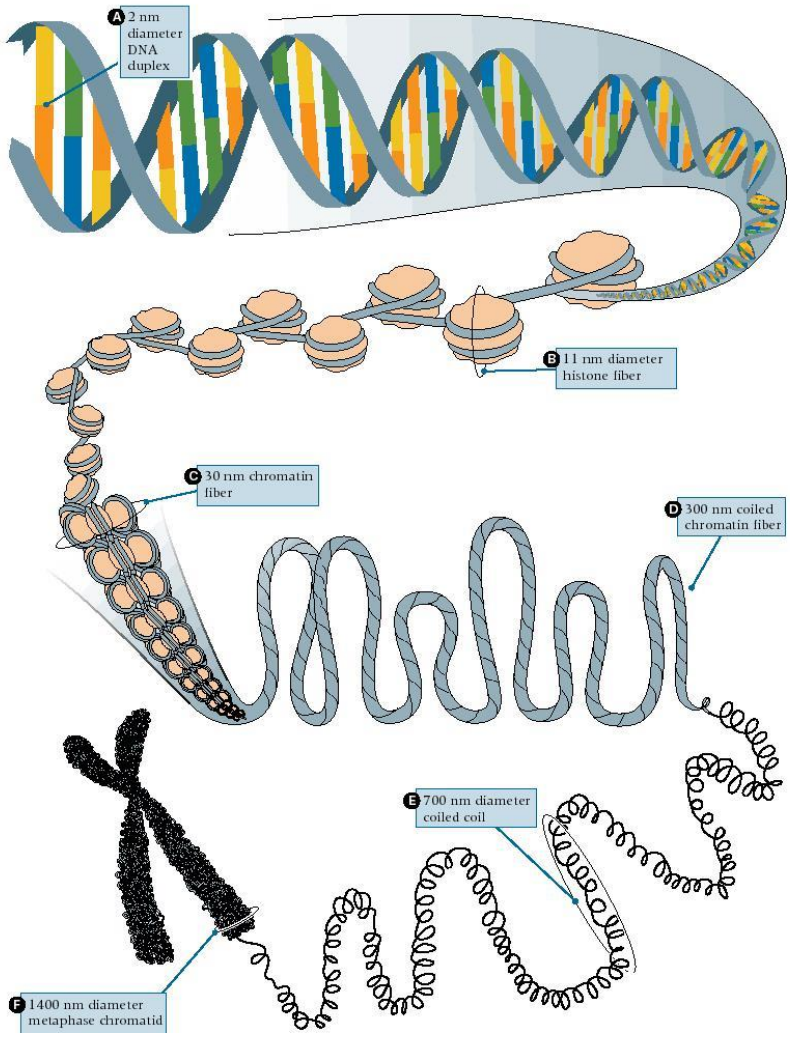


**Figure 1.4. DNA organization in higher order structures.** DNA is necessarily packed within the nucleus. DNA double helix is organized around a histone octamer forming the 10 nm fiber which is folded into the 30 nm fiber. The latter forms large loops attached to a protein scaffold, which progressively organize into the chromosome.

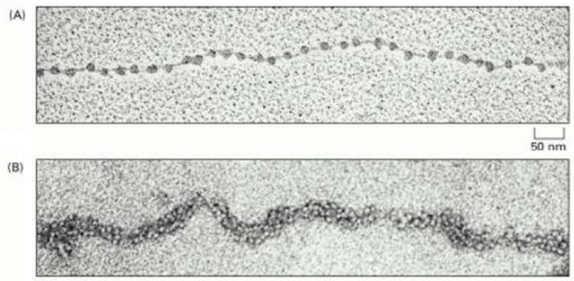


**Figure 1.5. Chromatin fibers. A.** An EM image shows the 10 nm chromatin fiber organized as beads on a string. **B.** Chromatin isolated from an interphase nucleus appears at EM as a thread 30 nm thick.

(*Alberts et al. 2008*)

Numerous proteins are involved in the DNA packaging – in addition, many proteins and RNA molecules are associated to the chromatin for the processes of gene expression, DNA replication and DNA repair.

Histones are relatively small, positive and highly conserved proteins. They are responsible for the first and most basic level of chromatin packing, discovered in 1974. In fact, these proteins form a histone complex composed of two molecules of each histone (H2A, H2B, H3 and H4). 146 bp of DNA, called core DNA, are wrapped around the histone octamer forming the nucleosome. The linker histone H1 sits on the top of the structure and keeps DNA in place, interacting also with the linker DNA – however, it is not required for this level of packing. The linker DNA lies between two nucleosomes and can vary in length from a few nucleotide pairs up to about 80. Electron microscope (EM) images of the eukaryotic genome clearly show beads on a string, visualized as a 10-11 nm fiber (*Alberts et al., 2008*) (**Fig. 1.5 A**). The beads represent DNA wrapped around the histone core while the string the linker DNA. The formation of nucleosomes shortens a DNA molecule to about one-third of its initial length.

Chromatin in a living cell rarely adopts the form of beads on a string: in fact, the nucleosomes are packed on top of one another, generating regular arrays in which the DNA is more condensed. Thus, when nuclei are very gently lysed onto an EM grid, most of the chromatin shows the form of a fiber with a diameter of about 30 nm (**Fig. 1.5 B**). This conformation is poorly understood due to its difficult maintaining in vitro. However, two models describe the 30 nm fiber (**Fig. 1.6**): the classic solenoid model involves consecutive nucleosomes arranged in a turn of a helix; the recent model suggests that nucleosomes adopt a zig-zag structure that twists or supercoils. To maintain this structure, histone tails promote the nucleosome

to nucleosome linkage, most notably the H4 tail, and histone H1 also plays an important role.

The 30 nm fiber is further compacted into more complex structures. It forms looped domains containing 50-100 kb of DNA attached to proteins associated with the nuclear scaffold. The final condensation during the metaphase leads to chromosomes and requires a number of ATP-hydrolyzing enzymes, including topoisomerase II. A fully condensed metaphase chromosome consists of two sister chromatids connected at the centromere.

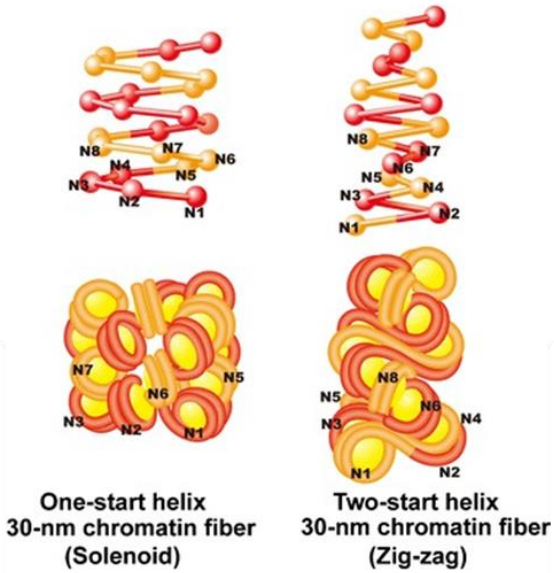


**Figure 1.6. 30 nm chromatin fiber.** Two classical models of 30 nm chromatin fibers are shown. The solenoid model involves consecutive nucleosomes in a turn of a helix. The zig-zag model suggests that nucleosomes adopt a structure forming twists or supercoils. This organization is due to histone tails and histone Hl.

(*Maeshima et al. 2014*)

In the interphase nucleus, chromatin is present in two different forms, reflecting the level of cell activity. Heterochromatin is a tightly packed form of DNA, functionally divisible in constitutive and facultative heterochromatin. Constitutive heterochromatin may regulate the genes near itself, is usually repetitive and forms functional structures, such as centromeres or telomeres. Facultative heterochromatin shares the compact structure of constitutive heterochromatin and is the result of genes that were silenced but that can become transcriptionally active under specific stimuli.

Euchromatin is a lightly packed form of chromatin enriched in genes that are under active transcription – probably euchromatin shows the structure of beads along the string.

At EM heterochromatin appears in numerous compact domains, which are irregular and darkly stained, nearby the nuclear envelope and around nucleoli (*Brown et al. 1997; Francastel et al. 1999; Lundgren et al. 2000; Cmarko et al. 2003*). Transcriptionally active loci constitute the euchromatin, which appears as dispersed and not simply detectable fibers and is localized at the surface of compact chromatin domains in the perichromatin region or toward the interchromatin space (*Fakan 1994; Puvion and Puvion-Dutilleul 1996; Spector 1996; Cmarko et al. 1999*).

## *2. REGULATION OF CHROMATIN STRUCTURE AND GENE EXPRESSION*

Chromatin structure is fundamental for gene expression but also for other biological processes, i.e. DNA replication and repair, apoptosis and chromosome segregation. In fact, chromatin condensation affects the accessibility of protein complexes involved in the cited processes, such as transcription factors. Consequently, chromatin structure plays a central role in the development, growth and maintenance of eukaryotic organisms. Alterations of chromatin remodelling are associated with human diseases, including cancer and, in fact, one of the therapeutic strategies consists in the targeting of chromatin remodelling pathways.

Chromatin structure and functionality are regulated by epigenetic modifications and chromatin remodelling mechanisms and are also affected by the surrounding environment.

## 2.1. The epigenetic modifications

In 1942, epigenetics was defined as "the branch of biology studying the causal interaction between genes and their products which bring the phenotype into being". Nowadays, epigenetic research concerns the study of heritable changes in gene expression without changes in DNA sequence.

The major type of DNA modification is cytosine methylation. However, There are other important epigenetic markers, first of all the histone modifications.

### 2.1.1. DNA methylation

In eukaryotes, DNA methylation is the major epigenetic modification and one of the most important events occurring in vivo.

This modification occurs at position 5 of a cytosine in the context of a CG-dinucleotide, although sometimes non-CpG methylation is also observed (*Li et al. 2015*). Regions of high CG density are called CpG islands and they are mainly located in the 5' promoter ends of genes. However, cytosine methylation also occurs in the coding region of highly expressed genes, so that up to 4.25% of cytosines in the human genome are methylated.

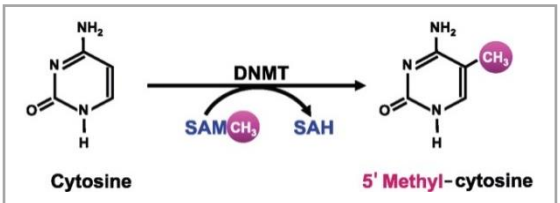


**Figure 1.7. DNA methylation.** A methyl group is transferred from SAM to a cytosine in CpG island by DNMT, producing 5mC.

DNA methylation is mediated by DNA-methyltransferases (DNMTs), which transfer a methyl group from S-adenosyl-L-methionine (SAM) to DNA cytosine, creating 5-methylcytosine (5mC) (**Fig. 1.7**). The DNMTs belong to a highly conserved protein family (*Zhang and Xu 2017*), where DNMT1, DNMT3A and DNMT3B were firstly identified (*Zhang and Xu 2017*). DNMT1 is required for the maintenance of the methylation pattern: during DNA replication, DNMT1 methylates the daughter strand in

accordance with the methylated sites of the parental DNA (*Li and Zhang 2014*). DNMT3A and DNMT3B are known as de novo methyltransferases because they are responsible for establishing new methylation patterns during embryogenesis, setting up genomic imprints during cell development and modulating gene expression (*Li and Zhang 2014*). These two proteins have distinct functions, showing both spatial and temporal differences (*Li and Zhang 2014; Smith and Meissner 2013*). Recently, a new de novo DNA methyltransferase, DNMT3C, was identified in murine germ cells, methylating the young retrotransposons (*Barau et al. 2016*). The DNMT family also includes two additional members: DNMT2 is not currently considered a DNA methylase whereas it methylates tRNAs (*Goll et al. 2006*); DNMT3L does not show a catalytic activity but it is an important regulator, which facilitates cytosine methylation operating in the form of heterotetramers with DNMT3A (*Chen and Li 2004*). Both the establishment and maintenance of global genomic methylation are necessary for cell proliferation and differentiation.

An active demethylation pathway exists. Methylated marks can be erased by three sequential steps of oxidation of 5mC to 5-hydroxymethylcytosine (5hmC), 5-formylcytosine (5fC) and 5-carboxylcytosine (5caC). This oxidation reaction is performed by ten-eleven translocation enzymes (TETs); a mechanism of base excision repair removes 5fC or 5caC to replace cytosine (*Kohli and Zhang 2013; Pastor et al. 2013; Wu and Zhang 2014*) (**Fig. 1.8**). However, these modified nucleotides are also known to affect DNA flexibility, nucleosome stability and, consequently, gene expression (*Ngo et al. 2016*).

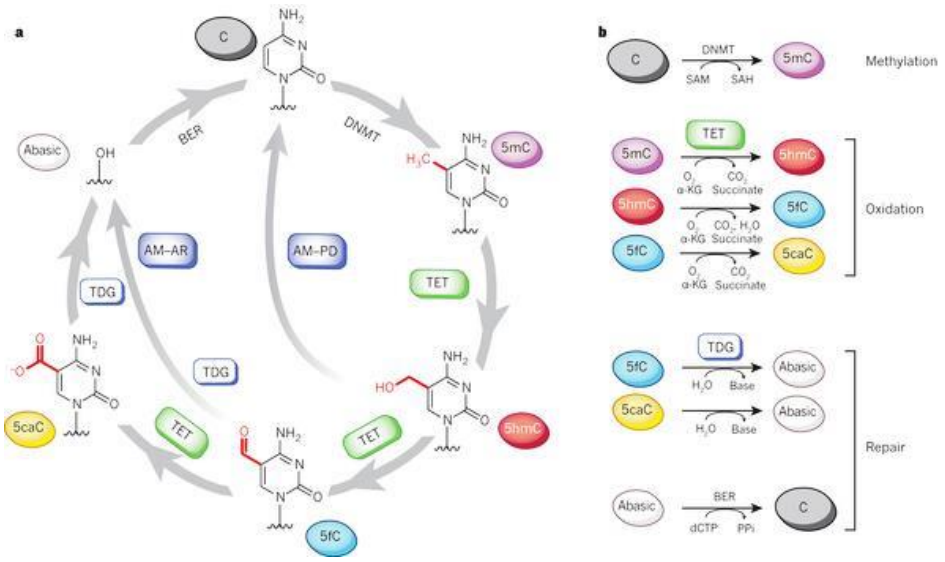


**Figure 1.8. Demethylation pathway. A.** 5mC can be consecutively oxidized to 5hmC, 5fC and 5caC by TETs. The active modification (AM) can be followed by passive dilution (PD) to convert 5hmC in unmodified C in a replication-dependent manner. In the AM followed by active restoration (AR), 5fC or 5caC is excised by thymidine DNA glycosylase (TDG) generating an abasic site. A process of base excision repair (BER) regenerates unmodified C. **B.** The individual reactions in the pathway are shown (α-ketoglutarate, α-KG – S-adenosylmethionine, SAM – S-adenosylhomocysteine, SAH – deoxycytidine triphosphate, dCTP – pyrophosphate, PPi).

(*Kohli and Zhang 2013*)

DNA methylation affects gene expression in two possible ways. First, 5mC itself prevents the binding of transcriptional factors to the gene by changing the consensus motif (*Choy et al. 2010*). Moreover, methylated DNA is recognized by proteins known as methyl-CpG-binding domain proteins (MBDs) which recruit transcriptional repressor complexes, including histone deacetylases (HDACs): The latter modify histones, thus forming compact and inactive chromatin (*Ferguson et al. 2011*) (**Fig. 1.9**). This modification is also involved in other processes, like X-chromosome inactivation and genomic imprinting, and controls chromosome stability (*Hendrich and Bird 1998; Robertson 2005*); it plays an essential role in mammalian embryonic development (*Li et al. 1992*). However, recent

works showed that the bulky methyl groups restrict the DNA conformational fluctuations of the structural parameters, increasing DNA stiffness: this 5mC reduction of DNA flexibility suppresses DNA looping around the histone complex, facilitating the loosening of DNA ends to obtain a more open nucleosome conformation (*Jimenez-Useche and Yuan 2012; Ngo et al. 2016*). Moreover, a reduced mechanical stability of nucleosomes containing many copies of 5mC was shown. Therefore, although until now DNA methylation was considered to lead to a more compact chromatin structure, as described above, it could be possible an opposite effect of 5mC on chromatin structure.

Alterations of DNA methylation are known to occur in several human diseases, such as imprinting disorders (Prader–Willi Syndrome, PWS) or repeat-instability disorders (Fragile X Syndrome, FRAXA) (*Robertson 2005*). Moreover, some human diseases can arise from mutations in the DNA methylation machinery (Systemic Lupus Erythematosus, SLE) (*Robertson 2005*). Alterations in the methylation pattern of coding gene promoters are implicated in tumorigenesis and cancer progression (*Esteller 2008; Suva et al. 2013; Feinberg et al. 2016*). In fact, hypermethylation of tumor suppressor genes as well as hypomethylation of oncogenes are known to be typically implicated in cancer developing (*Gonzalo 2010*).

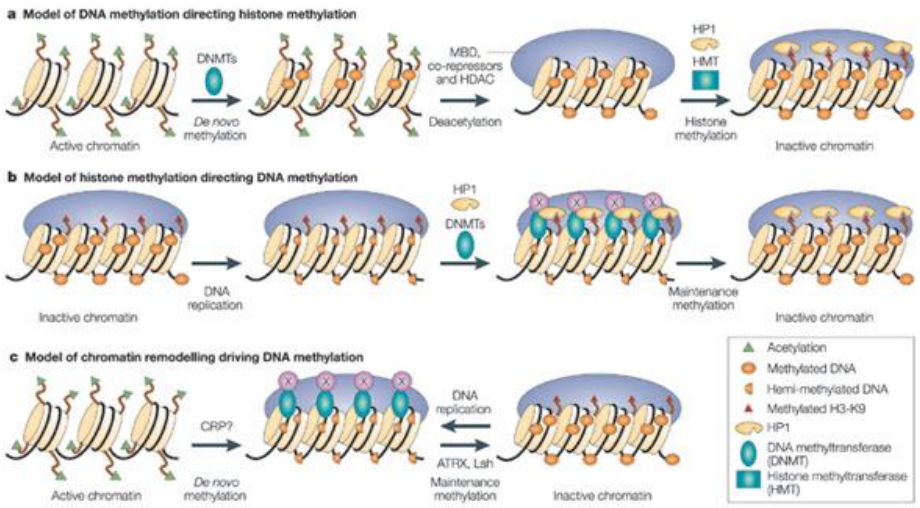


**Figure 1.9. DNA epigenetic modifications.** DNA methylation and histone modifications are considered interdependent processes. **A.** MBDs recognize the methyl group and recruit transcriptional repressors and HDACs, which induce histone deacetylation and, consequently, chromatin compaction and silencing. Moreover, histone methyltransferases (HMTs) are called methylating the histone H3 lysine 9 thus stabilizing the inactive chromatin state. **B.** However, histone methylation was also proposed to affect DNA methylation. In fact, H3K9me3 recruits heterochromatin protein 1 (HP1), which in turn binds DNMTs to maintain DNA methylation stabilizing the inactive chromatin. **C.** It was also shown that chromatin remodelling could drive DNA methylation and histone modification by unwrapping nucleosomal DNA to increase its accessibility for modifying enzymes.

(*Li 2002*)

### *2.1.2. Histone modifications*

As for DNA, histone can be post-translationally modified: a large number of histone post-translational modifications (PTMs) is known, including methylation, acetylation, phosphorylation and ubiquitylation (*Geiman and Robertson 2002*) (**Fig. 1.10**). The protruding histone N-terminal tails are the sites of active modifications. These affect inter-nucleosomal interactions and, consequently, chromatin structure and expression by merely being there and recruiting remodelling enzymes, which are responsible of nucleosome reposition (*Bannister and Kouzarides 2011*).

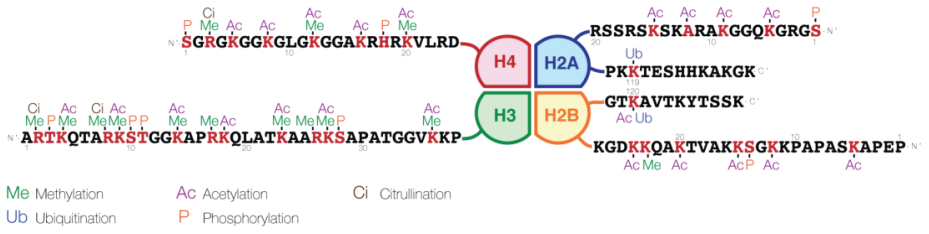


**Figure 1.10. Modifications on histone tails.**

Histone methylation mainly occurs on lysines and arginines without modifying the protein charge and can involve more than one methyl group. This modification can either increase or silence gene transcription depending on the methylated residue and the number of attached methyl groups; it could be also influenced by the vicinity of acetyl groups. In this view, whereas H3K9me3 is known to mark constitutive heterochromatin and H3K27me3 is a temporary signal associated to facultative heterochromatin, H3K4me2 and H3K4me3 are generally associated with transcriptional activation, although they can also repress transcription in particular conditions (*Bonnet-Garnier et al. 2012; Greer and Shi 2012*). H4K20me1 is involved in the chromatin compaction and in the consequent transcriptional repression, as for H4K20me3. The described effects of the histone tail methylation are mediated by proteins or protein complexes recruited on modified residues; in fact, it is unlikely that it can perturb chromatin structure since this modification is small and does not alter the charge of histones.

Numerous histone lysine methyltransferases (HKMTs) have been identified, all capable of transferring the methyl group from SAM to the ε-amino group of a lysine. On the other hand, there are two classes of arginine methyltransferases which catalyze the transfer of a methyl group from SAM to the ω-guanidine group of an arginine within a variety of substrates:

therefore, they are generally referred to as protein arginine methyltransferases (PRMTs).

Histone methylation was for a long time considered a stable modification. Then, some mechanisms were first suggested as possible demethylation pathways and later experimentally verified.

The acetylation of lysines is a highly dynamic and regulated process. This modification is mediated by histone acetyltransferases (HATs), utilizing acetyl-CoA for the transfer of an acetyl group to the ε-amino group of lysines. Histone acetylation, introducing a negative charge, effectively neutralize histone positivity, disrupting electrostatic interactions between histones and DNA and leading to a less compact chromatin structure, which facilitates DNA access by protein machineries involved in transcription. This effect is also mediated by chromatin-remodelling complexes bound to acetylated lysines (*Mujtaba et al. 2007; Zeng et al. 2010*). Therefore, H3K9ac and H3K27ac, for example, are associated with transcription activation.

Histone deacetylases reverse lysine acetylation, restoring the histone positive charge and the local compact chromatin structure, showing HDACs predominantly as transcriptional repressors (*Bannister and Kouzarides 2011*). DNA methylation can influence local histone acetylation: it was shown that the methyl-CpG binding protein 2, MeCP2, recruited by 5mC, binds HDAC, modifying chromatin architecture and inducing gene silencing (*Eden et al. 1998; Jones et al. 1998*).

Taking place on serines, threonines and tyrosines predominantly on H3 tail, the phosphorylation of histones is a highly dynamic event. The levels of this modification are controlled by kinases and phosphatases (*Oki et al. 2007*). All the identified histone kinases transfer a phosphate group from ATP to the hydroxyl group of the target amino-acid. However, it is unclear how the

enzyme recruitment to its specific site on chromatin occurs: possibly, a chromatin-binding factor mediates this association before the direct contact between the enzyme and DNA (*Bannister and Kouzarides 2011*).

As for acetylation, phosphorylation adds significant negative charge to the histone, undoubtedly reducing chromatin condensation. Furthermore, phosphorylated residues act as platforms for recruitment, assembly and retention of chromatin-associated factors and were suggested to induce H3 tail acetylation (*Rossetto et al. 2012*). Therefore, phosphorylation is generally associated with transcriptional activation, in particular of proliferative genes. The best known function of histone phosphorylation occurs during the cellular response to the DNA damage. Nevertheless, H3S10phos, as well as H2AT120phos, is involved in chromatin compaction during mitosis.

In contrast to the previously described histone modifications, ubiquitylation of lysines results in a larger covalent modification because ubiquitin is a polypeptide of 76 amino acids. The reaction is mediated by three enzymes, which can modulate the degree of ubiquitylation. Adding an extremely large molecule to a histone, ubiquitylation seems to induce a change in the nucleosome conformation, which in turn affects intra-nucleosomal interactions and interactions with other chromatin-binding complexes. Two well-characterized sites are in H2A and H2B: H2AK119ub1 is involved in gene silencing whereas H2BK123ub1 plays an important role in transcriptional initiation and elongation (*Wang et al. 2004; Lee et al. 2007; Kim et al. 2009*). The modification is reversible via the action of isopeptidases, called de-ubiquitin enzymes.

A cross-talk between different histone modifications exists through these following multiple mechanisms (*Kouzarides 2007*).

- A competitive antagonism between different modifications targeting the same site may be present.
- The protein binding to a specific modification can be disrupted by an adjacent modification.
- Cooperation between modifications could be present, recruiting efficiently specific factors.
- One modification may be dependent upon another.
- The modified site can alter the substrate of an enzyme whose activity will be compromised.

This interactions between different histone modifications represent the so called "histone code" (*Turner 2002; Peterson and Laniel 2004*), which is very important for transcriptional regulation and chromatin structure dynamics. In particular, there is an interconnection and interdependence between the modifications of the H3 and H4 tails.

Histone H3 seems to be intimately connected to DNA methylation status of the chromatin region in which it occurs. About that, different studies indicate that the establishment and maintenance of DNA methylation are dependent upon lysine 9 methylation of histone 3 (*Tamaru and Selker 2001; Jackson et al. 2002*). H3K9me1 is a binding site for the heterochromatin protein HP1 (*Bannister et al. 2001; Lachner et al. 2001*), the major component of heterochromatin, contributing to the maintenance of transcriptionally silent state and targeting DNMT3 to heterochromatin sites (*Bachman et al. 2001*).

Changes in histone epigenetic modifications can lead to cancer initiation and progression. As for DNA methylation, aberrant histone modification

profiles may actually give rise to cancer via at least two mechanisms (*Bannister and Kouzarides 2011*):

- aberrant regulation of gene expression of oncogenes or tumor suppressors;
- alterations of genome integrity and chromosome segregation.

| | |
|---|---|
| **H3K9me3** | HISTONE 3 TRIMETHYL-LYSINE 9 |
| **H3K27me3** | HISTONE 3 TRIMETHYL-LYSINE 27 |
| **H3K4me2** | HISTONE 3 DIMETHYL-LYSINE 4 |
| **H3K4me3** | HISTONE 3 TRIMETHYL-LYSINE 4 |
| **H4K20me1** | HISTONE 4 METHYL-LYSINE 20 |
| **H4K20me3** | HISTONE 4 TRIMETHYL-LYSINE 20 |
| **H3K9ac** | HISTONE 3 ACETYL-LYSINE 9 |
| **H3K27ac** | HISTONE 3 ACETYL-LYSINE 27 |
| **H3S10phos** | HISTONE 3 PHOSPHORILATED SERIN 10 |
| **H2AT120PHOS** | HISTONE 2A PHOSPHORILATED THREONIN 120 |
| **H2AK119ub1** | HISTONE 2A MONO-UBIQUITINILATED LYSIN 119 |
| **H2BK123ub1** | HISTONE 2B MONO-UBIQUITINILATED LYSIN 123 |
| **H3K9me1** | HISTONE 3 METHYL-LYSINE 9 |

**Table 1.2. Abbreviations of histone modifications.**

## *2.2. The chromatin remodelling*

The interaction between the histone core and DNA is also regulated by a process named chromatin remodelling, which creates nucleosome-free regions for gene expression. Chromatin remodelling consists of the following processes (*Wang et al. 2005*) (**Fig. 1.11**):

- nucleosome reposition (slide, twist and loop) – the position of a nucleosome changes along DNA;
- nucleosome remodelling – DNA becomes more accessible because the interaction with the histone core is reduced;
- nucleosome displacement or histone eviction – DNA and histones are completely disassociated;

- nucleosome replacement – the histone core is substituted by histone variants.

This process is mediated by ATP-dependent chromatin remodelling complexes, which have an ATPase domain. These latter use the energy from the hydrolysis of ATP to modify chromatin architecture. There are at least five families of chromatin remodelers in eukaryotes, including SWI/SNF (switch/sucrose non-fermentable) – the remodelling mechanism appears to be distinct from one family member to another.

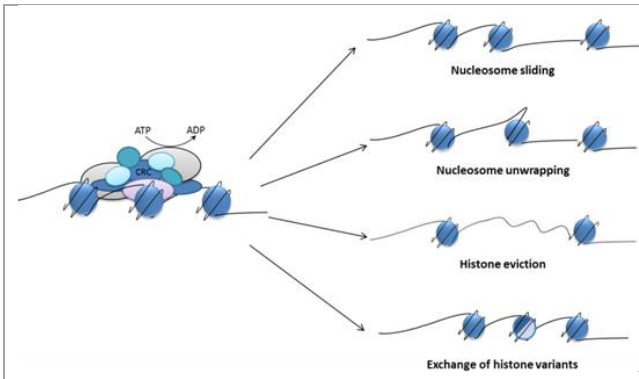


**Figure 1.11. Chromatin remodelling.** Change of nucleosome position (sliding), dissociation of DNA-histone interaction (unwrapping) and histone eviction alter the nucleosomal DNA accessibility to transcription factors. Histone variants can be also introduced into the nucleosome.

(*Zhong et al. 2013*)

## *2.3. The role of ions*

Several studies have demonstrated that chromatin organization depends on the concentration and type of ionic species (*Gan and Schlick 2010*).

The ionic atmosphere around the nucleosome core was described (*Davey et al. 2002; Gan and Schlick 2010*). The sodium ions ($Na^+$) form a layer along the DNA wound around the histone core, penetrating into the interior of the histone complex (*Materese et al. 2009*). Monovalent anions, principally the chlorine ions ($Cl^-$), interact with the positively charged regions of the nucleosome, i.e. the N-termini of histone α-helices, forming negligible small patches. Divalent ions, in particular magnesium ($Mg^{2+}$) and calcium ions ($Ca^{2+}$), form a dense layer around nucleosomal DNA and unburied regions

of histone tails, providing an enhanced screening compared to monovalent ions and completely covering the nucleosome core. Moreover, $Mg^{2+}$ extends also beyond the nucleosome surface shielding more effectively the DNA charge. It seems that specific binding sites for $Mg^{2+}$ and $Ca^{2+}$ ions exist (*Davey et al. 2002*).

The role of ion distribution in nucleosome stability has been demonstrated. The monovalent anion location suggests that they reduce the electrostatic interaction between histones and DNA (*Davey et al. 2002*). On the contrary, $Mg^{2+}$ and $Ca^{2+}$ neutralize the DNA charge, thus stabilizing histone-DNA interactions within the nucleosome core (*Materese et al. 2009; Korolev et al. 2010; Yang and Hayes 2011*). Instead, monovalent cations have been shown to not increase nucleosome stability (*Gan and Schlick 2010*).

The chromatin folding into more complex structure is profoundly influenced by the ionic environment. It was demonstrated that anions or monovalent cations are not requested for the chromatin folding. Even potassium ($K^{+}$) was shown to induce an unfolding of the chromatin fiber, probably because its specific localization inhibits the nucleosome-nucleosome interaction, thus preventing the condensation (*Korolev et al. 2010; Allahverdi et al. 2011*). On the other hand, due to the extended DNA neutralization within the nucleosome mediated by divalent ions, internucleosomal repulsions in higher order chromatin structures are diminished (*Materese et al. 2009*), facilitating the chromatin folding. Moreover, $Mg^{2+}$ and $Ca^{2+}$ lie on linker DNA and exposed chromatin surfaces, inducing the neutralization of these chromatin regions: this event promotes chromatin compaction and, consequently, its silencing.

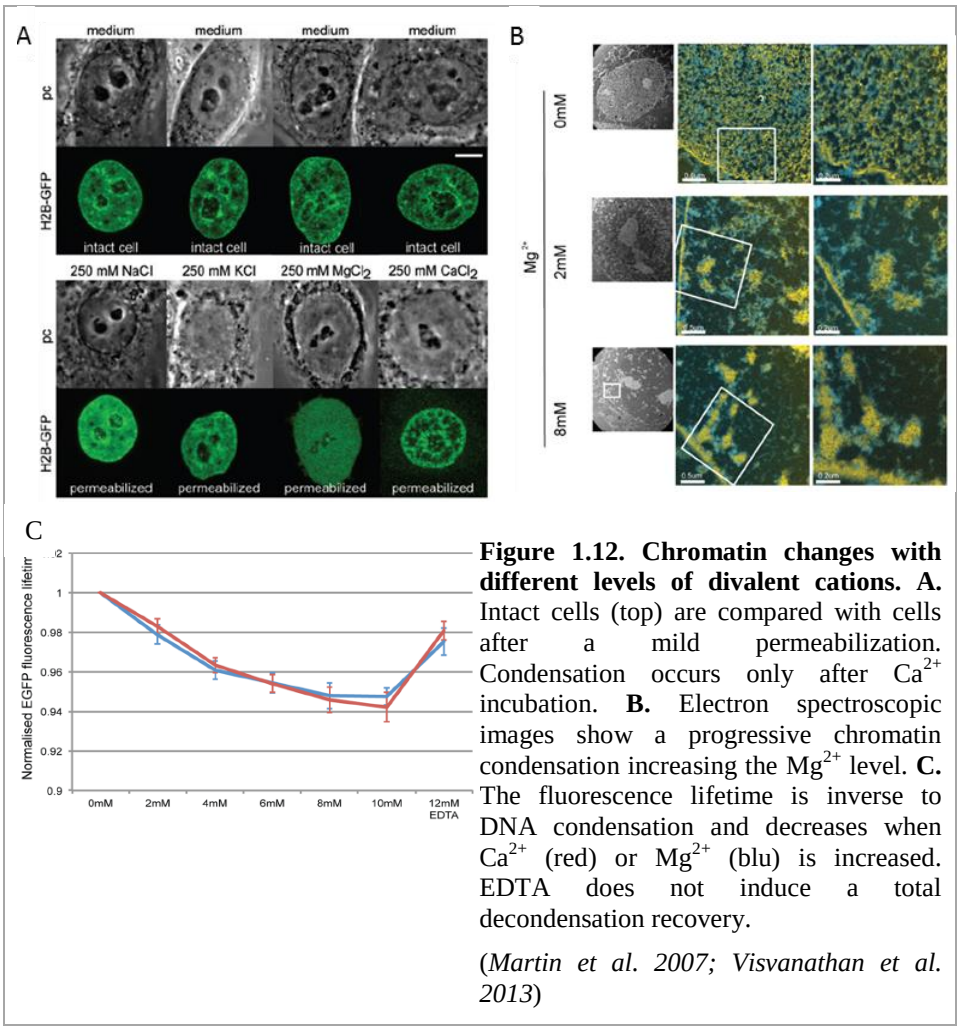


**Figure 1.12. Chromatin changes with different levels of divalent cations. A.** Intact cells (top) are compared with cells after a mild permeabilization. Condensation occurs only after $Ca^{2+}$ incubation. **B.** Electron spectroscopic images show a progressive chromatin condensation increasing the $Mg^{2+}$ level. **C.** The fluorescence lifetime is inverse to DNA condensation and decreases when $Ca^{2+}$ (red) or $Mg^{2+}$ (blu) is increased. EDTA does not induce a total decondensation recovery.

(*Martin et al. 2007; Visvanathan et al. 2013*)

The effect of either calcium or magnesium on chromatin condensation was described in several studies concerning the incubation with different level of these ions (*Caño et al. 2006; Martin et al. 2007; Visvanathan et al. 2013*). An increase of $Mg^{2+}$ and $Ca^{2+}$ results in different types of condensed chromatin structures with probably different stability; at the same time, the enlargement of the interchromatin space could be detected. It seems that even small changes in the level of intracellular divalent cations may affect chromatin condensation and, therefore, gene expression (**Fig. 1.12**). As for control, the effect of an excess of EDTA (ethylenediaminetetraacetic acid)

chelating free divalent ions was analyzed: it has been shown that EDTA treatment determines chromatin decondensation (**Fig. 1.12 C**), although the level of decompaction is not complete. This phenomenon could be explained in two ways: cations show a higher affinity for their multiple binding sites on chromatin compared to EDTA; the types of structural chromatin conformation may differently resist to reversal due to their different stability.

Finally, the effect of ions on the most condensed form of chromatin, chromosomes, was analyzed. $Ca^{2+}$, $Mg^{2+}$, $Na^{+}$ and $K^{+}$ map on chromatids: in particular, $Ca^{2+}$ is enriched in chromosomal DNA axis whereas $Mg^{2+}$ is homogenously distributed along the entire chromosome (*Strick et al. 2001*). Cells depleted of $Ca^{2+}$ and $Mg^{2+}$ showed partially decondensed chromosomes, underlining their involvement in the chromosome formation and maintenance (*Phengchat et al. 2016; Strick et al. 2001*). These ions seem to mediate an electrostatic neutralization and are responsible of interactions with non-histone proteins.

### *2.3.1. Ca and Mg effect on epigenetic modifications*

The ion effect on chromatin structure is reflected in the changes in chromatin functionality. The latter is also altered because the ion distribution around chromatin fibers can affect the interaction between DNA and transcription factors. Moreover, a relationship between calcium and epigenetic modifications was recently described, revealing a possible role of ions in the modifications of the epigenetic pattern. In fact, a recent study showed that the reactivation of epigenetically silenced tumor suppressor genes was dependent on $Ca^{2+}$ signaling and calcium-calmodulin kinase (CAMK) activation through the removal of MeCP2 from the repressed promoters – this protein is known to interact with HDACs (*Raynal et al. 2016*). Another study showed that an increase in the calcium level can

activate two kinds of kinases leading to an epigenetic change, i.e. histone hyperacetylation, along the body of the genes that contain calcium-responsive exons: this event determines chromatin decondensation increasing the transcriptional elongation rate of RNA polymerase II (Pol II) (*Sharma et al. 2015*). It also seems that $Ca^{2+}$ binding sites are present on DNMTs of vertebrates (*Wang et al. 2014*), suggesting a possible regulation pathway of DNA methylation mediated by $Ca^{2+}$-signaling.

## *2.4. Other processes*

Epigenetic modifications are probably the main processes regulating chromatin structure. As described above, the ionic environment also plays a very important role in the formation and maintenance of chromatin conformation. However, other mechanisms are documented to affect chromatin structure revealing this latter as a very complex aspect of cell biology.

- Although the definition of lncRNAs remains controversial, these are generally defined as long functional ribonucleic acids that do not encode proteins. In particular, some well-studied regulatory lncRNAs are known to control DNA methylation and histone modifications via the recruitment of DNMTs and histone-modifying enzymes (*Böhmdorfer and Wierzbicki 2015*). They also affect chromatin structure interacting with specific chromatin remodelers, which are responsible of the nucleosome positioning and chromosome looping (*Böhmdorfer and Wierzbicki 2015*).
- The reversible chromatin hypercompaction has been described when ATP levels are depleted both in interphase and mitotic cells (*Visvanathan et al. 2013*). Even though transcription is implicated in the maintaining of decompacted chromatin state and ATP depletion results

in the transcription inhibition, the ATP-dependent hypercondensation is not caused by the loss of transcription activity because the direct block of transcription did not lead to the same chromatin compaction. Therefore, other mechanisms are probably responsible of the chromatin conformation upon ATP depletion.

- Some experiments and simulations showed that the characteristic compact structure of metaphase chromosomes is conserved in a crowded media (*Hancock 2012*). This result revealed that a further unconsidered factor for chromatin compaction is represented by the crowding of macromolecules in the surrounding environment. In vivo, the crowding linear polymers could be the polynucleosome chains and the nucleosome-nucleosome interactions are some of the entropic forces, which may significantly contribute to the chromatin compaction.
- Several studies showed that the environmental cues can change the epigenetic modifications, resulting in long-term alteration of the gene expression (*Mazzio and Soliman 2012*). One of the well documented environmental stress is the heat shock, which is known to induce changes in the cell organization and function (*Richter et al. 2010*). The heterogeneous ribonucleoprotein (hnRNP) A1 associated protein, HAP, is generally associated to the perichromatin fibrils (PF): after heat shock, it is identified on clusters of perichromatin granules (PG), thus constituting HAP bodies (*Chiodi et al. 2000*). These bodies contain the heat shock transcription factor 1 (HSF1), the key transcription factor of the heat shock response whose levels are obviously increased after the treatment (*Weighardt et al. 1999*). During the heat stress, the activity of HSF1 induces the global deacetylation of histones, thus modulating the chromatin structure: consequently, condensed chromatin regions appear enlarged, especially around the nucleolus (*Fritah et al. 2009*).

## 3. THE STRUCTURE OF RNA AND ITS MODIFICATIONS

The role of RNAs as important factors in essential cellular processes, from DNA replication to protein synthesis, has become even clearer.

RNA (ribonucleic acid) shows a great structural versatility compared with DNA. It is a chain-like molecule composed by nucleotides joined by phosphodiester bonds (**Fig. 1.13**). Each subunit is formed by a ribose sugar, a phosphate group and a nitrogenous base – in RNA uracil (U) substitutes thymine (**Fig. 1.1**). Consequently, RNA differs from DNA for the presence of the ribose and uracil and for the single-stranded structure.

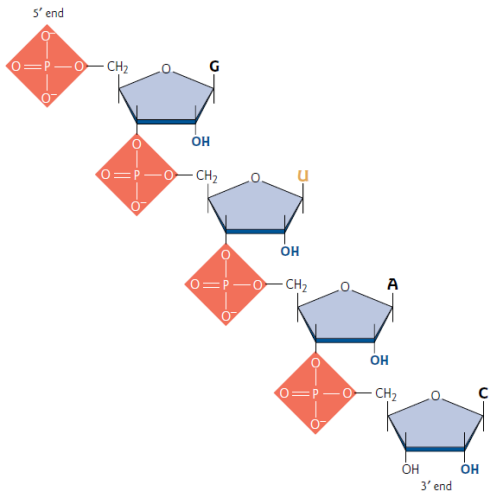


**Figure 1.13. RNA structure.** RNA is a single chain, contains uracil in place of thymine and has a hydroxyl group on the 2′ carbon of its sugar.

*(Allison 2007)*

The single-stranded RNA folds into a variety of secondary structures, stabilized by Watson–Crick base pairing, unconventional base pairing and base stacking hydrophobic interactions. Some of the common secondary structures are shown in **Fig. 1.14**: these include bulges, base-paired helices or stems, single-stranded hairpins or internal loops and junctions. For example, differently from DNA, RNA helix formation occurs within the single-stranded chain of nucleotides and the A-type RNA helix is present instead of the B-helix characteristic of DNA. A-RNA shows a deep major groove, which is not well suited for interactions with specific ligands, and a minor

groove, including the ribose 2′-OH groups, which are good hydrogen bond acceptors, making it accessible to RNA binding proteins.

Organized RNA secondary structural domains interact to form three-dimensional structures. Hydrogen bonding and base stacking interactions are involved in the formation of the tertiary structure together with a variety of long-range interactions. Since RNA is negatively charged, the formation of the three-dimensional structure also requires charge neutralization, either through the binding of basic proteins or of monovalent and divalent metal ions. Common RNA folding motifs include the pseudoknot, the A-minor motif, tetraloops, ribose zippers and kink-turns. For example, pseudoknot motif results from the interaction between a single-stranded loop and a complementary sequence outside this loop; the A-minor motif forms by single-stranded adenosines making contacts with the minor grooves of RNA double helices; a ribose zipper is made by helix–helix interactions between the ribose and the pyrimidine base, involving the minor groove surfaces. RNA folding patterns, as globular proteins, are responsible of the chemical reactivity and the specific interactions with other molecules, such as proteins, nucleic acids and small ligands.

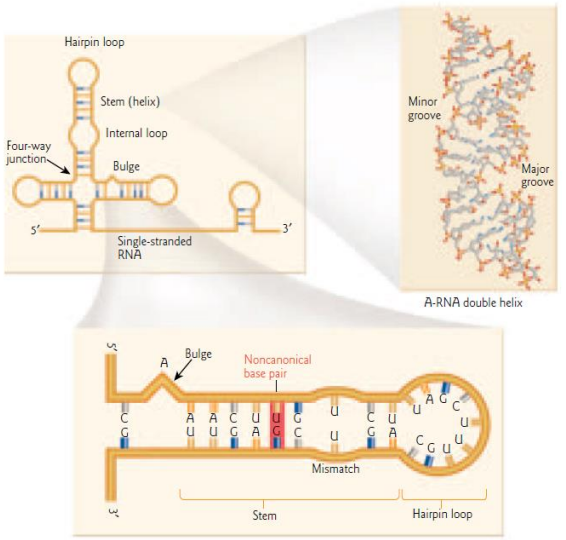


**Figure 1.14. RNA secondary structures.** RNA structural motifs include base-paired stems with also non-canonical base pairs (lower inset), hairpin loops, internal loops, bulges and junctions. Base-paired stems form an A-type helix in which minor groove and major groove are highlighted (top inset).

*(Allison 2007)*

During the RNA maturation, various chemical modifications are introduced into ribonucleotide residues at the base or at the ribose 2′-OH or both (*Machnicka et al. 2013*). About 150 post-transcriptional RNA modifications have been recognized: the variety of chemical groups and their positions in RNA are illustrated in **Fig. 1.15**. The localization and the abundance of these numerous modifications vary between different RNA molecules, organisms and organelles and according to the physiological environment and growth conditions of the cell. These modifications are involved in RNA localization, stability and activity, although for most of them the function is still unclear, and were shown to be linked with human diseases (*Li and Mason 2014*). The majority of modified nucleotides is present in transfer and ribosomal RNAs. In fact, the human rRNA contains more than 200 modifications among which the major ones are 2′-O-methyl nucleotides, pseudouridines and methylated bases; rRNA modifications commonly control ribosome assembly (*Liu and Pan 2015*). The human tRNA contains about 14 modifications (various methylated bases, pseudouridines, 2′-O-methyl nucleotides and more chemically complex bases): according to their position, tRNA modifications generally regulate stability, modulate folding and are involved in the decoding capacity (*Liu and Pan 2015*). However, modifications have also been found in small non-coding RNAs, such as snRNAs and snoRNAs, and more recently in regulatory RNAs, as siRNAs, miRNAs and piRNAs (*Machnicka et al. 2013*). The presence of modified bases in mRNAs was also demonstrated (*Machnicka et al. 2013*).

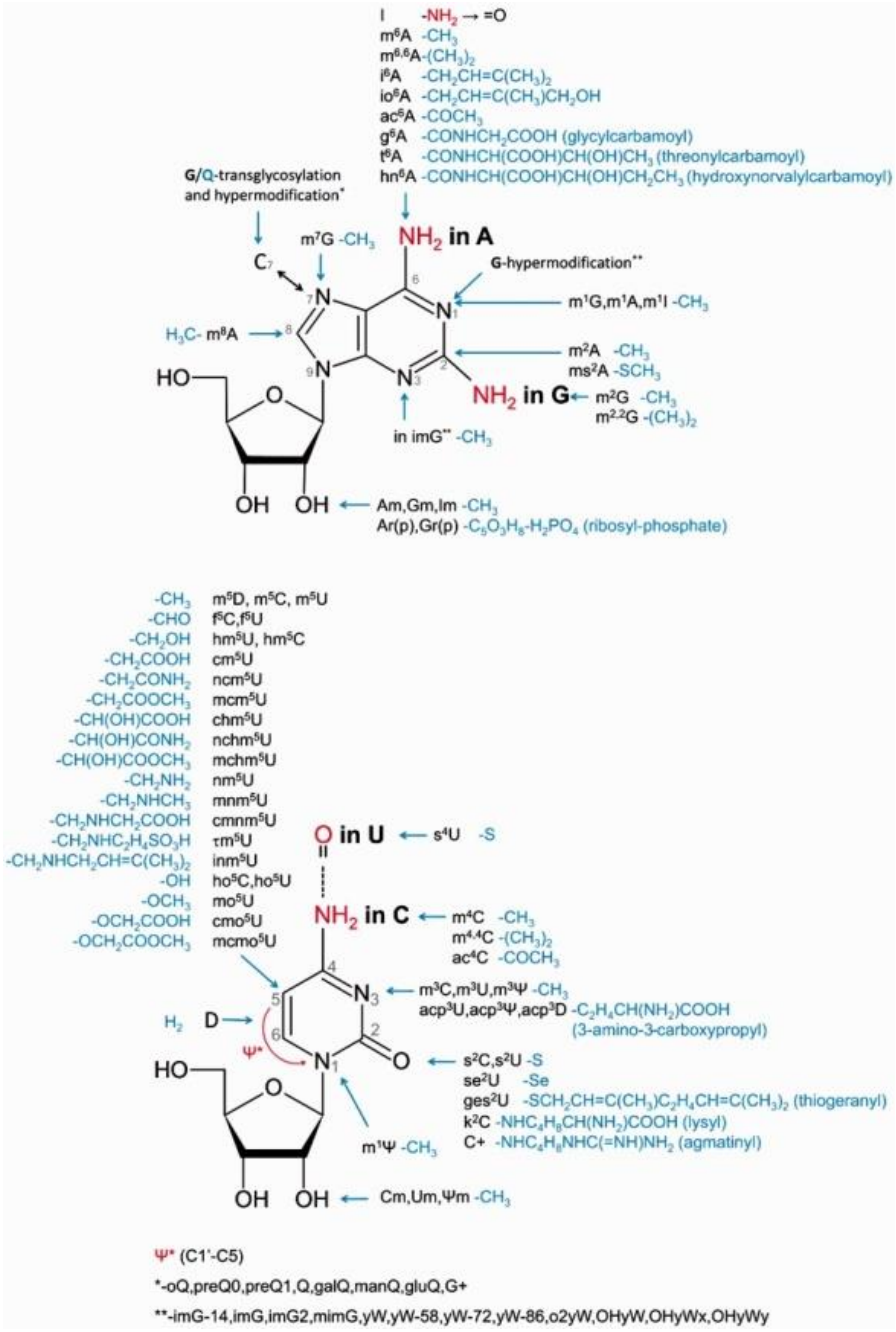


**Figure 1.15. The variety of RNA modifications.** Several chemical groups can be introduced enzymatically during the process of RNA maturation at various locations. Nucleotides in RNA can also be doubly or triply modified.

(*Machnicka et al. 2013*)

Among these modifications, RNA methylation is one of the most common (*Kellner et al. 2010*). In particular, 5mC is widely studied.

Several modified sites were found in rRNA of all three domains of life: two are known in human 28S rRNA; none were found in eukaryotic 18S rRNA and little is known about 5mC in mitochondrial rRNA. However, the 5mC function in rRNA seems to be implicated in tRNA identification, peptidyl-transferase activity and, consequently, translational fidelity of the ribosome (*Motorin et al. 2009; Squires and Preiss 2010*). Thanks to their modification status, eukaryotic tRNAs are subject to quality control and decay pathways. 5mC is commonly present in the anticodon loop and in the central core of archeal and eukaryotic tRNA: its function seems to be linked to the structural and metabolic stabilization of the molecule. In fact, placed in the $Mg^{2+}$ binding site of the anticodon loop, it stabilizes tRNA secondary structure being involved in codon recognition (*Squires and Preiss 2010; Liu and Jia 2014*). Moreover, the modified residue at the anticodon wobble is not involved in splicing of the pre-tRNA and it shows a suppressor activity. In the tRNA variable region, 5mC affects aminoacylation. Several 5mC sites in tRNAs have been mapped but others probably remain still undiscovered (*Squires and Preiss 2010*).

Works leading to the mRNA cap discovery found internal 5mC residues at low levels in mammalian mRNA (*Dubin and Taylor 1975*) but the possible occurrence of 5mC in mRNA was largely ignored. This modification was later confirmed in mRNA and candidate sites were detected in thousands mRNAs, indicating that 5mC is not only present on highly specialized mRNAs (*Squires et al. 2012*). It is localized in the untranslated regions (UTRs): due to the proximity of mRNA methylation sites to the binding ones of Argonaute protein, the central component of miRNA-RISC (RNA inducing silencing complex) complex, mRNA 5mC could be involved in

miRNA degradation pathway, protecting mRNAs against innate antiviral defence mechanisms – however, there are no clear evidence about the methylation involvement in mRNA stability. A role in promoting mRNA efficient translation was also suggested thanks to the 5mC enrichment after the translation initiation sites (*Squires et al. 2012; Dominissini and Rechavi 2017*). Moreover, 5mC could modulate the formation of specific RNA structures or affect interactions with post-transcriptional regulators, being involved in several post-transcriptional processes, as splicing or editing (*Squires and Preiss 2010*) – a methyl-CpG-binding protein was demonstrated to regulate RNA splicing (*Young et al. 2005*). The mRNA Aly/R export factor, ALYREF, was identified as a bona fide 5mC reader, strongly showing the 5mC involvement in ALYREF-mediated nuclear-cytoplasmic shuttling of mRNA (*Dominissini and Rechavi 2017; Yang et al. 2017*) (**Fig. 1.16**). However, 5mC function is still largely unknown.

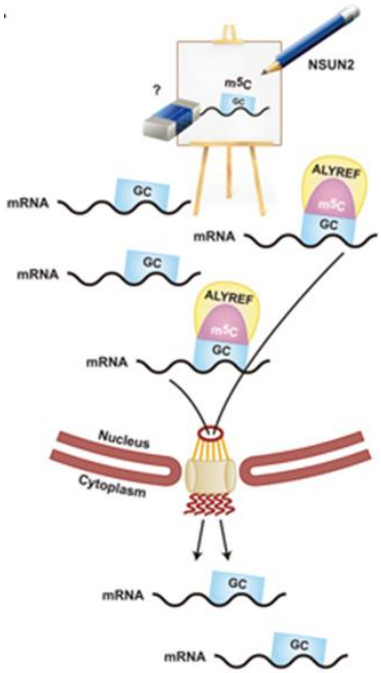


**Figure 1.16. 5mC as an epitranscriptomic mark regulating nuclear export.** 5mC in GC-rich regions of mRNA molecules is mediated by the NSUN2 writer. This epigenetic modification allows the recruitment of the ALYREF: this 5mC reader mediates nuclear export.

(*Dominissini & Rechavi, 2017*)

RNA 5mC-methyltransferases (RNA-5mC MTases) have been found in different eukaryotic organisms (*Squires and Preiss 2010; Blanco and Frye 2014*). Two MTases have been implicated in eukaryotic tRNA modification: DNMT2 was one of the first MTases identified and its methylation is restricted to only C38 in the anticodon loop; NSUN2 can methylate tRNA in several sites. Similarly to NSUN2, the other members of the human NSUN1-7 family show a methyltransferase activity on tRNA or rRNA, also in mitochondria, even if for some of them the substrates have not been yet identified. In addition, NSUN1 and NSUN5, as well as NSUN2 and NSUN4, have been identified as mRNA-binding proteins: in particular, NSUN2, as well as DNMT2, has been shown to modify only certain mRNAs in human cells (*Gilbert et al. 2016*), as long as NSUN2 was demonstrated to be the main RNA methyltransferase, mediating 5mC installation on mRNA (*Dominissini and Rechavi 2017;Yang et al. 2017*).

Similarly to DNA, RNA 5mC can be further modified to 5hmC, 5fC and 5caC by TET family enzymes (*Shen et al. 2014*).

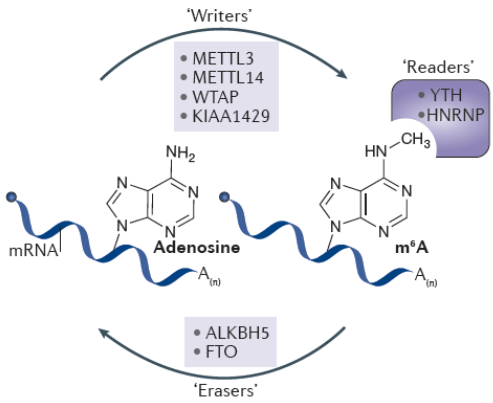


**Figure 1.17. m6A modification.** The deposition, removal and recognition of m6A are carried out by factors termed writers, erasers and readers, respectively. Mammalian m6A writers (METTL3 and METTL14) form a protein complex stabilized by WTAP and KIAA1429. FTO and ALKBH5 are the two reported m6A erasers. The function of m6A is mediated by reader proteins, identified in members of the YT521-B hnRNPs.

(*Zhao et al 2016*)

Discovered during the 1970s (*Desrosiers et al. 1974*), 6-methyladenosine (m6A), the most abundant mRNA modification, is present around the stop codons, in the 3′ UTR and within long internal exons

(*Narayan and Rottman 1988*). Methyltransferase-like 3 (METTL3) and methyltransferase-like 14 (METTL14) were shown to form a human complex, stabilized by the Wilms tumor 1-associated protein (WTAP), in which both the components of the core complex are catalytic subunits (*Liu et al. 2014*) (**Fig. 1.17**). The WTAP allows the interaction between the METTL subunits, localizes the complex on target mRNA and enhances the methylation efficiency (*Fu et al. 2014; Ping et al. 2014*). Moreover, WTAP interacts with many proteins, recruiting other regulators or enzymes to the methyltransferase complex, as the vir-like m6A-methyltransferase associated protein, KIAA1429: these additional factor may affect the methylation activity and selectivity through direct interactions or post-translational modifications (*Fu et al. 2014*). As for 5mC, this is a reversible modification which takes place through successive oxidation steps – two dioxygenases, FTO (fat mass and obesity associated protein) and ALKBH5 (alkylation repair homolog 5), are known to efficiently convert m6A to adenosine (*Jia et al. 2011*). The m6A biological function is dependent on reader proteins: to date, it was demonstrated the m6A involvement in mRNA stability, degradation, splicing, localization and translation (*Fu et al. 2014; Wang et al. 2014*).

- ✓ The characterization of the methyltransferase complex, as well as m6A function, is also carried out in *Drosophila melanogaster*.

  m6A level increases during early embryogenesis, dropping dramatically in the rest of this process. However, two new peaks can be detected in the third larval stage and during pupal phases and, even if it decreases in adults, it results relatively abundant in heads and ovaries. m6A is localized at the same mammal sites. The METTL3 ortholog is Ime4 (inducer of meiosis 4) while the METTL14 ortholog is renamed dMettl14 (*Drosophila* methyltransferase-like 14): both of these enzymes

are required to form m6A in *Drosophila*. Fl(2)d (female lethal d) and vir (virilizer) are homologs of WTAP and KIAA1429, respectively: these proteins were shown to be components of the methyltransferase complex, describing Fl(2)d as a stabilizing factor. spenito (nito) can interact with Fl(2)d and Ime4 so that it was proposed as a novel component of the complex. YT521-B was recognized as a reader protein: it binds m6A being the principal mediator of m6A function in pre-mRNA splicing. The involvement of m6A modification in neuronal function and sex determination, primarily via YT521-B, was also described.

## *4. TECHNICAL APPROACHES TO STUDY EPIGENETIC MODIFICATIONS*

Different methods have been developed for the discrimination of CpG methylation status (*Harrison and Parle-McDermott 2011*) – some approaches make possible the mapping of 5mC at single base resolution allowing to obtain a complete epigenetic profile.

The earliest epigenetic studies were based on the discrimination between methylated and unmethylated cytosines through separation techniques, such as high-performance liquid chromatography (*Gehrke et al. 1984*). The identification of modified residues was also obtained via digestion with methylation-sensitive restriction enzymes (*Bestor et al. 1984*). Despite having different applications, these methods can only describe the ratio of methylated-unmethylated cytosines. Consequently, alternative techniques have been proposed: for example, tritiated methyl groups were enzymatically incorporated into CpG sites to detect radioactivity levels to be correlated to the DNA methylation ones (*Wu et al. 1993*).

One of the common approaches for the detection of DNA methylation is the bisulfite conversion-based method. In fact, C and 5mC react differently to

the treatment with sodium bisulfite: unmethylated C is converted to U while 5mC remains unconverted. Therefore, DNA, previously treated with bisulfite, retains only methylated cytosines allowing the detection of methylation pattern (*Frommer et al. 1992*). However, the development of DNA microarray technology determined a revolution in the epigenetic studies: the hybridization of methylated or unmethylated fragments to an array of known probes allowed the identification and the quantification of genome modified areas (*Huang et al. 1999; Gitan et al. 2002; Weber et al. 2005*). Moreover, more recently, sequencing-based approaches, like next generation sequencing was used to obtain a complete epigenetic profile (*Cokus et al. 2008; Maunakea et al. 2014*).

However, due to the antibody accessibility to 5mC (*Adouard et al. 1985*), global DNA methylation levels are often detected at fluorescence microscopy using anti-5mC antibody or anti-methylated DNA binding proteins antibodies (*Santos et al. 2002; Kobayakawa et al. 2007*). Recently, methylation-specific fluorescence in situ hybridization (MeFISH) was developed for the visualization of DNA methylation status at specific sequences, using the difference in the osmium oxidation rate between C and 5mC (*Li et al. 2013*). Beside this fluorescence microscopic visualization of 5mC, an EM study concerning DNA methylation dynamics was carried out during a plant programmed cell death process (*Solís et al. 2014*).

Several of the methods for DNA methylation analysis have been adapted to detect modified nucleotides on RNAs, including 5mC (*Hussain et al. 2013; Motorin et al. 2009*). Nucleotide modifications can be detected according to physico-chemical properties, differential chemical reactivity and enzymatic turnover. Based on the different physico-chemical properties of modified RNAs, separation techniques typically include chromatography, i.e. thin layer chromatography (TLC) and high-performance liquid chromatography

(HPLC), or mass spectrometry (MS) – sometimes a combination of both (LC-MS) is used allowing the detection of modified nucleotides even in the sub-picomolar range. 5mC differential reactivity towards chemical reagents allows the application of PCR- or affinity-based techniques for sequencing, structural probing or footprinting applications of end-labelled nucleic acids. Bisulfite sequencing was first adapted for the 5mC detection on RNA in 2009, resulting in quantification of RNA methylation levels (*Schaefer et al. 2009*).

However, these methods required high amounts of RNA and identified modified sites only in highly abundant RNAs, such as rRNAs and tRNAs. In the last years, next generation sequencing allowed to develop more sensitive techniques: in 2012, it was combined to the bisulfite conversion providing the first transcriptome-wide view of 5mC (*Squires et al. 2012*).

Other techniques are used for RNA 5mC detection. RNA immunoprecipitation (RIP) followed by deep sequencing allows to detect global 5mC level using a monoclonal antibody against 5mC (**Fig. 1.18**). Similar approaches can be used to detect enzyme-specific deposition of 5mC: 5-azacytidine-mediated RNA immunoprecipitation (Aza-IP) and methylation-individual nucleotide resolution crosslinking immunoprecipitation (miCLIP) (**Fig. 1.18**), in which a temporary covalent bond between the catalytic site of RNA methyltransferase and the carbon 6 of targeted cytosine is formed.

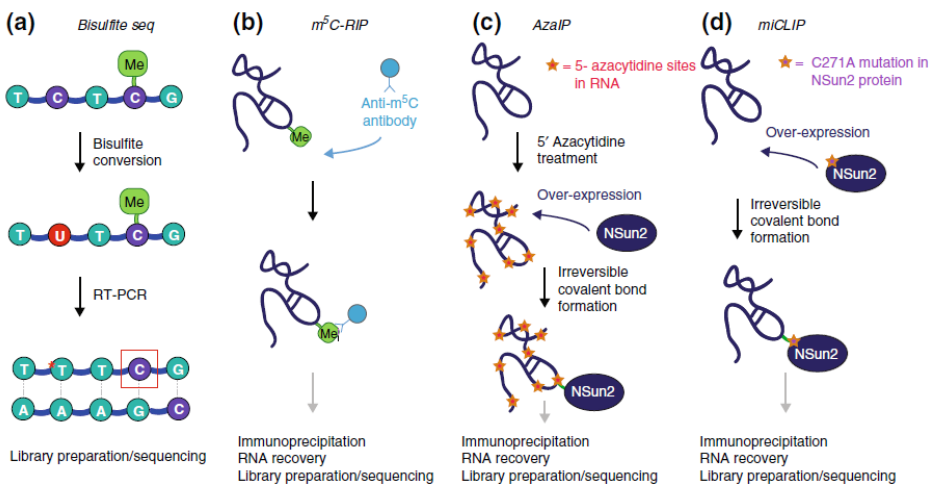


**Figure 1.18. Techniques for 5mC detection on RNA. A.** Bisulfite sequencing: the bisulfite-mediated conversion occurs only on unmethylated cytosine. The asterisk indicates the conversion while the square the unconverted base. **B.** 5mC-RIP: anti-5mC antibody covalently bonds the modified residues. **C.** Aza-IP: 5-azacytidine is randomly introduced into nascent RNA and it is recognized by NSUN2. **D.** miCLIP: C271A mutation is introduced in RNA in order to be bonded by NSUN2.
In 5mC-RIP, Aza-IP and miCLIP the covalent bond is followed by immunoprecipitation.

(*Hussain et al. 2013*)

A variety of techniques from biochemistry and biophysics to chemical biology allows to isolate histones and to evaluate their modifications, determining the biological relevance of the combinatorial codes. Electrophoretic and chromatographic methods can be applied to obtain histone separation and to purify them (*Bloom and Anderson 1978; Gurley et al. 1991*). The traditional methods for the histone analysis concern the use of site-specific antibodies: these immunological assays include western blotting, immunofluorescence and ELISA techniques (*Crane-Robinson et al. 1997; Bonnet-Garnier et al. 2012*), which allow the characterization of the total changes in the level of histone post-transcriptional modifications across the whole genome. These modifications can be also quantified with specific colorimetric or fluorometric assays. The genome localization of a

histone modification and its relative abundance can be identified through chromatin immunoprecipitation (ChIP) using a specific antibody. Moreover, the level of PTMs can be defined testing the activity of writer or eraser enzymes – these applications allow also the characterization of the modification pathways. DNA microarrays and deep sequencing are also traditionally used (*Karch et al. 2013*). However, MS is a very known strategy and an essential tool to characterize histone modifications, since a histone PTM induces a mass shift: it can identify multiple novel modifications and measure the co-occurrence of the modifications on the same protein – high-resolution analysers are commonly used to carry out histone PTM analysis (*Bonenfant et al. 2006; Karch et al. 201*3).

# 2. AIM OF RESEARCH

The lack of an extensive ultrastructural analysis of epigenetic modifications prompted us to study nucleic acid methylation as well as histone modifications at transmission electron microscope (TEM).

This high-resolution approach was focused on:

- the visualization of DNA methylation status and histone PTM distribution on chromatin areas in the cell nucleus;
- the localization of RNA methylation sites.

In particular, the analysis pointed to the regulation of chromatin structure to better understand the role of 5mC in chromatin conformation in light of the recent works describing the nucleosome destabilization following DNA methylation (*Jimenez-Useche and Yuan 2012; Ngo et al. 2016*). To this purpose, hepatocytes were chosen for their often large heterochromatin regions on which a study concerning the modification distribution could be reasonable. On the other hand, HeLa cells were selected for their high transcription rate to increase the probability of detecting RNA fibrils, revealing possible modifications.

However, to integrate the analysis on the chromatin structure regulation, epigenetic modifications were studied at TEM after specific treatments which are known to induce chromatin condensation, i.e. low or high concentration of divalent cations ($Ca^{2+}$ and $Mg^{2+}$) and heat shock (*Martin et al. 2007; Fritah et al. 2009*). Differentiating erythrocytes were used as another model for this analysis because they physiologically modify the status of chromatin compaction during their maturation: the relationship between chromatin remodelling and compaction and the 5mC level on heterochromatin regions was investigated together with the distribution pattern of the chosen chromatin epigenetic modifications.

In the Laboratory of Dr J. Y. Roignant (Institute of Molecular Biology, IMB, Mainz – Germany), the characterization of the methyltransferase complex, the identification of a main m6A reader and the analysis of the function of this modification in *Drosophila melanogaster* were carried out. Preliminary data in their analysis indicated the presence of two novel components of m6A-methyltransferase complex: this work also intended to define Hakai and CG7358 involvement in the protein complex.

# 3. MATERIALS AND METHODS

## 1. CELLS, TISSUES AND TREATMENTS

This study has been carried out on different tissue and cell models. In mouse liver, as well as bone marrow, the peripheral condensed chromatin regions are generally evident allowing to better analyze the distribution of epigenetic modifications on DNA. Moreover, in the bone marrow, different developing stages with consequently different level of condensed chromatin can be detected. On the other hand, for the analysis of RNA methylation, proliferating HeLa cells were chosen for their high transcription level which increases the probability of RNA transcript detection. However, in the analysis of RNA methylation, hepatocytes were also examined to ascertain the 5mC presence on mRNA also in normal cells.

Finally, to deepen the role of 5mC on chromatin structure, the cells underwent treatments known to induce DNA compaction.

### 1.1. Cells in vitro

HeLa cells were grown in Dulbecco's Minimal Essential Medium (DMEM) supplemented with 10% foetal bovine serum (FBS), 1% glutamine, 100 U/mL penicillin and streptomycin in a 5% $CO_2$ humidified atmosphere at 37°C. The cells were grown in 25 $cm^2$ plastic flasks and detached by a mild trypsinization or scraping when the 90% confluence was reached. They were differently processed according to the final analysis.

#### 1.1.1. Cells for EM immunocytochemistry

After collecting cells in fresh 15 mL tubes by a gentle centrifugation at 800 rpm for 5 minutes at room temperature (RT), the samples were fixed with 4% paraformaldehyde (PFA) in the culture medium for 2 hours at 4°C – the PFA fixation allows for a good preservation of antigen integrity. Then, the

cells were centrifuged at 2000 rpm for 10 minutes at RT and rinsed thoroughly with phosphate buffered saline (PBS). They were also incubated in 0.5 M $NH_4Cl$ in PBS for 30 minutes at RT to block free aldehyde groups and rinsed again with several changes of PBS. The cell pellets were pre-embedded in 2% Agar in $H_2O$ to better handle the sample during the following steps. The samples were dehydrated in graded ethanol and embedded in LRWhite resin, which allows better antigen retrieval. The resin polymerization occurred for 24 hours at 60°C. Finally, thin sections of 70-80 nm were obtained with a Reichert OM3 ultramicrotome and collected on formvar-carbon-coated or naked nickel or gold grids (200 Mesh).

#### *1.1.2. Cells for EM morphological analysis*

The cells were collected in fresh 15 mL tubes by a gentle centrifugation and fixed with 2.5% glutaraldehyde (Gt) in their culture medium for 2 hours at RT – Gt is preferred for good morphology preservation. After a centrifugation at 2000 rpm for 10 minutes at RT and several washes with PBS, the cells were post-fixed in 1% aqueous osmium tetroxide ($OsO_4$) for 2 hours at RT for lipid fixation in order to preserve the membranous structures – several washes in $H_2O$ followed. Therefore, the cell pellets were pre-embedded in 2% Agar in $H_2O$, dehydrated in graded acetone and embedded in Epon resin. Finally, after 48 hours at 60°C to allow the resin polymerization, thin sections were obtained as previously described and collected on nude nickel grids (200 Mesh).

#### *1.1.3. Cells for fluorescence immunocytochemistry*

After trypsinization, HeLa cells were seeded on glass coverslips and left growing until 70-80% confluence. The samples were fixed in 2% PFA in their culture medium for 30 minutes at RT and washed with PBS three times. PBS was substituted by cold 70% ethanol and the cells were directly used or stored at -20°C.

## 1.1. Tissues

Samples from mouse liver and rat bone marrow were quickly collected in the fixation solution of 4% PFA in Sörensen phosphate buffer at pH 7.2 for 2 hours at 4°C. Then, after PBS washes and $NH_4Cl$ 30 minute incubation, the tissues were directly dehydrated in graded ethanol to be embedded in LRWhite resin. Finally, the embedded samples were polymerized and thin sections were collected on coated nickel grids.

However, the described procedure was not directly carried out since these embedded samples were present in the material archive of Prof. M. Biggiogera from the University of Pavia and Lausanne.

## 1.2. Treatments

### 1.2.1. Fluorouridine incubation

To label RNA fibrils, both HeLa cells and mouse liver were incubated with 5 mM fluoro-uridine (FU) for 15 minutes at 37°C before proceeding with the fixation and embedding for ultrastructural analysis (*Dundr and Raska 1993; Trentani et al. 2003*). The short incubation time allowed to specifically label the nascent RNA transcripts and, consequently, to analyze PF, that are (pre-)mRNAs (*Fakan 1994*).

### 1.2.2. Incubation with different concentrations of divalent cations

HeLa cell samples were also used to analyze the effect of divalent cations changes on chromatin structure and epigenetic modifications. These cells were addressed to three different analyses: ultrastructural immunocytochemistry, EM morphology and fluorescence immunocytochemistry: therefore, after the treatment described below, the cells were prepared as in the **Paragraphs 1.1.1, 1.1.2** and **1.1.3**, respectively.

First of all, the cells were divided into two different groups and each group in 3 flasks undergoing the treatment with different concentration of $Ca^{2+}$, $Mg^{2+}$ and EGTA (ethylene glycol-bis-β-aminoethyl ether-N,N,N',N'-tetraacetic acid). The treatment was carried out before the scraping, which was chosen to avoid further stress to the cells and possible negative interactions with trypsin. The experimental conditions of the two cell groups are listed below. For each type of handling the control sample (CTR) was not treated.

- The new buffer was prepared with 150 mM NaCl, 6 mM KCl, 1.5 mM $CaCl_2$ and 1 mM $MgCl_2$ in culture medium. Then, calcium-concentrated solution (CA) was obtained modifying the NaCl concentration to 120 mM and the $CaCl_2$ concentration to 20 mM; magnesium-concentrated solution (MG) resulted decreasing the NaCl concentration to 120 mM and increasing the $MgCl_2$ concentration to 20 mM; in calcium- and magnesium-free solution (Egta) 0.5 mM EGTA chelating divalent cations was added and $CaCl_2$ and $MgCl_2$ were substituted by 2 mM NaCl. All the solutions were brought to pH 7.4 with an osmolality of 338 mmol/kg. The culture medium was removed from 3 different flasks to be replaced with 5 mL of one of three different solutions (*Poletto et al. 2016*).
- The second treatment involved the following changes: in CA $Ca^{2+}$ concentration was 200 mM; in MG $MgCl_2$ was concentrated to 200 mM; EGTA concentration was increased to 5 mM in Egta. The pH and osmolality were also adjusted as previously described.

#### *1.2.3. Heat shock*

The analysis of the regulation of chromatin structure by DNA methylation was also performed on HeLa cells undergone heat shock, which is known to induce DNA compaction (*Fritah et al. 2009*).

The treatment was carried out before the trypsinization and, then, the heat shocked samples (HS), as well as the CTR, were processed for EM immunocytochemistry. The heat shock was obtained by an incubation for 90 minutes at 43°C. A recovery period in the culture medium of 60 minutes at 37°C, added with Hepes (4-2-hydroxyethyl-1-piperazineethanesulfonic acid), followed.

## *2. EM ANALYSIS*

### *2.1. EM immunocytochemistry*

The grids were floated on normal goat serum (NGS) diluted 1:50 in PBS for 5 minutes at RT to block antibody aspecific bonding. Then, the samples were incubated with the primary antibody overnight at 4°C. In double labelling reactions, two different primary antibodies were utilized. The primary antibody was diluted in PBS containing 0.1% Bovine Serum Albumin (BSA) and 0.05% Tween20 (T) (PBTB). The concentration depended on the specific antibody used: the list of the primary antibodies and their different combinations for the double labelling is present in **Table 3.1**. The sections were rinsed with PBS-T (PBT) two times for 5 minutes at RT and equally with PBS. After NGS, the grids were incubated with the specific secondary antibody coupled with colloidal gold of 12 nm. In double labelling reactions a 12 nm and 6 nm colloidal gold secondary antibodies were used. They were all diluted 1:20 in PBS for 30 minutes at RT. Finally, the samples were rinsed with PBS twice for 5 minutes at RT and then with $H_2O$.

| PRIMARY Ab | Ab SPECIES | Ab DILUTION | Ab TARGET |
|---|---|---|---|
| Anti-5mC (GTX629448, GeneTex) | MOUSE | 1:500 EM | 5mC |
| Anti-5mC (GTX128455, GeneTex) | RABBIT | 1:500 EM | 5mC |
| Anti-DNMT3A (GTX129125, GeneTex) | RABBIT | 1:10 EM 1:100 FLUO | DNMT3A |
| Anti-H3K27me3 (GTX121184, GeneTex) | RABBIT | 1:50 EM | H3K27me3 |
| Anti-H3K9me3 (GTX121677, GeneTex) | RABBIT | 1:10 EM | H3K9me3 |
| Anti-H4K20me3 (GTX128960, GeneTex) | RABBIT | 1:200 EM | H4K20me3 |
| Anti-5mC + anti-H3K27me3 | MOUSE/RABBIT | 1:500/1:50 | 5mC + H3K27me3 |
| Anti-5mC + anti-H3K9me3 | MOUSE/RABBIT | 1:500/1:10 | 5mC + H3K9me3 |
| Anti-5mC + anti-H4K20me3 | MOUSE/RABBIT | 1:500/1:200 | 5mC + H4K20me3 |
| Anti-5mC + anti-DNMT3A | MOUSE/RABBIT | 1:500/1:10 | 5mC + DNMT3A |
| Anti-5mC + anti-FU | RABBIT/RAT | 1:500/1:10 | 5mC + FU |
| Anti-5mC + C8V (courtesy of Dr. T.Martin) | MOUSE/CHICKEN | 1:500/1:500 | 5mC + hnRNP core protein |
| Anti-5mC + H20 (courtesy of Dr. R.Lührmann) | RABBIT/MOUSE | 1:500/1:200 | 5mC + 7-methylguanosine |
| Anti-5mC + anti-RNase A (ab94417, Abcam) | MOUSE/RABBIT | 1:500/1:50 | 5mC + RNase |
| DNMT3A + FU | RABBIT/MOUSE | 1:500/1:10 | 5mC + FU |
| DNMT3A + C8V | RABBIT/CHICKEN | 1:500/1:500 | 5mC + hnRNP core protein |
| DNMT3A + H20 | RABBIT/MOUSE | 1:500/1:200 | 5mC + 7-methylguanosine |
| Anti-m6A (courtesy of Dr. J.Y.Roignant) | RABBIT | 1:100 | m6A |

**Table 3.1. List of the primary antibodies used for both EM and fluorescence (FLUO) immunocytochemistry.** It is also shown the combinations with which these antibodies were used.

As a control of the specificity, some grids were incubated in parallel in the PBTB mixture from which the primary antibody was excluded and then processed as described above. As a further control, before proceeding with the incubation with anti-5mC antibody, some grids were incubated with DNase (500 U/mL) for 2 hours at 37°C and with Proteinase K (PK; 1 mg/mL) for 15 minutes at 37°C.

## 2.2. EM in situ hybridization

Electron microscopy in situ hybridization (EMISH) was performed to recognize the poly(A) tail of mRNA. A pre-hybridization solution containing 20% baker RNA, 20% dextran and 4X saline sodium citrate (SSC) was firstly prepared. The sections were incubated with this solution for 15 minutes at RT to allow the following hybridization for 3 hours at 37°C. The hybridization mixture was prepared by adding biotin-labelled poly-d(T) probe to the pre-hybridization solution to give a final concentration of 1 μM of the oligonucleotide. Stringency washes in SSC were performed to remove probes aspecifically bonded: the grids were floated onto 4X SSC two times for 5 minutes at 37°C; 5 minutes washes in SSC 4X, 2X and 1X at RT followed. The samples were incubated with NGS 1:100 in PBS for 3 minutes and, later, with the anti-biotin antibody coupled with 10 nm colloidal gold for 30 minutes at RT. The anti-biotin antibody was diluted 1:10 in PBS. Finally, the grids were rinsed with PBS and $H_2O$.

An immuno-labelling using anti-5mC antibody was performed on these samples as described in the previous paragraph and 5mC was identified by a 6 nm gold secondary antibody.

## 2.3. Staining procedures

Sections were stained with one of the following procedures at RT.

- REGRESSIVE EDTA TECHNIQUE FOR RNPs (*Bernhard 1969*): coated nickel grids were incubated in uranyl acetate for 2 minutes, in EDTA for 30 seconds to remove uranyl from DNA and, finally, in lead citrate for other 2 minutes to increase the uranyl contrast.
- TERBIUM CITRATE STAINING FOR RNA (*Biggiogera and Fakan 1998; Biggiogera and Masiello 2017*): specimens collected on naked grids were floated on 50 μL drops of terbium citrate for 30 minutes and quickly

washed in $H_2O$ for 10 and then 5 seconds. This staining method gives a very low contrast despite its accuracy.

- ✓ To prepare terbium citrate, 5 mL of 0.2 M terbium nitrate was added dropwise to an equal volume of 0.2 M sodium citrate, stirring continuously. Then, drops of 1 N NaOH were added gently stirring to allow the complete salt dissolution. Finally, pH was brought to 8.2-8.5 with NaOH and controlled after 24 hours.

- OSMIUM AMMINE STAINING FOR DNA (*Masiello and Biggiogera 2017a; Vázquez-Nin et al. 1995*): sections on naked gold grids were hydrolyzed with 5N HCl for 30 minutes to remove DNA purines; then, several $H_2O$ washes were performed to incubate the samples in osmium ammine-B (OA) for 1 hour to allow the bonding of OA with the pseudo-aldehydic groups on the deoxyribose; finally, the grids were rinsed thoroughly with $H_2O$.
  - ✓ 10 mg of osmium ammine-B were dissolved in 4.8 mL of double distilled water; 200 μL of 5 N HCl and 190 mg of sodium metabisulfite were consecutively added. The reagent required an activation time of 30 minutes.
- URANYL ACETATE AND LEAD CITRATE STAINING: the samples prepared for the morphological analysis were only stained with uranyl acetate for 10 minutes and, after numerous washes, lead citrate for 2 minute. The specimens were finally thoroughly rinsed.

After the staining, all the samples were observed on a Zeiss EM900 transmission electron microscope operating at 80kV.

### *3. FLUORESCENCE IMMUNOCYTOCHEMISTRY*

After rehydration with short washes in PBS, the slides were incubated with the primary antibody overnight at 4°C – the used antibody is indicated in

**Table 3** with its specific concentration. Antibody excess was removed by rinsing samples with PBS. Specimens were then incubated with the specific secondary antibody coupled with Alexa Fluor 488 for 45 minutes at RT. The secondary antibody was diluted 1:200 in PBS. The samples were washed with PBS and counterstained with Hoechst 33258 (1 μg/mL in PBS) for DNA. Finally, after some washes, the coverslips were mounted in glycerol-PBS 1:1 to be observed at the fluorescence microscope Olympus BX51 with a mercury lamp of 100 W.

The immunoreaction required an incubation in the blocking solution. The latter was prepared with 0.3 M glycine, 1% BSA and 0.1% T. The incubation was performed for 30 minutes at RT before incubating the primary antibody overnight.

## *4. ELECTRON SPECTROSCOPIC IMAGING*

After the EM immunocytochemical reactions, HeLa cells incubated with high concentration of divalent cations were used for Electron Spectroscopic Imaging (ESI) on a Zeiss CEM902 TEM, integrated with an electron energy filter according to *Ottensmeyer* (*1984*), operating at 80 kV. The main characteristics of this technique are shown in **Fig. 3.1**.

The images were acquired through a TV camera and net mapping images of phosphorus, calcium and magnesium were thus obtained for CTR and each of the treated samples (CA, MG and Egta). The images were obtained at different energy losses (ΔE): one window for background evaluation and one edge window with a 100 pm objective aperture and a window width of 20 eV. For Ca mapping, care was taken to choose adequate values for the background images since the CaLz.3 edge (346.4 eV) has background dominated by the tail of the carbon ionization edge CK (283.4 eV), an element abundant in biological material. Therefore, the background window

was taken at ΔE = 332 eV and the Ca window at ΔE = 350 eV. For magnesium the parameters were respectively 30 eV and 50 eV and for phosphorus 110 eV and 132 eV, respectively.

The image analysis for the mapping of the chosen elements was performed with ImageJ program using a "one window-method" and power law calculation for the background evaluation (*Boutinard Rouelle-Rossier et al. 1993*).

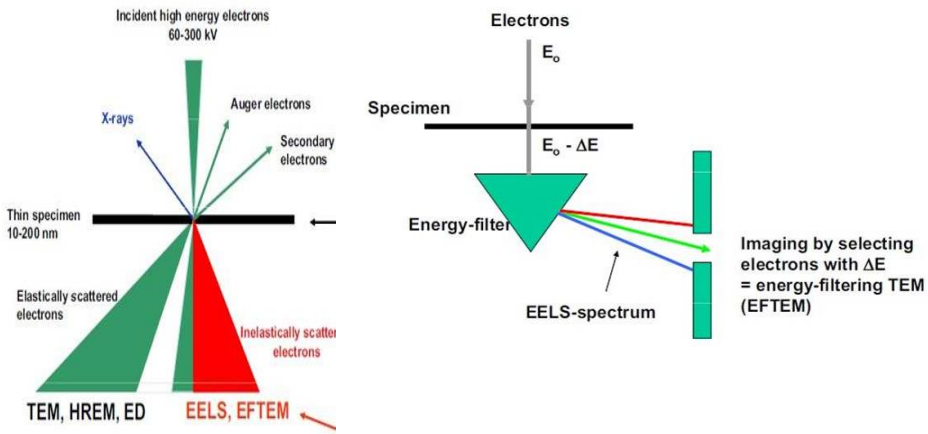


**Figure 3.1. Electrons-specimen interactions and EELS spectrum measurement.** If a thin section is illuminated with a beam of high-energy electrons, even if the majority of the electrons will pass unhindered through the sample, some will be scattered elastically or inelastically. Inelastically scattered electrons result in a loss of energy, which is characteristic of the element in the sample: in fact, if the electron beam emerging from the sample is passed through a magnetic prism (energy filter), the spectra of the electron energy loss of the different elements can be obtained. The final image is reformed using only the electrons of a specific element on a detector.

## 5. STATISTICAL ANALYSIS

The statistical analysis was performed to confirm the results of enzymatic digestions on hepatocyte nuclei. 10 nuclei showing similarities in size were selected so that the operator counted the gold grains for 5mC on the condensed chromatin regions in untreated and digested samples. The data were organized in Excel and analyzed through a t-test between the control sample and each sample undergone the enzymatic digestion.

The gold grain number describes the level of the antigen that we are searching for, allowing a semi-quantitative analysis at EM: therefore, the statistical analysis was performed to define the level of DNA methylation and of each histone modification known to be present on heterochromatin in hepatocyte nuclei. Ten nuclei were selected showing same size of condensed chromatin areas to exclude that possible differences could be attributed to different nucleus and chromatin dimensions. The operator counted the gold grains on condensed chromatin regions without taking into account nucleolus associated chromatin. The data were organized in Excel to graphically show the abundance of each epigenetic modification.

Considering the EM feature of a cell nucleus and according to the data in literature (*Cmarko et al. 2003*), the condensed chromatin areas can be arbitrarily divided in three regions (**Fig. 3.2**):

- zone 1 – the peripheral region near the nuclear envelope;
- zone 2 – the central region;
- zone 3 – the inner region toward the interchromatin space.

To analyze possible differences in the distribution of each epigenetic modification on the inner and peripheral parts of the same chromatin region, the gold grains were counted in both the zone 1 and zone 3 – the zone 2 was excluded to simplify the counting.

100 condensed chromatin regions in the hepatocyte nuclei with a similar surface were selected. Finally, a paired t-test was performed using GraphPad Prism 6 to understand if the labelling difference between the chromatin periphery (zone 1) and the chromatin surface (zone 3) is casual or not. Consequently, it was also possible to check in which region the investigated epigenetic modification was more abundant.

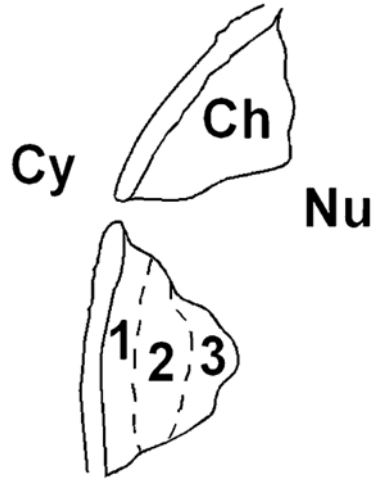


**Figure 3.2. EM chromatin structure.** The condensed chromatin areas can be divided in: zone1: it is the peripheral region nearby the nuclear envelope; zone2: this is the heterochromatin central region; zone3: it is superficial region toward the interchromatin space, surrounded by the perichromatin region.

*(Masiello and Biggiogera 2017b)*

To understand how divalent cations or heat shock, inducing chromatin condensation, affect the DNA methylation level, the total number of gold grains on the condensed chromatin regions (excluding the nucleolus associated chromatin) of HeLa control samples were counted to be compared with each treated sample (CA/MG/Egta or HS). For each experimental condition, 10 nuclei were chosen and two different operators counted each nucleus to ascertain the data. To be precise, the condensed chromatin area of the nucleus was calculated using ImageJ so that the labelling density was defined and used in Excel for a t-test. The same analysis were carried out for each of the analyzed histone modifications (H3K9me3, H3K27me3, and H4K20me3).

A statistical analysis was also conducted on erythrocytes at three different developing stages, selected according to their ratio between heterochromatin areas and interchromatin space: the premature form is characterized by small condensed chromatin regions close to the nuclear envelope and,

consequently, a large interchromatin space; the intermediate stage shows expanded heterochromatin which restricts the interchromatin space in small regions full of interchromatin granules (IG); the mature erythrocyte has the entire nucleus almost completely condensed. The density of 5mC or histone PTM labelling was detected as described above and an ANOVA test (followed by a Bonferroni test) was carried out to verify how DNA methylation or histone modifications change during a progressive chromatin compaction in a developmental process.

## *5.1. Analysis of the optical density*

In order to analyze the possible effect of calcium and magnesium on DNMT3A expression the optical density (OD), i.e. pixel density, was measured after DNMT3A labelling for fluorescence microscopy. The pictures were acquired in grey scale with an Olympus MagnaFire camera, keeping constant the magnification (100X), and 10 nuclei were analyzed for each of the four experimental conditions. Then, the OD of the entire nucleus was evaluated using an automatic function of ImageJ Program – the OD evaluated area excluded the nucleoli. During this calculation, the background from an adjoining region was always subtracted.

A statistical analysis was carried out calculating the OD average for the CTR and each treatment and the mean values, collected in Excel, were compared by t-test.

## 6. *ANALYSIS OF NOVEL COMPONENTS OF m6A-METHYLTRANSFERASE COMPLEX*

In the laboratory of Dr. J.Y. Roignant the following techniques were used to analyze the novel components of m6A-methyltransferase complex in *Drosophila melanogaster*: Hakai and CG7358.

### *6.1. Drosophila stocks and cell line*

*Drosophila melanogaster* w1118, Canton-S and Oregon-R were used as wild-type control flies. The flies stayed in plastic vial containing a layer of oat cereal mixed in fruit juice – this paste will be a sort of rotting fruit in which fly eggs are laid on and the larvae eat. To avoid smelling or mould growing white wine vinegar was added. A scouring pad was placed in the paste for fly climbing and larvae and pupate burrowing. A fine netting material covered the top of the vial to allow ventilation and to prevent escapes. The culture was kept at 25°C and after a couple of weeks the flies were transferred into fresh tubes.

w1118 flies used for staging experiments grew in small fly cages at 25°C. Flies laid embryos on apple juice plates: all the embryonic stages between 0 and 22 hours post fertilization (hpf) were collected. On the other hand, for the collection of larval stages, some embryos were transferred onto a new apple juice plate and incubated at 25°C until they reached a defined age between 24 and 110 hpf. Similarly, pupal stages were obtained transferring L3 larvae in a fresh vial at 25°C and collecting them every 2 h between 144 and 192 hpf. 1-3 day old adults were collected and gender separated; heads and ovaries were also collected.

*Drosophila* Schneider 2 cells (S2R+) derived from a primary culture of 20-24 hours old stage. The cells were grown as a semi-adherent monolayer at

RT in Schneider Insect Medium supplemented with 10% FBS and 1% Penicillin-Streptomycin.

## 6.2. Quantification of transcript level

A quantitative polymerase chain reaction (qPCR or real-time PCR) was performed to allow a quantitative analysis of the two genes of interest.

### 6.2.1. RNA isolation and cDNA synthesis

Total RNA from different developmental stages as well as adult and some adult tissues was isolated. Trizol reagent was added to the cell pellets and, after a 15 minutes incubation, chloroform was also added: the cells were centrifuged at high speed to collect the aqueous phase. RNA was purified using isopropanol and, after the centrifugation to collect the RNA pellet, washed with 70% ethanol. Finally, when ethanol was completely evaporated, the pellet was resuspended in RNase-free water and the concentration calculated. DNA was also removed by DNase-I treatment and the sample was stored at -80°C.

cDNA was synthetized from 3 µg of total RNA in a reaction volume of 20 µL. Firstly, RNA was incubated with random primers (90 ng/ µL) and dNTP mix (10 mM) for 5 minutes at 65°C to allow the annealing; then, the specific buffer (containing 5 mM $MgCl_2$ and 10 mM DTT, dithiothreitol) and the M-MLV Reverse Transcriptase enzyme (200 U/µL) were added for the following retro-transcription – the enzyme was finally inactivated at 75°C. The reaction mix contained also a RNase inhibitor (40 U/µL).

### 6.2.2. qPCR

Transcript levels were quantified using Power SYBR® Green PCR Master Mix. An oligonucleotide (oligo) mix, containing both the forward (F) and reverse (R) oligonucleotides, and a template mix, containing cDNA, were prepared for each sample, as shown in **Table 3.2**. Hakai oligo (data not

shown) and CG7358 oligo (not shown) were used for each developmental stage, adult gender and tissue; as control, Rpl15 oligo (not shown) were used to amplify a constitutively expressed endogenous gene. Three replicates were carried out for each experimental condition. Once prepared the mix, the samples were loaded in the PCR plate and sealed and the qPCR machine was set.

The qPCR program defined for each sample the $C_T$ value, i.e. the cycle number necessary to reach the fluorescence threshold. For each experimental condition and for each gene, it was calculated the $2^{(-\Delta\Delta Ct)}$ which, depending on the control $C_T$ and the $C_T$ of the developmental stage 0, represents the initial transcript level of the analyzed gene in the selected developmental stage, adult gender or tissue.

## *6.3 Detection of protein localization*

In order to detect the cellular localization of the targeted proteins, the genes were cloned to be transfected and, consequently, expressed in S2R+ cells.

### *6.3.1. Cloning*

The PCR was carried out using specific oligonucleotides (not shown). The reaction components are listed in the **Table 3.3** in a final volume of 25 µL. An initial period of 5 minutes at 94°C was followed by 40 cycles of 30 seconds at 94°C, 40 seconds at 58°C and 1 minute at 72°C; finally, the final elongation was performed for 10 minutes at 72°C. The PCR products were analyzed by electrophoresis and a new PCR was performed to obtain the correct amount of the amplicons by gel elution (SmartPure Kit). The DNA amplicons were cloned in the pPAC vector44 with N-terminal myc tag (**Fig. 3.3**), as described below.

- The digestion of the PCR products using both EcoRV and AgeI (10 U/µL) created the correct DNA ends – these products were purified.

- The ligation assay allowed to insert the restriction products in the plasmid in the correct orientation using T4 DNA ligase (5 U/ µL).
- The transformation of Escherichia coli cells was performed by incubating the ligation products with the cells for 5 minutes in ice, 1 minute at 42°C and 5 minutes in ice – the transformed cells were grown for 45 minutes at 37°C and plated overnight (ON).
- Some bacterial colonies were inoculated in the culture medium ON to allow their growth and, consequently, the targeted DNA amplification.
- The plasmid DNA was purified (PureLink HiPure Plasmid Miniprep Kit) and the presence of the correct amplicons were checked by restriction and sequencing.

#### *6.3.2. Transfection*

Effectene was used to transfer the constructs into S2R+ cells. It was also transfected a construct for the expression of barentsz (btz) as an internal control and a cytoplasmic marker. For the transfection, 0.4 µg of Hakai or CG7358 construct as well as 400 ng of the btz-construct were incubated with 100 µL of the specific buffer and 3.2 µL of enhancer for 5 minutes at RT; 5 µL of Effectene reagent were also added and incubated for 10 minutes at RT. The transfection solution was joint with the cell suspension for 48 h.

#### *6.3.3. Immunolabelling*

After the incubation period, the cells were detached and diluted to be seeded in specific multiwell. After 30 minutes, they were fixed in 4% PFA, washed several times with PBS supplemented with 0.2% TRITON X (PBTX) and incubated with anti-myc antibody diluted 1:1000 in the washing solution containing also 10% donkey goat serum (DGS) ON at 4°C. The samples were washed in PBTX and incubated with the mouse secondary antibody diluted as the primary adding 1:1000 DAPI for 2 h at 4°C. The procedure

was concluded by several washes in PBTX. The samples were imaged with Leica SP5 confocal microscope using 63x oil immersion objective.

| | OLIGO MIX | | TEMPLATE MIX |
|---|---|---|---|
| **2X SYBR MIX** | 5 µL | **2X SYBR MIX** | 5 µL |
| **5 µM F/R MIX** | 2 µL | **cDNA** | 0.6 µL |
| **$H_2O$** | 3 µL | **$H_2O$** | 4.4 µL |

**Table 3.2. Components of the mix.** Oligo mix contains the specific forward and reverse oligonucleotides whereas the cDNA is in the template mix.

| REAGENT | VOLUME |
|---|---|
| F oligo (10 mM) | 1.25 µL |
| R oligo (10 mM) | 1.25 µL |
| cDNA | 2.5 µL |
| Buffer (5X) | 5 µL |
| dNTP mix (10 mM) | 0.5 µL |
| Phusion DNA Polymerase (2 U/ µL) | 0.25 µL |
| $H_2O$ | 14.25 µL |

**Table 3.3. Components of the PCR reaction.**

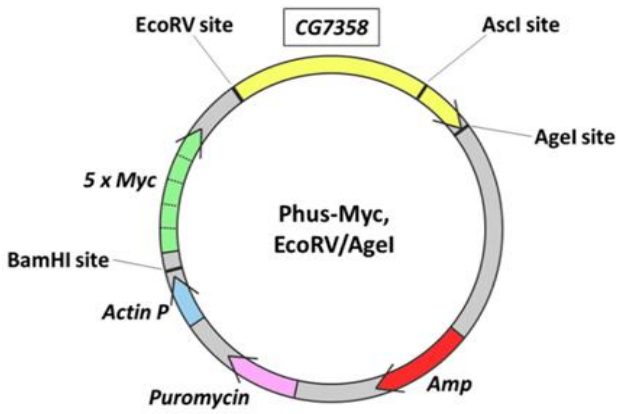


**Figure 3.3. pPAC vector44 chosen as the cloning plasmid.** It has a N-terminal Myc tag, the gene for the antibiotic resistance and restriction sites to allow the amplicon insertion (in this figure CG7358 is only shown).

## 6.3. Characterization of interacting proteins

The protein-protein interaction could be detected by co-immunoprecipitation (CoIP). For this application it was necessary a bigger amount of transfected cells: therefore, 1 μg of CG7358-myc construct were transfected together with 1 μg of Fl(2)d (female lethal d) construct – in the latter the tag was HA (Human influenza hemagglutinin). A control cell group was also prepared transfecting GFP (green fluorescence protein)-myc instead of CG7358. All the following procedures were conducted at 4°C.

After the transfection period, the cells were collected by a mild centrifugation (400 g for 10 minutes) and suspended in 1 mL of the lysis buffer prepared with 10 mM TRIS (2-Amino-2-hydroxymethyl-1,3-propanediol), 250 mM NaCl and 0.5% NP-40 (nonyl-phenoxypolyethoxyethanol) in $H_2O$ and supplemented with a protease inhibitor cocktail containing PMSF (phenylmethylsulfonyl fluoride) 1:100, Leupeptin 1:1000, Apolipoprotein 1:1000 and Pepstatin 1:1000. The samples were gently mixed on the wheel for 15 minutes and then centrifuged at 1000 g for 10 minutes to collect the supernatant (the cytoplasmic fraction) and resuspend the pellet (the nuclear fraction) in 300 μL of the lysis buffer. The nuclei were sonicated with 5 cycles of 30 seconds on and 30 off at low power. The two fractions were jointed and centrifuged at maximum for 15 minutes to remove cellular debris. The protein concentration was defined by Bradford assay (595 nm) using a BSA calibration line and a blank sample in which proteins were substituted by the extraction buffer to measure the absorbance due to the latter one. 2 mg of proteins were taken and the volume was increased, if necessary, to 900 μL with the lysis buffer. The primary anti-myc antibody (3 μg) was incubated with 15 μL of magnetic beads and 100 μL of the lysis buffer for 15 minutes. 100 μL of the primary antibody were added to the protein solution and the

samples were incubated ON in the wheel. For each sample, it was prepared a replicate in which RNase (500 U/µL) was added to understand if the possible protein interaction depends on RNA.

Using a magnetic rack, the supernatant was removed and the beads washed several times with the lysis buffer. The samples were then spin down to remove all the liquid inside. The pellet was resuspended in 6 µL of 4X LDS (lithium dodecyl sulfate) buffer, adding 15.6 µL of lysis buffer, and incubated for 10 minutes at 70°C. Finally, 2.4 µL of DTT) were added and a western blotting was performed.

The 10% polyacrylamide gel was prepared and the electrophoresis was carried out under reducing conditions. The proteins were electro-transferred to a nitrocellulose membrane (0.45 µm) operating in an immersion system. The protein transfer was checked through a Ponceau staining so that the membrane was washed with PBT and then blocked using 5% milk. A first incubation with anti-HA antibody was done ON at 4°C shaking continuously. The primary antibody was diluted 1:2000 in 5% milk. After several washes in PBT, the membrane was incubated with a goat anti-rabbit diluted 1:10000 in 5% milk for 1 hour at RT. The secondary antibody was conjugated with horseradish peroxidase (HRP). Final PBT washes followed.

Luminata Crescendo Western HRP substrate and Luminata Normal Western HRP substrate were used as substrates and the chemoluminesce was detected. After several washes, the membrane was also incubated with anti-myc antibody and a goat anti-mouse 1:10000 to detect again chemoluminesce.

# 4. RESULTS

## *1. REGULATION OF CHROMATIN STRUCTURE – I PART*

The first part of the analysis on the regulation of chromatin structure was carried out on mouse hepatocytes with sufficiently large areas of condensed chromatin along the nuclear envelope and associated to the nucleoli. After EDTA staining for RNPs, heterochromatin regions were bleached whereas, when specifically stained for DNA with OA, they were contrasted and DNA fibres dispersed in the interchromatin space could be also detected.

### *1.1. DNA methylation analysis*

EM immuno-gold labelling of thin sections localized 5mC on condensed chromatin. Firstly, the counting of the gold grains showed that DNA methylation was the less represented epigenetic modification occurring on heterochromatin compared to the other ones (**Graph 4.1**). A high variability of the 5mC labelling among the condensed chromatin regions of the same nucleus could be also detected (not shown). Curiously, the analysis of hepatocyte nuclei seemed to reveal a particular distribution, that could be defined a gradient distribution, of 5mC labelling changing from the surface of condensed chromatin to the nuclear envelope: in fact, the signal was mainly localized on the surface of chromatin facing the inner part of the nucleus (zone 3) (**Figs. 4.1 A, B**) while its density gradually decreased towards the nuclear envelope (zone 1), where the signal was almost absent. The statistical analysis confirmed that a significant difference between the mentioned regions existed (**Graph 4.3**). 5mC labelling, prevalently homogeneous, was also detectable on the nucleolus associated chromatin (**Fig. 4.1 C**) – few gold grains were visible on the nucleolus itself (**Fig. 4.1**

**C, arrows**), probably referred to methylated DNA fibres or methylated rRNA in the cases where no DNA was stained nearby.

- ✓ To further confirm the localization of 5mC on DNA, the results of enzymatic digestions were considered. The signal continued to be present after PK digestion (**Fig. 4.1 E**), thus demonstrating that proteins did not contribute to the labelling. However, their removal seemed to increase the yield, possibly for the unmasking of epitopes before covered by histone proteins. The labelling pattern remained likely the same, i.e. more abundant at chromatin surface. On the contrary, the immunopositivity drastically decreased from chromatin areas after DNA digestion (**Fig. 4.1 F**), giving right the 5mC detection on DNA. The statistical analysis confirmed the described results (**Graph 4.2**).

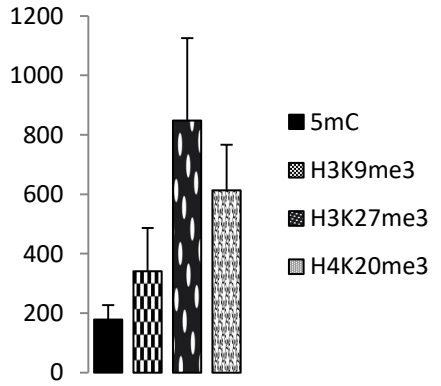


**Graph 4.1. Level of epigenetic modifications.** The semi-quantitative analysis of each epigenetic modification revealed that 5mC is scanty compared to the others, especially H3K27me3.

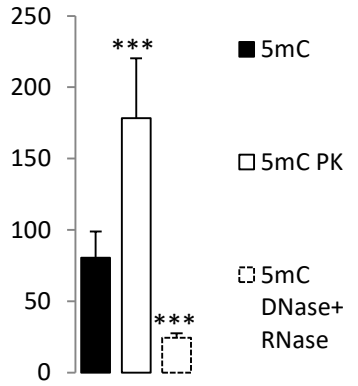


**Graph 4.2. 5mC level after enzymatic digestion.** 5mC is decreased when DNA is removed while it is increased when proteins are digested unmasking the epitopes (*p<0.01*).

The previously described 5mC distribution on DNA was confirmed by the localization of the DNMT3A enzyme prevalently on the heterochromatin surface and in the perichromatin region (**Fig. 4.1 D**).

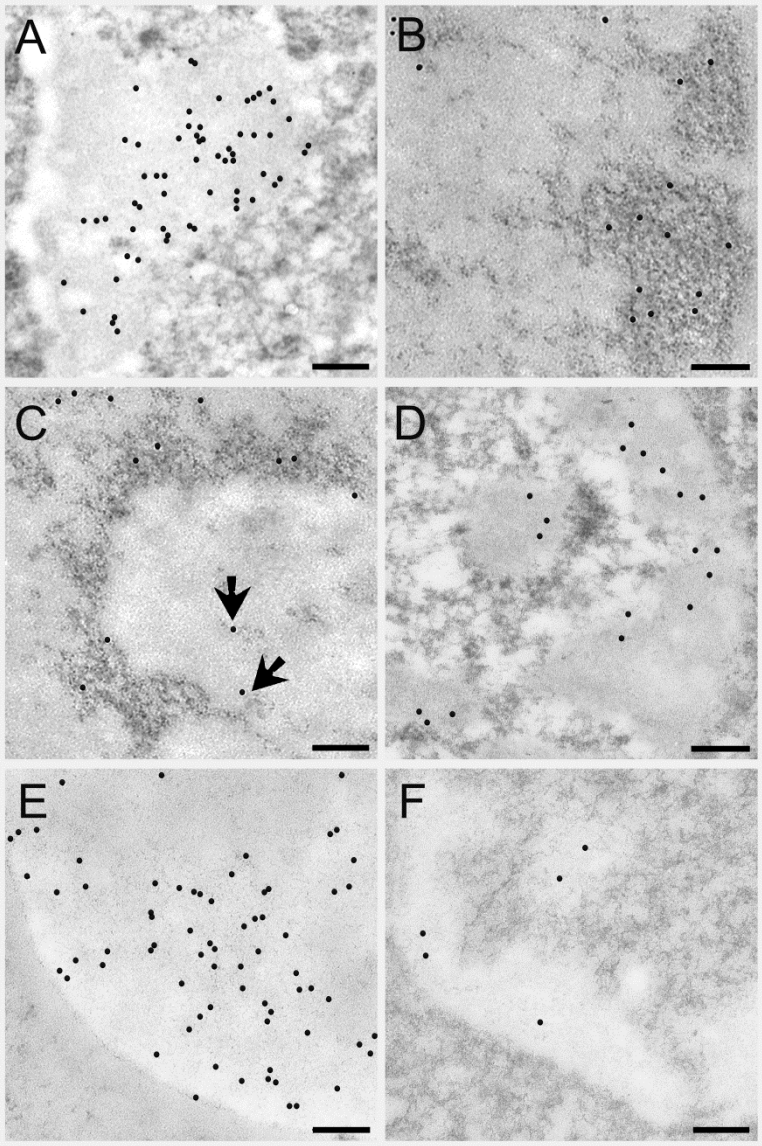


**Figure 4.1. 5mC and DNMT3A distribution on condensed chromatin regions in hepatocyte nuclei. A. B.** 5mC is mainly localized on heterochromatin, bleached after EDTA staining (**A**) or specifically stained with OA (**B**). In **A** the gradient distribution is particularly evident. **C.** 5mC signal is detected on OA stained nucleolus associated chromatin and DNA fibres (arrows). **D.** DNMT3A is distributed along the chromatin surface after EDTA staining. **E. F.** After PK (**E**) or DNase digestion (**F**) the 5mC labelling is respectively increased or largely removed on chromatin, thus demonstrating that the signal depends on DNA. *Bar: 150 nm (A,B,C) or 300 nm (D, E, F).*

The 12 nm gold grains were digitally enhanced by Paint Shop Pro 7.

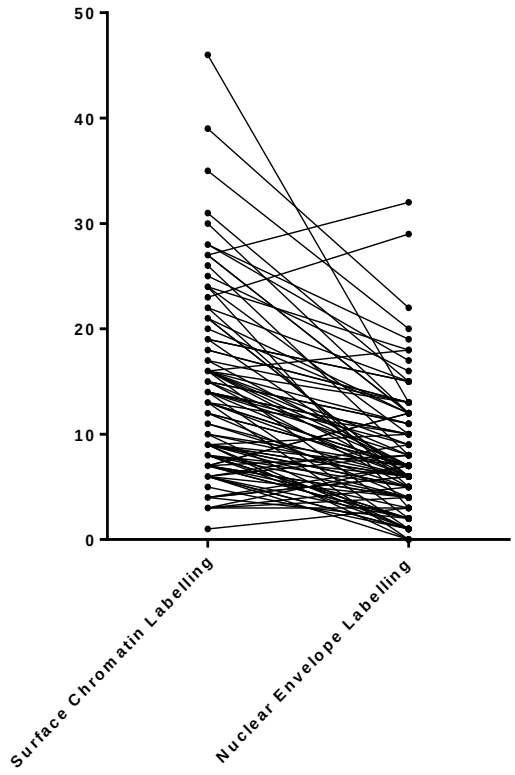


**Graph 4.3. 5mC gradient distribution.** A paired t test was performed to analyze the difference between the number of gold grains on the chromatin surface and nearby the nuclear envelope, considering the same condensed chromatin region. The graph shows that the surface labelling is generally higher than the nuclear envelope signal (*p<0.01*).

## *1.2. EM analysis of histone modifications*

Three different post-transcriptionally modified residues on histone tails were localized at EM: H3K9me3, a marker of constitutive heterochromatin (*Bonnet-Garnier et al. 2012*), H3K27me3, a marker of facultative heterochromatin (*Bonnet-Garnier et al. 2012*) and H4K20me3. The most abundant modification on condensed chromatin regions resulted H3K27me3, followed by H4K20me3 and H3K9me3 (**Graph 4.1**).

The EM micrographs show that both H3K9me3 and H4K20me3 were prevalently localized on the inner part of the condensed chromatin areas (zone 3), in the proximity of the interchromatin space (**Figs. 4.2 A, C, respectively**). On the contrary, H3K27me3 was found to be homogenously distributed on heterochromatin (**Fig. 4.2 B**). The differences between the

gold grains detected on the chromatin surface and nearby the nuclear envelope for H3K9me3 and H4K20me3 were statistically significant (**Graphs 4.4 A, B** ) while no relevant differences could be recorded for H3K27me3, confirming consequently the homogeneous distribution analyzed at TEM (**Graph 4.5**).

The distribution of each histone modification on DNA was also described by a double labelling with 5mC: the different types of epigenetic modifications tended to be accumulated on the condensed chromatin surface, except for H3K27me3 (not shown).

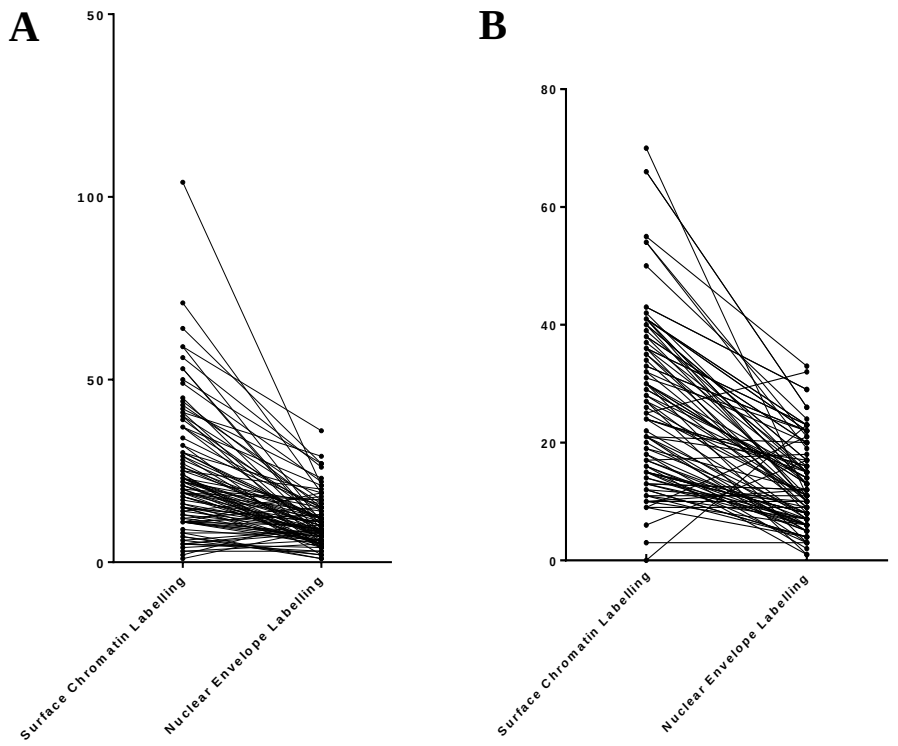


**Graph 4.4. H3K9me3 and H4K20me3 gradient distribution.** The paired t test revealed a significant difference between the labelling on the chromatin surface and nearby the nuclear envelope of the same condensed chromatin regions for both H3K9me3 (**A**) and H4K20me3 (**B**) (*p<0.01*).

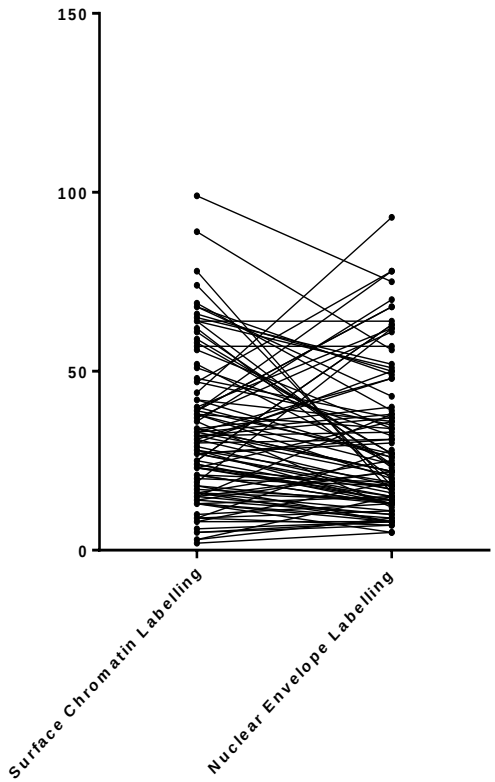


**Graph 4.5. H3K27me3 distribution.** The paired t test indicates the difference between the number of gold grains on the chromatin surface and nearby the nuclear envelope on the same condensed chromatin regions not significant. Generally, the surface labelling is similar to the nuclear envelope signal (*p>0.1*).

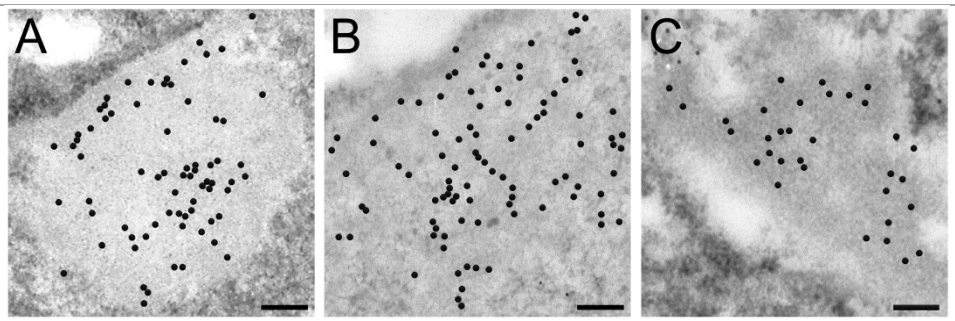


**Figure 4.2. Distribution of histone PTM on condensed chromatin regions in hepatocyte nuclei. A.** H3K9me3 is concentrated toward the interchromatin space. In the region 2 (see **Figure 3.1**) the labelling results almost absent. **B.** The distribution of H3K27me3 is homogeneous on heterochromatin. **C.** H4K20me3 is mainly localized on the chromatin surface than on its periphery. EDTA staining; *bar: 150 nm*.

The 12 nm gold grains were digitally enhanced by Paint Shop Pro 7.

## 2. REGULATION OF CHROMATIN STRUCTURE – II PART

The second part of the analysis of chromatin structure regulation was performed on cell models in which chromatin condensation was induced (modification of cation concentration or heat shock treatment) or physiological (erythrocytes).

### 2.1. Ionic environment, epigenetic modifications and chromatin condensation

#### 2.1.1. DNA methylation analysis

After the cell treatment and the immunolabelling, the sections were specifically stained for DNA with OA. The high-resolution analysis performed on the cells after the first treatment (20 mM $Ca^{2+}$ or $Mg^{2+}$ and 0.5 mM EGTA) revealed an increase in the number and volume of the condensed chromatin patches along the nuclear envelope or associated to the nucleoli (**Figs. 4.3 B, C, D, arrows**); on the contrary, they were scanty and relatively small in the CTR (**Fig. 4.3 A, arrows**). Diffuse loose DNA fibers were still present in all the nucleus, especially surrounding the condensed chromatin regions (**Figs. 4.4 B, C, D, arrows**), as in the CTR (**Fig. 4.4 A, arrows**), showing a not severe condensation state of chromatin. The second treatment (200 mM $Ca^{2+}$ or $Mg^{2+}$ and 5 mM EGTA) resulted in a clear and drastic condensation. OA staining proved to be very useful to this investigation: the chromatin fibers were no more visible and heterochromatin became highly compacted with the formation of bulky chromatin patches (**Figs. 4.3 B', C', D')**. Curiously, the differently treated samples showed a dissimilar chromatin organization with each other: in fact, in Egta the heterochromatin patches revealed a coarse compacted structure while $Mg^{2+}$ treatment seemed to result in highest compaction state of the chromatin.

- ✓ The chromatin condensation following the wide change of ion concentration was further confirmed by a morphological analysis (**Fig. 4.5**). In particular, a detachment of the condensed chromatin from the nuclear envelope was observed when the ionic environment was changed. However, although after the treatment the nuclear envelope showed some irregularities, such as deep invaginations or the osmotic swelling (**Fig. 4.5, arrowheads**), it was intact. Other morphological peculiarities were recognized in the cytoplasm of treated cells: in fact, the number of the vesicles and ribosomes seemed to increase. On the contrary, the cell membrane was not significantly altered.

Regarding the 5mC labelling, in control cells the signal was localized on the condensed chromatin patches as well as on the DNA surrounding fibers (**Fig. 4.4 A**). Following a moderate change in $Ca^{2+}$ concentration, a general reduction of 5mC could be detected: the gold grains were still visible on heterochromatin, especially on its surface toward the interchromatin space, whereas they were scantily distributed on chromatin fibers (**Fig. 4.4 B**). Nevertheless, when $Ca^{2+}$ level was severely increased, the DNA methylation improved, even if it seemed not proportional to the chromatin condensation level (**Fig. 4.4 B'**). When the effect of $Mg^{2+}$ was considered, no changes of 5mC labelling were recorded after 20 mM $Mg^{2+}$: the gold grains remained prevalently on chromatin surface and continued to be present on DNA fibers as in CTR (**Figs. 4.4 C, C'**). The signal was drastically increased after 200 mM $Mg^{2+}$, showing a homogeneous distribution. After calcium and magnesium removal, a prominent decrease in the DNA methylation profile could be always observed (**Figs. 4.4 D, 4.4 D'**). These results were further confirmed by a statistical analysis (**Graphs 4.6, 4.7**).

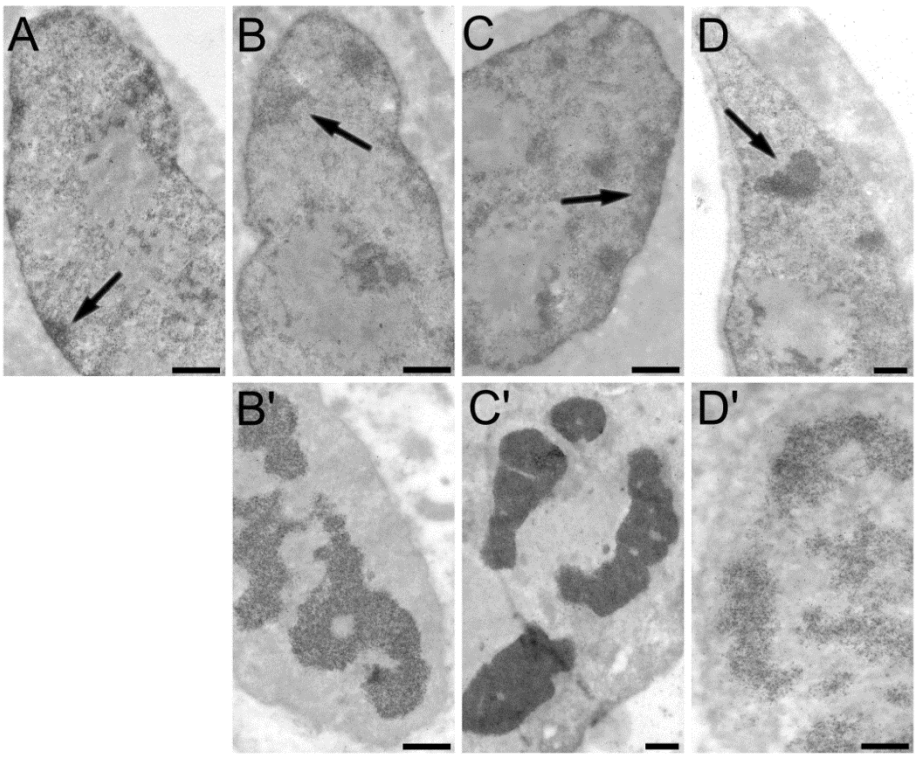


**Figure 4.3. Chromatin condensation following the changes of ion concentration.** HeLa cells were stained with OA for DNA. **A.** CTR cell shows small areas of condensed chromatin along the nuclear envelope, as the one indicated by the arrow. **B. C. D.** HeLa after 20 mM $Ca^{2+}$ (**B**), $Mg^{2+}$ (**C**) and 0.5 mM EGTA (**D**) show larger patches of condensed chromatin along the nuclear envelope (arrows), also more numerous than in CTR. **B'. C'.** HeLa after 200 mM $Ca^{2+}$ (**B'**) and $Mg^{2+}$ (**C'**) present a drastic increase in chromatin condensation, especially in MG. Chromatin is detached from the nuclear envelope. **D'.** In HeLa treated with 5 mM EGTA the chromatin condensation into large foci detached from the nuclear envelope is visible but it is characterized by a coarse non extreme compaction. *Bar: 500 nm*.

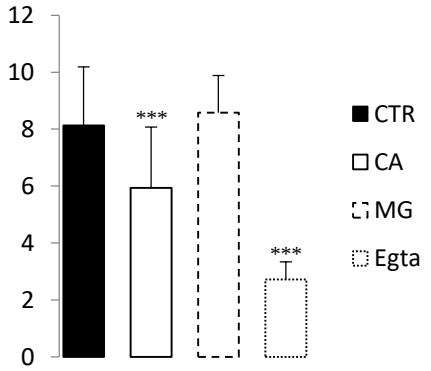


**Graph 4.6. 5mC level after a moderate change of ion concentration.** 5mC is moderately reduced by a $Ca^{2+}$ excess (20 mM) or more significantly decreased after divalent cation removal (0.5 mM EGTA) ($p<0.01$). Curiously, $Mg^{2+}$ level (20 mM) does not change DNA methylation ($p>0.1$).

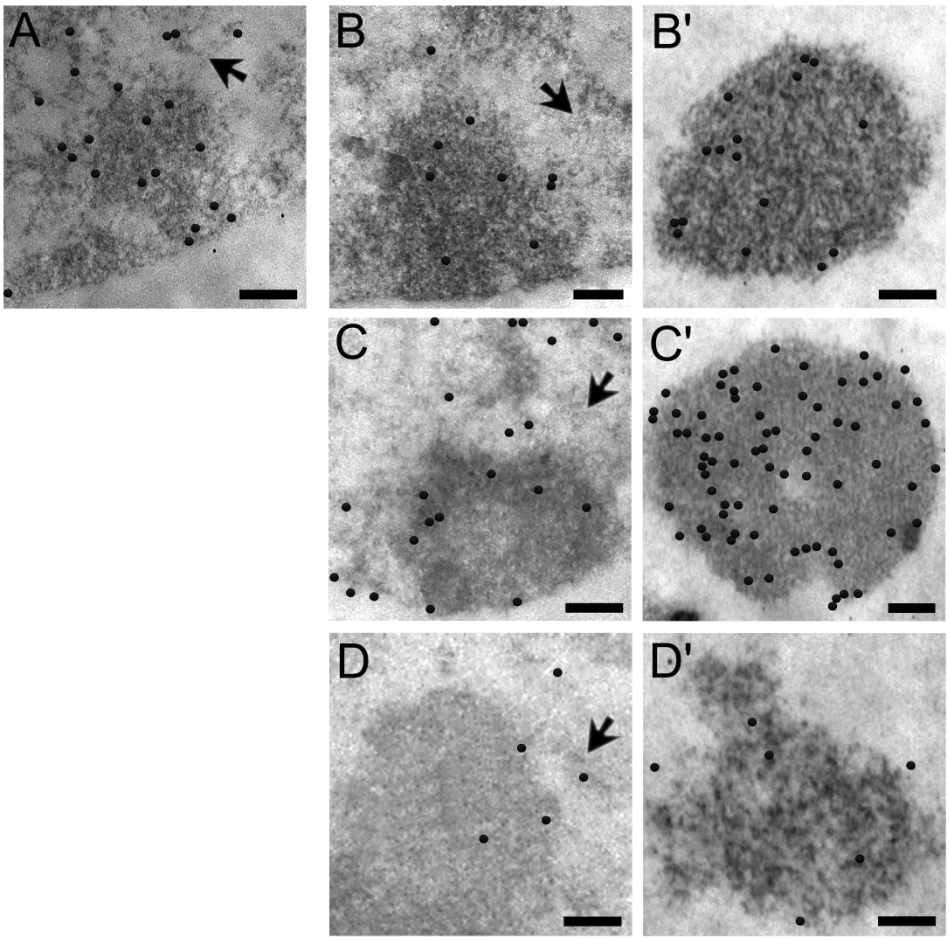


**Figure 4.4. 5mC distribution on condensed chromatin regions following changes of ion concentration. A.** 5mC is distributed on a CTR region of condensed chromatin: it appears more abundant on chromatin surface and on DNA fibers dispersed around the heterochromatin patch (arrow). **B.** After 20 mM $Ca^{2+}$, the signal is reduced on a quite expanded condensed chromatin area but especially on DNA fibers (arrow). **B'.** When the $Ca^{2+}$ concentration is drastically increased (200 mM), the chromatin becomes highly compacted such as no DNA fibers are still visible and shows a weak increase in the 5mC labelling, which is mainly localized on chromatin surface. **C.** 20 mM $Mg^{2+}$ incubation induces the formation of large chromatin patches; DNA fibers surround the chromatin regions (arrow); the 5mC signal seems unchanged compared to the CTR, even if clearly present on chromatin surface. **C'.** After 200 mM $Mg^{2+}$, chromatin is drastically condensed, assuming the highest compacted structure among all the treatments, and 5mC results highly increased and homogenously distributed – DNA fibers are not visible. **D, D'.** After the removal of free divalent cations with 0.5 (**D**) or 5 mM EGTA (**D'**) chromatin is condensed and the labelling seems very significantly reduced. Compared to the other condensed chromatin regions following the described treatments, the chromatin structure seems coarse. OA staining; *bar: 300 nm*.

The 12 nm gold grains were digitally enhanced by Paint Shop Pro 7.

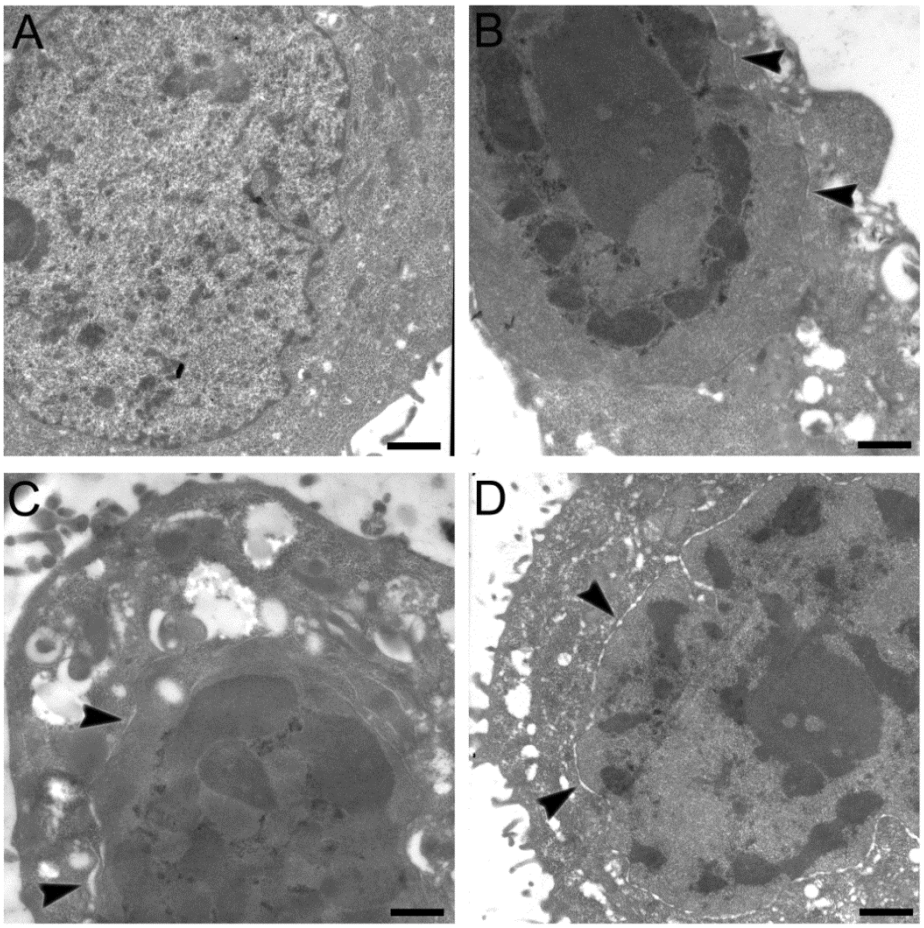


**Figure 4.5. Morphological analysis of HeLa cells after severe changes of ion concentration. A.** In CTR the condensed chromatin is represented by small areas along the nuclear envelope or around the nucleoli. No other peculiarities could be shown. **B. C. D.** After the treatment 200 mM $Ca^{2+}$ (**B**) or $Mg^{2+}$ (**C**) and 5 mM EGTA (**D**), chromatin is highly condensed and it is completely detached from the nuclear envelope. Although the latter shows irregularities, as invaginations, it is intact. The arrowheads indicate the osmotic swelling following the treatment. In the cytoplasm the number of vesicles and, presumably, of ribosomes is increased while the cell membrane seems more irregular but intact. *Bar: 1 μm*.

The results of the DNMT3A fluorescence labelling on HeLa cells after excessive changes in the ionic environment (200 mM $Ca^{2+}$ or $Mg^{2+}$ and 5 mM EGTA) were also considered to ascertain possible variations of DNA methylation. The analysis of the optical density (**Graph 4.8**) revealed a significant increase of DNMT3A amount in the CA and especially in MG, corresponding to the increase of the EM 5mC labelling. However, no changes in the amount of DNMT3A enzyme were revealed in the Egta despite the significant decrease of the DNA methylation level detected at ultrastructural level.

The immunofluorescence analysis also showed the distribution of DNMT3A inside the nucleus: in the control cells as well as in the treated samples, the enzyme was mainly localized in the interchromatin space, probably on the surface of condensed chromatin (**Fig. 4.6**). However, in CA and MG the cytoplasm signal seemed to increase according to the significant variation obtained with the optical density analysis whereas the cytoplasmic labelling after EGTA incubation was negligible, as in CTR. Curiously, the presence of a very weak signal was often detected in the nucleolus following the addition of either $Ca^{2+}$ or $Mg^{2+}$ (**Fig. 4.6 I**).

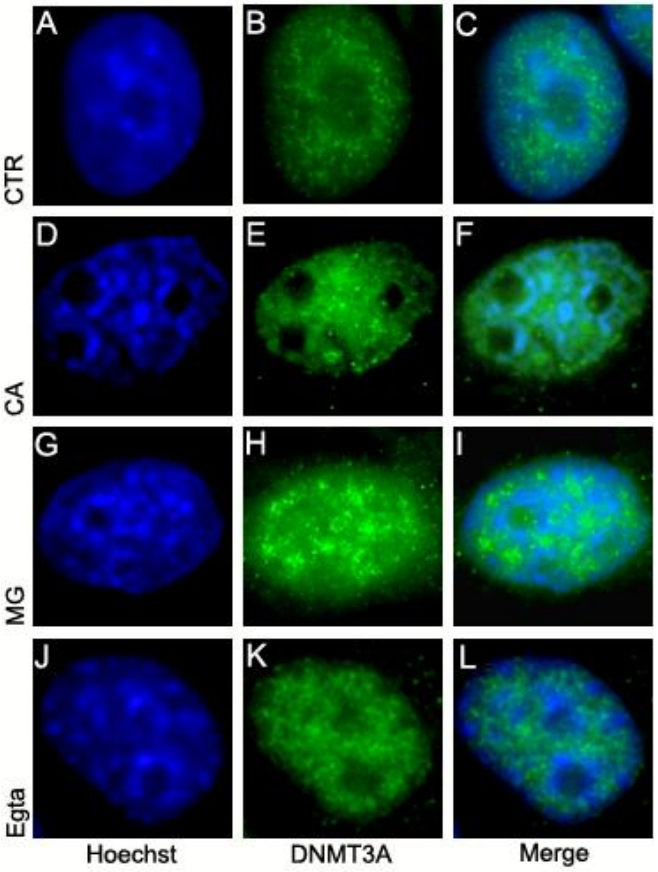


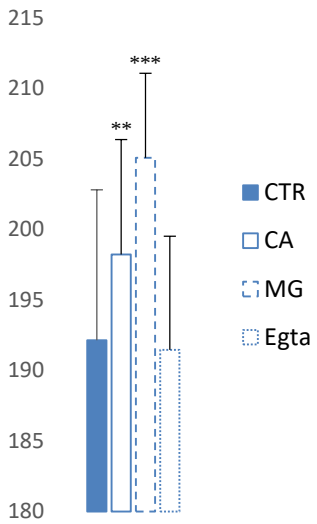


**Figure 4.6. DNMT3A fluorescence immunolabelling after drastic changes of $Ca^{2+}$ or $Mg^{2+}$ level.** The DNA staining with Hoechst 33258 shows the chromatin condensation after the changes in ion level (**D. G. J**), compared to CTR cell (**A**). When compared with CTR (**B**), an increase of the DNMT3A in $Ca^{2+}$- and especially $Mg^{2+}$-treated cells is detectable (**E. H**) while after ion removal DNMT3A seems not changed. The merged images reveal the DNMT3A distribution in the interchromatin space (**C. F. I. L**). A weak signal is present in the nucleolus following the addition of $Mg^{2+}$ (**I**).

**Graph 4.8. Level of DNMT3A after drastic changes of $Ca^{2+}$ or $Mg^{2+}$ concentration.** The histogram shows a significant increase in DNMT3A labelling when the level of $Ca^{2+}$ and, especially, of $Mg^{2+}$ is increased ($0.01<p<0.05$ and $p<0.01$, respectively). Differently, after the removal of divalent cations by EGTA, the amount of DNMT3A is not significantly changed compared to control cells.

### *2.1.2. Histone modification analysis*

The analysis of the level and distribution of the histone modifications was also carried out after 200 mM $Ca^{2+}$ or $Mg^{2+}$ and 5 mM EGTA. The effects of a drastic change in the ionic environment were only considered because it very clearly induced a high chromatin compaction, facilitating the analysis of the chromatin structure regulation by histone PTM.

As expected by the chromatin condensation following the drastic change in the cation concentration (**Figs. 4.3 B', C', D'**), the increase in the level of each histone modified residue (H3K9me3, H3K27me3 and H4K20me3) was statistically significant (**Graph 4.7**), except for magnesium-treated samples which did not show any modification in the amount of H3K9me3 and H3K27me3. However, a toward increase tendency could be detected also in these cells. Importantly, a reduction of any histone modification was never revealed, contrarily to 5mC.

No changes seemed to be present at EM level in the distribution of histone PTM in the treated samples compared to the CTR cells (**Fig. 4.7**), demonstrating that the treatment could induce a variation of the level of these epigenetic modifications but not of their chromatin localization. In this first high-resolution analysis, the distribution on highly compacted regions of heterochromatin appeared not homogeneous in the majority of the samples (**Fig. 4.7**): in fact, the signal seemed more concentrated on chromatin surface than along the nuclear envelope, except for H3K9me3 in MG and H4K20me3 in CTR and EGTA, showing a more homogeneous distribution on heterochromatin.

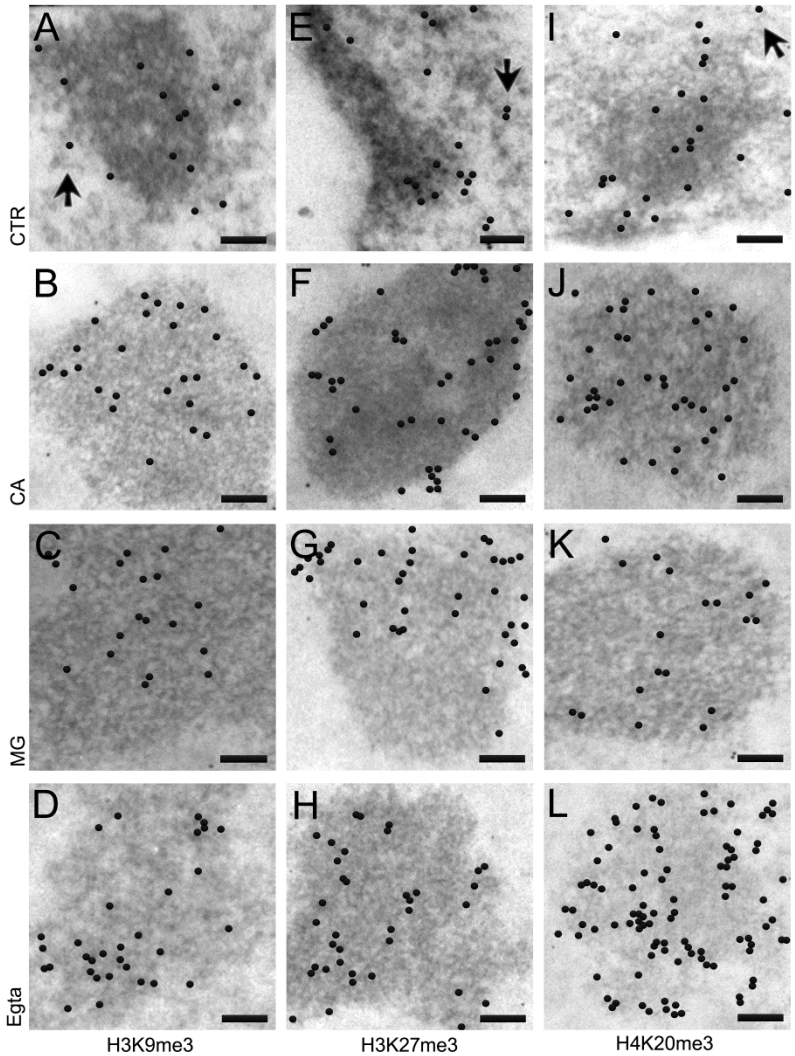


**Figure 4.7. Chromatin localization of histone modifications after severe changes in $Ca^{2+}$ and $Mg^{2+}$ concentration. A. B. C. D.** H3K9me3 is prevalently localized on chromatin surface in CTR (**A**), CA (**B**) and Egta (**D**) – in CTR the labelling can be detected also on DNA fibers (arrow). However, the H3K9me3 distribution after an increase of $Mg^{2+}$ appears more or less homogeneous. **E. F. G. H.** For H3K27me3, the labelling is mainly on chromatin surface in all the treated samples (**F. G. H**) as well as in the control (**E**), in which labelled DNA fibers are also detectable (arrow). **I. J. K. L.** H4K20me3 can be prevalently recognized on the chromatin surface in CA (**J**) and MG (**K**) – in CTR (**I**) the signal is detected on surrounding fibers (arrow). OA staining; *bar: 150 nm*.

The 12 nm gold grains were digitally enhanced by Paint Shop Pro 7.

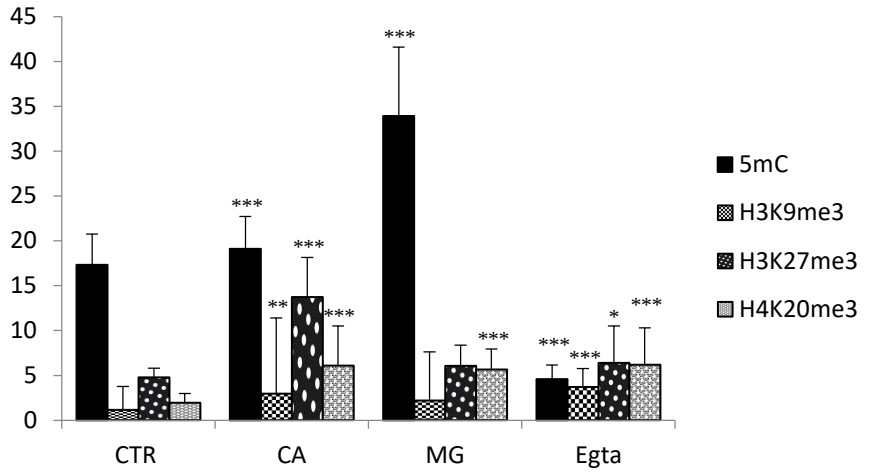


**Graph 4.7. Level of DNA methylation and histone modifications after a severe change of ion concentration.** 5mC significantly increases after $Ca^{2+}$ and especially $Mg^{2+}$ addition while it drastically decreases after cation removal. However, considering the level of condensation in CA, the DNA methylation density does not seem proportional (*p<0.01*). For H3K9me3, which is always very low compared to the other modifications, as well as H3K27me3, an increase of their level is detectable after $Ca^{2+}$ increase or EGTA treatment (*p=0.01, p<0.01, p<0.01* and *p=0.05*, respectively): nevertheless, even if after $Mg^{2+}$ addition this modification does not change significantly, a tendency to increase can be detected. Considering the last histone modification, a clear increase of H3K20me3 is revealed in all the conditions (*p<0.01*).
This analysis also reveals that 5mC is the most abundant modification differently from the data in **Graph 4.1** showing 5mC as the low abundant; on the contrary, the histone modifications maintain their relative abundance.

### *2.1.3. ESI analysis*

To better understand where the ions in excess localized or the sites from which they were removed, ESI analysis, an independent imaging technique, was performed in order to define how the ionic atmosphere was responsible of the final chromatin condensation. Phosphorus was detected at high resolution to localize the nucleic acids whereas calcium and magnesium to understand their distribution. ESI provided a quantitative and high contrasted images of chromatin fibres without the use of contrast agents. These results are very preliminary.

The detection of P in all the treated samples revealed a high chromatin condensation in accordance with the previously described results: in fact, the increase in the contrast displayed an accumulation and compaction of phosphorus on areas along the nuclear envelope (**Figs. 4.8 E, J, M**) in comparison with control cells (**Fig. 4.8 A**). Following the detection of calcium, the ESI results showed that in the control samples $Ca^{2+}$ and P were prevalently superimposed on DNA, especially on its surface, although some free ions were distributed in the interchromatin space or around the chromatin (**Fig. 4.8 B**). In cells with a calcium or magnesium excess, $Ca^{2+}$ seemed to still occupy an area on DNA but the distribution on its surface increased (**Figs. 4.8 F, J**); free $Ca^{2+}$ ions were also detected. As expected for the chelating function of EGTA, free cations were almost completely disappeared in Egta samples and the majority of $Ca^{2+}$ continued to be superimposed with P on condensed DNA (**Fig. 4.8 N**). On the other hand, after the detection of magnesium, ESI images showed that it was almost totally on chromatin in all the samples (**Figs. 4.8 C, G, K, O**) and probably it made a sort of cloud around DNA. However after EGTA, a decrease in the magnesium signal was detected (**Fig. 4.8 O**). In the merged images, $Ca^{2+}$, as well as P, was generally covered by the $Mg^{2+}$ signal, remaining only visible on the chromatin surface where it was probably very concentrated: in fact, when $Mg^{2+}$ was significantly reduced in Egta, $Ca^{2+}$ was also detectable on chromatin (**Figs. 4.8 D, H, L, P**).

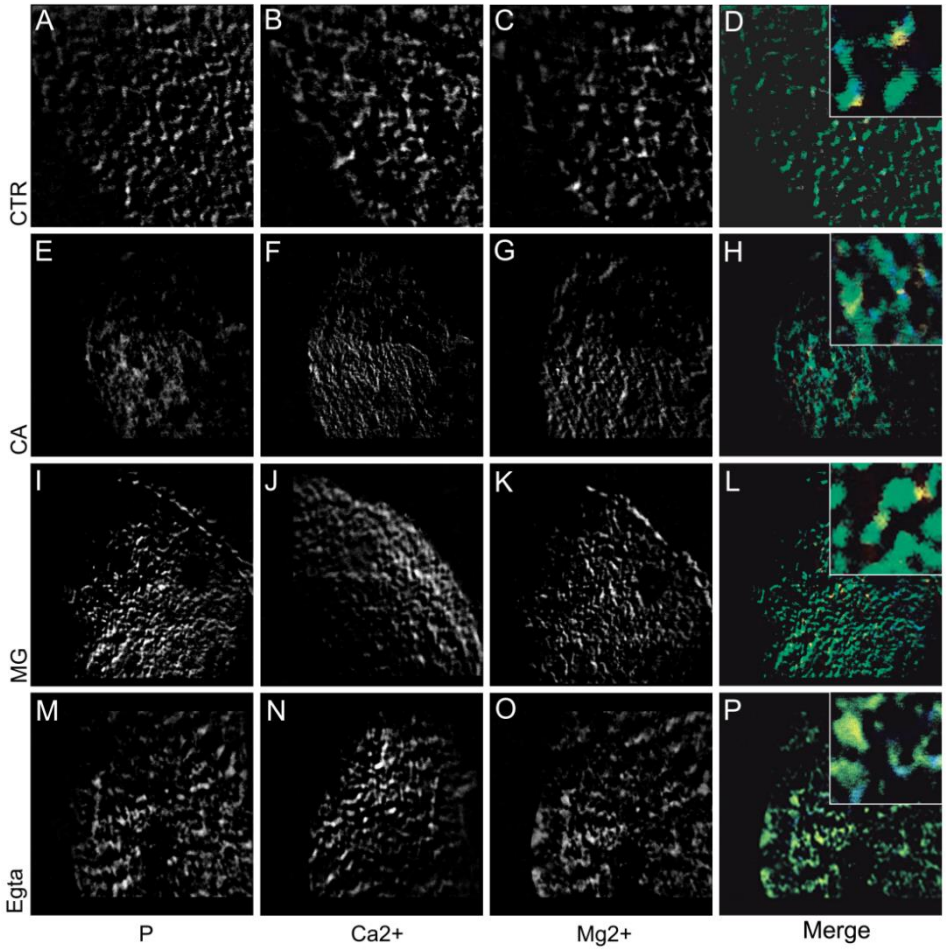


**Figure 4.8. ESI images. A. E. I. M.** In treated samples (**E. I. M**) an accumulation of P revealed a considerable chromatin condensation compared to control cells (**A**). However, chromatin organization seems different among the treated samples. **B.** $Ca^{2+}$ localization generally corresponds to P distribution in CTR and it seems more concentrated on chromatin surface. Nevertheless, few free ions are also distributed around the DNA fibers. **F. J.** In cells with a calcium excess or after $Mg^{2+}$ incubation, $Ca^{2+}$ still remains on DNA, although a more intense signal is dispersed on its surface. **N.** After divalent cation removal, $Ca^{2+}$ is located on P-positive regions and, reasonably, free cations are almost completely disappeared. **C. G. K. O.** The detection of $Mg^{2+}$ reveals that it is almost totally on chromatin in CTR (**C**) as well as in treated cells (**G. K. O**) and forms a sort of cloud around the condensed chromatin regions. However, after EGTA, a decrease in the $Mg^{2+}$ signal is detected (**O**). **D. H. L. P.** The merged images show that $Mg^{2+}$ (green) is always superimposed on P (blue), covering its signal but also $Ca^{2+}$ (yellow), which remains visible only on chromatin surface where it is particularly concentrated or dispersed in the interchromatin space, especially in CA (**H**) and MG (**L**). $Mg^{2+}$ is significantly reduced in Egta, allowing $Ca^{2+}$ detection also on chromatin (**P**). In these images the previously described characteristics are more visible. The inserts show a detail of the ion distribution.

## *2.2. Heat shock, epigenetic modifications and chromatin condensation*

DNA was specifically stained with OA to detect the chromatin organization after heat shock at TEM. In a control nucleus the very small heterochromatin regions were confined along the nuclear envelope showing a quite relaxed structure (**Fig. 4.9 A**) whereas the DNA fibers were very diffused. A heat shocked nucleus showed highly compacted chromatin regions nearby the nuclear envelope but also in the interchromatin space and an expanded nucleolus associated chromatin (**Fig. 4.9 B**); DNA fibers were coarser**.**

The combination of immunocytochemistry and OA staining allowed to analyze the level and the distribution pattern of each epigenetic modification on chromatin.

- Although the transcription rate of these cells, a not negligible 5mC labelling could be detected on condensed chromatin regions in CTR (**Fig. 4.9 C**). Curiously, after heat shock, which clearly induced chromatin condensation, the chromatin areas resulted much less labelled (**Fig. 4.9 D**). A t-test confirmed a statistically significant reduction of the 5mC labelling on heterochromatin after the heat shock (**Graph 4.9**). Concerning the EM distribution, the 5mC signal was often localized on chromatin surface in both CTR and HS.
- Histone modified residues (H3K9me3, H3K27me3 and H4K20me3) were also immunocytochemically localized on condensed chromatin areas before and after the heat shock (**Fig. 4.9**). A high variability of the labelling distribution was revealed moving from a condensed chromatin region to another one in the same nucleus: therefore, it was not possible to describe the prevalence of each histone modification on the chromatin surface (toward the interchromatin space) or nearby the nuclear

envelope, as on the contrary happened for 5mC. On the other hand, the statistical analysis showed that the level of the studied histone PTM was increased in the heat shocked HeLa cells compared to the CTR ones, unlike 5mC (**Graph 4.9**): as expected, histone modifications seemed to be correlated to the high chromatin compaction.

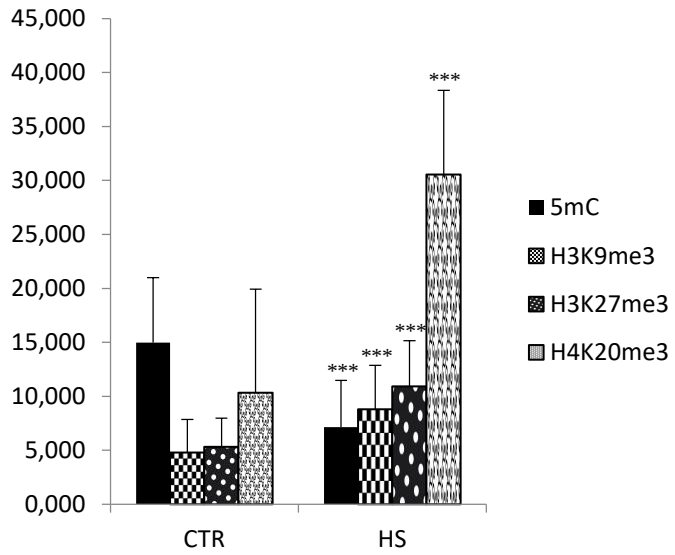


**Graph 4.9. Level of epigenetic modifications after heat shock.** The semi-quantitative analysis reveals that all the histone post-transcriptional modifications are significantly increased, especially H4K20me3 (*p<0.01*). Unexpectedly, 5mC is shown to be highly significantly reduced after heat shock (*p<0.01*).

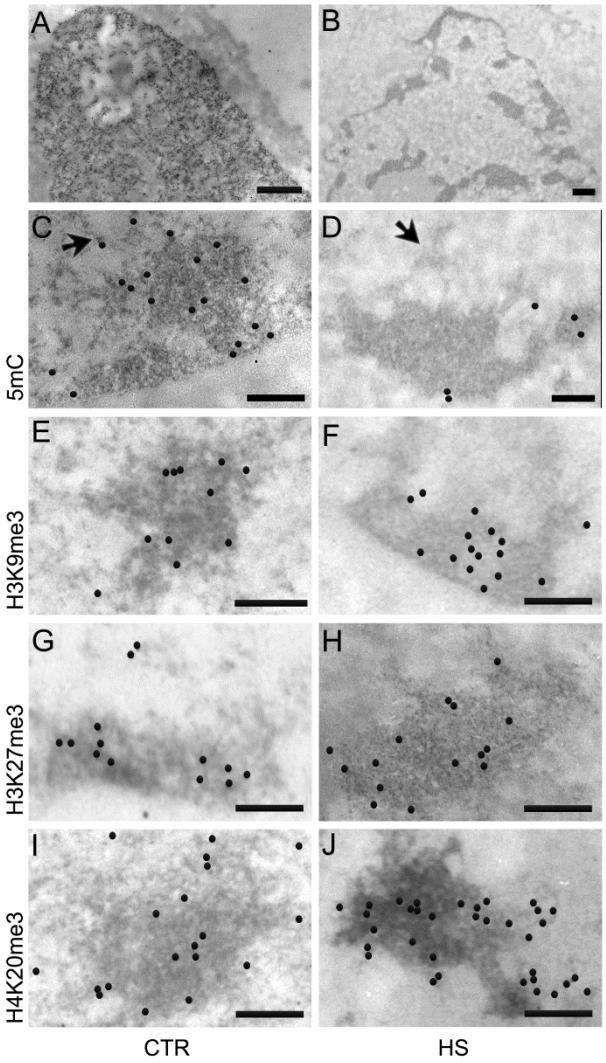


**Figure 4.9. Chromatin localization of epigenetic modifications after heat shock. A.** In a CTR nucleus heterochromatin regions are small and often localized nearby the nuclear envelope. The chromatin is prevalently organized in dispersed fibers. **B.** After heat shock, chromatin is condensed in larger regions along the nuclear envelope and in the interchromatin space. The nucleolus associated chromatin also results expanded. **C.** The arrow indicates a DNA fiber surrounding a control heterochromatin region, on which a relatively abundant 5mC labelling can be detected. **D.** The 5mC signal is drastically reduced on a condensed chromatin region of approximatively the same size after heat shock. Some unlabelled coarse DNA fibers can be also seen (arrow). **E. F. G. H. I. J.** The distribution of histone modifications on condensed chromatin is generally homogeneous and no differences can be detected between CTR and HS. An increase in the amount of labelling, especially for H4K20me3 (**I. J**), can be revealed. OA staining; *bar: 500 nm (A, B), 300 nm (C. D) or 200 nm (E. F. G. H. I. I. J).*

The 12 nm gold grains were digitally enhanced by Paint Shop Pro 7.

## 2.3. Epigenetic modifications during erythropoiesis

After the EDTA staining, the condensed chromatin regions were bleached while RNPs were contrasted. Therefore, this staining allowed to simply recognize three different developmental stages of erythrocytes: a premature form was characterized by normal areas of condensed chromatin along the nuclear envelope and a large interchromatin space (**Fig. 4.10 A**); the compacted chromatin regions nearby the nuclear envelope joined to form an extended heterochromatin area reducing the interchromatin space which was represented by an accumulation of interchromatin granules in the intermediate stage (**Fig. 4.10 B**); finally, in the mature form chromatin is almost completely condensed (**Fig. 4.10 C**).

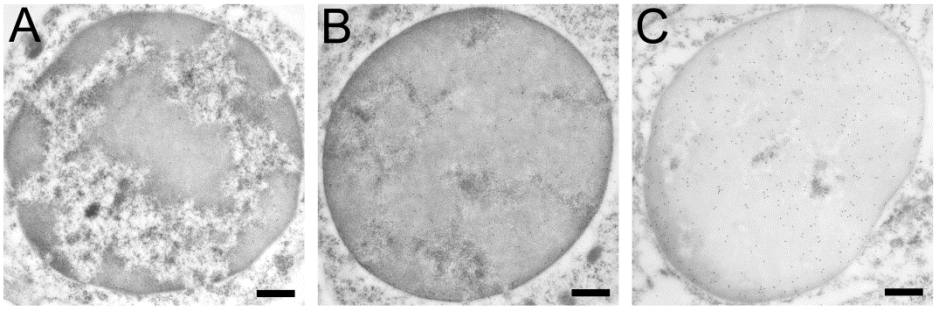


**Figure 4.10. Erythrocyte developmental stages. A.** The premature form shows several regions of condensed chromatin along the nuclear envelope and an extended interchromatin space. **B.** In the intermediate stage the condensed chromatin regions are no more clearly visible because they are joint. The interchromatin space is reduced in small areas in which a lot of IG are accumulated. **C.** Chromatin is almost completely condensed revealing that this nucleus is nearly to be expelled. EDTA staining; *bar: 500 nm*.

The distribution and the semi-quantitative analysis of the epigenetic modifications took into account were performed on these three different developmental stages.

### *2.3.1. DNA methylation changes during erythropoiesis*

**Figure 4.11** shows areas of condensed chromatin (approximatively of the same size) in which a clear increment of 5mC labelling could be detected during the progressive chromatin condensation occurring in the erythrocyte maturation: therefore, the mature stage was characterized by the highest level of labelling density. However, the statistical analysis demonstrated that chromatin condensation was not gradual because a significant increase of DNA methylation characterized only the transition from the intermediate to the mature form (**Graph 4.10**). In addition, the detailed analysis at TEM revealed that the 5mC level was not homogenous among the different chromatin regions of the premature stage in which the latter could be recognized. In several cases the gradient distribution, discussed in the **Paragraph 1.1**, was detected in which the 5mC signal was almost absent from the nuclear envelope vicinity being more concentrated along the chromatin surface.

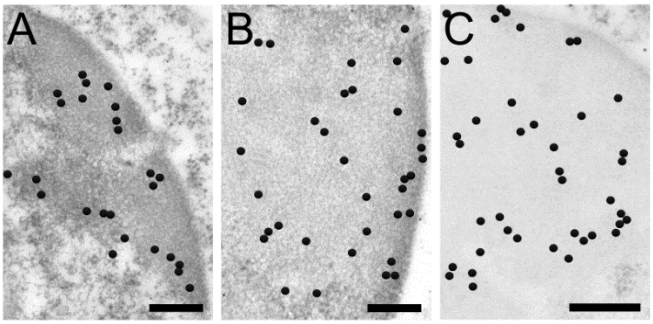


**Figure 4.11. 5mC distribution on erythrocytes during their development.** Three regions of condensed chromatin in the cell nucleus of a premature (**A**), intermediate (**B**) and mature (**C**) erythrocyte are shown. A progressive increase of 5mC gold grains can be detected. In **A** the gradient distribution can be also revealed. EDTA staining; *bar: 300 nm*.

The 12 nm gold grains were digitally enhanced by Paint Shop Pro 7.

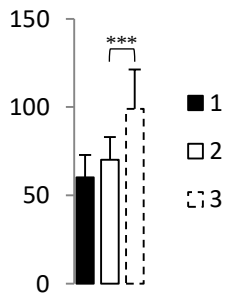


**Graph 4.10. 5mC labelling during erythrocyte development.** A significant increment of 5mC labelling could be detected only between the intermediate (2) and mature form (3) ($p<0.01$) (1=early stage).

### *2.3.2. Variation of histone modifications during erythropoiesis*

To further analyze the regulation of chromatin structure, the distribution and the level of histone post-transcriptional modifications were also studied in the erythrocytes at different developmental stages. This represents a cell model in which chromatin compaction was not induced by any treatment being a physiological process.

The distribution of the PTM varied significantly from a heterochromatin region to another in the same nucleus (not shown). A particular pattern of distribution on heterochromatin could be not described: however, the labelling was often concentrated on chromatin surface than nearby the nuclear envelope. This result, as the others shown previously, could confirm the localization of histone modifications described in the **Paragraph 1.2**, probably revealing the H3K27me3 distribution also on chromatin surface. However, a deep analysis is required.

As for 5mC, the level of each histone modified residue on condensed chromatin was statistically analyzed. All the three histone modifications showed the same behaviour: curiously, the amount of the signal recorded for the precocious developmental stage dropped in the intermediate erythrocyte form; then, the statistical analysis revealed no changes during the transition of the latter one to the mature cell. This data indicated that the change occurred drastically in the middle of the process without other modifications during the progression.

Therefore, while 5mC increased during the erythropoiesis, the histone PTM, considered here, seemed to decrease during this developmental process, pinpointing the regulation of the chromatin structure as a very complex process.

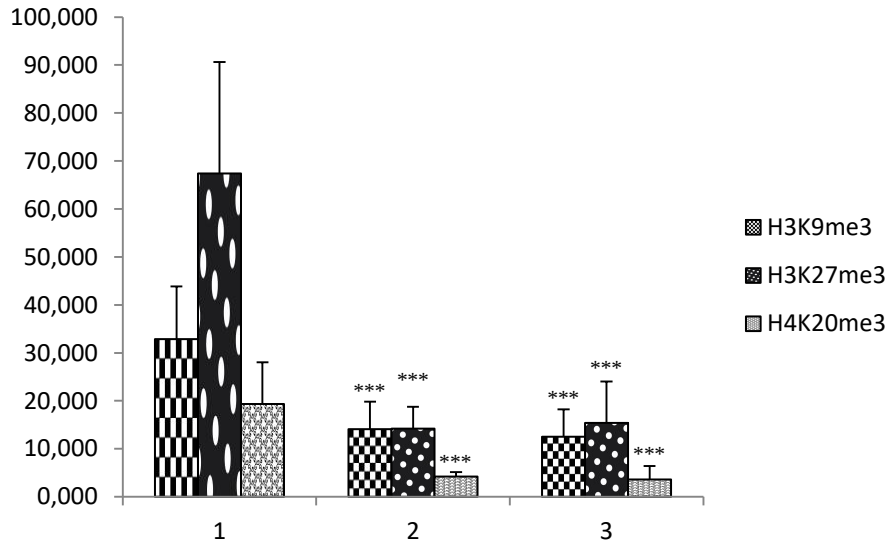


**Graph 4.11. Histone modification labelling during erythrocyte development.** Differently from 5mC, the level of each histone PTM decreases very significantly changing from the early stage (1) to the intermediate one (2) while no other changes in the amount of modified residues can be detected comparing the intermediate and mature stages (3) (*p<0.01*).

## *3. RNA METHYLATION*

The analysis of the 5mC localization on RNA was carried out firstly on HeLa cells to detect this modification with a higher probability according to their transcription rate: in fact, as tumor cells, the high transcription rate tumor cells allowed to analyze a huge amount of RNA fibrils and, consequently, to significantly define their possible epigenetic modifications. However, the presence of this RNA modified residue was confirmed in normal cells, i.e. hepatocytes, to exclude that RNA methylation was an aberrant process due to the neoplastic transformation. Therefore, all the described results were detected on these two different models. For clarity, not all the pictures were shown but only the most relevant and informative were chosen.

This analysis was supported by two distinct staining methods: EDTA and terbium staining were used. The first, although contrasting preferentially RNPs, allowed to detect RNA fibrils but the staining was not as fine as the terbium procedure, which specifically stains RNAs, permitting to obtain highly defined fibrils although at low contrast. The use of two staining techniques represented also a double check of our results.

A very preliminary EM study of m6A was also performed on HeLa cells as well as hepatocytes and using the two described staining procedures.

### *3.1. 5mC detection on RNA fibrils and RNA-containing granules*

During the evaluation of 5mC distribution within a cell nucleus, we found a constant and not negligible 5mC signal at the border of heterochromatin areas (not shown), in the PR where transcription by Pol II normally occurs (*Cmarko et al. 1999*). Moreover, this labelling was significantly reduced after a RNase treatment alone and in combination with DNase (not shown). Considering the 5mC localization in the PR and the labelling disappearance after RNA digestion, 5mC was thought to be detected at EM level on RNA molecules. Both EDTA regressive technique and terbium staining showed that the perichromatin labelling was due to RNAs: in fact, the 12 nm gold labelling for 5mC was present over RNA fibrils (**Fig. 4.12 A**). Furthermore, 5mC and RNase colocalization on fibrils definitively confirmed that the observed PR labelling depended on RNA (**Fig. 4.12 B**): in fact, even if it was not possible to define if the enzyme was working or not, it is normally localized on RNA.

The RNAs located in the PR are nascent fibrils (PF). After the incorporation for a well-defined period of RNA precursors, such as FU, PF could be marked. Therefore, to further confirm the presence of 5mC on nascent

RNA, a double labelling for 5mC and FU was performed. The result, shown in **Fig. 4.12 C**, revealed that 5mC and FU frequently localized together on specifically stained RNA fibrils. Moreover, a double labelling for 5mC and a hnRNP core protein was found to be present on PF (**Fig. 4.12 D**): hnRNPs are considered markers of in situ forms of nascent transcripts, i.e. PF (*Fakan 1994*).

Despite the ascertained presence of 5mC on nascent RNA fibrils, this modified nucleotide was also detected on perichromatin granules (**Fig. 4.12 E**) – the latter are considered to be a form of mature and stored mRNA leaving the nucleus later (*Fakan 2004*) – double labelled PG were also found (**Fig. 4.12 F**). Moreover, 5mC labelled PF were detected outside the nuclear envelope in the vicinity of the pore, in the cytoplasm close to ribosomes and in the exosomes (not shown). These data suggested that this modification could pertain to mRNA, being present during the entire lifespan of a RNA fibril. This hypothesis was confirmed by the double labelling for 5mC and 7-methylguanosine (7mG) on RNA PF (**Fig. 4.12 G**). Even if this capping is present on other RNA products of Pol II, it is considered specific for mRNA. Finally, the 5mC was immunocytochemically localized on RNA fibrils, also in close proximity of a ribosome, on which the poly(A) tail was recognized by in situ hybridization (**Figs. 4.12 H, I**): as well as 7mG, poly(A) tail is one of mRNA marker, despite its presence on other Pol II products.

### *3.1.1. DNMT3A localization on RNA fibrils and granules*

Unexpectedly, the study of DNMT3A distribution within the cell nucleus showed its localization on perichromatin RNA fibrils contrasted by EDTA regressive technique in HeLa cells as well as in hepatocytes. To confirm this surprising finding, terbium procedure was performed to specifically stain RNAs: the **Fig. 4.13 A** shows a terbium stained and DNMT3A labelled PF. DNMT3A was demonstrated to be present on nascent transcripts to verify the possibility that this enzyme is involved in the precocious RNA modification. This could be confirmed by its presence on IG (not shown), in which splicing factors are accumulated. As expected, DNMT3A colocalized with both FU and a hnRNP core protein (**Figs. 4.13 B, C**), which are known to label nascent transcripts as described before. However, as for 5mC, it was also localized on poly-adenylated and 7mG-capped RNA fibrils, as well as on PG (**Figs. 4.13 D, E, F**).

Finally, DNMT3A was also found to be localized on 5mC labelled PF, further confirming the possible link between this enzyme and this modification (**Fig. 4.13 G**).

## *3.2. Nucleolar distribution of 5mC*

5mC was also localized within the nucleolus (**Fig. 4.14 A**). Firstly, this modified nucleotide was detected in the granular component (GC) according to rRNA localization in this area: in fact, in this region ribosome subunits are assembled and matured but DNA is not present (*Vandelaer et al 1996*). This signal almost disappeared after RNase digestion (not shown). Then, 5mC was occasionally found in the fibrillar center (FC) of proliferating HeLa cells, as expected by the DNA presence in this region (*Derenzini et al. 1993*). Finally, a non-abundant labelling was also recognized on the dense fibrillar component (DFC) where rDNA is actively transcribed (*Fakan and*

*Puvion 1980; Biggiogera et al. 2001*): in this area the signal can be referred both to DNA and RNA. However, after RNA removal by enzymatic digestion, the 5mC immuno-gold labelling was no more detectable (not shown).

After a double labelling for 5mC and FU on HeLa cells, it was sometimes possible to recognize in the same nucleus a nucleolus highly labelled for both 5mC and FU and another one almost completely unlabelled (**Fig. 4.14 B**).

### *3.3. m6A localization at EM*

m6A is the most abundant RNA modification and it was recently shown to be a cotranscriptionally event (*Knuckles et al. 2017*). A very preliminary study was carried out on m6A at the ultrastructural level.

This modified nucleotide was localized immunocytochemically in the PR. Importantly, several m6A-labelled PF were detected in HeLa cells as well as hepatocyte nuclei, contrasted both with terbium staining and EDTA regressive technique (**Fig. 4.13 H**).

These results about the EM m6A localization are in accordance with the recent data in the literature showing m6A as a transcriptional modification. Moreover, the presence of this modified residue on RNA fibrils in both normal (hepatocytes) and neoplastic cells (HeLa) confirmed mRNA methylation as a physiological process.

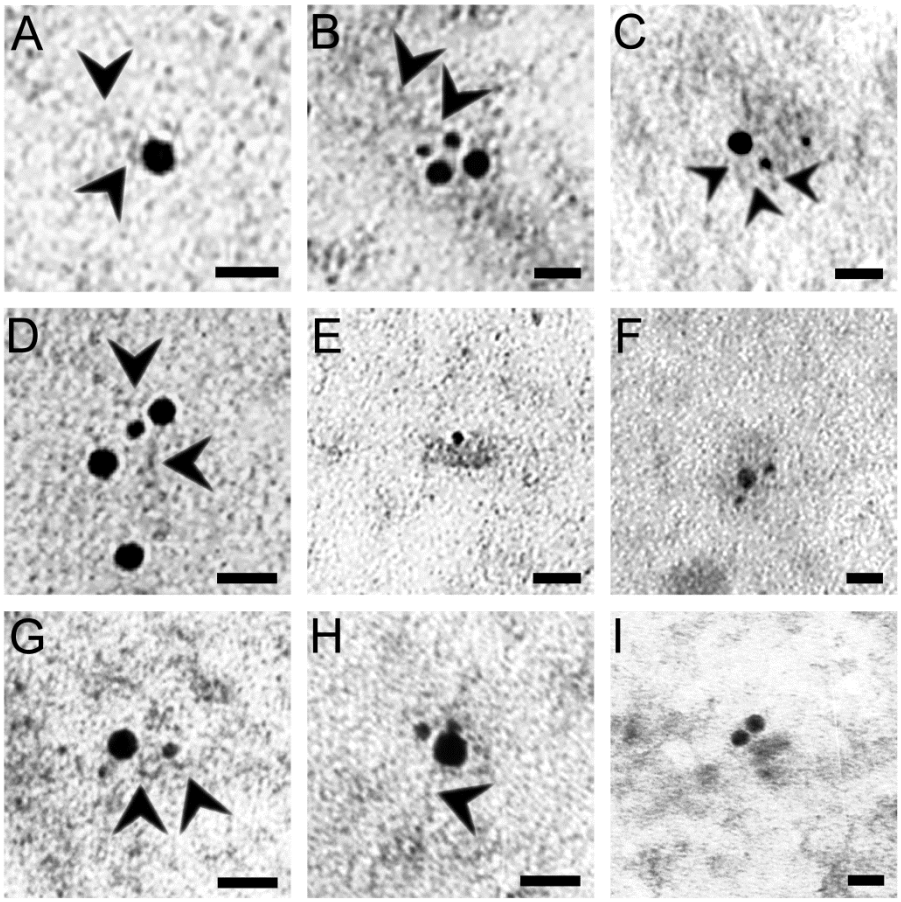


**Figure 4.12. 5mC detection on RNA. A.** 5mC is localized by a 12 nm gold grain on a RNA fibril, indicated by the arrowheads – HeLa cell; EDTA staining. **B.** A double labelling for 5mC (6 nm) and RNase (12 nm) is detected on a RNA fibril (arrowheads); this enzyme is localized on RNA even if it is inactive – Liver; EDTA regressive technique. **C.** 5mC often colocalizes with FU, a marker of nascent RNA, on RNA fibrils (arrowheads) – HeLa cell; terbium staining. **D.** The hnRNP core proteins are marker of PF: 5mC is localized on RNA fibrils (arrowheads) also labelled for a hnRNP core protein – HeLa cell; terbium staining. **E. F.** A PG was found to be labelled for 5mC alone (**E**) or with a hnRNP core protein (**F**) – HeLa cell and terbium staining or Liver and EDTA staining, respectively. **G.** 5mC is immunocytochemically detected on 7mG-positive RNA fibrils, indicated by the arrowheads, in the PR – Liver; terbium staining. **H. I.** A double labelling for 5mC and poly(A) tail is recognized on PF (arrowhead; **H**) or nearby a ribosome (**I**) – HeLa cell; terbium staining. *Bar: 25 nm*.

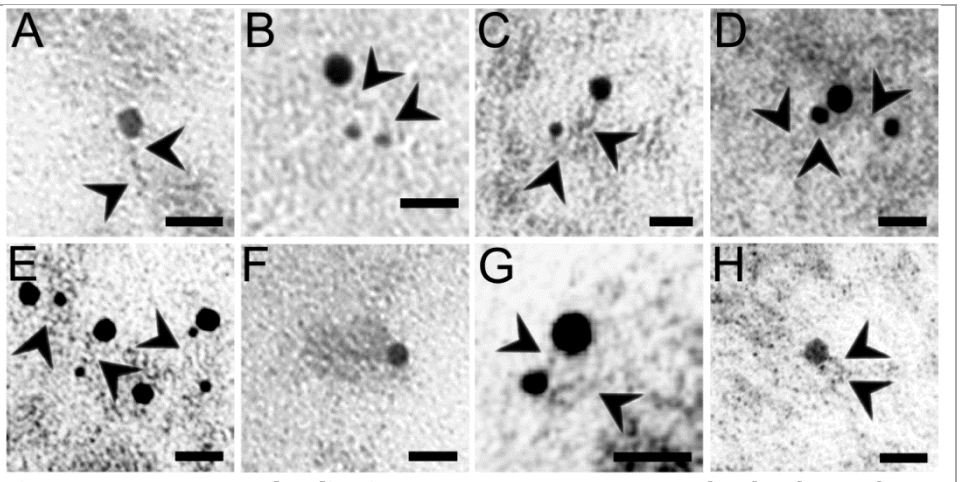


**Figure 4.13. DNMT3A localization on RNA. A.** DNMT3A is localized on terbium-positive RNA fibril (arrowheads) – Liver; terbium staining. **B. C.** RNA fibrils, indicated by the arrowheads, are shown to be labelled for both DNMT3A and FU (**B**) as well as a hnRNP core protein (**C**), which are markers of nascent transcripts – Liver and HeLa cell, respectively; EDTA staining. **D. E.** The arrowheads indicate the PF double labelled for DNMT3A together with poly(A) tail (**D**) and 7mG (**E**), specific markers of mRNA – Liver and HeLa cell, respectively; EDTA staining. **F.** A PG is shown to be labelled by DNMT3A, confirming the localization of this enzyme on RNA – Liver; terbium staining. **G.** Finally, DNMT3A is found on 5mC-labelled RNA fibril (arrowheads) to further confirm the possible link between RNA methylation and this enzyme – Liver; EDTA regressive technique. **H.** m6A localizes on PF (arrowheads), showing this modification as an early event also at EM level – HeLa cell; EDTA staining. *Bar: 25 nm*.

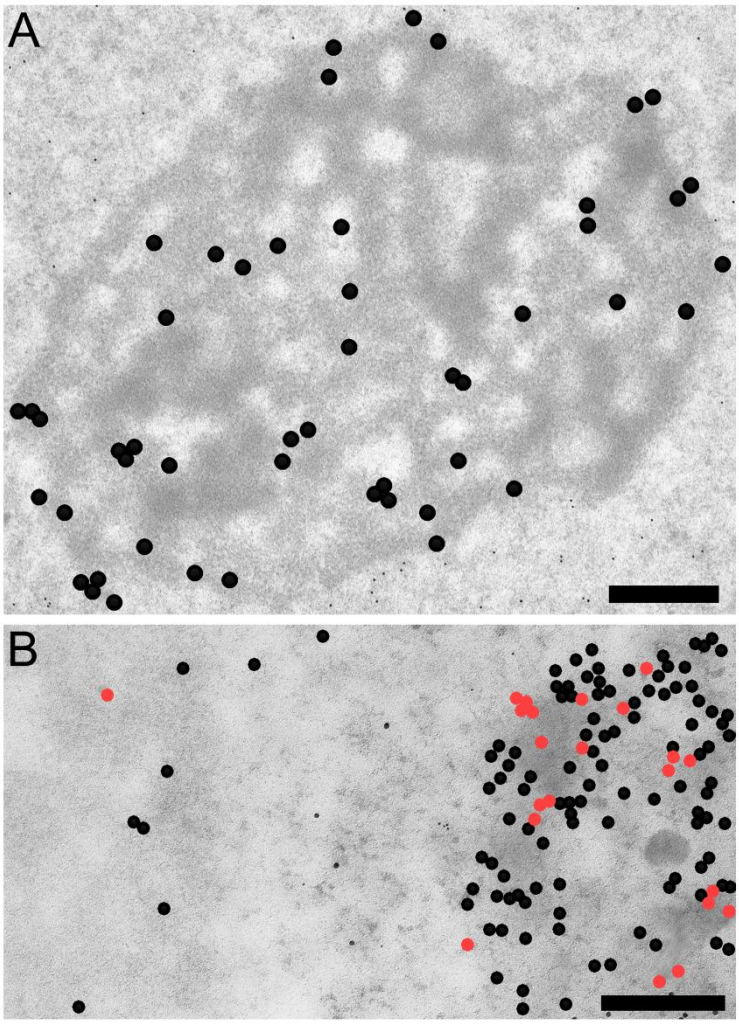


**Figure 4.14. 5mC distribution within the HeLa nucleolus. A.** 5mC is mainly localized on the GC. However, the signal is also visible in the DFC, which results as the darkly stained areas. Even if sometimes it is detectable, in this picture the 5mC labelling in the FC cannot be recognized. EDTA staining; *bar: 500 nm*. **B.** The picture shows an area of two different nucleoli in the same cell nucleus. FU (black), as well as 5mC (red), is more abundant in one of the two nucleoli. EDTA staining; *bar: 250 nm*.

The 12 and 6 nm gold grains were digitally enhanced by Paint Shop Pro 7.

## 4. *HAKAI AND CG7358 CHARACTERIZATION IN Drosophila melanogaster*

The cDNA was successfully synthetized to be used for the analysis of Hakai and CG7358 expression level by qPCR during the different developmental stages (**Graph 4.11**). Hakai was expressed during the first stages of embryogenesis, especially between 2 and 4 hpf, dropping at 10 hpf to remain lowly expressed in all the other stages and in adults, except for ovaries where its level resulted higher. On the other hand, CG7358 seemed to follow the same tendency of Hakai until 20-22 hpf, even if this transcript showed a huge pick around 2-8 hpf compared to Hakai; then, CG7358 level increased again during the pupal stages. It was highly expressed in adult male but not in female, where, however, there was a pick in heads and ovaries.

The level of Hakai and CG7358 were integrated with the m6A level, obtained in previous studies: they did not fit perfectly. However, the CG7358 level seemed to better follow m6A tendency, suggesting a possible correlation between this protein and the mRNA modification, without excluding a proper function of this protein component.

After the cloning and transfection, the two Hakai isoforms and the long one of CG7358 were overexpressed in *Drosophila* SR2+ cells to be localized by immunostaining (**Fig. 4.15**). Both the Hakai isoforms were detected in the cytoplasm: however, the short isoform was also abundant in the nucleus. Curiously, the long CG7358 isoform was found to be only localized in the cytoplasm, although the possible involvement of this protein in the RNA-methyltransferase complex.

CoIP was performed starting from cells transfected with CG7358 tagged by Myc and with the Fl(2)d-HA construct. As control, a parallel group of cells were transfected with GFP-Myc together with Fl(2)d-HA. The CoIP results

revealed that CG7358 could interact with Fl(2)d in a RNA independent manner (**Fig. 4.16**): in fact, an enrichment of Fl(2)d was detected in CG7358 transfected cells compared to the control samples showing the possible interaction between these two components; moreover, the protein level did not change if RNase was present (RNase+ samples) or not (RNase- samples).

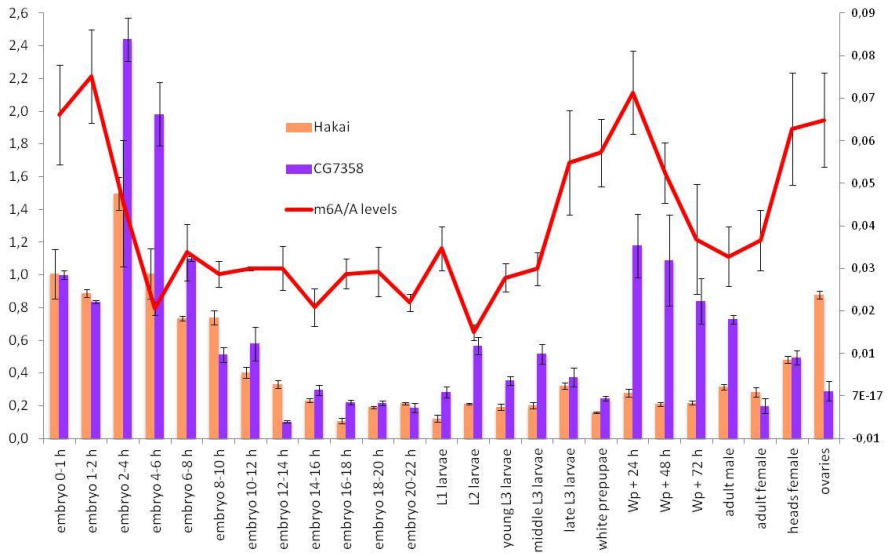


**Graph 4.12. Expression level of Hakai and CG7358.** Hakai transcript results highly expressed only in the first stages of embryogenesis (0-10 hpf) with a pick between 2 and 4 hpf. Then, this gene is very scantly expressed, also in adults. However, in female heads and in particular in ovaries, the Hakai level is increased. CG7358 is hugely expressed between 2 and 6 hpf as well as during the pupal stages and in adult males. The low abundance of CG7358 is recorded during all the other developmental stages. The m6A level is also described: there are three picks. One pick is at the very early stages of embryogenesis (0-4 hpf); the second is during the larval and pupal stages; m6a increases in female heads and ovaries.

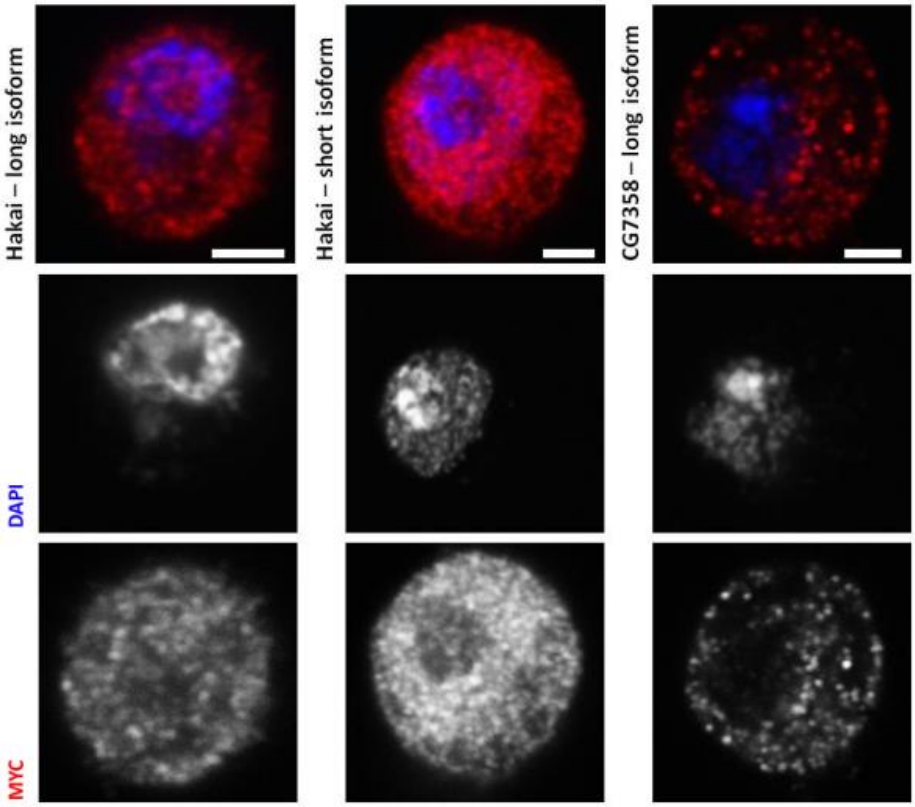


**Figure 4.15. The Hakai and CG7358 localization within the cell nucleus.** The Hakai long isoform is homogenously and scantly distributed in the cytoplasm and nucleus whereas the short isoform, although the presence in the cytoplasm, seems to be more expressed in the nucleus. The latter is the more expressed. Finally, CG7358 transcript is shown to be localized in the cytoplasm with no labelling detectable in the cell nucleus. SR2+ cells; *bar: 2.5 µm*.

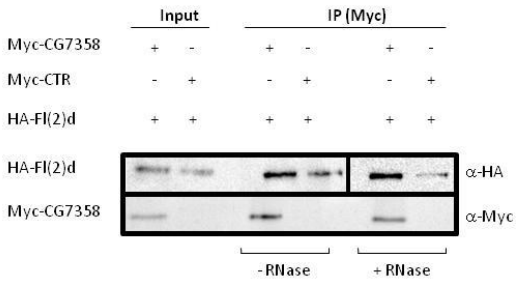


**Figure 4.16. CoIP results for CG7358-Fl(2)d interaction.** The input shows the type of the transfected construct in the sample, reported in each line. When revealed by anti-HA, Fl(2)d is more abundant in the sample transfected with Myc-CG7358 compared to the control one (Myc-GFP), revealing that a part of this component remains attached to CG7358. This result is not changed by RNase, showing that the possible interaction does not depend on RNA.

# 5. DISCUSSION

This research aimed at studying DNA methylation in an alternative way at EM level. Our unexpected findings prompted us to investigate deeply the regulation of chromatin structure, including histone modifications and condensation-inducing treatments, and the RNA methylation.

The analysis of 5mC distribution on condensed chromatin in mouse hepatocytes indicated this modification as the less represented among all the studied epigenetic modifications. One of the possible explanation is that DNA methylation could be less necessary in maintaining DNA condensation status and/or in controlling chromatin functionality. Considering different heterochromatin regions of the same cell nucleus, we found a high variability in the amount of labelled 5mC, in our opinion in relationship to the different chromosome territories *(Cremer and Cremer 2010*). However, the crucial point of our results about chromatin structure regulation is what we have called "5mC gradient distribution", which is supported by the DNMT3A localization on chromatin surface. In an interphase nucleus observed at TEM, the chromatin structure is related to its functional state: constitutive heterochromatin is reasonably localized at the periphery of condensed chromatin regions nearby the nuclear envelope, i.e. far from the PR where transcription occurs (*Fakan 1994; Cmarko et al. 2003*), while the genes undergoing silencing and activation (regulated genes) are present on the chromatin surface, facing the PR. Consequently, considering what is known about DNA methylation, we expected to find much more 5mC labelling than that found where unregulated and inactive loci are located, i.e. nearby the nuclear envelope. Our contrasting results could show that cytosine methylation is not required to guarantee the DNA condensed structure, being in accordance with the more recent findings

describing methylation as a modification reducing nucleosome stability (*Ngo et al. 2016*). On the other hand, 5mC accumulation toward the interchromatin space confirms its well-known role in regulating gene expression. However, differently from what has just been described, 5mC was shown to be homogeneously localized on nucleolus associated chromatin. Probably, the presence of satellite DNA justifies a stable and ubiquitous pattern of methylation, even if it does not seem to agree with the previously described relationship between DNA methylation and condensed chromatin structure. As for other data described below, this result highlights the complexity of the mechanisms regulating chromatin structure.

To better understand the regulation of chromatin structure, we also introduced the EM analysis of some histone modifications (H3K9me3, H3K27me3 and H4K20me3), which are known as heterochromatin markers (*Bonnet-Garnier et al. 2012*). The statistical analysis of 100 condensed chromatin regions showed that H4K20me3 and H3K9me3, although the latter is a marker of constitutive heterochromatin (definitely silenced genes), are widely localized on heterochromatin surface where regulated loci are present. Moreover, H3K27me3 unexpectedly shows a homogeneous distribution, although being a marker of facultative heterochromatin, generally localized toward the chromatin surface. It seems to us that the main function of histone modifications, as well as DNA methylation, is the gene switching-on and -off on the chromatin surface whereas they do not necessarily maintain the condensation status of constitutive heterochromatin.

In order to better understand how these selected epigenetic modifications affect chromatin structure, we used HeLa cells as model in which chromatin condensation was experimentally induced by changes in cation

concentration or heat shock treatment. Mouse erythrocytes were also analyzed because chromatin compaction occurs physiologically.

Our morphological results showed at EM level that both divalent cation removal and addition determine chromatin compaction, which seems to be concentration-dependent. Moreover, condensed chromatin organization looks dissimilar in the three different experimental conditions. This could be explained by two mechanisms: chromatin may have multiple binding sites for $Ca^{2+}$ and $Mg^{2+}$ with different affinity or two or more distinct forms of higher order structures with different stability may exist in the ionic environment (*Martin et al. 2007; Visvanathan et al. 2013*). ESI analysis represents an important tool to reveal the accumulation sites of divalent cations after their addition to test their involvement in the condensation: the majority of these ions seems to be localized around and on the chromatin suggesting that the charge neutralisation of the sugar phosphate backbone by divalent cations plays a central role in maintaining the chromatin compaction level. In the absence of free divalent cations, removed by chelation with EGTA, the lack of changes in the DNMT3A amount accompanied by a huge decrease in the DNA methylation level may firstly indicate that divalent cations are required for the activity of this enzyme, probably as cofactors in agreement with *Wang et al.* (*2014*). In addition, our immunocytochemical results revealed that DNA methylation is decreased in spite of the chromatin condensation: hence, these two processes do not seem to be necessarily correlated. Our conclusion is supported by the result of a moderate change in calcium concentration as well as by the very significant 5mC decrease in heat shocked cells, in which condensation was also found. However, the decrease of DNA methylation with the chromatin compaction also confirms its destabilizing effect on the condensed structure discussed in the previous section. The addition of higher amount of $Ca^{2+}$ or $Mg^{2+}$ (200

mM) induces indeed an increase of DNMT3A amount, DNA methylation and chromatin condensation. Nevertheless, it seems to us that the increase in the DNA methylation profile is not proportional to the chromatin condensation status, especially in CA, suggesting that chromatin organization is dependent not as much on DNA modification as on the ion accumulation around chromatin (ESI). In the majority of the samples, including HS and the physiological model, 5mC was found to be mainly on chromatin surface, as well as histone modified residues, in agreement with the possibility that the epigenetic modifications involve the chromatin surface to regulate gene expression. Furthermore, we noted that in CTR HeLa cells 5mC is more represented, in contrast with hepatocytes, although condensed chromatin is almost lacking: this means that DNA methylation could be not related to chromatin condensation.

The analysis of a physiological model of chromatin compaction (mouse erythrocytes) showed an increase of 5mC labelling and a parallel decrease of histone modifications during DNA compaction. These results can depend on the irreversibility of this process because the nucleus is totally condensed to be rejected at the end, further demonstrating the complexity of the studied process.

As for RNA, once confirmed that the perichromatin localization of 5mC pertains to RNA, this modified nucleotide was localized on nascent RNA: we may hypothesize that RNA methylation occurs co-transcriptionally, as a very precocious event. Nevertheless, 5mC was found to be also present on mature mRNA. Indicating that this modification can characterize mRNA during its entire lifespan, this last finding suggests a very important role, probably related to mRNA stability, according with *Squires et al.* (*2012*). It is important to underline that the abundance of other Pol II products, such as miRNA or snoRNAs, cannot justify the constant perichromatin 5mC

labelling, allowing, together with other data obtained here, to attribute 5mC localization on RNA to (pre-)mRNA. Unexpectedly, the EM localization of DNMT3A revealed its presence on both pre-mRNA and mRNA. The labelling on nascent RNA could confirm the methylation as an early event and allows one to suppose that DNMT3A could be in part responsible of RNA methylation. We also hypothesize that this event could be an error of the enzyme occurring during DNA methylation, even if the labelling on PG or poly-adenylated and capped mRNA seems in contrast with what just said. Considering the nucleolar 5mC distribution, we would like to underline only that this epigenetic modification is present in the DFC, where rRNA is actively transcribed (*Biggiogera et al. 2001*), further showing RNA methylation as a co-transcriptional process.

In parallel, a very preliminary study was carried out to characterize two possible novel components of the m6A-RNA methyltransferase complex in *Drosophila melanogaster*, i.e. HAKAI and CG7358. The most informative result derives from CoIP experiments, regarding only CG7358. The latter was shown to most probably interact with Fl(2)d, which is a very important stabilizing factor in the RNA methylating complex because it allows the two methylating enzymes (Ime4 and dMettl14) to be jointed. Besides, this interaction seems to not change with RNase treatment that means the possible connection between CG7358 and Fl(2)d does not require mRNA, even if we cannot say it is a direct interaction or mediated by another regulator factor. The involvement of these new component in the RNA methyltransferase complex is also suggested by the expression level of this gene during the developmental stages, mostly following the m6A level. However, the quantitative analysis and the immunolabelling also suggest a proper function of CG7358. On the contrary, these data seem to indicate that HAKAI is not a component of the methyltransferase complex.

- ✓ Before concluding, we would like to underline also some results obtained during this EM study that are not directly related to the regulation of chromatin structure but that have to be taken into account to understand this process.

  HeLa cells treated with different concentration of divalent cations represented a very complex and articulated research model. Their morphological analysis at EM showed some nuclear irregularities, first of all the detachment of the condensed chromatin from the nuclear envelope. We believe that the drastic changes in the ionic environment can affect the nuclear lamina, causing the observed chromatin detachment. This could mean that this phenomenon itself is in some way responsible of the high chromatin compaction, which therefore does not necessarily requires an epigenetic modification. Moreover, in these cells DNMT3A was found to be present in the nucleolus, probably as a sort of stress response in order to deal with the physiological alteration. In fact, another study showed the translocation of the transcription factor ATF4 (mammalian activating transcription factor 4) from the nucleus to the nucleolus upon stress conditions (*Galimberti et al. 2016*). This result underlines that a stress response must be considered in studying the final chromatin condensation status.

  We also observed that a moderate change in $Ca^{2+}$ concentration (20 mM) induces a reduction of 5mC labelling whereas the addition of bigger amount (200 mM) its increase: in our opinion, changes of chromatin structure in response to variations of cation concentration could be slow – this is also demonstrated by the not significant 5mC increase after 20 mM $Mg^{2+}$.

  On the other hand, the ESI analysis highlighted a possible different effect of $Ca^{2+}$ and $Mg^{2+}$ on chromatin to be considered in the general

analysis of chromatin structure. In fact, magnesium was shown to be mainly on DNA, in contrast with calcium which is preferentially around DNA: $Mg^{2+}$ has a relatively smaller size than $Ca^{2+}$, allowing to better penetrate within the chromatin, and probably it has more binding sites. On the contrary, calcium shows higher affinity for DNA since it remains on it more than the other ion after EGTA chelation.

# 6. CONCLUSIONS AND PERSPECTIVES

This research represents an **EM epigenetic analysis**.

To our knowledge, it is the first study of the distribution of epigenetic modifications carried out at high-resolution in order to understand the mechanisms regulating chromatin structure. Considering the "5mC gradient distribution" on chromatin surface, we hypothesize that this epigenetic modification, in regulating gene expression on chromatin surface, starts the compaction process but it is subsequently removed to allow condensation permanence. In fact, the bulky methyl group of cytosines was shown to reduce DNA fluctuations and, therefore, its flexibility, hindering the molecule to wrap firmly around the histone core (*Ngo et al. 2016*). This means that on chromatin surface we can detect the direct result of DNMT3A activity, i.e. 5mC, while in the proximity of the nuclear envelope we can only see the final effect of this modification, which is chromatin condensation, as the consequence of a previous and earlier methylation. The prevalent accumulation of histone modifications also on chromatin surface could indicate the same involvement in the regulation of chromatin structure. In our opinion, the chromatin condensation status is preserved by other mechanisms which need further investigations.

As for RNA, this study represents the first detection of methylated RNA (5mC and m6A) at EM level, proposing a tool to analyze the single molecule. In conclusion, we propose the RNA methylation of cytosines as a cotranscriptional event to guarantee the mRNA stability, for example representing a signal for RNase to avoid degradation, and a possible DNMT3A involvement in this modification.

Other studies will be necessary to describe the relationship between epigenetic modifications and chromatin structure, firstly reconsidering and

confirming some results and then analyzing other parameters. One important point to be explained is how the chromatin condensation is maintained. Moreover, in parallel it will be interesting to examine in depth the influence of the ionic environment on DNA methylation, histone PTM and chromatin structure, including the nuclear lamina. The EM approach to study (pre-)mRNA methylation could be supported by biomolecular techniques in order to define DNMT3A involvement in this modification.

# 7. REFERENCES

Adouard V, Dante R, Niveleau A, Delain E, Revet B, Ehrlich M. The accessibility of 5-methylcytosine to specific antibodies in double-stranded DNA of Xanthomonas phage XP12. European Journal of Biochemistry, 1985; 152:115–121

Alberts B, Johnson A, Lewis J, Raff M, Roberts K, Walter P. Molecular Biology of the Cell. Garland Science, 2008; 5th Edition

Allahverdi A, Yang R, Korolev N, Fan Y, Davey C A, Liu C F, Nordenskiöld L. The effects of histone H4 tail acetylations on cation-induced chromatin folding and self-association. Nucleic Acids Research, 2011; 39:1680–1691

Allison L. Fondemental Molecular Biology. Blackwell Publishing, 2007; 1st Edition.

Bachman K E, Rountree M R, Baylin S B. Dnmt3a and Dnmt3b are transcriptional repressors that exhibit unique localization properties to heterochromatin. The Journal of Biological Chemistry, 2001; 276:32282–32287

Bannister A J, Zegerman P, Partridge J F, Miska E A, Thomas J O, Allshire R C, Kouzarides T. Selective recognition of methylated lysine 9 on histone H3 by the HP1 chromo domain. Nature, 2001; 410:120–124

Bannister A J, Kouzarides T. Regulation of chromatin by histone modifications. Cell Research, 2011; 21:381–395

Barau J, Teissandier A, Zamudio N, Roy S, Nalesso V, Hérault Y, Guillou F, Bourc'his D. The DNA methyltransferase DNMT3C protects male germ cells from transposon activity. Science, 2016; 354:909–912

Bernhard W. A new staining procedure for electron microscopical cytology. Journal of Ultrastructure Research, 1969; 27:250–265

Bestor T H, Hellewell S B, Ingram V M. Differentiation of two mouse cell lines is associated with hypomethylation of their genomes. Molecular and Cellular Biology, 1984; 4:1800–1806

Biggiogera M, Fakan S. Fine Structural Specific Visualization of RNA on Ultrathin Sections. Journal of Histochemistry & Cytochemistry, 1998; 46:389–395

Biggiogera M, Malatesta M, Abolhassani-Dadras S, Amalric F, Rothblum L I, Fakan S. Revealing the unseen: the organizer region of the nucleolus. Journal of Cell Science, 2001; 114:3199–3205

Biggiogera M, Masiello I. Visualizing RNA at Electron Microscopy by Terbium Citrate. Methods in Molecular Biology, 2017; 1560:277-283

Blanco S, Frye M. Role of RNA methyltransferases in tissue renewal and pathology. Current Opinion in Cell Biology, 2014; 30:1–7

Bloom K S, Anderson J N. Fractionation and characterization of chromosomal proteins by the hydroxyapatite dissociation method. The Journal of Biological Chemistry, 1978; 253:4446–4450

Böhmdorfer G, Wierzbicki A T. Control of Chromatin Structure by Long Noncoding RNA. Trends in Cell Biology, 2015; 25:623–632

Bonenfant D, Coulot M, Towbin H, Schindler P, van Oostrum J. Characterization of histone H2A and H2B variants and their post-translational modifications by mass spectrometry. Molecular & Cellular Proteomics, 2006; 5:541–552

Bonnet-Garnier A, Feuerstein P, Chebrout M, Fleurot R, Jan H U, Debey P, Beaujean N. Genome organization and epigenetic marks in mouse germinal vesicle oocytes. The International Journal of Developmental Biology, 2012; 56:877–887

Boudinard Rouelle-Rossier V, Biggiogera M, Fakan S. Ultrastructural detection of calcium and magnesium in the chromatoid body of mouse spermatids by electron spectroscopic imaging and electron energy loss spectroscopy. Journal of Histochemistry & Cytochemistry, 1993; 41:1155–1162

Brown K E, Guest S S, Smale S T, Hahm K, Merkenschlager M, Fisher A G. Association of transcriptionally silent genes with Ikaros complexes at centromeric heterochromatin. Cell, 1997; 91:845–854

Caño S, Caravaca J M, Martín M, Daban J R. Highly compact folding of chromatin induced by cellular cation concentrations. Evidence from atomic force microscopy studies in aqueous solution. European Biophysics Journal, 2006; 35:495–501

Chen T, Li E. Structure and Function of Eukaryotic DNA Methyltransferases. In Current topics in developmental biology, 2004; 60:55–89

Chiodi I, Biggiogera M, Denegri M, Corioni M, Weighardt F, Cobianchi F, Riva S, Biamonti G. Structure and dynamics of hnRNP-labelled nuclear bodies induced by stress treatments. Journal of Cell Science, 2000; 113:4043–4053

Choy M K, Movassagh M, Goh H G, Bennett M R, Down T A, Foo R S Y. Genome-wide conserved consensus transcription factor binding motifs are hyper-methylated. BMC Genomics, 2010; 11:519

Cmarko D, Verschure P J, Martin T E, Dahmus M E, Krause S, Fu X D, van Driel R, Fakan S. Ultrastructural analysis of transcription and splicing in the cell nucleus after bromo-UTP microinjection. Molecular Biology of the Cell, 1999; 10:211–223

Cmarko D, Verschure P J, Otte A P, van Driel R, Fakan S. Polycomb group gene silencing proteins are concentrated in the perichromatin compartment of the mammalian nucleus. Journal of Cell Science, 2003; 116:335–343

Cokus S J, Feng S, Zhang X, Chen Z, Merriman B, Haudenschild C D, Pradhan S, Nelson S F, Pelligrini M, Jacobsen S E. Shotgun bisulphite sequencing of the Arabidopsis genome reveals DNA methylation patterning. Nature, 2008; 452:215–219

Crane-Robinson C, Hebbes T R, Clayton A L, Thorne A W. Chromosomal mapping of core histone acetylation by immunoselection. Methods, 1997; 12:48–56

Cremer T, Cremer M. Chromosome territories. Cold Spring Harbor Perspectives in Biology, 2010; 2:1–22

Davey C A, Sargent D F, Luger K, Maeder A W, Richmond T J. Solvent Mediated Interactions in the Structure of the Nucleosome Core Particle at 1.9Å Resolution. Journal of Molecular Biology, 2002; 319:1097–1113

Derenzini M, Farabegoli F, Trerè D. Localization of DNA in the fibrillar components of the nucleolus: a cytochemical and morphometric study. The Journal of Histochemistry and Cytochemistry 1993; 41:829–836

Desrosiers R, Friderici K, Rottman F. Identification of methylated nucleosides in messenger RNA from Novikoff hepatoma cells. Proceedings of the National Academy of Sciences of the United States of America, 1974; 71:3971–3975

Dominissini D, Rechavi G. 5-methylcytosine mediates nuclear export of mRNA. Cell Research, 2017; 27:717–719

Dubin D T, Taylor R H. The methylation state of poly A-containing messenger RNA from cultured hamster cells. Nucleic Acids Research, 1975; 2:1653–1668

Dundr M, Raska I. Nonisotopic ultrastructural mapping of transcription sites within the nucleolus. Experimental Cell Research, 1993; 208:275–281

Eden S, Hashimshony T, Keshet I, Cedar H, Thorne A W. DNA methylation models histone acetylation. Nature, 1998; 394:842

Esteller M. Epigenetics in Cancer. New England Journal of Medicine, 2008; 358:1148–1159

Fakan S. Perichromatin fibrils are in situ forms of nascent transcripts. Trends in Cell Biology, 1994; 4:86–90

Fakan S. The functional architecture of the nucleus as analysed by ultrastructural cytochemistry. Histochemistry and Cell Biology, 2004; 122:83–93

Fakan S, Puvion E. The ultrastructural visualization of nucleolar and extranucleolar RNA synthesis and distribution. International Review of Cytology, 1980; 65:255–299

Feinberg A P, Koldobskiy M A, Göndör A. Epigenetic modulators, modifiers and mediators in cancer aetiology and progression. Nature Reviews Genetics, 2016; 17:284–299

Ferguson L R, Tatham A L, Lin Z, Denny W A. Epigenetic regulation of gene expression as an anticancer drug target. Current Cancer Drug Targets, 2011; 11:199–212

Francastel C, Walters M C, Groudine M, Martin D I. A functional enhancer suppresses silencing of a transgene and prevents its localization close to centrometric heterochromatin. Cell, 1999; 99:259–269

Fritah S, Col E, Boyault C, Govin J, Sadoul K, Chiocca S, Christians E, Khochbin S, Jolly C, Vourc'h C. Heat-shock factor 1 controls genome-wide acetylation in heat-shocked cells. Molecular Biology of the Cell, 2009; 20:4976–4984

Frommer M, McDonald L E, Millar D S, Collis C M, Watt F, Grigg G W, Molloy P L, Paul C L. A genomic sequencing protocol that yields a positive display of 5-methylcytosine residues in individual DNA strands. Proceedings of the National Academy of Sciences of the United States of America, 1992; 89:1827–1831

Fu Y, Dominissini D, Rechavi G, He C. Gene expression regulation mediated through reversible $m^6A$ RNA methylation. Nature Reviews. Genetics, 2014; 15:293–306

Galimberti V, Kinor N, Shav-Tal Y, Biggiogera M, Brüning A. The stress-inducible transcription factor ATF4 accumulates at specific rRNA-processing nucleolar regions after proteasome inhibition. European Journal of Cell Biology, 2016; 95:389–400

Gan H H, Schlick T. Chromatin ionic atmosphere analyzed by a mesoscale electrostatic approach. Biophysical Journal, 2010; 99:2587–2596

Gehrke C W, McCune R A, Gama-Sosa M A, Ehrlich M, Kuo K C. Quantitative reversed-phase high-performance liquid chromatography of major and modified nucleosides in DNA. Journal of Chromatography, 1984; 301:199–219

Geiman T M, Robertson K D. Chromatin remodeling, histone modifications, and DNA methylation-how does it all fit together? Journal of Cellular Biochemistry, 2002; 87:117–125

Gilbert W V, Bell T A, Schaening C. Messenger RNA modifications: Form, distribution, and function. Science, 2016; 352:1408–1412

Gitan R S, Shi H, Chen C M, Yan P S, Huang T H M. Methylation-specific oligonucleotide microarray: A new potential for high-throughput methylation analysis. Genome Research, 2002; 12:158–164

Goll M G, Kirpekar F, Maggert K A, Yoder J A, Hsieh C-L, Zhang X, Golic K G, Jacobsen S E, Bestor, T. H. Methylation of tRNAAsp by the DNA Methyltransferase Homolog Dnmt2. Science, 2006; 311:395–398

Gonzalo S. Epigenetic alterations in aging. Journal of Applied Physiology, 2010; 109:586–597

Greer E L, Shi Y. Histone methylation: a dynamic mark in health, disease and inheritance. Nature Reviews Genetics, 2012; 13:343–357

Gurley L R, London J E, Valdez J G. High-performance capillary electrophoresis of histones. Journal of Chromatography, 1991; 559:431–443

Hancock R. Structure of metaphase chromosomes: a role for effects of macromolecular crowding. PloS One, 2012; 7:36045

Harrison A, Parle-McDermott A. DNA methylation: a timeline of methods and applications. Frontiers in Genetics, 2011; 2:74

Hendrich B, Bird A. Identification and characterization of a family of mammalian methyl-CpG binding proteins. Molecular and Cellular Biology, 1998; 18:6538–6547

Huang T H, Perry M R, Laux D E. Methylation profiling of CpG islands in human breast cancer cells. Human Molecular Genetics, 1999; 8:459–470

Hussain S, Aleksic J, Blanco S, Dietmann S, Frye M. Characterizing 5-methylcytosine in the mammalian epitranscriptome. Genome Biology, 2013; 14:215

Jackson J P, Lindroth A M, Cao X, Jacobsen S E. Control of CpNpG DNA methylation by the KRYPTONITE histone H3 methyltransferase. Nature, 2002; 416:556–560

Jia G, Fu Y, Zhao X, Dai Q, Zheng G, Yang Y, Yi C, Lindhal T, Pan T, Yang Y G, He C. N6-Methyladenosine in nuclear RNA is a major substrate of the obesity-associated FTO. Nature Chemical Biology, 2011; 7:885–887

Jimenez-Useche I, Yuan C. The effect of DNA CpG methylation on the dynamic conformation of a nucleosome. Biophysical Journal, 2012; 103:2502–2512

Jones P L, Veenstra G J, Wade P A, Vermaak D, Kass S U, Landsberger N, Strouboulis J, Wolffe A P. Methylated DNA and MeCP2 recruit histone deacetylase to repress transcription. Nature Genetics, 1998; 19:187–191

Karch K R, Denizio J E, Black B E, Garcia B A. Identification and interrogation of combinatorial histone modifications. Frontiers in Genetics, 2013; 4:264

Kellner S, Burhenne J, Helm M. Detection of RNA modifications. RNA Biology, 2010; 7:237–247

Kim J, Guermah M, McGinty R K, Lee J S, Tang Z, Milne T A, Shilatifard A, Muir T W, Roeder R G. RAD6-Mediated Transcription-Coupled H2B Ubiquitylation Directly Stimulates H3K4 Methylation in Human Cells. Cell, 2009; 137:459–471

Knuckles P, Carl S H, Musheev M, Niehrs C, Wenger A, Bühler M. RNA fate determination through cotranscriptional adenosine methylation and microprocessor binding. Nature Structural & Molecular Biology, 2017; 24:561–569

Kobayakawa S, Miike K, Nakao M, Abe K. Dynamic changes in the epigenomic state and nuclear organization of differentiating mouse embryonic stem cells. Genes to Cells, 2007; 12:447–460

Kohli R M, Zhang Y. TET enzymes, TDG and the dynamics of DNA demethylation. Nature, 2013; 502:472–479

Korolev N, Allahverdi A, Yang Y, Fan Y, Lyubartsev A P, Nordenskiöld L. Electrostatic origin of salt-induced nucleosome array compaction. Biophysical Journal, 2010; 99:1896–1905

Kouzarides T. Chromatin Modifications and Their Function. Cell, 2007; 128:693–705

Lachner M, O'Carroll D, Rea S, Mechtler K, Jenuwein T. Methylation of histone H3 lysine 9 creates a binding site for HP1 proteins. Nature, 2001; 410:116–120

Lee J S, Shukla A, Schneider J, Swanson S K, Washburn M P, Florens L, Shilatifard A.Histone crosstalk between H2B Monoubiquitination and H3 Methylation Mediated by COMPASS. Cell, 2007; 131:1084–1096

Li D, Zhang B, Xing X, Wang T. Combining MeDIP-seq and MRE-seq to investigate genome-wide CpG methylation. Methods, 2015; 72:29–40

Li E. Chromatin modification and epigenetic reprogramming in mammalian development. Nature Reviews Genetics, 2002; 3:662–673

Li E, Bestor T H, Jaenisch R. Targeted mutation of the DNA methyltransferase gene results in embryonic lethality. Cell, 1992; 69:915–926

Li E, Zhang Y. DNA methylation in mammals. Cold Spring Harbor Perspectives in Biology, 2014; 6:019133

Li S, Mason C E. The Pivotal Regulatory Landscape of RNA Modifications. Annual Review of Genomics and Human Genetics, 2014; 15:127–150

Li Y, Miyanari Y, Shirane K, Nitta H, Kubota T, Ohashi H, Okamoto A, Sasaki H. Sequence-specific microscopic visualization of DNA methylation status at satellite repeats in individual cell nuclei and chromosomes. Nucleic Acids Research, 2013; 41:186

Liu J, Jia G. Methylation Modifications in Eukaryotic Messenger RNA. Journal of Genetics and Genomics, 2014; 41:21–33

Liu J, Yue Y, Han D, Wang X, Fu Y, Zhang L, Jia G, Yu M, Lu Z, Deng X, Dai Q, Chen W, He C. A METTL3-METTL14 complex mediates mammalian nuclear RNA N6-adenosine methylation. Nature Chemical Biology, 2014; 10:93–95

Liu N, Pan T. RNA epigenetics. Translational Research, 2015; 165:28–35

Lundgren M, Chow C M, Sabbattini P, Georgiou A, Minaee S, Dillon N. Transcription factor dosage affects changes in higher order chromatin structure associated with activation of a heterochromatic gene. Cell, 2000; 103:733–743

Machnicka M A, Milanowska K, Osman Oglou O, Purta E, Kurkowska M, Olchowik A, Januszewski W, Kalinowski S, Dunin-HorKawicz S, Rother K M, Helm M, Bunicki J M, Grosjean H. MODOMICS: a database of RNA modification pathways--2013 update. Nucleic Acids Research, 2013; 41:262–267

Maeshima K, Imai R, Tamura S, Nozaki T. Chromatin as dynamic 10-nm fibers. Chromosoma, 2014; 123:225–237

Martin R M, Görisch S M, Leonhardt H, Cardoso M C. An unexpected link between energy metabolism, calcium, chromatin condensation and cell cycle. Cell Cycle, 2007; 6:2422–2424

Masiello I, Biggiogera M. Osmium Ammine for Staining DNA in Electron Microscopy. Methods in Molecular Biology, 2017a; 1560:261-267

Masiello I, Biggiogera M. Ultrastructural localization of 5-methylcytosine on DNA and RNA. Cellular and Molecular Life Sciences, 2017b; 74:3057-3064

Materese C K, Savelyev A, Papoian G A. Counterion Atmosphere and Hydration Patterns near a Nucleosome Core Particle. Journal of the American Chemical Society, 2009; 131:15005–15013

Maunakea K, Nagarajan R P, Bilenky M, Ballinger T J, Souza D, Fouse S D, Johnson E B, Hong C, Nielsen C, Zhao Y, Turecki G, Delaney A, Varhol R, Thiessen N, Shchors K, et al. Conserved role of intragenic DNA methylation in regulating alternative promoters. Nature, 2014; 466:253–257

Mazzio E A, Soliman K F A. Basic concepts of epigenetics: impact of environmental signals on gene expression. Epigenetics, 2012; 7:119–130

Motorin Y, Lyko F, Helm M. 5-methylcytosine in RNA: Detection, enzymatic formation and biological functions. Nucleic Acids Research, 2009; 38:1415–1430

Mujtaba S, Zeng L, Zhou M M. Structure and acetyl-lysine recognition of the bromodomain. Oncogene, 2007; 26:5521–5527

Narayan P, Rottman F M. An in vitro system for accurate methylation of internal adenosine residues in messenger RNA. Science, 1988; 242:1159–1162

Ngo T T M, Yoo J, Dai Q, Zhang Q, He C, Aksimentiev A, Ha T. Effects of cytosine modifications on DNA flexibility and nucleosome mechanical stability. Nature Communications, 2016; 7:10813

Oki M, Aihara H, Ito T. Role of histone phosphorylation in chromatin dynamics and its implications in diseases. Sub-Cellular Biochemistry, 2007; 41:319–336

Ottensmeyer F P. Electron spectroscopic imaging: parallel energy filtering and microanalysis in the fixed-beam electron microscope. Ultrastruct Res. 1984; 88:121-134

Pastor W A, Aravind L, Rao A. TETonic shift: biological roles of TET proteins in DNA demethylation and transcription. Nature Reviews Molecular Cell Biology, 2013; 14:341–356

Peterson C L, Laniel M A. Histones and histone modifications. Current Biology, 2004; 14:546–551

Phengchat R, Takata H, Morii K, Inada N, Murakoshi H, Uchiyama S, Fukui K. Calcium ions function as a booster of chromosome condensation. Scientific Reports, 2016; 6:38281

Ping X L, Sun B F, Wang L, Xiao W, Yang X, Wang W J, Adhikari S, Shi X, Lv Y, Chen Y S, Zhao X, Li A, Yang Y, Dahal U, Lou X M, et al. Mammalian WTAP is a regulatory subunit of the RNA N6-methyladenosine methyltransferase. Cell Research, 2014; 24:177–189

Poletto V, Galimberti V, Guerra G, Rosti V, Moccia F, Biggiogera M. Fine structural detection of calcium ions by photoconversion. European Journal of Histochemistry, 2016; 60:2695

Puvion E, Puvion-Dutilleul F. Ultrastructure of the nucleus in relation to transcription and splicing: roles of perichromatin fibrils and interchromatin granules. Experimental Cell Research, 1996; 229:217–225

Raynal N J M, Lee J T, Wang Y, Beaudry A, Madireddi P, Garriga J, Malouf G G, Dumont S, Dettman E J, Gharibyan V, Ahned S, Chung W, Childers W E, Abou-Gharbia M, Henry R A, et al. Targeting Calcium Signaling Induces Epigenetic Reactivation of Tumor Suppressor Genes in Cancer. Cancer Research, 2016; 76:1494–1505

Richter K, Haslbeck M, Buchner J. The heat shock response: life on the verge of death. Molecular Cell, 2010; 40:253–266

Robertson K D. DNA methylation and human disease. Nature Reviews. Genetics, 2005; 6:597–610

Rossetto D, Avvakumov N, Côté J. Histone phosphorylation: a chromatin modification involved in diverse nuclear events. Epigenetics, 2012; 7:1098–1108

Santos F, Hendrich B, Reik W, Dean W. Dynamic reprogramming of DNA methylation in the early mouse embryo. Developmental Biology, 2002; 241:172–182

Schaefer M, Pollex T, Hanna K, Lyko F. RNA cytosine methylation analysis by bisulfite sequencing. Nucleic Acids Research, 2009; 37:12

Sharma A, Nguyen H, Cai L, Lou H. Histone hyperacetylation and exon skipping: a calcium-mediated dynamic regulation in cardiomyocytes. Nucleus, 2015; 6:273–278

Shen L, Song C X, He C, Zhang Y. Mechanism and Function of Oxidative Reversal of DNA and RNA Methylation. Annual Review of Biochemistry, 2014; 83:585–614

Smith Z D, Meissner A. DNA methylation: roles in mammalian development. Nature Reviews Genetics, 2013; 14:204–220

Solís M T, Chakrabarti N, Corredor E, Cortés-Eslava J, Rodríguez-Serrano M, Biggiogera M, Risueño M C, Testillano P S. Epigenetic changes accompany developmental programmed cell death in tapetum cells. Plant and Cell Physiology, 2014; 55:16–29

Spector D L. Nuclear organization and gene expression. Experimental Cell Research, 1996; 229:189–197

Squires J E, Preiss T. Function and detection of 5-methylcytosine in eukaryotic RNA. Epigenomics, 2010; 2:709–715

Squires J E, Patel H R, Nousch M, Sibbritt T, Humphreys D T, Parker B J, Suter C M, Preiss T. Widespread occurrence of 5-methylcytosine in human coding and non-coding RNA. Nucleic Acids Research, 2012; 40:5023–5033

Strick R, Strissel P L, Gavrilov K, Levi-Setti R. Cation-chromatin binding as shown by ion microscopy is essential for the structural integrity of chromosomes. The Journal of Cell Biology, 2001; 155:899–910

Suva M L, Riggi N, Bernstein B E. Epigenetic Reprogramming in Cancer. Science, 2013; 339:1567–1570

Tamaru H, Selker E U. A histone H3 methyltransferase controls DNA methylation in Neurospora crassa. Nature, 2001; 414:277–283

Trentani A, Testillano P S, Risueño M C, Biggiogera M. Visualization of transcription sites at the electron microscope. European Journal of Histochemistry, 2003; 47:195–200

Turner B M. Cellular memory and the histone code. Cell, 2002; 111:285–291

Vandelaer M, Thiry M, Goessens G. Isolation of nucleoli from ELT cells: a quick new method that preserves morphological integrity and high transcriptional activity. Experimental Cell Research, 1996; 228:125–131

Vázquez-Nin G H, Biggiogera M, Echeverría O M. Activation of osmium ammine by SO2-generating chemicals for EM Feulgen-type staining of DNA. European Journal of Histochemistry, 1995; 39:101–106.

Visvanathan A, Ahmed K, Even-Faitelson L, Lleres D, Bazett-Jones D P, Lamond A I. Modulation of Higher Order Chromatin Conformation in Mammalian Cell Nuclei Can Be Mediated by Polyamines and Divalent Cations. PloS One, 2013; 8:67689

Wang H, Wang L, Erdjument-Bromage H, Vidal M, Tempst P, Jones R S, Zhang Y. Role of histone H2A ubiquitination in Polycomb silencing. Nature, 2004; 431:873–878

Wang K Y, Chen C C, Shen C K J. Active DNA demethylation of the vertebrate genomes by DNA methyltransferases: deaminase, dehydroxymethylase or demethylase? Epigenomics, 2014; 6:353–363

Wang Y, Curry H M, Zwilling B S, Lafuse W P. Mycobacteria inhibition of IFN-gamma induced HLA-DR gene expression by up-regulating histone deacetylation at the promoter region in human THP-1 monocytic cells. Journal of Immunology, 2005; 174:5687–5694

Wang Y, Li Y, Toth J I, Petroski M D, Zhang Z, Zhao J C. N6-methyladenosine modification destabilizes developmental regulators in embryonic stem cells. Nature Cell Biology, 2014; 16:191–198

Weber M, Davies J J, Wittig D, Oakeley E J, Haase M, Lam W L, Schübeler D. Chromosome-wide and promoter-specific analyses identify sites of differential DNA methylation in normal and transformed human cells. Nature Genetics, 2005; 37:853–862

Weighardt F, Cobianchi F, Cartegni L, Chiodi I, Villa A, Riva S, Biamonti G. A novel hnRNP protein (HAP/SAF-B) enters a subset of hnRNP complexes and relocates in nuclear granules in response to heat shock. Journal of Cell Science, 1999; 112:1465–1476

Wu H, Zhang Y. Reversing DNA Methylation: Mechanisms, Genomics, and Biological Functions. Cell, 2014; 156:45–68

Wu J, Issa J P, Herman J, Bassett D E, Nelkin B D, Baylin S B. Expression of an exogenous eukaryotic DNA methyltransferase gene induces transformation of NIH 3T3 cells. Proceedings of the National Academy of Sciences of the United States of America, 1993; 90:8891–8895

Yang X, Yang Y, Sun B F, Chen Y S, Xu J W, Lai W Y, Li A, Wang X, Bhattarai D P, Xiao W, Sun H Y, Zhu Q, Ma H L, Adhikari S, Sun M. 5-methylcytosine promotes mRNA export-NSUN2 as the methyltransferase and ALYREF as an m5C reader. Cell Research, 2017; 27:606–625

Yang Z, Hayes J J. The divalent cations Ca2+ and Mg2+ play specific roles in stabilizing histone-DNA interactions within nucleosomes that are partially redundant with the core histone tail domains. Biochemistry, 2011; 50:9973–9981

Young J I, Hong E P, Castle J C, Crespo-Barreto J, Bowman A B, Rose M F, Kang D, Richman R, Johnson J M, Berget S, Zoghbi H Y. Regulation of RNA splicing by the methylation-dependent transcriptional repressor methyl-CpG binding protein 2. Proceedings of the National Academy of Sciences, 2005; 102:17551–17558

Zeng L, Zhang Q, Li S, Plotnikov A N, Walsh M J, Zhou M M. Mechanism and regulation of acetylated histone binding by the tandem PHD finger of DPF3b. Nature, 2010; 466:258–262

Zhang W, Xu J. DNA methyltransferases and their roles in tumorigenesis. Biomarker Research, 2017; 5:1

Zhao B S, Roundtree I A, He C. Post-transcriptional gene regulation by mRNA modifications. Nature Reviews Molecular Cell Biology, 2016; 18:31–42

Zhong Y, Kanagaratham C, Radzioch D. Chromatin Remodelling During Host-Bacterial Pathogen Interaction. In Chromatin Remodelling. InTech, 2013

# LIST OF ORIGINAL MANUSCRIPTS

Angeletti F, Fossati G, Pattarozzi A, Würth R, Solari A, Daga A, **Masiello I**, Barbieri F, Florio T, Comincini S. Inhibition of the Autophagy Pathway Synergistically Potentiates the Cytotoxic Activity of Givinostat (ITF2357) on Human Glioblastoma Cancer Stem Cells. Frontiers in Molecular Neuroscience, 2016; 9:107.

Biggiogera M, **Masiello I**. Visualizing RNA at Electron Microscopy by Terbium Citrate. Methods in Molecular Biology, 2017; 1560:277-283.

**Masiello I**, Biggiogera M. Osmium Ammine for Staining DNA in Electron Microscopy. Methods in Molecular Biology, 2017; 1560:261-267.

**Masiello I**, Biggiogera M. Ultrastructural localization of 5-methylcytosine on DNA and RNA. Cellular and Molecular Life Sciences, 2017; 74:3057-3064.

**Masiello I**, Biggiogera M. Electron microscope detection of 5-methylcytosine on DNA and RNA. Methods in Molecular Biology. *In press.*

Rangone B, Ferrari B, Astesana V, **Masiello** I, Veneroni P, Zanellato I; Osella D, Bottone M G. A new platinum-based pro-drug candidate: its anti-cancer effects in B50 neuroblastoma rat cells. *Submitted.*

Knuckles P, Lence T, Haussman I, Jacob D, Kreim N, Carl S H, **Masiello I**, Hares T, Villaseñor R, Hess D, Andrade-Navarro M A, Biggiogera M, Helm M, Soller M, Bühler M and Roignant J Y. Zc3h13/Flacc is required for adenosine methylation by bridging the mRNA binding factor Rbm15/Spenito to other components of the m6A machinery. *Submitted*.

# CONGRESS COMMUNICATIONS

**Masiello I**, Biggiogera M. Unusual methylation on nascent RNA fibrils and stored RNA granules. 61° GEI Congress and 36° Congress of Italian Istochemystry Society – Pisa (Italy), 7-10 June 2015.

**Masiello I**, Nacci L, Morini J, Valli R, Minelli A, Danesino C, Biggiogera M. Probing nucleolar and ribosomal function in Shwachman-Diamond disease at trasmission electron microscopy (TEM). 8° International Congress of Shwachman-Diamond Sydrome – Verona (Italy), 17-20 April 2016.

Biggiogera M, Tollemeto V, Bina V, Abou Alezz M, **Masiello I**. Transcription time window applied to RNA modifications in HeLa cells. Nuclear structure and dynamics, through the microscopes – Pavia (Italy), 7-8 July 2016.

**Masiello I**, Comincini S, Biggiogera M. Ultrastructural analysis of nucleic acid methylation. Nuclear structure and dynamics through the microscopes – Pavia (Italy), 7-8 July 2016.

Biggiogera M, Abou Alezz M, Bina V, Stortiero M, Tollemeto V, **Masiello I**. Heterogeneity of perichromatin fibril associated factors. 25° Wilhelm Bernhard Workshop on the Cell Nucleus - Nizhny Novgorod (Russia), 19-22 June 2017.

Rangone B, Ferrari B, Zanellato I, **Masiello I**, Roda E, Priori EC, Veneroni P, Osella D, Bottone MG. Effects of the new cisplatin-based pt(IV)ACPOA prodrug in CNS tumor cell line. 35° National Conference of the Italian Society of Cytometry (GIC) – Paestum (Italy), 3-6 October 2017.

frontiers in Molecular Neuroscience

ORIGINAL RESEARCH
published: 27 October 2016
doi: 10.3389/fnmol.2016.00107

# Inhibition of the Autophagy Pathway Synergistically Potentiates the Cytotoxic Activity of Givinostat (ITF2357) on Human Glioblastoma Cancer Stem Cells

*Francesca Angeletti[1], Gianluca Fossati[2], Alessandra Pattarozzi[3], Roberto Würth[3], Agnese Solari[3], Antonio Daga[4], Irene Masiello[1], Federica Barbieri[3], Tullio Florio[3*†] and Sergio Comincini[1*†]*

[1] Department of Biology and Biotechnology, University of Pavia, Pavia, Italy, [2] Preclinical Research Department Italfarmaco Research Center, Italfarmaco S.p.A, Cinisello Balsamo, Italy, [3] Department of Internal Medicine, Centre of Excellence for Biomedical Research, University of Genova, Genova, Italy, [4] Regenerative Medicine, IRCCS Azienda Ospedaliera Universitaria San Martino - IST, Genova, Italy

OPEN ACCESS

**Edited by:**
Jean-Marc Taymans,
French Institute of Health and Medical Research (INSERM), France

**Reviewed by:**
Claudia Manzoni,
University of Reading, UK
Manoj B. Menon,
Hannover Medical School, Germany

***Correspondence:**
Sergio Comincini
sergio.comincini@unipv.it
Tullio Florio
tullio.florio@unige.it

[†] These authors have contributed equally to this work.

**Received:** 18 July 2016
**Accepted:** 07 October 2016
**Published:** 27 October 2016

**Citation:**
Angeletti F, Fossati G, Pattarozzi A, Würth R, Solari A, Daga A, Masiello I, Barbieri F, Florio T and Comincini S (2016) Inhibition of the Autophagy Pathway Synergistically Potentiates the Cytotoxic Activity of Givinostat (ITF2357) on Human Glioblastoma Cancer Stem Cells. Front. Mol. Neurosci. 9:107. doi: 10.3389/fnmol.2016.00107

Increasing evidence highlighted the role of cancer stem cells (CSCs) in the development of tumor resistance to therapy, particularly in glioblastoma (GBM). Therefore, the development of new therapies, specifically directed against GBM CSCs, constitutes an important research avenue. Considering the extended range of cancer-related pathways modulated by histone acetylation/deacetylation processes, we studied the anti-proliferative and pro-apoptotic efficacy of givinostat (GVS), a pan-histone deacetylase inhibitor, on cell cultures enriched in CSCs, isolated from nine human GBMs. We report that GVS induced a significant reduction of viability and self-renewal ability in all GBM CSC cultures; conversely, GVS exposure did not cause a significant cytotoxic activity toward differentiated GBM cells and normal mesenchymal human stem cells. Analyzing the cellular and molecular mechanisms involved, we demonstrated that GVS affected CSC viability through the activation of programmed cell death pathways. In particular, a marked stimulation of macroautophagy was observed after GVS treatment. To understand the functional link between GVS treatment and autophagy activation, different genetic and pharmacological interfering strategies were used. We show that the up-regulation of the autophagy process, obtained by deprivation of growth factors, induced a reduction of CSC sensitivity to GVS, while the pharmacological inhibition of the autophagy pathway and the silencing of the key autophagy gene *ATG7*, increased the cell death rate induced by GVS. Altogether these findings suggest that autophagy represents a pro-survival mechanism activated by GBM CSCs to counteract the efficacy of the anti-proliferative activity of GVS. In conclusion, we demonstrate that GVS is a novel pharmacological tool able to target GBM CSC viability and its efficacy can be enhanced by autophagy inhibitory strategies.

**Keywords: glioblastoma multiforme, programmed cell death, histone deacetylase inhibitor, cancer stem cell, autophagy**

## INTRODUCTION

Glioblastoma (GBM) is fatal, highly invasive brain tumor still displaying poor prognosis (Ohgaki and Kleihues, 2013) even after aggressive multi-modal therapy, including neurosurgery, radiotherapy, and chemotherapy with temozolomide (Stupp et al., 2005). Different GBM features are responsible for the therapeutic failure: the peculiar structure of the brain and the invasive behavior of GBM prevent complete surgical tumor excision; the brain blood barrier prevents systemically administered chemotherapeutics to reach the central nervous system (CNS) in clinically effective concentrations (Omuro and Deangelis, 2013), the molecular complexity of GBM showing a variety of genetic alterations, strongly influencing the therapy outcome, since different mutations might determine different drug sensitivity (Brennan et al., 2013; Patel et al., 2014). In addition, the presence of cancer stem cells (CSCs) within the tumor mass is responsible for the recurrence after therapy (Vescovi et al., 2006; Florio and Barbieri, 2012). CSC theory proposes that tumor development is dependent on a small cell population endowed with self-renewal and multilineage differentiation ability, a strong resistance to conventional chemotherapy, and the ability to propagate the tumor when xenografted in animal models (Wurth et al., 2014). Since the most aggressive or refractory cancers contain the highest number of CSCs, the therapeutic importance of the eradication of this particular cancer cell subpopulation is a relevant research goal to overcome GBM therapy resistance (Al-Hajj et al., 2004; Singh et al., 2004).

The wide variety of genetic alterations in GBM necessitates the use of strategies targeting processes like chromatin remodeling, which can revert the altered status of multiple genes. The wide range of cellular and molecular effects mediated by histone deacetylase inhibitors (HDACi) make these drugs suitable candidates for the treatment of such heterogeneous tumors (Lee et al., 2015). HDACi act through the inhibition of histone deacetylases, enzymes that control chromatin remodeling and acetylation of histone and non-histone proteins (Ververis and Karagiannis, 2012). Pharmacologically-induced unbalanced acetylation (histone acetyl transferase activity) and deacetylation (HDAC activity) in favor of the former, creates an hyperacetylated status, promotes a relaxed chromatin structure and an accessible DNA backbone for the transcriptional machinery favoring the activation/repression of gene transcription (Peart et al., 2005), by which HDACi induce cell death (Bolden et al., 2013), cell cycle arrest, senescence (Pazolli et al., 2012), differentiation, or autophagy (Robert et al., 2011) in tumor cells. In GBM cells, HDACi reduce proliferation *via* cell cycle arrest and apoptosis, suppress tumor growth in experimental *in vivo* models, and potentiate the effects of radiotherapy, cytotoxic agents and immune-therapeutics (Thurn et al., 2011). Several HDACi, including SAHA, trichostatin A, valproic acid, belinostat, have been tested in GBM models, and several clinical trials, based on HDACi monotherapy or as drug association strategies are concluded or ongoing (De Souza and Chatterji, 2015).

We report the efficacy of givinostat (GVS), a pan-histone deacetylase inhibitor, on human GBM CSC viability and self-renewal and the involvement of apoptosis and macroautophagy (hereafter referred as autophagy) in this response.

## MATERIALS AND METHODS

### Tumor Samples, Cell Cultures, and Chemicals

Nine glioma post-surgical specimens were obtained from the Neurosurgery Department of the IRCCS-AOU San Martino IST, (Genova, Italy) after patients' informed consent and Institutional Ethical Committee approval. All patients underwent surgery for the first time and never received chemo- or radio-therapy. Tumors were derived from 6 males and 3 females and the mean age was 57.5 years. Pathological analysis classified gliomas as grade IV glioblastoma ($n = 8$), or grade III anaplastic astrocytoma ($n = 1$) according to World Health Organization criteria. Cell cultures deriving for each tumor sample were coded as GBM1 to GBM9. Patients and tumors details are reported in **Supplementary Table 1**.

All GBM-derived CSCs were previously isolated and characterized (Gatti et al., 2013; Wurth et al., 2013). Tumor samples were immediately processed to obtain cell cultures enriched in CSCs. Briefly, cell suspension obtained after mechanical dissociation, was filtered through a 40 μm strainer (BD Biosciences, San Jose, CA, USA) to remove aggregates, and cultivated in serum-free medium containing DMEM-F12/Neurobasal (1:1), B27 supplement (Gibco-Thermofisher, Paysley, UK), 2 mM L-glutamine (Lonza, Basel, Switzerland), 1% penicillin-streptomycin (Lonza), 15 μg/ml insulin (Sigma-Aldrich, St.Louis, MO, USA), 2 μg/ml heparin (Sigma-Aldrich) and completed with recombinant human bFGF (10 ng/ml; Miltenyi Biotec, Cologne, Germany) and EGF (20 ng/ml; Miltenyi Biotec) (Bajetto et al., 2013). This medium is defined as "complete medium." These cells gave rise to floating tumor-spheres after 2 weeks, but can also growing as stem cells in monolayer, after spheres disaggregation and in presence of Matrigel (BD Biosciences, San Jose, CA, USA), without losing expression of stem cell markers, spherogenic properties, differentiation and tumorigenic potential (Griffero et al., 2009).

All the cell cultures analyzed in this study were previously characterized for tumor-initiating capacity by orthotopic xenograft, induced by injection of 10,000 sphere-derived cells in 6–8-weeks old non-obese diabetic severe combined immunodeficient (NOD/SCID) mice (Charles River Laboratories, Wilminglon, MA, USA), as detailed in previous studies (Carra et al., 2013; Gritti et al., 2014; Corsaro et al., 2016). Animals were housed in pathogenic-free conditions, and handled in agreement with the institutional and national guidelines for the care and use of laboratory animals (Italian D.lgs 26/2014); the experimental plan was approved by the IRCCS AOU S. Martino-IST (Genova, Italy) Institutional Animal Care and Use Committee (IACUC).

To induce differentiation, GBM CSC cultures were seeded and maintained for 2 weeks in DMEM/F12 supplemented

with 2 mM L-glutamine, penicillin-streptomycin and 10% FBS (Euroclone, Milano, Italy). Deprivation of growth factors was induced removing bFGF, EGF, and the B27 supplement from the culture medium.

Three human GBM established cell lines were also used: T98G, U373-MG, and U138-MG (ATCC). GBM cell lines were grown in DMEM supplemented with 2 mM L-glutamine, penicillin-streptomycin and 10% FBS.

Human umbilical cords ($n = 2$) were collected from full-term women, immediately after cesarean section at the Gynecology Department of International Evangelical Hospital (Genova, Italy), after informed consent and approval by Institutional Ethic Committee. After vessel removal, cords were digested with collagenase I-S (0.5 μg/ml, Sigma-Aldrich) for 1 h to expose Wharton-Jelly and isolated cells cultured in DMEM (10% FBS, 2 mM L-Glutamine). MSCs were used after full characterization by flow cytometry (MSC Phenotyping Kit, Miltenyi Biotec), as defined by International Society for Cellular Therapy (Dominici et al., 2006).

The pan-HDAC inhibitor givinostat (ITF2357) was kindly provided by Italfarmaco S.p.A. (Cinisello Balsamo, Italy). Givinostat was dissolved in DMSO at the stock concentration of 10 mM and for all experiments it was diluted in the specific medium to obtain the final concentrations. Rapamycin (Cell Signaling Technology, Danvers, MA, USA) and bafilomycin-A1 (Sigma-Aldrich), were used to promote the induction and inhibition of autophagy, respectively. Both were dissolved in DMSO at the stock concentration of 100 μM, and for all experiments drugs were diluted in the specific medium to obtain the appropriate concentration. Controls received the same amount of residual DMSO (not exceeding 0.1%) than treated samples.

## Sphere-Formation Assay

GBM CSCs were seeded in complete medium without Matrigel, in 48-well plates at 1000 cells/well. After 24 h cells were exposed to increasing concentration of GVS (0.1–2 μM), and sphere-formation capacity was monitored after 7 days, to allow spheres generation. The number of spheres in wells was quantified using a digital camera mounted on a transmitted light microscope and visually calculated by three independent operators. To further demonstrate the inhibitory activity of GVS on sphere-formation process, GBM-derived tumor-spheres, generated in the absence or presence of GVS (0.1–0.5 μM), were disaggregated and re-plated in fresh medium avoid of GVS. Spheres-formation efficiency (SFE) (Wurth et al., 2016), calculated as the number of formed spheres/1000 plated cells, was re-evaluated after 7 days.

## MTT and Trypan-Blue Dye Exclusion Assays

Mitochondrial activity, as index of cell viability, was evaluated by measuring the reduction of 3-(4,5-dimethylthiazol-2-yl)-2,5-diphenyltetrazolium bromide (MTT, Sigma-Aldrich,). GBM CSCs were plated into 96 or 48-well plates (pre-coated with Matrigel), and the number of cells/well (ranging from 1000 to 5000) was adjusted depending on different proliferation rates and time of treatment. At the end of each treatment, cells were incubated with MTT solution (2.5 mg/ml), for 2 h. After MTT removal, the formed purple formazan crystals were dissolved in DMSO, and absorbance measured at 570 nm wavelength (Pattarozzi et al., 2008).

Trypan blue exclusion assay was used to evaluate cell viability reduction induced by GVS treatment. Initially, 5000 cells/well were seeded in 24-well plates, pre-coated with Matrigel. After 24 h, cells were treated with increasing concentration of GVS for additionally 48, 72, and 96 h. Every 24 h, viable cells were counted in the presence of Trypan blue 0.4% w/v (Bio-Rad, Marnesla-Coquette, France), to distinguish between dead and live cells, using the TC-20® automated cell counter (Bio-Rad) (Villa et al., 2016).

## Drug Synergism Evaluation

To determine potential synergistic drug effects on growth of CSCs GBM1, GBM2, and GBM3, cells were exposed to various combinations of GVS (0.5 μM) and bafilomycin-A1 (1.25–50 nM). Cell viability was determined by MTT assay after 48 and 72 h of treatment. Drug interactions (synergistic, additive, antagonistic) were determined by the median effect analysis method, as described (Chou and Talalay, 1984; Chou, 2010), using the CompuSyn software (ComboSyn Inc., Paramus, NJ, USA). This approach takes into account the potency, the shape, and the slope of the dose-dependent neutralization curve of each drug alone and in combination, to calculate a combination index (CI). A CI value of 1 indicates an additive effect, $<1$ indicates synergism, and $>1$ indicates antagonism.

## Annexin V/PI Double Staining

GBM CSCs were treated with GVS and bafilomycin-A1 alone or in association for 48 or 72 h, depending on the experiments. After the treatment, cells were washed gently with PBS, trypsinized, pelleted, secondly washed in PBS and finally counted. According to Annexin V-FITC Apoptosis detection Kit (eBioscience, Hatfield, UK), cells were resuspended in the Annexin Binding Buffer at the concentration of 2–5 $\times$ $10^5$ cells/ml, then 5 μl of Annexin-V was added to 195 μL of the cell suspension and incubated for 15 min, at the room temperature and protected from direct light. Propidium Iodide (20 μg/ml) was added and cells were analyzed by flow cytometry (FACSCanto II flow cytometer, BD Biosciences) recording 10,000 events per sample. Annexin V-positive cells were considered in the early stages of apoptosis, whereas cells in the late stages of apoptosis were Annexin V- and PI-positive (Carra et al., 2013).

## Real-Time PCR Expression Analysis

Total RNA from GBM CSCs was extracted using the Aurum Total RNA Mini Kit (Bio-Rad), according to the manufacturer's instruction, and reverse transcribed into cDNA using the iScript cDNA Synthesis Kit (Bio-Rad). Single stranded cDNA products were analyzed by Real-time PCR using the SsoFast™ Eva Green Supermix (Bio-Rad,) on a CFX96 Touch Real-time PCR (Bio-Rad). Cycling conditions were set at 94°C for 30 s, 60°C for 30 s and 72°C for 30 s, for 37 cycles. Primers, for *MAP1LC3B* amplification, were pre-designed by PrimePCR (Bio-Rad). Human *HPRT1* and *TBP* pre-designed primers (Bio-Rad)

were used as internal controls. Levels of target genes in each sample were normalized on the basis of *HPRT1* and *TBP* amplification and reported as relative values (Mathur, 2014).

## Immunoblotting Analysis

Following specific treatments, cells were lysed in buffer containing 1% Igepal, 20 mM Tris–HCl, pH 8, 137 mM NaCl, 10% glycerol, 2 mM EDTA, 1 mM phenylmethylsulfonyl fluoride, 1 mM sodium orthovanadate, 10 mM NaF (all from Sigma-Aldrich), and the "Cømplete protease inhibitor mixture" (Roche) for 20 min at 4°C. Nuclei were removed through centrifugation (5000 rpm at 4°C for 10 min); total protein concentration was measured with Bradford assay (Bio-Rad). Proteins (40–60 μg) were resuspended in Laemmli buffer (2% SDS, 62.5 mM Tris, pH 6.8, 0.01% bromophenol blue, 1.43 mM β2-mercaptoethanol,and 0.1% glycerol) and were separated on 10 or 12% (depending on protein size) SDS-PAGE, and subsequently transferred onto PVDF membrane (Bio-Rad) (Massa et al., 2004). The following antibodies were used: anti-LC3B, anti-Beclin1, anti-Atg7, and anti-acetyl-α-tubulin (Lys40) (all from Cell Signaling Technologies). β-actin (Cell Signaling Technologies) and α-tubulin (Sigma Aldrich) were used as internal control to ensure equal loading and transfer of proteins. Antibodies were all diluted at 1:1000 in 3% bovine serum albumin (BSA), except α-tubulin which was diluted 1:7500 in Tween 20 (0.1%)/PBS. Species-specific peroxidase-linked ECL secondary antibodies (GE Healthcare USA, 1:5000 dilutions) were used. Protein signals and densitometric analysis were performed using the Clarity Western ECL substrate (BioRad) and the Chemi-Doc System (Bio-Rad).

## LC3B-GFP Autophagosome and Electron Microscopy Analysis

For autophagosome detection, GBM CSCs were seeded at the density of 5000 cells/well in 48-well plates pre-coated with Matrigel. After 12 h, cells were transduced with BacMam LC3B-GFP viral particles (multiplicity of infection, MOI = 30), according to the Premo Autophagy Sensor Kit (Invitrogen, Carlsbad, CA, USA). After 16 h of incubation, cells were treated with GVS (0.5 μM), bafilomycin-A1 (10 nM, added 4 h before the end of the time interval), the combination of the two drugs, or vehicle (controls); LC3B-GFP signals were monitored after additional 24 h, using an inverted fluorescence microscope (40X magnification, Eclipse Nikon TS100, Minato, Japan). GFP-positive vesicles were analyzed in number and shape (area) using the Autocounter tool as described (Fassina et al., 2012).

For ultrastructural analysis, GBM CSCs were grown at 75% confluence, and treated with GVS (0.5 μM) or vehicle. Samples were prepared according to Marchesi et al. (2014). Specifically, after 48 h p.t, cells were harvested by centrifugation at 800 rpm for 3 min and fixed with 2% glutaraldehyde in medium, maintained for 2 h at room temperature. Cells were then rinsed in PBS (pH 7.2) overnight and post-fixed in 1% aqueous $OsO_4$ for 2 h at room temperature. Cells were pre-embedded in 2% agarose in water, dehydrated in acetone, and finally embedded in epoxy resin (Electron Microscopy Sciences, EM-bed812). Ultrathin sections (50–60 nm) were collected on formvar-carbon-coated nickel grids and stained with uranyl acetate and lead citrate. The specimens were finally observed with a Zeiss EM900 electron microscope equipped with a 30 μm objective aperture and operating at 80 kV.

## Cell Transfection and Atg7 Silencing

To modulate Atg7 protein expression, GBM2 CSCs (80% confluence) were transiently transfected with Lipofectamine LTX reagent (Invitrogen) in presence of pooled Silencer select validated si*ATG7* sequences (s20650, s20651; Ambion, USA) at the final concentration of 150 nM or with the mock solution alone, as negative control. To perform the viability assay (MTT), cells were plated in 96-well plates (2000 cells/well) and assayed after 24, 48, and 72 h p.t. For protein lysates, transfection was performed on cells seeded on 60 mm petri dishes with the same concentration of pooled si*ATG7* sequences.

## Statistical Analysis

All reported experiments were carried out in triplicate and performed at least three times. Data were reported as means ± SEM. All statistical analysis (ANOVA followed by Dunnett's *post-hoc* test, or unpaired two-tailed Student's *t*-test), were calculated with Graph-Pad Prism 5.0. $p \leq 0.05$ was considered statistically significant.

# RESULTS

## GVS Affects the Viability of GBM Cell Lines and CSC Enriched Cultures

Different established human GBM cell lines (i.e., U87-MG, U138-MG, and T98G) were initially tested to evaluate the effect of GVS on cell viability, using the MTT assay. Time-course (from 24 to 96 h) and dose-response (GVS 0.1–2 μM) experiments were performed. GVS reduced cell viability in a concentration- and time-dependent manner (**Supplementary Figure 1**), although no effects were observed for short time treatments (24 h) or GVS concentrations lower than 0.25 μM.

Due to the higher translational potential of GBM CSCs compared to cell lines (Lee et al., 2006), we confirmed the effect of GVS on the viability of CSC-enriched cultures isolated from nine human GBMs. GVS induced anti-proliferative effects in all CSC cultures grown as monolayers in a concentration- and time-dependent manner, with, also in this case, lower efficacy observed for shorter treatments (**Figure 1**, **Supplementary Table 2**). The mean GVS $IC_{50}$, calculated after 72 h of treatment, was 0.85 μM but this value decreased proportionally with GVS exposure time, confirming the time-dependent activity of the drug (**Table 1**).

Growing CSCs as monolayer on Matrigel allows for better cellular and biochemical characterization without interfering with stem-like characteristics (Griffero et al., 2009; Wurth et al., 2013), although the ability to grow as tumor-spheres is a defining feature of these cells. Thus, we verified whether this experimental condition interfere with CSC drug responsivity. Comparing GVS (0.1–2 μM) effects on CSCs grown as either tumor-spheres or monolayer, we observed no differences in drug sensitivity (data not shown).

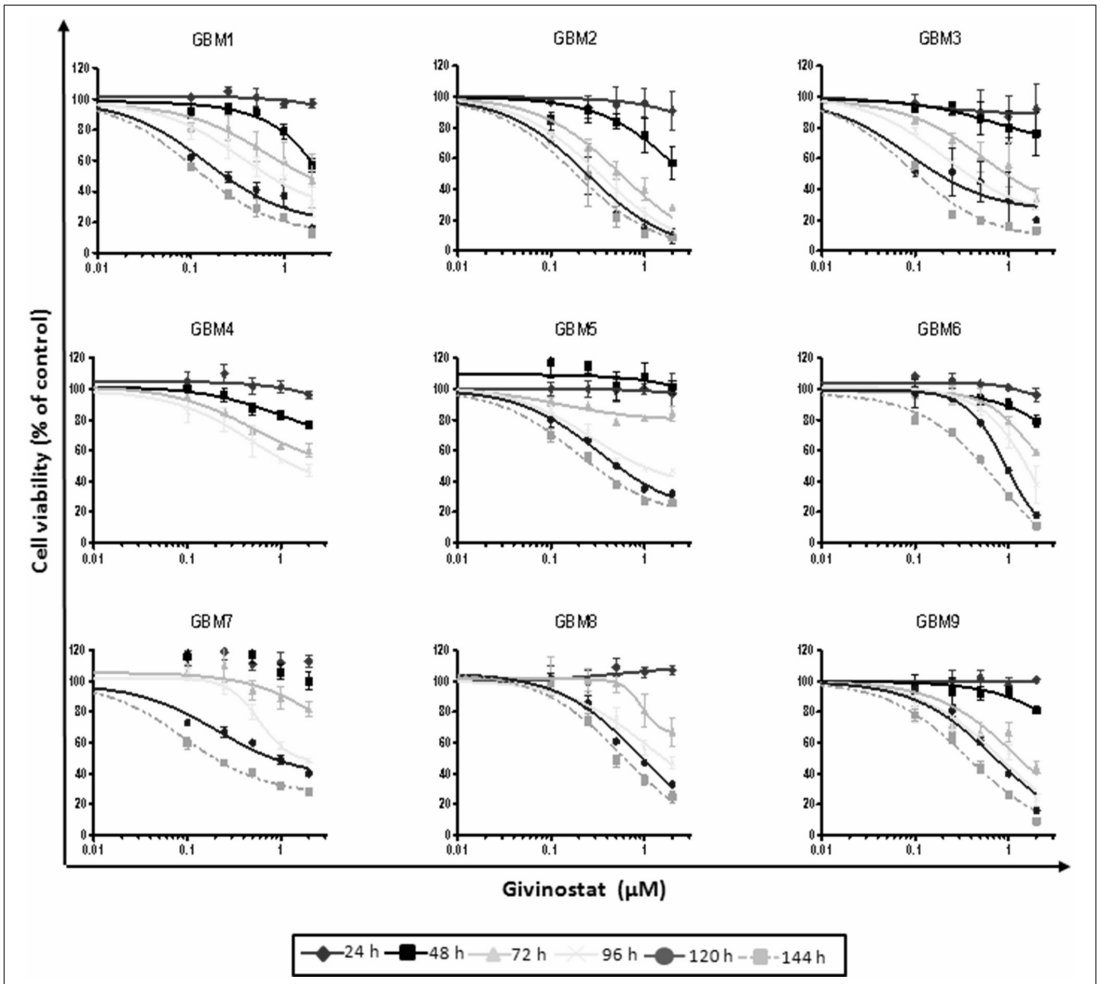


**FIGURE 1 | GVS dose-response curves (0.1–2.0 μM) in nine adherent GBM cell cultures enriched in CSCs.** Cell viability was determined by MTT assay after 24–144 h of treatment. Experiments were performed in triplicate and percentage of inhibition was calculated vs. untreated control cells.

The cellular and molecular mechanisms of GVS activity on GBM CSCs were analyzed in the most responsive CSC cultures (GBM1, GBM2, and/or GBM3) (**Table 1**), in comparison, in selected experiments, with less responsive cultures (GBM7, GBM8, GBM9). To evaluate the contribution of cytostatic or cytotoxic effects of GVS, GBM1, and GBM2 CSCs were assayed by Trypan blue exclusion test, after treatment with GVS (0.5–2 μM for 48–96 h). Forty-eight hour treatment caused cytostatic effect at all concentrations tested (with the exception of GBM1 treated with high GVS concentration) with no changes in the number of dead cells compared to untreated cells at $T_0$. However, extending treatment time, cells started to die in a concentration- and time-dependent manner (**Supplementary Figure 2**).

To establish the minimum time of GVS exposure required to decrease CSC viability, we performed cell growth recovery experiments (Favoni et al., 2010). GBM1, GBM2, and GBM3 cultures treated with 0.5 μM GVS, were washed and incubated in drug-free fresh medium. Cell viability by MTT assay determined either immediately after medium replacement or after additional 24–72 h (see **Supplementary Figure 3** for the experimental scheme). Twenty-four hour treatment decreased growth rate and the low proliferative activity partly persisted during the following 24 h, but after additional recovery time the cells reacquired an

**TABLE 1 | $IC_{50}$ value (microM) of GBM CSCs exposed for different time intervals to GVS.**

| CSCs | 72 h | 96 h | 120 h | 144 h |
|---|---|---|---|---|
| GBM1 | 0.63 | 0.35 | 0.15 | 0.11 |
| GBM2 | 0.55 | 0.33 | 0.24 | 0.19 |
| GBM3 | 0.56 | 0.20 | 0.09 | 0.09 |
| GBM4 | 0.51 | 0.49 | – | – |
| GBM5 | Not reached | 0.28 | 0.32 | 0.19 |
| GBM6 | 1.47 | 0.93 | 0.93 | 0.66 |
| GBM7 | 1.19 | 1.54 | 0.20 | 0.09 |
| GBM8 | 1.23 | 1.01 | 0.89 | 0.57 |
| GBM9 | 1.29 | 0.83 | 0.72 | 0.37 |
| MEAN $IC_{50}$ VALUE (RANGE) | 0.85 (0.51–1.47) | 0.66 (0.20–1.54) | 0.44 (0.09–0.93) | 0.30 (0.09–0.66) |

*Calculations were performed using GraphPad Prism software. (Not reached, absence of a significant GVS activity; empty boxes, not performed).*

exponential-like growth rate, reaching levels comparable to non-treated cells. The extension of the treatment with GVS to 48 or 72 h delayed the time to recovery causing, after 72 h of treatment, a significant reduction in cell viability (**Supplementary Figure 4**).

## GVS Inhibition of Cell Survival Is Specific for CSCs and Is Diminished after Differentiation

GVS anti-proliferative effect was also tested in differentiated GBM cells obtained by shifting CSC cultures from growth factor-enriched to FBS-containing medium. After 14 days, differentiated GBM CSCs lose *in vivo* tumorigenicity and stem cell marker expression and exhibit glial and/or neuronal marker expression (Gritti et al., 2014; Banelli et al., 2015). GVS did not affect the viability of differentiated GBM1 and GBM2 cells (hereafter named GBM1 DIFF and GBM2 DIFF), even after 144 h of treatment with the highest concentration of drug (**Supplementary Figure 5A**). Furthermore, GVS treatment of two cultures of normal human umbilical cord-derived mesenchymal stem cells (MSCs) caused no reduction of viability at all concentrations and times tested in MSC1, whereas only the highest GVS concentration (2 μM) slightly reduced MSC2 viability (**Supplementary Figure 5B**). These results confirm that independently from the culturing conditions, the antitumoral effects of GVS are selectively directed against CSC specific proliferation mechanisms, with GBM DIFF cells and MSCs mostly insensitive to the drug.

Self-renewal is a defining feature of both normal and cancer stem cells. Tumor-sphere formation is considered an indirect index of self-renewal of CSCs (Soeda et al., 2008). To understand whether GVS affects GBM CSC self-renewal, we performed a spherogenesis assay. GBM1, GBM3, GBM5, GBM7, and GBM9 CSCs were plated at 1000 cells/well in the presence of increasing concentrations of GVS and allowing to generate spheres for 7 days. As reported in **Figure 2A** (and quantified in **Figure 2B**), GVS inhibited spherogenesis in a dose-dependent manner. At low GVS concentrations, tumor-spheres were less compact and organized, while a clear reduction of number and size of spheres was observed on increasing the drug concentration. At the highest concentrations tested (GVS 1 and 2 μM), the inhibition of cell viability in all the cultures was predominant and masked the drug effect on spherogenesis, making difficult the interpretation of the results. A statistically significant reduction of the number of spheres was seen in GBM1, GBM3, and GBM9 starting from the GVS concentration of 0.25–0.5 μM which had low effect on CSC viability, suggesting that GVS inhibition of sphere formation is independent from anti-proliferative effects. An additional experimental approach was performed using GBM1, GBM2, and GBM3 preformed tumor-spheres, which were treated with low GVS concentrations (0.1–0.5 μM) for 7 days, disaggregated and re-plated in GVS-free medium (**Figure 3A,B**). While untreated CSCs regenerate spheroids, pre-treatment with GVS dose-dependently abolished their spherogenesis ability.

## Effects of GVS on Apoptosis/Autophagy Processes in GBM CSCs

GVS was tested for the ability to interfere with apoptosis and autophagy processes. GBM1, GBM2, and GBM3 CSCs, treated with GVS (up to 2 μM) for 72 h, were tested in AnnexinV-PI double staining by FACS analysis (**Figure 4**), showing a concentration-dependent increase of cells entering the early phases of apoptosis (approximately 30% for GBM1 and GBM3, and 50% for GBM2).

To study GVS modulation of autophagy, as a preliminary evaluation we analyzed the relative expression of *MAP1LC3B*, coding for LC3B, in GVS-treated GBM1, GBM2, and GBM3 CSCs by Real-time PCR. GVS treatment induced a transient increase in *MAP1LC3B* mRNA content (detectable after 24 and 48 h, and back to the baseline after 72 h, **Supplementary Figure 6**). Then, the effect of GVS on LC3-II and Beclin1 protein content was investigated in GBM1, GBM2, GBM3, GBM6, GBM7, and GBM9 cells. CSCs were treated for 72 h with GVS (0.5–2 μM) or with the autophagy inducer rapamycin (50 nM, for 72 h): LC3-II and Beclin1 showed an increased amount following GVS treatment, often higher than those caused by rapamycin administration (**Figure 5**). Increased acetyl-α-tubulin content, a direct marker of HDAC6 inhibition (Haggarty et al., 2003), was observed following GVS administration, confirming the efficacy of the drug on its specific target (**Figure 5**).

To verify whether GVS-mediated increase in LC3-II and Beclin1 was the resultant of autophagy activation, GBM1, GBM2, and GBM3 CSCs were transduced with a baculovirus LC3B-GFP expressing vector. Cells were treated with GVS (0.5 μM), bafilomycin-A1 (10 nM) or with the combination of the two drugs and analyzed for the amount of GFP-positive vesicles, using the Autocounter tool as described (Fassina et al., 2012). GVS, bafilomycin-A1 and the combined treatment induced significant increases of fluorescent vesicles in the investigated cells; furthermore, the additive results in increasing GFP puncta in the combined GVS+bafilomycin-A1, compared to bafilomycin-A1 alone administration, suggested a direct increase of the autophagy flux induced by GVS

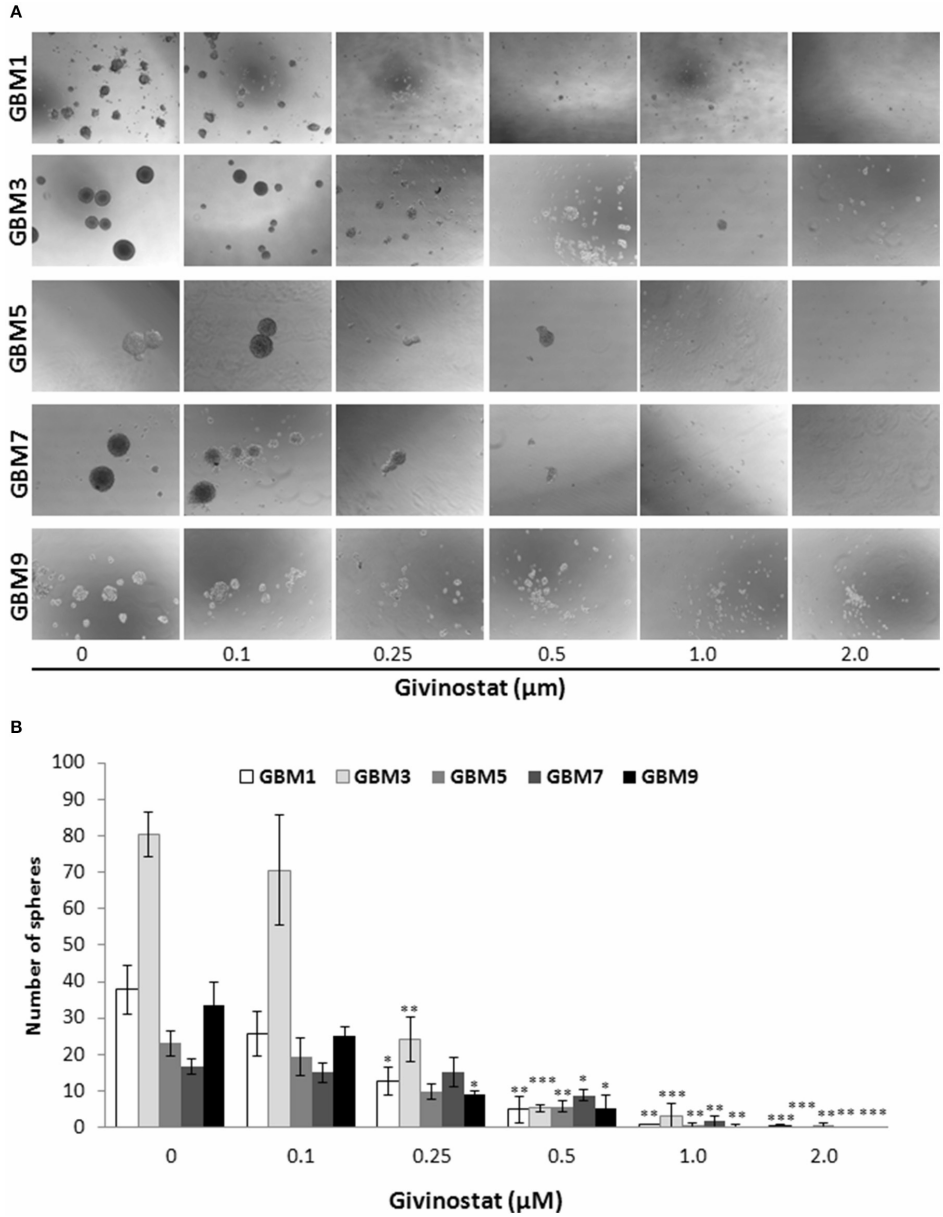


**FIGURE 2 | GVS effect on GBM CSC sphere formation. (A)** GBM1, GBM3, GBM5, GBM7, and GBM9 were maintained in the selective medium for stem cells in the absence or presence of increasing concentrations of GVS. Sphere formation was visually monitored and after 14 days the number of spheres/well was counted. Representative microphotographs (magnification 10X) are reported. **(B)** Histogram reports the mean sphere number from four experiments (*$p < 0.05$, **$p < 0.01$, ***$p < 0.001$, ANOVA followed by Dunnett's *post-hoc* test).

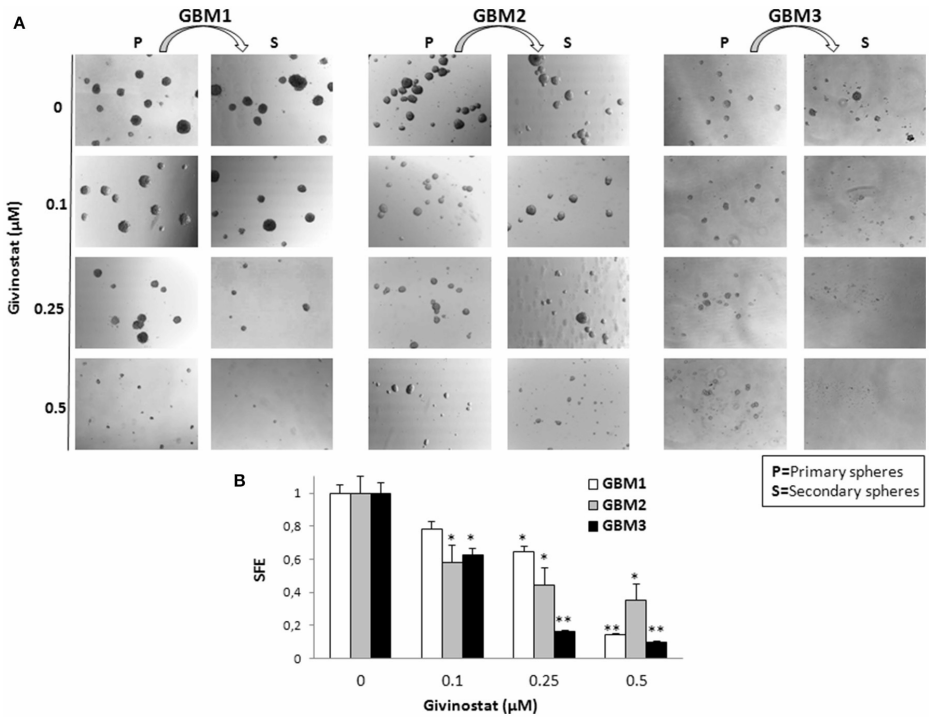


**FIGURE 3 | GVS effect on GBM CSCs on self-renewal measured as secondary sphere formation. (A)** GBM1, GBM2, and GBM3 were grown in stem cell permissive conditions for 7 days to allow sphere appearance (*P* = Primary spheres) in the presence or absence of increasing concentration of GVS. Spheres were then disaggregated and single cells were replated in medium without GVS and, following further 7 days, the formation of secondary spheres (S) was evaluated. Microphotographs (magnification 10X) are representative of GVS inhibitory effect on spherogenesis. **(B)** Histograms indicate the sphere-formation efficiency (SFE) of secondary spheres (mean number of spheres/number of cells seeded per well) for each condition against untreated controls. Control value was set at 1 (*$p < 0.05$ and **$p < 0.01$ using ANOVA followed by Dunnett's *post-hoc* test).

(**Figures 6A,B**). Transmission electron microscope analysis of GVS-treated cells, revealed a high number of double membrane autophagic-like vesicles containing partially undigested material. Features of mitophagy (the presence of mitochondria within autophagosomes), multivesicular bodies and phagophores (a site of autophagosome formation) were also scored (**Figure 6C**).

## Functional Role of Autophagy in GVS-Treated GBM CSCs

The functional significance of the autophagy induced by (or in response to) GVS treatment was assessed using different known autophagy inhibitors/inducers (Klionsky et al., 2016).

To arrest the autophagy process, GBM1, GBM2, and GBM3 CSCs were pre-treated with bafilomycin-A1 (up to 50 nM) for 2 h before being incubated with GVS (0.5 μM). Cell viability was evaluated by MTT assay. Forty-eight hours of combined treatment with bafilomycin-A1 and GVS induced a significant decrease in cell viability, compared to bafilomycin-A1 or GVS alone (the combination of bafilomycin-A1+GVS reduced GBM1 viability of 57% compared to −25% of bafilomycin-A1 and −23% GVS; in GBM2 the combined treatment caused a reduction of −74%, in comparison to bafilomycin-A1 −31% and GVS −20%; while in GBM3 we observed −46% viability after bafilomycin-A1+GVS, compared to −8% of bafilomycin-A1 and −20% GVS), with a further increase in the cytotoxic effect induced by the combined treatment after 72 h (**Figure 7A**). To determine the statistical significance of the GVS/bafilomycin-A1 association, the combination index (CI) values were calculated and plotted using the CompuSyn software (**Supplementary Figure 7**): CI values above 1 are indicative of antagonism, while below 1 of synergism. GBM1, GBM2, and GBM3 showed CI values <1 starting from the combination GVS 0.5 μM/bafilomycin-A1 2.5 nM for GBM1 (range, 0.2–0.6 at 48 h; 0.07–0.6 at 72 h), GVS 0.5 μM/bafilomycin-A1 5 nM for GBM2 (range, 0.3–0.9 at 48 h, 0.3–0.9 at 72 h) and GVS 0.5 μM/bafilomycin-A1 2.5 nM for GBM3 (range: 0.4–0.6 at 48 h; 0.02–0.4 at 72 h), confirming a synergistic effect exerted by GVS in association with the autophagy inhibitor bafilomycin-A1. Similar results were obtained when the effects of

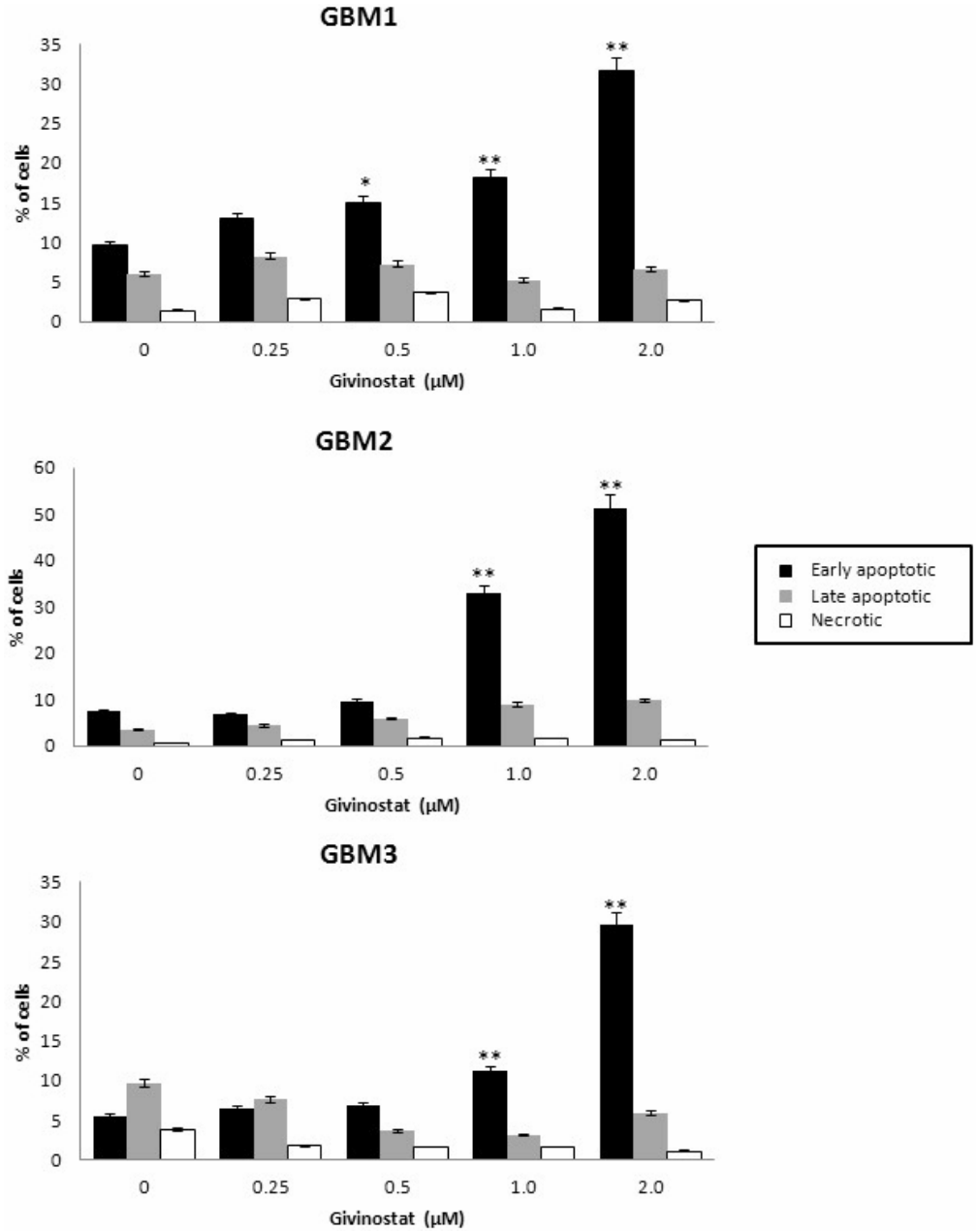


**FIGURE 4 | *In vitro* assessment of apoptosis in GBM1, GBM2, and GBM3 CSCs.** FACS analysis of Annexin V-PI staining was used to observe the induction of apoptosis and/or necrosis by GVS. Histograms represent the percentage of each cell population (early apoptotic, late apoptotic and necrotic) after 72 h of GVS treatment (0.25, 0.5, 1.0, and 2.0 μM). Statistical analysis was performed using ANOVA followed by Dunnett's *post-hoc* test (*$p < 0.05$, **$p < 0.01$).

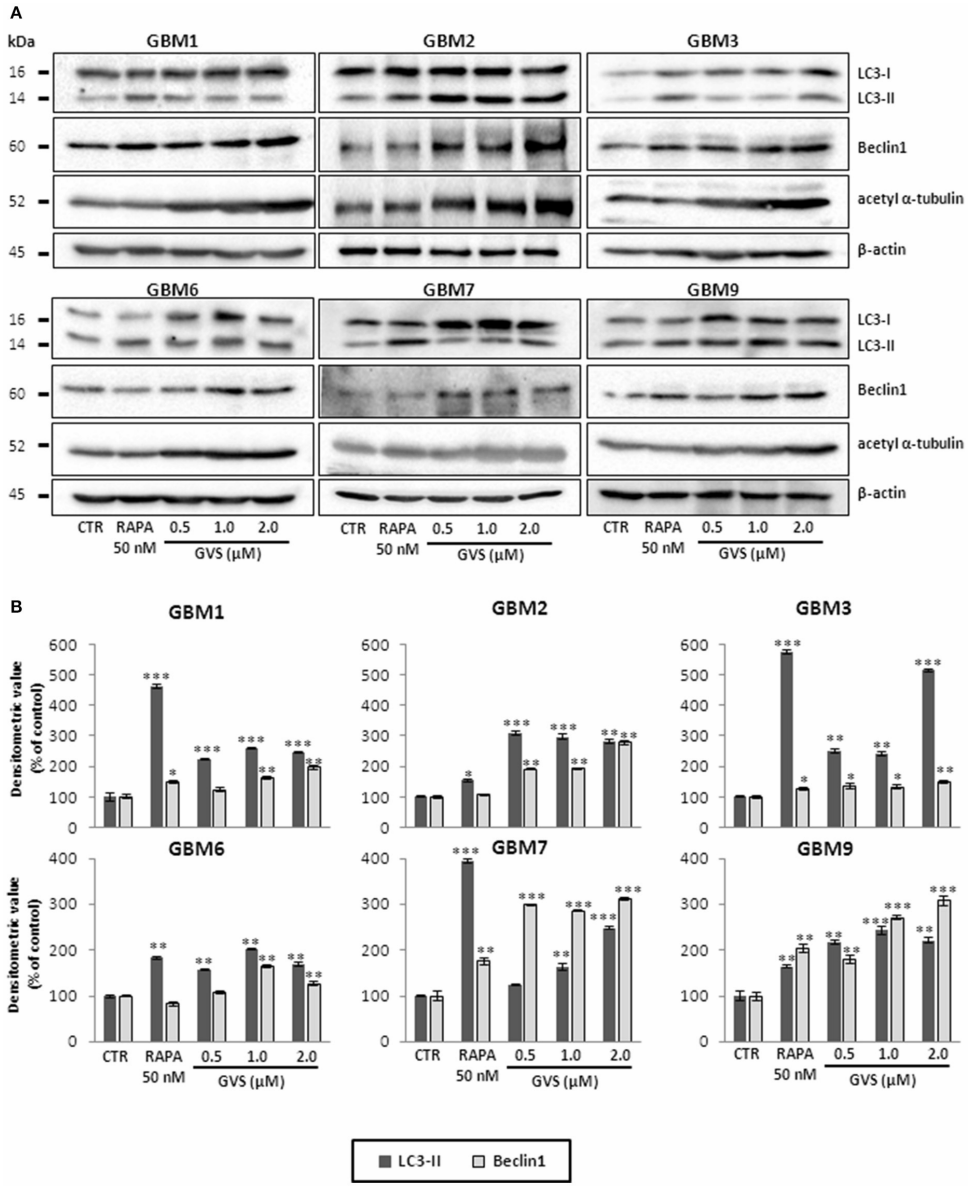


**FIGURE 5 | Modulation of autophagic marker expression following GVS administration in GBM1, GBM2, GBM3, GBM6, GBM7, and GBM9 CSCs. (A)** LC3-I, LC3-II, Beclin1 and acetyl-α-tubulin protein levels was determined by immunoblotting. β-actin was used as protein loading control. Lysates were obtained from cells treated for 72 h with GVS (0.5, 1.0, and 2.0 μM) or rapamycin (50 nM). **(B)** Densitometric analysis of protein expression. Values were normalized to β-actin expression and reported as percentage of untreated controls. Experiments were performed in triplicate, data represent mean ± SEM, (*$p$ <0.05; **$p$ <0.01, ***$p$ < 0.001, ANOVA followed by Dunnett's *post-hoc* test).

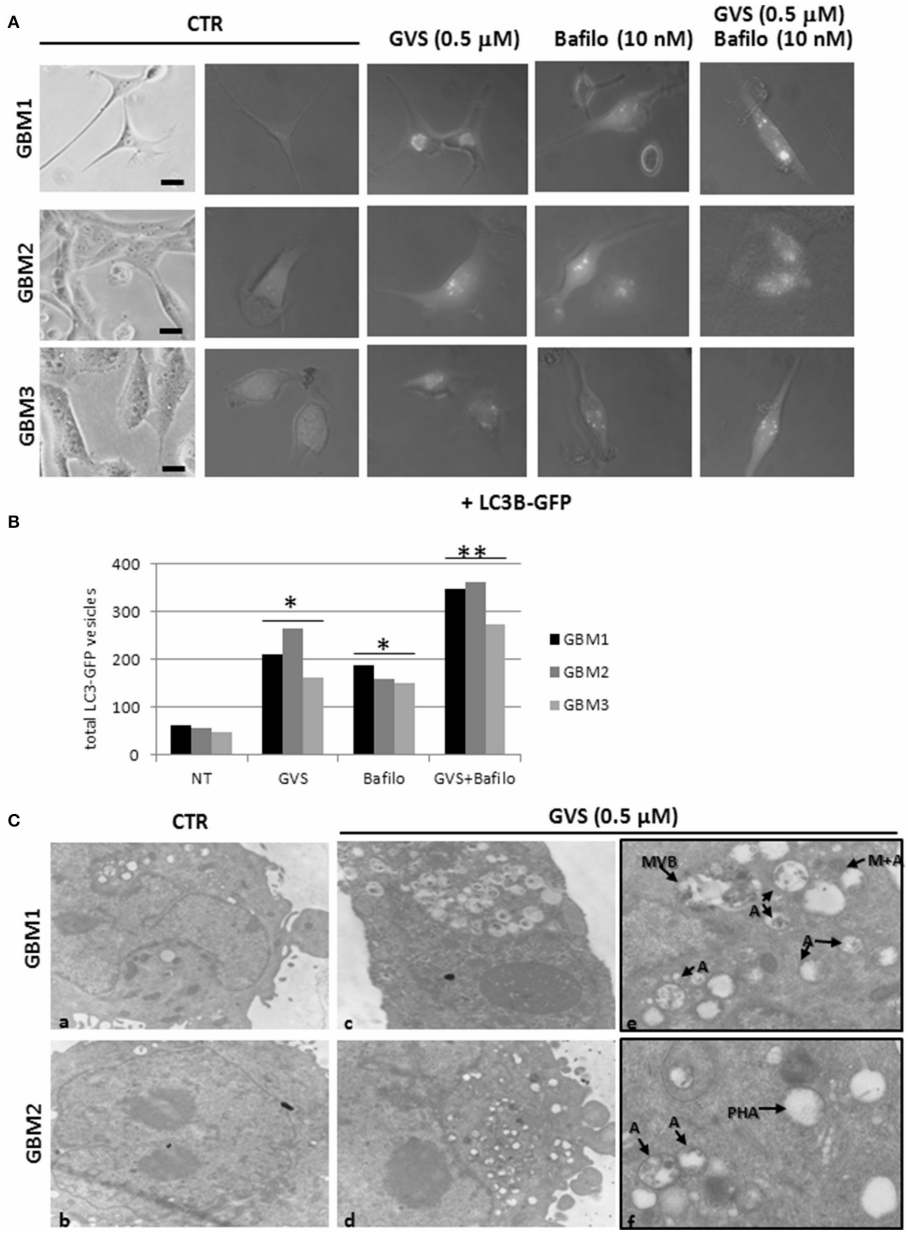


**FIGURE 6 | LC3B-GFP expression in GBM CSCs exposed to GVS. (A)** Cells were transduced with baculovirus LC3B-GFP expressing vector. GVS (0.5 μM) was added 16 h after transduction to allow LC3B-GFP expression. Bafilomycin-A1 (10 nM), alone or in combination with GVS (0.5 μM), was added 4 h before the end of the 24 h interval. LC3-GFP signals were monitored using an inverted fluorescence microscope (40X magnification). **(B)** Evaluation of numbers of LC3-GFP vesicles was performed using Autocounter tool. GFP-positive vesicles were considered with area >1 $mm^2$ in 50 cells for each treatment. Statistical analysis was performed

*(Continued)*

**FIGURE 6 | Continued**
using ANOVA followed by Dunnett's *post-hoc* test (*$p < 0.05$, **$p < 0.01$) comparing GVS, bafilomycin-A1, GVS+bafilomycin-A1 treatments to the respective untreated (CTR) GBM CCSs. **(C)** Representative ultra-structures analysis using transmission electron microphotographs of GBM1 and GBM2 treated with GVS (0.5 μM) for 72 h. GBM1 and GBM2 cells ($10^6$) were grown at 75% confluence and treated (**c–f**) or not (**a,b**) with GVS. Cells were harvested, fixed and stained for ultra-structural visualization. Specimens were then observed with a Zeiss EM900 electron microscope. Magnifications are 7000X (**a–d**) and 12000X (**e,f**). "A" indicates large intracellular vesicles, likely autophagosomes; "M+A" indicates a mitochondrion fused with a vesicle (mitophagy), "MVB" indicates a multivesicular body, finally "PHA" indicates a phagophore (isolation membrane) assembly site.

the combined GVS (0.5 μM)/bafilomycin-A1 (5 nM) treatment was investigated on the induction of apoptosis in GBM2 and GBM3 CSCs. As compared to single drug treatments, the drug combination increased the percentage of apoptotic cells (GBM2: 41.27% of early+late apoptotic cells with the association, vs. 19.84 and 6.25% for GVS and bafilomycin-A1, respectively; for GBM3, 16.4% of early+late apoptotic cells with the association, vs. 5.89 and 6.25% for GVS and bafilomycin-A1, respectively). Also the percentage of PI-positive, necrotic cells was increased with the combined treatment with GVS and bafilomycin-A1 (**Figure 7B**). These results suggested that the inhibition of autophagy by bafilomycin-A1 facilitated GVS-dependent apoptotic cell death in GBM CSCs. Furthermore, GVS+bafilomycin-A1 treatment produced an increase of LC3-II and p62 content, as compared to the amount of these proteins following individual drugs treatments. Conversely, in presence of the autophagy-activator rapamycin or with GVS alone, p62 protein levels were reduced as a result of the increase in autophagy-mediated protein degradation (**Figures 8A,B**).

To better decipher the role of autophagy in GVS antitumor activity, GBM2 CSCs were transfected with si*ATG7* validated sequences, to arrest autophagy by reducing the intracellular content of Atg7. The efficacy of gene silencing was verified 24 h post-transfection when Atg7 protein was significantly down-regulated as compared to mock and not-transfected cells (**Figure 9**, left panel). Treatment of si*ATG7*-GBM2 with GVS caused a further decrease of cell viability (**Figure 9**, right panel), confirming that the arrest of autophagy enhances GVS tumor cytotoxicity, as also showed by bafilomycin-A1 treatment.

Finally, a widely adopted culture-starvation scheme was applied to activate autophagy in GBM1 and GBM2 CSCs. In detail, CSCs were deprived of growth factors for 60 h before being treated with GVS (up to 2 μM) and cell viability measured by MTT assay. Deprivation of growth factors prevented GVS-dependent cell death, and the activation of autophagy in these conditions was demonstrated by increased LC3-II and reduction in p62 protein levels (**Supplementary Figure 8**).

## DISCUSSION

In this paper we report that in human GBM stem cells, the inhibition of autophagy using both chemical and RNAi approaches increases the antitumor efficacy of givinostat.

Givinostat (ITF2357, GVS) is a hydroxamic acid-derivative, orally active, pan-HDACi. GVS has anti-inflammatory, anti-neoplastic and anti-angiogenic properties (Leoni et al., 2005), with pro-apoptotic effects in hepatocellular carcinoma (Armeanu et al., 2005), non-small cells lung cancer (Del Bufalo et al., 2014) and acute myeloid leukemia cells (Galimberti et al., 2010).

We report the efficacy of GVS in reducing viability of human GBM CSCs, the subpopulation responsible for GBM resistance to conventional therapy and patients' fatal outcome (Bonavia et al., 2011; Chen et al., 2012; Florio and Barbieri, 2012). *In vitro,* CSCs retain genotypic and phenotypic features of the tumor they are derived from, which are progressively lost when the cells are grown in FBS-containing media, as occurs in established cell lines (Lee et al., 2006). Thus, results obtained using CSC-enriched cultures possess a higher traslational impact than those obtained adopting established cell lines. CSC-enriched cultures, obtained from nine human GBMs, were cultured both as spheroids and monolayers retaining the stem-like biological and phenotypical characteristics (expression of stem cell markers, multilineage differentiation, self-renewal, and tumorigenicity *in vivo*; Griffero et al., 2009; Wurth et al., 2013).

Firstly, we documented that GVS powerfully reduces viability of all CSCs analyzed, independently from the genotypical and phenotypical heterogeneity observed in the GBMs: we observed a prolonged pharmacological activity that could be useful during *in vivo* experimental schemes. GVS also inhibited CSC self-renewal, a mechanism necessary to preserve CSCs within the tumor microenvironment. It is important to highlight that the culture conditions used to grow CSCs (non-adherent tumor-spheres or monolayers in the presence of Matrigel) did not affect GVS efficacy. In contrast, differentiated GBM cells or normal stem cells are modestly affected by GVS-induced cell death. Accordingly, previous studies reported that GVS is cytotoxic for hepatoma cell lines but not for normal human hepatocytes (Armeanu et al., 2005), and, in agreement with our results, that MSCs are resistant to GVS at concentrations higher than 1 μM for at least 72 h (Golay et al., 2007). The reduced activity against non-tumor stem cells while impairing CSC viability, renders GVS an interesting candidate for further clinical evaluations. In addition, we report that GVS had a lower effect on differentiated CSC, further supporting the selectivity of GVS against CSC subpopulation.

It was reported that antitumor activity of GVS depends on the activation of apoptotic pathways (Pathil et al., 2006; Golay et al., 2007; Galimberti et al., 2010). We report that the effect of GVS on GBM CSC viability is associated not only with apoptotic cell death but also with the activation of macroautophagy. Autophagy is a central cell degradation system involved in several physiological and pathophysiological events (Rabinowitz and White, 2010), including cancer (Mathew et al., 2009; Macintosh and Ryan, 2013). A functional link between HDACi and autophagy was demonstrated in cancer cells (Zhang and Zhong, 2014). To this regard, we evaluated

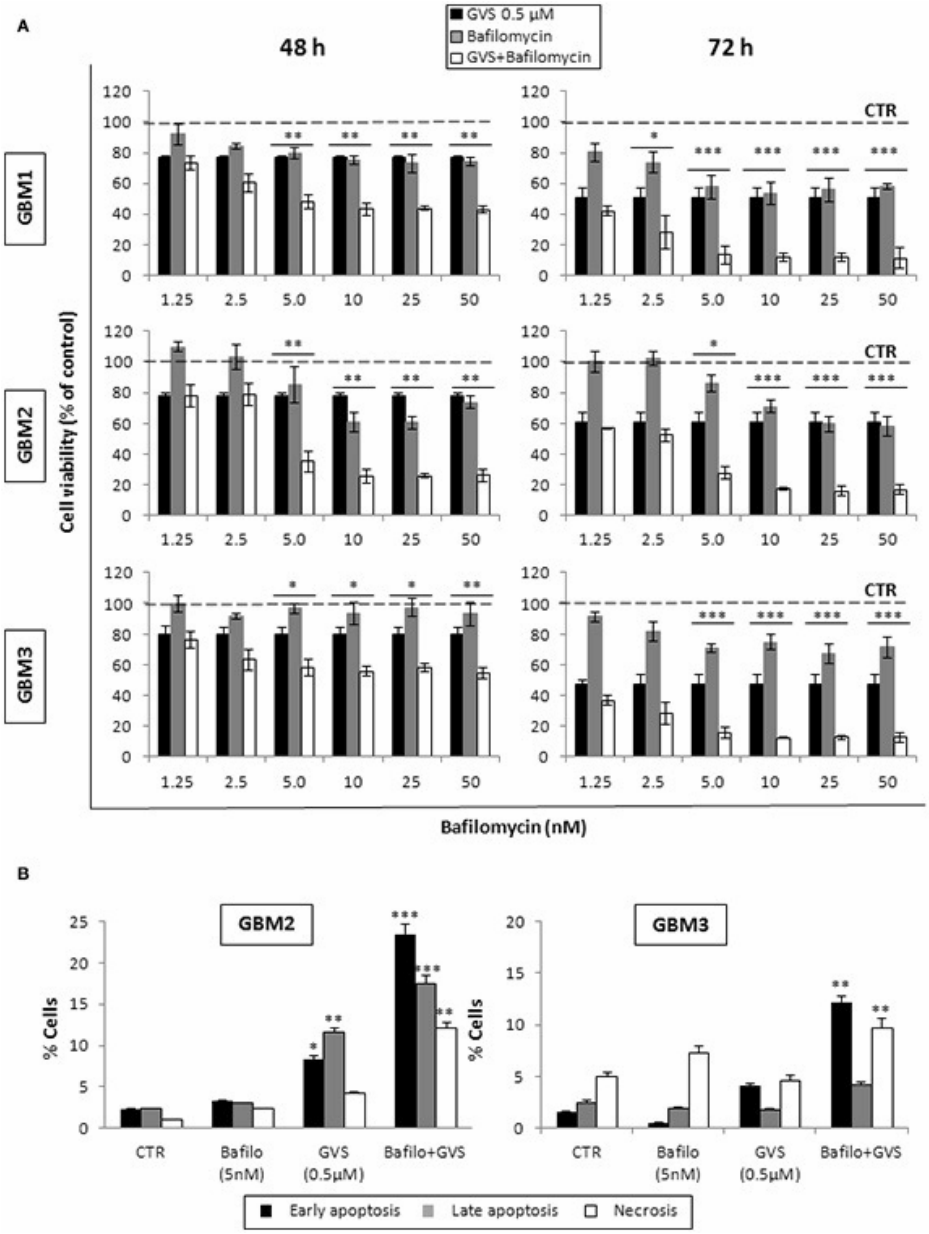


**FIGURE 7 | Evaluation of the role of autophagy in GVS inhibitory effect on GBM CSCs. (A)** GBM1, GBM2 and GBM3 CSCs were treated with GVS 0.5 μM (black bars), bafilomycin-A1 1.25, 2.5, 5, 10, 25, and 50 nM (gray bars) or with the combination of all doses of the two drugs (pre-treatment with bafilomycin-A1 for 2 h; white bars) for 48 and 72 h. Cell viability was monitored by MTT assay. Statistical significance was calculated using ANOVA followed by Dunnett's *post-hoc* test; (*$p < 0.05$, **$p < 0.01$; ***$p < 0.001$, vs. control). **(B)** *In vitro* assessment of apoptosis in GBM2 and GBM3 cells treated with bafilomycin-A1 (5 nM) or GVS (0.5 μM), alone or in combination. FACS analysis of Annexin V-PI staining was used to measure apoptosis/necrosis. Histograms represent the percentage of each cell population after 48 h of drug exposure. Statistical analysis was performed using ANOVA followed by Dunnett's *post-hoc* test (*$p < 0.05$, **$p < 0.01$, ***$p < 0.0001$ vs. control).

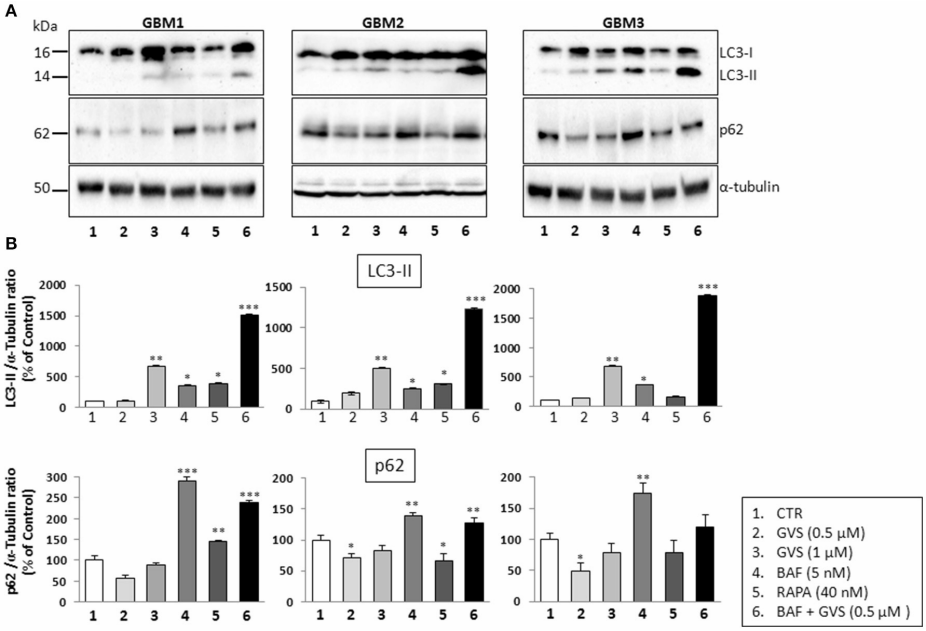


**FIGURE 8 | Effect of the combined treatment with GVS and bafilomycin-A1 on the LC3-II and p62 protein levels. (A)** Representative immunoblots of LC3-II and p62 protein levels. Cell lysates were obtained from GBM1, GBM2, and GBM3 CSCs treated with GVS (0.5–1.0 μM), bafilomycin-A1 (5 nM), rapamycin (40 nM), and with GVS 0.5 μM/bafilomycin-A1 combination (2 h pre-treatment with bafilomycin-A1). α-tubulin content was used as loading control. **(B)** Densitometric analysis of LC3-II and p62 protein levels. Data were normalized against α-tubulin and expressed as percentage of untreated control values. Statistical analysis was performed using ANOVA followed by Dunnett's *post-hoc* test (*$p < 0.05$, **$p < 0.01$;***$p < 0.001$ vs. control) comparing GVS, bafilomycin-A1, rapamycin, GVS+ bafilomycin-A1 treatments to the respective untreated (CTR) GBM CCSs.

the capability of GVS to modify the autophagy process in CSCs, measuring the expression of main ATG proteins. In particular, GVS treatment produced increasing amount of key autophagy executory proteins LC3-II and Beclin1, clearly suggesting that the drug administration induced marked differences within the autophagy process. To further confirm this result, the effect of GVS on autophagy was also assessed by autophagosome analysis. Autophagosomes express LC3-II on the outer membranes, while LC3-I isoform, originated by different post-translational modifications, has a typical cytoplasmic diffuse expression pattern. GVS treatment of GBM CSCs, previously transduced with LC3-GFP baculovirus, induced a significant accumulation of discrete fluorescent LC3-GFP puncta, likely representing autophagosomes. Moreover, increased levels of LC3-GFP in the presence of GVS or compounds interfering with the autophagosome-lysosome fusion (i.e., bafilomycin-A1), was indicative of an increase of the synthesis of autophagy-related membranes (autophagy induction) rather than a reduction in vesicle clearance as for autophagy blockage (Klionsky et al., 2016). Moreover, transmission electron microscopy ultrastructural evaluation highlighted a marked increase in autophagy-like vesicles after GVS exposure. Altogether, these molecular and cellular features indicate that GVS treatment induces the activation of autophagy in GBM CSCs.

As widely discussed (Choi et al., 2013; Macintosh and Ryan, 2013; White, 2015), the contradictory role of autophagy in cancer makes difficult to understand whether this mechanism is *per se* beneficial or inhibitory for the malignant progression. The possible dual functional role of autophagy, i.e., promoting programmed cell death fate or conferring a pro-survival favorable phenotype to the cancer cell, can determine the success or failure of anti-cancer therapies (Palumbo and Comincini, 2013). This opposite behavior represents an adaptive response of the tumor cells to the therapy, and is associated to several tumor-environmental conditions, such as specific or off-targets effects of the drug used, tumor cell type and the state of stem-like or differentiated cells (Galluzzi et al., 2015). To decipher the contribution of the autophagy process to the cytotoxic effects of GVS, autophagy in GBM CSCs was positively or negatively modulated using different experimental approaches. To obtain the autophagy inhibition: the down-regulation of key genes and/or proteins and the blockade of the autophagy flux preventing the fusion of autophagosomes with lysosomes; to activate the autophagy process: rapamycin

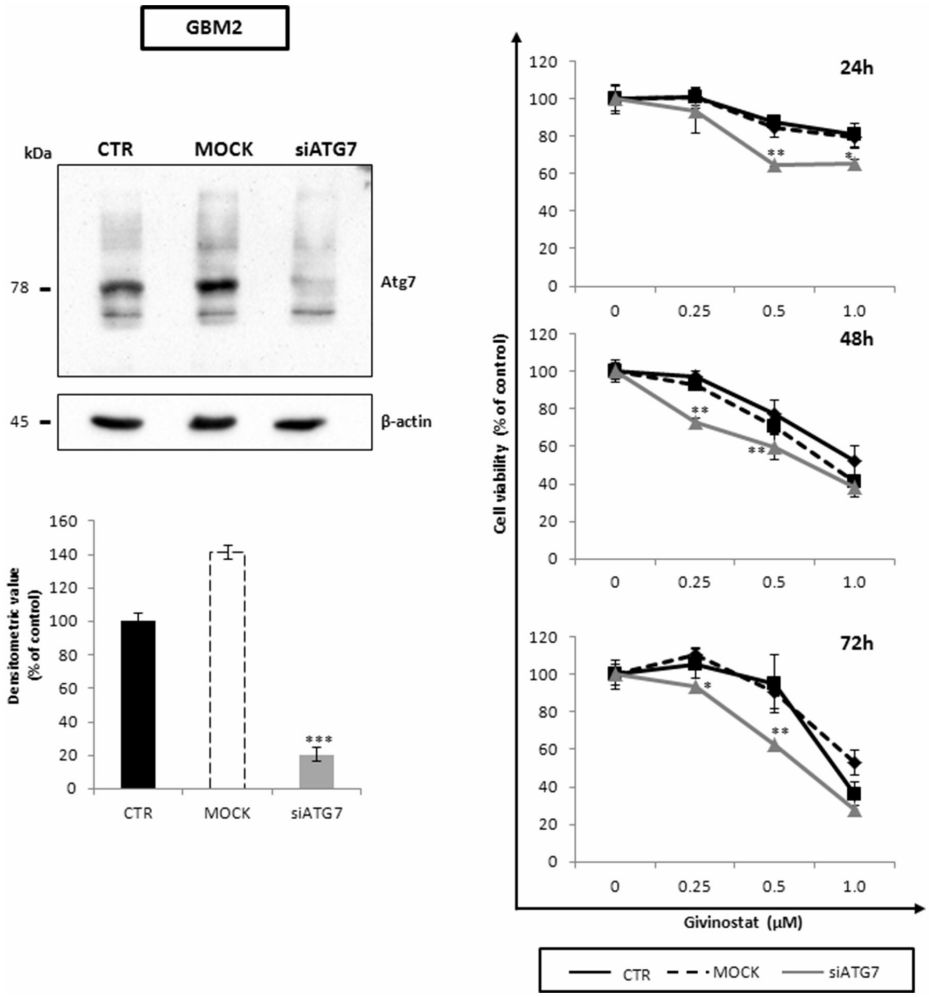


**FIGURE 9 | Atg7 silencing effects on cell viability along with GVS in GBM CSCs.** Equal amount of proteins obtained from GBM2 control (CTR), GBM2 transfected without si*ATG7* (MOCK) and GBM2 transfected with si*ATG7* were assayed. Immunoblotting analysis (left panels) was performed, 24 h post-transfection, in order to ensure *ATG7* silencing and Atg7 downregulation. β-actin was used as loading control. MTT cell viability assay (right panels) was performed at 24, 48, and 72 h after GVS administration (0.25, 0.5, and 1.0 μM), in CTR, MOCK and si*ATG7* transfected GBM2 cells. Statistical analysis was performed using ANOVA followed by Dunnett's *post-hoc* test (*$p < 0.05$, **$p < 0.01$; ***$p < 0.001$ vs. control).

treatment or growing cells in medium deprived of growth factors.

Bafilomycin-A1, used to inhibit the autophagy flux, is a specific inhibitor of the late phase of autophagy that prevents the acidification of the autophagic vacuoles and inhibits the fusion between autophagosomes and lysosomes (Yamamoto et al., 1998). In parallel, the inhibition of autophagy was achieved by down-regulating *ATG7* gene by siRNA. Silencing *ATG7,* or other key autophagy genes, provides an effective strategy to arrest this pathway blocking the autophagosomes formation and the degradation processes (Saiki et al., 2011; Criollo et al., 2012; Klionsky et al., 2016). In this way, we show that the inhibition of autophagy by both molecular and pharmacological approaches, increases the anti-proliferative and pro-apoptotic effects of GVS on GBM CSCs. This result was confirmed in cells in which autophagy was activated by deprivation of growth factors. The

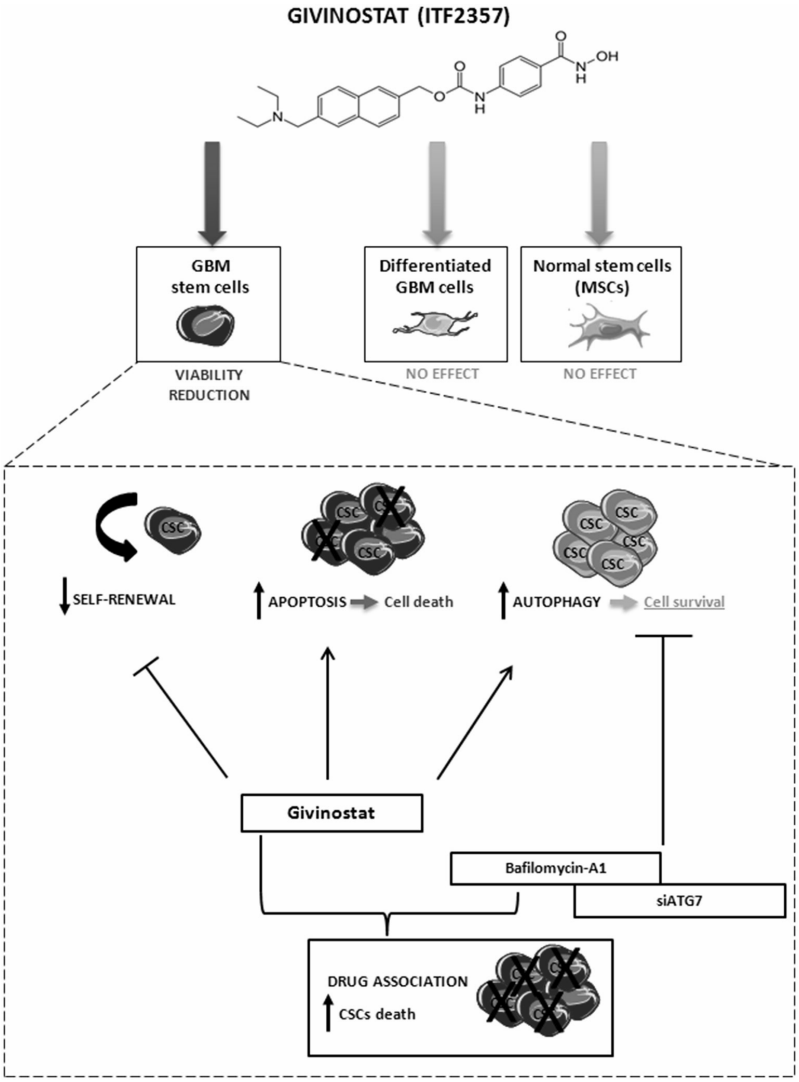


**FIGURE 10 | Schematic representation of the effect of GVS on GBM CSCs, differentiated GBM cells and MSCs.** GVS reduced CSC viability through apoptosis activation and self-renewal impairment; at the same time, GVS induced activation of the autophagy process that resulted in a partial protection of CSCs from GVS pharmacological activity. The autophagy flux arrest, mediated by bafilomycin-A1 co-administration or by *ATG7* silencing, enhanced the GVS pro-apoptotic activity, therefore suggesting a pro-survival effect of the autophagic process to counteract the effect of GVS. Importantly, GVS did not reduce cells viability in differentiated GBM cells and MSCs.

depletion of nutrients is one of the main stimuli triggering autophagy (Mizushima and Klionsky, 2007). When the nutrients' supply is limited, cells activate autophagy to generate a source of metabolic substrates to sustain the energetic requirement for survival (Kang and Avery, 2008). We report that deprivation of growth factors in CSCs and the consequent activation of autophagy results in a protective effect against GVS antitumor activity.

Taken together, these findings suggest that the activation of autophagy occurring during GVS treatment has a cytoprotective

effect that, supporting CSC survival, reduces HDACi efficacy. In other terms, tumor cells respond to GVS-induced cell death with the activation of autophagy, a process directed to catabolize damaged proteins and organelles. Lastly, our data indicate that combined treatment with GVS followed by autophagy inhibition has strikingly synergistic anti-tumor activity in GBM, similarly to lung (Del Bufalo et al., 2014), hepatoma (Liu et al., 2010; Yuan et al., 2014), breast (Rao et al., 2012) cancer models. Consistent with these data, we propose a mechanistic evaluation of the possible synergism between GVS effects and autophagy inhibition that enhances the loss of GBM CSC viability (**Figure 10**).

On the other hand, our results differ from previous studies showing that the combined treatment with imipramine and ticlopidine elicits cell-lethal autophagy in mouse models of gliomagenesis (Shchors et al., 2015). However, it must be pointed out that the quantitatively and qualitatively different modulations of autophagy in our and in the previous study might result in either pro-survival or cytotoxic effects (White et al., 2015).

In conclusion, we demonstrate that GVS is a promising pharmacological agent; its inhibitory activity against CSC proliferation and self-renewal, accomplished with high potency and efficacy, allows us to consider GVS as a novel possible adjuvant approach for GBM treatment. The identification of GVS as a drug specifically directed against CSCs could represent a significant pharmacological alternative for GBM patients. Moreover, our results suggest that, in light of the cellular and biological complexity of GBM, GVS therapeutic efficacy could be intensified by the association with autophagy inhibitors, since these compounds could synergize and revert the resistance to therapeutic interventions of CSCs, and reduce the drug concentration required to achieve a significant tumor mass reduction.

## AUTHOR CONTRIBUTIONS

Conceived and designed the experiments: SC, TF, FB, FA, and GF. Performed the experiments: FA, AP, RW, AD, SC, and AS. Analyzed the data: all the authors. Contributed reagents/materials/analysis tools: SC, TF, and GF. Wrote the manuscript: FA, TF, SC, and GF.

## ACKNOWLEDGMENTS

This work was supported by a grant from Italian Association from cancer Research (AIRC) to TF. The authors thank Italfarmaco S.p.A. for supplying ITF2357 and for the financial support. GF is an employee of Italfarmaco S.p.A.

## SUPPLEMENTARY MATERIAL

The Supplementary Material for this article can be found online at: http://journal.frontiersin.org/article/10.3389/fnmol.2016.00107/full#supplementary-material

**Supplementary Figure 1 | GVS dose-response curves (0.1–2 μM) on U87-MG, U138-MG, and T98G cell viability.** Every 24 h, cell viability was determined by MTT assay for up to 96 h. Experiments were performed in triplicate and the percentage of viability was calculated *vs*. untreated control cell. Statistical analysis was performed with ANOVA test followed by Dunnett's *post-hoc* test (*$p < 0.05$, **$p < 0.01$, ***$p < 0.001$).

**Supplementary Figure 2 | Trypan blue exclusion assay on GBM1 and GBM2 CSCs.** Analysis was performed after GVS (0.5, 1, 2 μM) exposure from 48 to 72 h (black columns represent cells number at $T_0$). Data represent the mean and the SD of three independent replicates; (for dead cells: *$p < 0.05$, **$p < 0.01$, ***$p < 0.001$, by ANOVA test followed by Dunnett's *post-hoc* test).

**Supplementary Figure 3 | Schematic representation of the experimental plan of time-scale cell growth recovery test.**

**Supplementary Figure 4 | Cell growth recovery assay performed on GBM1, GBM2, and GBM3 CSCs.** Cells were treated with GVS (0.5 μM), for 24, 48, and 72 h. After each time of exposure, culture medium was replaced with a fresh one devoid of GVS and cell viability was tested by MTT assay at $T_0$ (time of medium replacement), and after 24, 48, and 72 h. Histograms indicate the percentage of cell survival compared to untreated control value at $T_0$ (*$p < 0.05$; **$p < 0.01$, ***$p < 0.001$, on ANOVA test followed by Dunnett's *post-hoc* test).

**Supplementary Figure 5 | GVS dose-response curves performed on (A) differentiated GBM1 and GBM2 CSCs and (B) human umbilical cord-derived MSCs.** Cell viability was tested after 24–144 h of GVS treatment (0.1–2 μM) and was determined by MTT assay. Experiments were performed in triplicate and percentage of inhibition was calculated vs. untreated control. Statistical analysis was performed with ANOVA test followed by Dunnett's *post-hoc* test (*$p < 0.05$, **$p < 0.01$).

**Supplementary Figure 6 | *MAP1LC3B* expression in GBM1, GBM2, and GBM3 CSCs.** Cells were treated with GVS (1 μM) for 24, 48, and 72 h and assayed for *MAP1LC3B* mRNA levels by Real time qPCR. Results are given as relative mRNA expression, in arbitrary units of the ratio of the target RNA over *HPRT1* and *TBP* expression levels. Statistical analysis was performed with ANOVA test followed by Dunnett's *post-hoc* test. Bars represent the mean of three independent experiments ± SD (*$p < 0.05$; **$p < 0.01$).

**Supplementary Figure 7 | CompuSyn software evaluation of the synergistic effect of GVS in combination with bafilomycin-A1 in GBM CSCs.** Isobolograms of drug combination on GBM1, GBM2, and GBM3 CSC viability after treatment for 48 and 72 h, are represented. Combination index (CI) is represented by symbols above (indicate antagonism between drugs) or below the line (indicate synergy) and in the Table on the right.

**Supplementary Figure 8 | Effect of deprivation of growth factors on GVS activity in GBM CSCs.** GBM1 and GBM2 CSCs were maintained in the absence of growth factors for 60 h; after this period cells were treated with GVS (0.1, 0.25, 0.5, 1.0, and 2.0 μM) for further 48 h and viability was assessed by MTT assay. In parallel the same study was performed on GBM1 and GBM2 maintained in complete stem medium. Statistical analysis was performed with unpaired two-tailed *t*-test (*$p < 0.05$, **$p < 0.01$;***$p < 0.001$). To confirm that deprivation of growth factors really increases autophagy, immunoblotting analysis was performed on cell lysates. LC3-I, LC3-II, and p62 protein levels were assayed (right panels).

**Supplementary Table 1 | Main clinical-pathological features of tumors, and tumorigenic potential in mice of GBM-derived cell cultures enriched in CSCs.**

**Supplementary Table 2 | Inhibition percentage value and statistical significance of GVS antiproliferative effect on GBM CSCs.** Data were obtained from mean percentage of cell viability of treated cells vs. untreated control cells for each concentration and time point of GVS exposure. Statistical analysis was performed with ANOVA test followed by Dunnett's *post-hoc* test; *$p < 0.05$, **$p < 0.01$, ***$p < 0.001$ (NS, non-significant; blank boxes, not performed).

## REFERENCES


Al-Hajj, M., Becker, M. W., Wicha, M., Weissman, I., and Clarke, M. F. (2004). Therapeutic implications of cancer stem cells. *Curr. Opin. Genet. Dev.* 14, 43–47. doi: 10.1016/j.gde.2003.11.007

Armeanu, S., Pathil, A., Venturelli, S., Mascagni, P., Weiss, T. S., Gottlicher, M., et al. (2005). Apoptosis on hepatoma cells but not on primary hepatocytes by histone deacetylase inhibitors valproate and ITF2357. *J. Hepatol.* 42, 210–217. doi: 10.1016/j.jhep.2004.10.020

Bajetto, A., Porcile, C., Pattarozzi, A., Scotti, L., Aceto, A., Daga, A., et al. (2013). Differential role of EGF and BFGF in human GBM-TIC proliferation: relationship to EGFR-tyrosine kinase inhibitor sensibility. *J. Biol. Regul. Homeost. Agents* 27, 143–154.

Banelli, B., Carra, E., Barbieri, F., Wurth, R., Parodi, F., Pattarozzi, A., et al. (2015). The histone demethylase KDM5A is a key factor for the resistance to temozolomide in glioblastoma. *Cell Cycle* 14, 3418–3429. doi: 10.1080/15384101.2015.1090063

Bolden, J. E., Shi, W., Jankowski, K., Kan, C. Y., Cluse, L., Martin, B. P., et al. (2013). HDAC inhibitors induce tumor-cell-selective pro-apoptotic transcriptional responses. *Cell Death Dis.* 4:e519. doi: 10.1038/cddis.2013.9

Bonavia, R., Inda, M. M., Cavenee, W. K., and Furnari, F. B. (2011). Heterogeneity maintenance in glioblastoma: a social network. *Cancer Res.* 71, 4055–4060. doi: 10.1158/0008-5472.CAN-11-0153

Brennan, C. W., Verhaak, R. G., Mckenna, A., Campos, B., Noushmehr, H., Salama, S. R., et al. (2013). The somatic genomic landscape of glioblastoma. *Cell* 155, 462–477. doi: 10.1016/j.cell.2013.09.034

Carra, E., Barbieri, F., Marubbi, D., Pattarozzi, A., Favoni, R. E., Florio, T., et al. (2013). Sorafenib selectively depletes human glioblastoma tumor-initiating cells from primary cultures. *Cell Cycle* 12, 491–500. doi: 10.4161/cc.23372

Chen, J., Li, Y., Yu, T. S., Mckay, R. M., Burns, D. K., Kernie, S. G., et al. (2012). A restricted cell population propagates glioblastoma growth after chemotherapy. *Nature* 488, 522–526. doi: 10.1038/nature11287

Choi, A. M. K., Ryter, S. W., and Levine, B. (2013). Autophagy in human health and disease. *New Engl. J. Med.* 368, 651–662. doi: 10.1056/NEJMra1205406

Chou, T. C. (2010). Drug combination studies and their synergy quantification using the Chou-Talalay method. *Cancer Res.* 70, 440–446. doi: 10.1158/0008-5472.CAN-09-1947

Chou, T. C., and Talalay, P. (1984). Quantitative analysis of dose-effect relationships: the combined effects of multiple drugs or enzyme inhibitors. *Adv. Enzyme Regul.* 22, 27–55. doi: 10.1016/0065-2571(84)90007-4

Corsaro, A., Bajetto, A., Thellung, S., Begani, G., Villa, V., Nizzari, M., et al. (2016). Cellular prion protein controls stem cell-like properties of human glioblastoma tumor-initiating cells. *Oncotarget* 7, 38638–38657. doi: 10.18632/oncotarget.9575

Criollo, A., Chereau, F., Malik, S. A., Niso-Santano, M., Marino, G., Galluzzi, L., et al. (2012). Autophagy is required for the activation of NFκB. *Cell Cycle* 11, 194–199. doi: 10.4161/cc.11.1.18669

Del Bufalo, D., Desideri, M., De Luca, T., Di Martile, M., Gabellini, C., Monica, V., et al. (2014). Histone deacetylase inhibition synergistically enhances pemetrexed cytotoxicity through induction of apoptosis and autophagy in non-small cell lung cancer. *Mol. Cancer* 13:230. doi: 10.1186/1476-4598-13-230

De Souza, C., and Chatterji, B. P. (2015). HDAC inhibitors as novel anti-cancer therapeutics. *Recent Pat. Anticancer Drug Discov.* 10, 145–162. doi: 10.2174/1574892810666150317144511

Dominici, M., Le Blanc, K., Mueller, I., Slaper-Cortenbach, I., Marini, F. C., Krause, D. S., et al. (2006). Minimal criteria for defining multipotent mesenchymal stromal cells. The international society for cellular therapy position statement. *Cytotherapy* 8, 315–317. doi: 10.1080/14653240600855905

Fassina, L., Magenes, G., Inzaghi, A., Palumbo, S., Allavena, G., Miracco, C., et al. (2012). AUTOCOUNTER, an ImageJ JavaScript to analyze LC3B-GFP expression dynamics in autophagy-induced astrocytoma cells. *Eur. J. Histochem.* 56:e44. doi: 10.4081/ejh.2012.e44

Favoni, R. E., Pattarozzi, A., Lo Casto, M., Barbieri, F., Gatti, M., Paleari, L., et al. (2010). Gefitinib targets EGFR dimerization and ERK1/2 phosphorylation to inhibit pleural mesothelioma cell proliferation. *Curr. Cancer Drug Targets* 10, 176–191. doi: 10.2174/156800910791054130

Florio, T., and Barbieri, F. (2012). The status of the art of human malignant glioma management: the promising role of targeting tumor-initiating cells. *Drug Discov. Today* 17, 1103–1110. doi: 10.1016/j.drudis.2012.06.001

Galimberti, S., Canestraro, M., Savli, H., Palumbo, G. A., Tibullo, D., Nagy, B., et al. (2010). ITF2357 interferes with apoptosis and inflammatory pathways in the HL-60 model: a gene expression study. *Anticancer Res.* 30, 4525–4535.

Galluzzi, L., Pietrocola, F., Bravo-San Pedro, J. M., Amaravadi, R. K., Baehrecke, E. H., Cecconi, F., et al. (2015). Autophagy in malignant transformation and cancer progression. *EMBO J.* 34, 856–880. doi: 10.15252/embj.201490784

Gatti, M., Pattarozzi, A., Bajetto, A., Würth, R., Daga, A., Fiaschi, P., et al. (2013). Inhibition of CXCL12/CXCR4 autocrine/paracrine loop reduces viability of human glioblastoma stem-like cells affecting self-renewal activity. *Toxicology* 314, 209–220. doi: 10.1016/j.tox.2013.10.003

Golay, J., Cuppini, L., Leoni, F., Micò, C., Barbui, V., Domenghini, M., et al. (2007). The histone deacetylase inhibitor ITF2357 has anti-leukemic activity *in vitro* and *in vivo* and inhibits IL-6 and VEGF production by stromal cells. *Leukemia* 21, 1892–1900. doi: 10.1038/sj.leu.2404860

Griffero, F., Daga, A., Marubbi, D., Capra, M. C., Melotti, A., Pattarozzi, A., et al. (2009). Different response of human glioma tumor-initiating cells to epidermal growth factor receptor kinase inhibitors. *J. Biol. Chem.* 284, 7138–7148. doi: 10.1074/jbc.M807111200

Gritti, M., Würth, R., Angelini, M., Barbieri, F., Peretti, M., Pizzi, E., et al. (2014). Metformin repositioning as antitumoral agent: selective antiproliferative effects in human glioblastoma stem cells, via inhibition of CLIC1-mediated ion current. *Oncotarget* 5, 11252–11268. doi: 10.18632/oncotarget.2617

Haggarty, S. J., Koeller, K. M., Wong, J. C., Grozinger, C. M., and Schreiber, S. L. (2003). Domain-selective small-molecule inhibitor of histone deacetylase 6 (HDAC6)-mediated tubulin deacetylation. *Proc. Natl. Acad. Sci. U.S.A.* 100, 4389–4394. doi: 10.1073/pnas.0430973100

Kang, C., and Avery, L. (2008). To be or not to be, the level of autophagy is the question: dual roles of autophagy in the survival response to starvation. *Autophagy* 4, 82–84. doi: 10.4161/auto.5154

Klionsky, D. J., Abdelmohsen, K., Abe, A., Abedin, M. J., Abeliovich, H., Acevedo Arozena, A., et al. (2016). Guidelines for the use and interpretation of assays for monitoring autophagy (3rd edition). *Autophagy* 12, 1–222. doi: 10.1080/15548627.2015.1100356

Lee, J., Kotliarova, S., Kotliarov, Y., Li, A., Su, Q., Donin, N. M., et al. (2006). Tumor stem cells derived from glioblastomas cultured in bFGF and EGF more closely mirror the phenotype and genotype of primary tumors than do serum-cultured cell lines. *Cancer Cell* 9, 391–403. doi: 10.1016/j.ccr.2006.03.030

Lee, P., Murphy, B., Miller, R., Menon, V., Banik, N. L., Giglio, P., et al. (2015). Mechanisms and clinical significance of histone deacetylase inhibitors: epigenetic glioblastoma therapy. *Anticancer Res.* 35, 615–625.

Leoni, F., Fossati, G., Lewis, E. C., Lee, J. K., Porro, G., Pagani, P., et al. (2005). The histone deacetylase inhibitor ITF2357 reduces production of pro-inflammatory cytokines in vitro and systemic inflammation *in vivo*. *Mol. Med.* 11, 1–15. doi: 10.2119/2006-00005.Dinarello

Liu, Y. L., Yang, P. M., Shun, C. T., Wu, M. S., Weng, J. R., and Chen, C. C. (2010). Autophagy potentiates the anti-cancer effects of the histone deacetylase inhibitors in hepatocellular carcinoma. *Autophagy* 6, 1057–1065. doi: 10.4161/auto.6.8.13365

Macintosh, R. L., and Ryan, K. M. (2013). Autophagy in tumour cell death. *Semin. Cancer Biol.* 23, 344–351. doi: 10.1016/j.semcancer.2013.05.006

Marchesi, N., Osera, C., Fassina, L., Amadio, M., Angeletti, F., Morini, M., et al. (2014). Autophagy is modulated in human neuroblastoma cells through direct exposition to low frequency electromagnetic fields. *J. Cell. Physiol.* 229, 1776–1786. doi: 10.1002/jcp.24631

Massa, A., Barbieri, F., Aiello, C., Arena, S., Pattarozzi, A., Pirani, P., et al. (2004). The expression of the phosphotyrosine phosphatase DEP-1/PTPeta dictates the responsivity of glioma cells to somatostatin inhibition of cell proliferation. *J. Biol. Chem.* 279, 29004–29012. doi: 10.1074/jbc.M403573200

Mathew, R., Karp, C. M., Beaudoin, B., Vuong, N., Chen, G., Chen, H. Y., et al. (2009). Autophagy suppresses tumorigenesis through elimination of p62. *Cell* 137, 1062–1075. doi: 10.1016/j.cell.2009.03.048

Mathur, D. (2014). Selection of suitable housekeeping genes for expression analysis in glioblastoma using quantitative RT-PCR. *Ann. Neurosci.* 21, 62–63. doi: 10.5214/ans.0972.7531.210207

Mizushima, N., and Klionsky, D. J. (2007). Protein turnover via autophagy: implications for metabolism. *Annu. Rev. Nutr.* 27, 19–40. doi: 10.1146/annurev.nutr.27.061406.093749

Ohgaki, H., and Kleihues, P. (2013). The definition of primary and secondary glioblastoma. *Clin. Cancer Res.* 19, 764–772. doi: 10.1158/1078-0432.CCR-12-3002

Omuro, A., and Deangelis, L. M. (2013). Glioblastoma and other malignant gliomas: a clinical review. *JAMA* 310, 1842–1850. doi: 10.1001/jama.2013.280319

Palumbo, S., and Comincini, S. (2013). Autophagy and ionizing radiation in tumors: the "survive or not survive" dilemma. *J. Cell. Physiol.* 228, 1–8. doi: 10.1002/jcp.24118

Patel, A. P., Tirosh, I., Trombetta, J. J., Shalek, A. K., Gillespie, S. M., Wakimoto, H., et al. (2014). Single-cell RNA-seq highlights intratumoral heterogeneity in primary glioblastoma. *Science* 344, 1396–1401. doi: 10.1126/science.1254257

Pathil, A., Armeanu, S., Venturelli, S., Mascagni, P., Weiss, T. S., Gregor, M., et al. (2006). HDAC inhibitor treatment of hepatoma cells induces both TRAIL-independent apoptosis and restoration of sensitivity to TRAIL. *Hepatology* 43, 425–434. doi: 10.1002/hep.21054

Pattarozzi, A., Gatti, M., Barbieri, F., Würth, R., Porcile, C., Lunardi, G., et al. (2008). 17beta-estradiol promotes breast cancer cell proliferation-inducing stromal cell-derived factor-1-mediated epidermal growth factor receptor transactivation: reversal by gefitinib pretreatment. *Mol. Pharmacol.* 73, 191–202. doi: 10.1124/mol.107.039974

Pazolli, E., Alspach, E., Milczarek, A., Prior, J., Piwnica-Worms, D., and Stewart, S. A. (2012). Chromatin remodeling underlies the senescence-associated secretory phenotype of tumor stromal fibroblasts that supports cancer progression. *Cancer Res.* 72, 2251–2261. doi: 10.1158/0008-5472.CAN-11-3386

Peart, M. J., Smyth, G. K., van Laar, R. K., Bowtell, D. D., Richon, V. M., Marks, P. A., et al. (2005). Identification and functional significance of genes regulated by structurally different histone deacetylase inhibitors. *Proc. Natl. Acad. Sci. U.S.A.* 102, 3697–3702. doi: 10.1073/pnas.0500369102

Rabinowitz, J. D., and White, E. (2010). Autophagy and metabolism. *Science* 330, 1344–1348. doi: 10.1126/science.1193497

Rao, R., Balusu, R., Fiskus, W., Mudunuru, U., Venkannagari, S., Chauhan, L., et al. (2012). Combination of pan-histone deacetylase inhibitor and autophagy inhibitor exerts superior efficacy against triple-negative human breast cancer cells. *Mol. Cancer Ther.* 11, 973–983. doi: 10.1158/1535-7163.MCT-11-0979

Robert, T., Vanoli, F., Chiolo, I., Shubassi, G., Bernstein, K. A., Rothstein, R., et al. (2011). HDACs link the DNA damage response, processing of double-strand breaks and autophagy. *Nature* 471, 74–79. doi: 10.1038/nature09803

Saiki, S., Sasazawa, Y., Imamichi, Y., Kawajiri, S., Fujimaki, T., Tanida, I., et al. (2011). Caffeine induces apoptosis by enhancement of autophagy via PI3K/Akt/mTOR/p70S6K inhibition. *Autophagy* 7, 176–187. doi: 10.4161/auto.7.2.14074

Shchors, K., Massaras, A., and Hanahan, D. (2015). Dual targeting of the autophagic regulatory circuitry in gliomas with repurposed drugs elicits cell-lethal autophagy and therapeutic benefit. *Cancer Cell* 28, 456–471. doi: 10.1016/j.ccell.2015.08.012

Singh, S. K., Hawkins, C., Clarke, I. D., Squire, J. A., Bayani, J., Hide, T., et al. (2004). Identification of human brain tumour initiating cells. *Nature* 432, 396–401. doi: 10.1038/nature03128

Soeda, A., Inagaki, A., Oka, N., Ikegame, Y., Aoki, H., Yoshimura, S., et al. (2008). Epidermal growth factor plays a crucial role in mitogenic regulation of human brain tumor stem cells. *J. Biol. Chem.* 283, 10958–10966. doi: 10.1074/jbc.M704205200

Stupp, R., Mason, W. P., van Den Bent, M. J., Weller, M., Fisher, B., Taphoorn, M. J., et al. (2005). Radiotherapy plus concomitant and adjuvant temozolomide for glioblastoma. *N. Engl. J. Med.* 352, 987–996. doi: 10.1056/NEJMoa 043330

Thurn, K. T., Thomas, S., Moore, A., and Munster, P. N. (2011). Rational therapeutic combinations with histone deacetylase inhibitors for the treatment of cancer. *Future Oncol.* 7, 263–283. doi: 10.2217/fon.11.2

Ververis, K., and Karagiannis, T. C. (2012). Overview of the classical histone deacetylase enzymes and histone deacetylase inhibitors. *ISRN Cell Biol.* 2012:12. doi: 10.5402/2012/130360

Vescovi, A. L., Galli, R., and Reynolds, B. A. (2006). Brain tumour stem cells. *Nat. Rev. Cancer* 6, 425–436. doi: 10.1038/nrc1889

Villa, V., Thellung, S., Corsaro, A., Novelli, F., Tasso, B., Colucci-D'amato, L., et al. (2016). Celecoxib inhibits prion protein 90-231-mediated pro-inflammatory responses in microglial cells. *Mol. Neurobiol.* 53, 57–72. doi: 10.1007/s12035-014-8982-4

White, E. (2015). The role for autophagy in cancer. *J. Clin. Invest.* 125, 42–46. doi: 10.1172/JCI73941

White, E., Mehnert, J. M., and Chan, C. S. (2015). Autophagy, metabolism, and cancer. *Clin. Cancer Res.* 21, 5037–5046. doi: 10.1158/1078-0432.CCR-15-0490

Würth, R., Barbieri, F., and Florio, T. (2014). New molecules and old drugs as emerging approaches to selectively target human glioblastoma cancer stem cells. *Biomed Res. Int.* 2014:126586. doi: 10.1155/2014/126586

Würth, R., Barbieri, F., Pattarozzi, A., Gaudenzi, G., Gatto, F., Fiaschi, P., et al. (2016). Phenotypical and pharmacological characterization of stem-like cells in human pituitary adenomas. *Mol. Neurobiol.* doi: 10.1007/s12035-016-0025-x. [Epub ahead of print].

Würth, R., Pattarozzi, A., Gatti, M., Bajetto, A., Corsaro, A., Parodi, A., et al. (2013). Metformin selectively affects human glioblastoma tumor-initiating cell viability: a role for metformin-induced inhibition of Akt. *Cell Cycle* 12, 145–156. doi: 10.4161/cc.23050

Yamamoto, A., Tagawa, Y., Yoshimori, T., Moriyama, Y., Masaki, R., and Tashiro, Y. (1998). Bafilomycin A1 prevents maturation of autophagic vacuoles by inhibiting fusion between autophagosomes and lysosomes in rat hepatoma cell line, H-4-II-E cells. *Cell Struct. Funct.* 23, 33–42. doi: 10.1247/csf.23.33

Yuan, H., Li, A. J., Ma, S. L., Cui, L. J., Wu, B., Yin, L., et al. (2014). Inhibition of autophagy signi fi cantly enhances combination therapy with sorafenib and HDAC inhibitors for human hepatoma cells. *World J. Gastroenterol.* 20, 4953–4962. doi: 10.3748/wjg.v20.i17.4953

Zhang, J., and Zhong, Q. (2014). Histone deacetylase inhibitors and cell death. *Cell. Mol. Life Sci.* 71, 3885–3901. doi: 10.1007/s00018-014-1656-6

**Conflict of Interest Statement:** GF is an employee of Italfarmaco S.p.A.

The other authors declare that the research was conducted in the absence of any commercial or financial relationships that could be construed as a potential conflict of interest.

# Chapter 21

# Visualizing RNA at Electron Microscopy by Terbium Citrate

**Marco Biggiogera and Irene Masiello**

## Abstract

Although the EDTA regressive technique allows the visualization of RNPs, this widely used method is not intended to be specific for RNA alone. A fine ultrastructural visualization of RNA on ultrathin sections can be obtained with terbium citrate: this method gives a weak contrast but a very fine end product which allows observations at a high resolution level.

The procedure is very simple since it consists only of a period of incubation and very short washes, which are the crucial point of this technique to avoid the Tb removal from RNA. This method does not require any special type of fixation and embedding.

**Key words** RNA staining, Terbium citrate, Cytochemistry, Electron microscopy, EDTA regressive stain, Lanthanides

## 1 Introduction

Selective RNA staining at electron microscopy (EM) has been pursued for a long time in the absence of a specific method: while for DNA a Feulgen-type reaction existed as a selective and reliable cytochemical procedure, no specific and selective procedure was present for RNA, not even at light microscopy level.

The most commonly used approach was the EDTA regressive staining for ribonucleoproteins [1] which, as clearly stated by the author, was never intended for RNA alone. Some techniques were proposed for the detection of both RNA and DNA [2–4]. By applying these methods after the enzymatic removal of DNA, it was possible to recognize only RNA on thin sections. In other papers, RNA was detected by RNase–gold complexes [5], anti-RNA antibodies or after the incorporation of labeled RNA precursors. Platinum quinolone was proposed [6] but this approach has shown several limitations.

The basic reason for this problem in revealing RNA lies in the absence of any chemical group characteristic of RNA: the hydroxyl group of the sugar in the DNA structure makes the difference for

Carlo Pellicciari and Marco Biggiogera (eds.), *Histochemistry of Single Molecules: Methods and Protocols*, Methods in Molecular Biology, vol. 1560, DOI 10.1007/978-1-4939-6788-9_21, 

the reactivity toward hydrolysis while for RNA no such specific markers are present.

Since data in literature described that lanthanide elements interact with guanine sites at single-stranded nucleic acids [7, 8], a series of experiments was carried out with lanthanides, a family of strictly correlated chemical elements called rare earths. In trying to find a reliable method for RNA, we have examined 134 different procedures to bind an electron dense element as a marker of RNA. Many of these elements were found to be useful in staining RNA (terbium, ytterbium, europium, lutetium) but the most useful for electron microscopy proved to be terbium (Tb): its chloride or nitrate form almost does not give rise to staining. For this reason we applied a substitution reaction [9], as in the case of lead citrate [10].

Terbium is capable of binding the RNA guanosine [7] with an efficiency of about 16,000 fold with respect to DNA guanosine [11]. The binding occurs usually within 30–60 min and reaches saturation: therefore, overnight staining does not improve contrast (unpublished results) and overstaining or unspecific staining is avoided. On the other hand, pH proved to be critical: application at pH below 7.5 does not result in staining. This staining method can be applied on acrylic and epoxy sections, although with two different procedures, and it is not dependent on the type of fixation (except for osmium); it can be used after embedding, immunocytochemistry and EM in situ hybridization (EMISH).

This technique shows a weak contrast, even if the stained structures appear more contrasted after a few minutes of eye adaptation but the staining is very fine allowing studies at high resolution. With this approach perichromatin fibrils (PFs), perichromatin granules (PGs), interchromatin granules (IGs) and the nucleolus are contrasted in the nucleus while in the cytoplasm only ribosomes are stained. Actually, it is possible to see single RNA molecules within PGs and ribosomes.

As control, enzymatic digestions are carried out: DNase or pronase do not modify the staining, confirming that DNA and proteins do not interfere with the result; RNase and Nuclease S1 digestions prevent the formation of an electron-dense product, indicating that the staining depends on single strand RNA [9].

## 2 Materials

### 2.1 Sample Preparation

All kind of cells or tissues can be processed for EM to reveal specifically RNA through Tb-staining.

#### 2.1.1 Reagents

1. 67 mM Sörensen buffer pH 7.4: dissolve 11.88 g $Na_2HPO_4$-$2H_2O$ in 1 L of distilled water (Solution A); dissolve 9.08 g of $KH_2PO_4$ in 1 L of distilled water (Solution B); mix 81.8 mL of Solution A and 18.2 mL of Solution B.

2. 4% paraformaldehyde in Sörensen buffer pH 7.4; store at 4 °C for 1–2 months (*see* **Note 1**).
3. 2.5% glutaraldehyde in Sörensen buffer pH 7.4; store at 4 °C for 1–2 months (*see* **Note 1**).
4. 2% agar (necessary for pre-embedding isolated cells): dissolve 1 g of agarose in 50 mL of warm distilled water and store at 4 °C.
5. Graded ethanol or acetone in distilled water: 30%, 50%, 70%, 90% and absolute ethanol or acetone; store at room temperature.
6. LRWhite resin: the activation of LRWhite resin is obtained by adding 9.9 g of benzoyl peroxide in 500 mL of resin under gentle agitation by magnetic stirrer (*see* **Note 2**); store at 4 °C.
7. EMbed-812 resin: mix under gentle agitation by magnetic stirrer (*see* **Note 2**) 20 g of EMbed-812, 16 g of dodecenyl succinic anhydride and 8 g of nadic methyl anhydride and finally add 1.2 mL of benzyl-dimethylamine under a fume hood; let the reagent mix for at least 30 min (*see* **Note 2**) and store it at −20 °C (thaw the resin for at least 20 min before use).

### 2.2 Preparation of Terbium Citrate

1. Freshly double-distilled or ultrapure water.
2. 1 N sodium hydroxide: dissolve 4 g of NaOH in 100 mL of distilled water.
3. 0.2 M terbium (III) nitrate: dissolve 435 mg of terbium (III) nitrate in 5 mL of double-distilled or ultrapure water.
4. 0.5 M sodium citrate buffer (for epoxy sections): dissolve 735 mg of trisodium citrate dihydrated in 5 mL of double-distilled or ultrapure water; adjust the pH to 12 with 1 N NaOH.
5. 0.2 M sodium citrate buffer: dissolve 294 mg of trisodium citrate dihydrated in 5 mL of double-distilled or ultrapure water.
6. Terbium citrate: stirring continuously, 0.2 M terbium nitrate must be added dropwise to the 0.2 M sodium citrate—a white precipitate is formed. The precipitate tends to dissolve at the beginning and afterwards forms coarse precipitates and flocculates. Add then 1 N NaOH dropwise while gently stirring until the precipitates dissolve completely (around pH 6.7–7.0): the solution must become transparent. Finally, adjust the pH to 8.2–8.5 with 1 N NaOH. Control the pH after 24 h to readjust it if necessary (*see* **Note 3**). Store the solution in a syringe fitted with a filter (see below): it is stable for several weeks at room temperature.

## 3 Equipment

1. 0.22 μm pore filter.
2. Plastic syringe and pipettes.
3. Thin sections obtained using an ultramicrotome.
4. 200 mesh gold, copper or nickel grids to collect the thin sections.
5. Parafilm sheet to be used as a support for the staining procedure.
6. Filter paper to dry the grids where indicated.
7. Transmission electron microscope to observe the stained sections.

## 4 Methods

### 4.1 Sample Processing

The samples can be fixed either with 4% paraformaldehyde in Sörensen buffer for 2 h at 4 °C or in 2.5% glutaraldehyde in Sörensen buffer for 2 h at room temperature. After the removal of fixative with a pipette, the specimens are rinsed thoroughly with Sörensen buffer first and then with PBS.

Pre-embedding in 2% agar in $H_2O$ is only necessary when working with cells in suspension. Dehydration in graded ethanol or acetone follows and the samples are respectively embedded either in LRWhite or Epon resin.

Thin sections are collected on nickel, copper or gold grids (*see* **Note 4**).

### 4.2 Staining Procedure

#### 4.2.1 For Epoxy Sections

1. Place a 30 μL drop of 0.5 M sodium citrate pH 12 on the Parafilm sheet.
2. Float the grid (sections facing down) on the drop of sodium citrate for 1 h at room temperature (*see* **Note 5**).
3. Remove the excess of solution by blotting quickly the grid with a filter paper: do not allow to dry.
4. Put a 50 μL drop of terbium citrate on the support.
5. Incubate the specimen (sections facing down) for 1 h at room temperature on terbium citrate for the staining. In the meantime, prepare two large drops of distilled water (100–150 μL). Do not dry the grid with filter paper, so move the sample on the first drop of water for 30 s and then on the other for 15 s without blotting the grid between the two steps (*see* **Note 6**).
6. Dry the grid (*see* **Note 7**).
7. Observe the stained sections with an electron microscope operating at 80 kV (*see* **Note 8**).

#### 4.2.2 For Acrylic Sections

1. Put a 50 μL drop of terbium citrate on the support.
2. Stain the specimen with terbium citrate for 30 min at room temperature (sections facing down).
3. In the meantime, prepare two drops of 100–150 μL of distilled water.
4. Without blotting the grid after terbium staining, rinse it on the first drop for 10 s and on the other for 5—do not blot the grid between two washes (*see* **Note 6**).
5. Dry the grid (*see* **Note 7**).
6. Observe the stained sections with an electron microscope operating at 80 kV (*see* Fig. 1) (*see* **Note 8**).

## 5 Notes

1. Check the possible presence of precipitates in the fixative solutions: in this case, discard and prepare a fresh fixative.
2. Avoid the formation of bubbles in the resin mixture since they may remain during resin polymerization not allowing the preparation of good sections.
3. At pH lower than 8.0, precipitates are formed within 2–3 days. Therefore, it is very important to check the pH after 24 h and the possible presence of precipitates before the use. The use of a syringe fitted with a filter can help to remove particles.
4. LRWhite sections have a higher inherent contrast, even if Epon sections give good staining results since chromatin is devoid of contrast. The staining can be performed on nickel, copper or gold grids, equally. It is recommended to use thinner sections (with silver-to-grey interference color) without formvar support which can decrease the contrast. An amorphous carbon-film is advisable. The idea is to ameliorate the signal-to-noise ratio in order to enhance contrast since Tb staining is a very low contrast technique. Marinozzi rings are generally not used for this cytochemical staining.
5. Treatment with alkaline sodium citrate is necessary to avoid the overnight incubation in terbium citrate using epoxy sections.
6. The critical step of this procedure is rinsing: the Tb-RNA bond is weak and a long rinsing will remove the staining. For the same reason, it is recommended not to blot the grid after terbium staining or during the short washes to avoid Tb removal from RNA. It was tested that an improvement in the retention of staining can be achieved adjusting the water pH to 9–10 using 0.1 N NaOH: in these conditions, the staining appears to be more stable and contrasted (unpublished data).

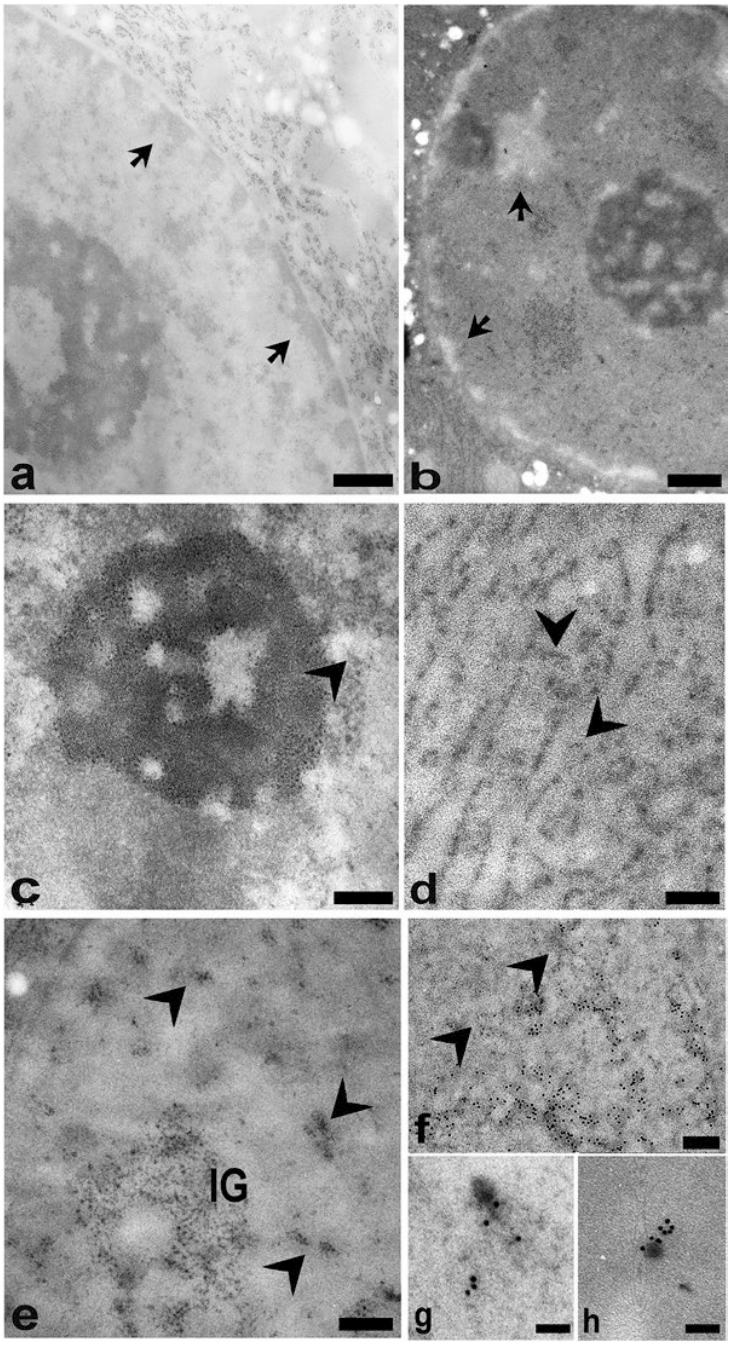


**Fig. 1** RNA staining. Panel (**a**) rat liver, glutaraldehyde fixation, LR White embedding. The nucleolus and ribosomes are stained while the peripheral condensed chromatin (*arrows*) exhibits only inherent contrast. Bar = 500 nm. (**b**) as in (**a**) but Epon embedding. Note the unstained chromatin areas (arrows). Bar = 500 nm. (**c**) a nucleolus with an evident granular component. Bar = 250 nm. (**d**) ribosomes with single RNA molecules interspersed (*arrowheads*). Bar = 250 nm. (**e**) a cluster of interchromatin granules (IGs) and perichromatin fibrils (*arrowheads*). Bar = 250 nm. (**f**) anti-DNA immunolabelling followed by Tb staining. Note the perichromatin fibrils (*arrowheads*) emerging from labeled DNA areas. Bar = 250 nm. (**g**, **h**) *Chironomus thummy* salivary glands; Balbiani ring granules with the tail labeled by a poly d(T) probe. Bar = 100 nm

7. A post staining with lead citrate for 5 s can increase the contrast but it determines a complete loss of specificity.
8. During the direct observation, the unstained chromatin areas (which are white) help the localization of the cells. In TEM equipped with a digital image capture system the contrast enhancement will help in localizing the stained molecules. Although the contrast is weak, the negatives and printed micrographs are satisfactory. Grids stained with Tb do not fade. To our experience, sections stained under these conditions can still be observed after 10–15 years.

## Acknowledgments

The authors are grateful to Ms. Francine Flach and Prof. Stan Fakan. Part of this work has been carried out at the CME, University of Lausanne, Switzerland.

This chapter is dedicated to the memory of Vàclav Kopečný and Jean-Luc Courtens.

### References

1. Bernhard M (1969) A new staining procedure for electron microscopical cytology. J Ultrastruct Res 27:250–265
2. Chan-Curtis V, Belt VD, Ladoulis CT (1970) Cytochemical localization of nucleic acids by acriflavine-phosphotungstate complex for fluorescence microscopy and electron microscopy. J Histochem Cytochem 18:609–627
3. Biggiogera M, Flach Biggiogera F (1989) Ethidium bromide- and propidium iodine-PTA staining of nucleic acids at electron microscopic level. J Histochem Cytochem 37: 1161–1166
4. Derenzini M, Farabegoli F (1990) Selective staining of nucleic acids by osmium ammine complex in thin sections from Lowicryl-embedded samples. J Histochem Cytochem 28:1495–1501
5. Bendayan M (1982) Ultrastructural localization of nucleic acids by the use of enzyme-gold complexes: influence of fixation and embedding. Bio Cell 43:153–156
6. Scott JE (1973) Affinity, competition and specific interactions in the biochemistry and histochemistry of polyelectrolytes. Biochem Soc Trans 1:787–806
7. Ringer DP, Burchett S, Kizer DP (1978) Use of terbium fluorescence enhancement to selectively monitor DNA and RNA guanine residues and their alteration by chemical modification. Biochemistry 17:4818–4825
8. Hörer OL, Zaharia CN, Marcu A (1977) Terbium fluorescence in aqueous solutions of nucleic acids. Rev Roum Biochim 14:175–179
9. Biggiogera M, Fakan S (1998) Fine structural specific visualization of RNA on ultrathin sections. J Histochem Cytochem 46:389–395
10. Reynolds ES (1963) The use of lead citrate at high pH as an electron-opaque stain in electron microscopy. J Cell Biol 17:208–212
11. Ringer DP, Howell BA, Kizer DE (1980) Use of terbium fluorescence enhancement as a new probe for assessing the single-strand content of DNA. Anal Biochem 103:337–342

# Chapter 19

# Osmium Ammine for Staining DNA in Electron Microscopy

**Irene Masiello and Marco Biggiogera**

## Abstract

The osmium ammine staining allows the specific detection of DNA in the cell nucleus and represents one of the most used techniques for EM cytochemistry.

The procedure is a Feulgen-type reaction, consisting of an acid hydrolysis to obtain free aldehyde groups on DNA followed by their binding to osmium ammine, a Schiff-type reagent. Osmium ammine is polyamminic electron-dense compound commercially available.

Here, we describe the staining procedure for ultrathin sections and the different procedures for the preparation of the reagent for acrylic and epoxy sections.

**Key words** DNA staining, Osmium ammine, Cytochemistry, Feulgen reaction, Schiff reagent, Electron microscopy

## 1 Introduction

The greatest achievement of Alain Gautier, a pioneer in electron microscopy (EM), is the translation of the Feulgen reaction to EM level. Basically, the reaction described by Robert Feulgen in 1924 for light microscopy consists of two steps: first, an acid hydrolysis leading to removal of purine bases from the deoxyribose, engendering aldehyde groups; second, the reaction of free aldehyde groups with the Schiff reagent resulting in specifically stained DNA. The Schiff reagent must be activated by $SO_2$ [1] and have at least one amino group which can bind the aldehydic one giving a specific stain. Osmium ammine (OA) has been used as a Schiff-type reagent for the specific DNA staining in ultrathin sections since it fulfills the described requirements and, importantly, it is an electron dense compound which can be revealed at EM [2, 3]. Moreover, OA was proved to be specific and with high resolution [4, 5].

However, the preparation technique led to an almost 50% failure rate. In 1989, Olins and coworkers synthesized a different reagent, called Osmium Ammine-B, in a much simpler and reproducible way [6]. The reagent is now commercially available and the

Carlo Pellicciari and Marco Biggiogera (eds.), *Histochemistry of Single Molecules: Methods and Protocols*, Methods in Molecular Biology, vol. 1560, DOI 10.1007/978-1-4939-6788-9_19, © Springer Science+Business Media LLC 2017

results are reproducible. Finally, a useful modification for preparing the active reagent has been proposed by Vázquez-Nin and collaborators [7]. The purpose of the latter paper was to avoid the use of bubbling $SO_2$ (potentially dangerous) through the addition of $SO_2$-generating chemicals, as it is done for light microscopy. The preparation method is not expensive, safe, simple and reproducible, giving the same results of the original technique.

Some controls can be performed to test the efficiency of this staining method for EM cytochemistry both on acrylic sections and epoxy ones: after the removal of DNA by DNase treatment prior to HCl, no structures are stained by OA; treatment with dimedone in 1 % acetic acid (1 h at 37 °C) after HCl and before OA suppresses DNA staining by specifically blocking aldehyde groups [8].

After OA treatment of acrylic sections in the absence of HCl hydrolysis DNA as well as RNA can be stained: this process involves the binding of OA to the negative charges of nucleic acids and it is related to the low pH of the staining solution [9]. Nevertheless, this staining cannot be carried out on Epon sections. Interestingly, a variation of the Feulgen reaction involving pyrimidines allows the staining of DNA (unpublished data): the removal of pyrimidines from DNA is obtained by incubating the samples with 1 N NaOH; the Feulgen-type reagent binds the apypirimidinic sites staining selectively DNA, as for the normal reaction.

The procedure described here provides two different protocols for the preparation of the reagent using acrylic sections or epoxy ones.

## 2 Materials

### 2.1 Sample Preparation

Any kind of cells or tissues can be processed for EM to reveal specifically DNA through OA-staining.

#### 2.1.1 Reagents

1. 67 mM Sörensen buffer pH 7.4: dissolve 11.88 g $Na_2HPO_4$-$2H_2O$ in 1 L of distilled water (Solution A); dissolve 9.08 g of $KH_2PO_4$ in 1 L of distilled water (Solution B); mix 81.8 mL of Solution A and 18.2 mL of Solution B.
2. 4 % paraformaldehyde in Sörensen buffer pH 7.4; store at 4 °C for 1–2 months (*see* **Note 1**).
3. 2.5 % glutaraldehyde in Sörensen buffer pH 7.4; store at 4 °C for 1–2 months (*see* **Note 1**).
4. 2 % agar (necessary for pre-embedding isolated cells): dissolve 1 g of agarose in 50 mL of warm distilled water and store at 4 °C.
5. Graded ethanol or acetone in distilled water: 30 %, 50 %, 70 %, 90 % and absolute ethanol or acetone; store at room temperature.

6. LRWhite resin: the activation of LRWhite resin is obtained by adding 9.9 g of benzoyl peroxide in 500 mL of resin under gentle agitation by magnetic stirrer; store at 4 °C.
7. EMbed-812 resin: mix under gentle agitation by magnetic stirrer 20 g of EMbed-812, 16 g of dodecenyl succinic anhydride and 8 g of nadic methyl anhydride and finally add 1.2 mL of benzyl-dimethylamine under a fume hood; let the reagent mix for at least 30 min (*see* **Note 2**) and store it at −20 °C (thaw the resin for at least 20 min before use).

### 2.2 Preparation of the Schiff-Type Reagent, Osmium Ammine-B

It is necessary to always prepare a fresh solution of OA (*see* **Note 3**).

1. *For acrylic sections*: dissolve 10 mg of osmium ammine-B (*see* **Note 4**) in 4.8 mL of double distilled water. After the reagent has completely dissolved (*see* **Note 3**), add 200 μL of 5 N HCl (final concentration 0.2 N) and mix the solution; add 190 mg of sodium metabisulfite (final concentration 0.2 N) and stir. The reagent is ready for use 30 min after dissolving the sodium metabisulfite.
2. *For Epoxy sections*: dissolve 10 mg of osmium ammine-B (*see* **Note 4**) in 2.5 mL of double distilled water. After the reagent has completely dissolved (*see* **Note 3**), add 2.5 mL of glacial acetic acid (final concentration 8 N) and mix; then add 38 mg of sodium metabisulfite (final concentration 40 mM) and stir. The solution is ready for use 30 min after dissolving the sodium metabisulfite. Freshly prepared 5 N HCl (*see* **Note 5**) and fresh distilled water are necessary.

### 2.3 Equipment

1. 5 N HCl: dilute 42 mL of 12 N HCl in 58 mL of distilled water under a fume hood.
2. 200 mesh gold grids or Marinozzi rings to place thin sections.
3. Thin sections obtained using an ultramicrotome.
4. Embryo dishes for the staining procedure.
5. Filter paper to dry the grids during the procedure.

## 3 Methods

### 3.1 Sample Processing

1. The samples can be fixed either in 4% paraformaldehyde in Sörensen buffer for 2 h at 4 °C or in 2.5% glutaraldehyde in Sörensen buffer for 2 h at room temperature (*see* **Note 6**). After the removal of fixative with a pipette, the specimens are rinsed thoroughly with Sörensen buffer first and then with PBS.
2. Pre-embedding in 2% agar in $H_2O$ is only necessary when working with cells in suspension. Dehydration in graded ethanol or acetone follows. Finally, the samples are embedded either in LRWhite or Epon resin.

3. Thin sections of 70–80 nm are collected on naked gold grids (*see* **Note 7**). Alternately, the sections can be floated onto the different solutions within Marinozzi rings and, after the final rinsing, put on a formvar-coated grid which in this case can be made of nickel or copper.

### 3.2 OA-Staining of Sections

Carry out all passages at room temperature. The procedure is the same using acrylic or epoxy sections.

1. Fill an embryo dish with 5 N HCl and float the grid, sections facing down, on the solution for 30–45 min (*see* **Note 8**) to allow the formation of free aldehyde groups (*see* **Note 9**).
2. Blot with a filter paper.
3. After filling an embryo dish with distilled water, rinse the specimen pipetting 5–10 times.
4. Rinse the sample three times for 2 min (*see* **Note 10**).
5. Blot with a filter paper.
6. Fill up an embryo dish with the solution of osmium ammine-B and incubate the sample in the reagent solution for 1 h to stain DNA (*see* **Note 11**) under the fume hood, since $SO_2$ fumes are released.
7. Dry quickly with a filter paper.
8. After filling an embryo dish with distilled water, rinse the specimen thoroughly by pipetting (10–15 times). Wash the sample three times for 5 min. Finally, let the specimen float on distilled water at least for 20 min: pipetting is recommended using a Pasteur (*see* **Note 12**).
9. Dry the sections with a filter paper.
10. Examine the stained grids with an electron microscope operating at 80 kV (Fig. 1).

The stain can penetrate through the entire section [9], thus staining all the DNA embedded in its thickness (*see* **Note 13**).

## 4 Notes

1. Check for possible presence of precipitates in the fixative solutions: if any, discard and prepare a fresh fixative.
2. Avoid the formation of bubbles in the Epon mixture since they may remain during resin polymerization not allowing the preparation of good sections.
3. The complete dissolution of osmium ammine-B avoids the formation of its precipitates, which prevents the correct visualization of the samples. For the same reason, freshly prepared reagent solution is suggested.

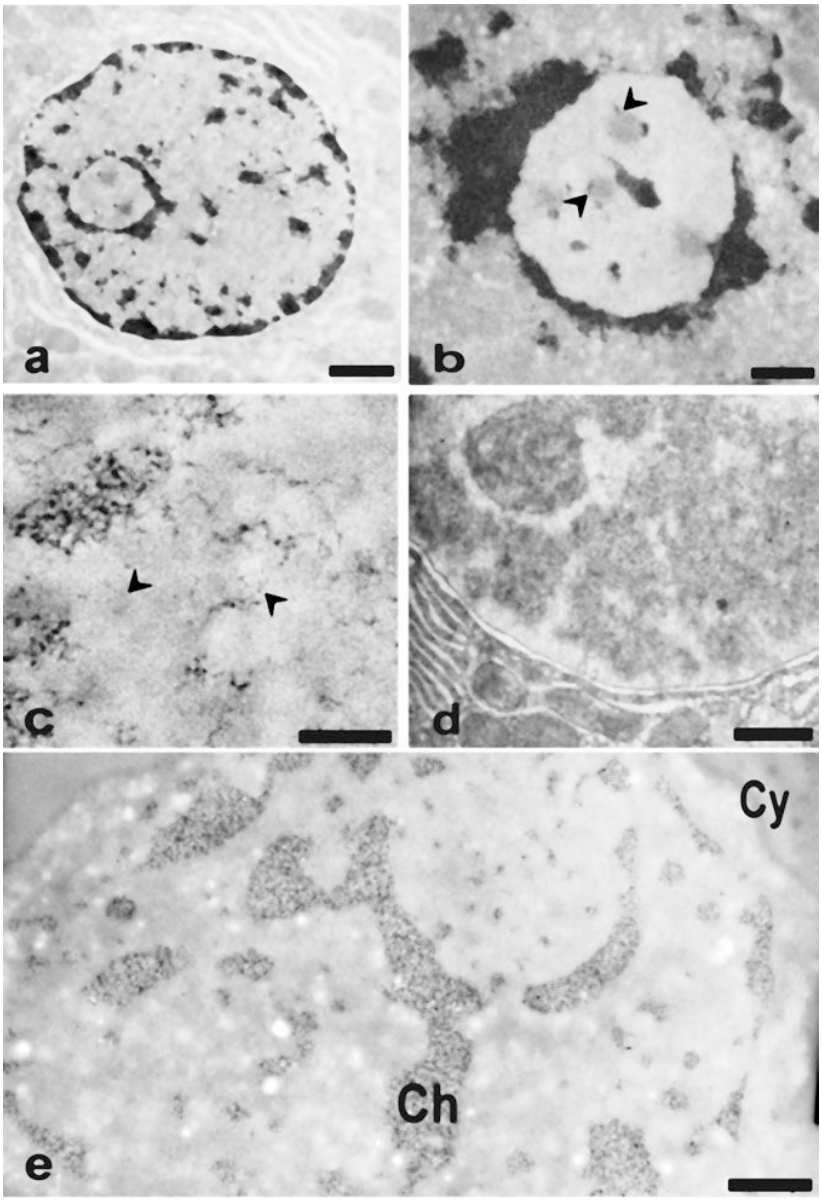


**Fig. 1** DNA staining. (**a**) Rat liver, PFA fixation, LR White embedding. 5 N HCl for 30 min, OA for 60 min. (**b**) Rat liver, PFA fixation, Epon embedding. Staining as in (**a**). Note the thin DNA fibers inside the nucleolus which looks electron lucent due to loss of proteins after hydrolysis. (**c**) HeLa cell, LR White embedding. At the periphery of the condensed chromatin extremely thin fibers are visible. (**d**) Rat liver. Dimedone blockade of aldehyde groups after 5 N HCl. The treatment with OA does not result in staining of DNA. (**e**) Mouse P815 cell, high pressure freezing, cryosubstitution in Lowycryl K11M. Immunolabeling for histone H2B followed by 1N HCl for 10 min and OA for 30 min. Bar in **a**, **b**, **d**, **e** = 1 μm. Bar in **c** = 500 nm

4. Since osmium ammine is an organometallic compound, it can interact electrostatically with the walls of recipient used for weighing. Therefore, it is recommended to use glass or paper to avoid electrostatic interactions (which are enhanced by plastic tubes).
5. Since HCl is gaseous, its leakage from the solution during the storage is possible changing the final concentration. Therefore, fresh HCl is recommended to allow the activation of osmium ammine-B and the correct removal of purine from DNA.
6. PFA fixation is suggested: in fact, glutaraldehyde should be avoided due to the high risk of free aldehyde groups. If necessary, after glutaraldehyde fixation an incubation with 0.5 M $NH_4Cl$ in PBS for 30 min will block the free aldehyde groups which will give rise to false positive staining (several washes with $H_2O$ are necessary). It is possible to perform the blocking reaction also after paraformaldehyde fixation.
7. The formvar–carbon coat as well as nickel grids are degraded by acid hydrolysis. Moreover, golden-plated grids increase the possibility of section detachment during the procedure.
8. The incubation time in HCl is dependent on the thickness of the sections and on the biological material involved. Usually, within the proposed range (30–45 min) there is little risk of damaging the section by excessive depolymerization of DNA.
9. When staining sections of isolated nuclei or high pressure frozen, cryosubstituted material with no chemical fixation, care must be taken for the hydrolysis step, eventually adjusting both the concentration and time: 5 N can be reduced to 1 N and 30 min can be reduced to 10–15 min.
10. Results do not change by increasing the time of rinses or their pH.
11. For acrylic sections DNA is stained also in 15–30 min. This staining method reaches saturation so the result does not change increasing the time of incubation in OA.
12. By rinsing thoroughly and pipetting, one can remove possible precipitates of OA given the tendency of this compound to precipitate after the staining.
13. While the sections stained with the classical OA [3] are stable and visible after years (at least 30), the sections treated with the commercial reagent lack stability and the stain goes to the surface of the section in form of roundish precipitates after at least 1 year. Epoxy sections appear more contrasted by osmium ammine-B than by the reagent solution prepared according to the original recipe while on acrylic sections both staining methods give the same results.

## Acknowledgments

The authors would like to thank Ms. Francine Flach for excellent technical skill in preparing the ultrathin sections.

### References

1. Kasten FH (1960) The chemistry of Schiff's reagent. Int Rev Cytol 10:1–100
2. Cogliati R, Gautier A (1973) Demonstration of DNA and polysaccharides using a new Schiff-type reagent. C R Acad Sci 276:3041–3044
3. Gautier A (1976) Ultrastructural localization of DNA in ultrathin tissue sections. Int Rev Cytol 44:113–191
4. Derenzini M, Hernandez-Verdun D, Bouteille M (1982) Visualization in situ of extended DNA filaments in nucleolar chromatin of rat hepatocytes. Exp Cell Res 141(2):463–469
5. Biggiogera M, Courtens JL, Derenzini M et al (1996) Osmium ammine: review of current applications to visualize DNA in electron microscopy. Biol Cell 87:121–132
6. Olins AL, Moyer BA, Kim SH et al (1989) Synthesis of a more stable osmium ammine electron dense stain. J Histochem Cytochem 37: 395–398
7. Vázquez-Nin GH, Biggiogera M, Echeverrìa OM (1995) Activation of osmium ammine by $SO_2$-generating chemicals for EM Feulgen-type staining of DNA. Eur J Histochem 39:101–106
8. Pickett-Heaps JD (1967) Preliminary attempts at ultrastructural polysaccharide localization in root tip cells. J Histochem Cytochem 15: 442–455
9. Derenzini M, Farabegoli F (1990) Selective staining of nucleic acids by osmium ammine complex in thin sections from Lowicryl-embedded samples. J Histochem Cytochem 28:1495–1501

Cell. Mol. Life Sci.
DOI 10.1007/s00018-017-2521-1

Cellular and Molecular Life Sciences

ORIGINAL ARTICLE

# Ultrastructural localization of 5-methylcytosine on DNA and RNA

**Irene Masiello[1] · Marco Biggiogera[1]**

Received: 12 January 2017 / Revised: 9 March 2017 / Accepted: 4 April 2017


**Abstract** DNA methylation is the major epigenetic modification and it is involved in the negative regulation of gene expression. Its alteration can lead to neoplastic transformation. Several biomolecular approaches are nowadays used to study this modification on DNA, but also on RNA molecules, which are known to play a role in different biological processes. RNA methylation is one of the most common RNA modifications and 5-methylcytosine presence has recently been suggested in mRNA. However, an analysis of nucleic acid methylation at electron microscope is still lacking. Therefore, we visualized DNA methylation status and RNA methylation sites in the interphase nucleus of HeLa cells and rat hepatocytes by ultrastructural immunocytochemistry and cytochemical staining. This approach represents an efficient alternative to study nucleic acid methylation. In particular, this ultrastructural method makes the visualization of this epigenetic modification on a single RNA molecule possible, thus overcoming the technical limitations for a (pre-)mRNA methylation analysis.

**Keywords** 5mC · mRNA methylation · Methylation gradient · Epigenetics · EM immunolabelling · Electron microscopy

✉ Marco Biggiogera
marco.biggiogera@unipv.it

[1] Laboratory of Cell Biology and Neurobiology, Department of Biology and Biotechnology, University of Pavia, Via Ferrata 9, 27100 Pavia, Italy

## Introduction

In eukaryotes DNA methylation is the major epigenetic modification. It is mediated by DNA-methyltransferases (DNMTs) at position 5 of cytosine followed by guanosine (CpG island) and induces transcriptional gene silencing. This modification is involved in regulation of gene expression, X-chromosome inactivation, genomic imprinting and chromosome stability [1, 2]. It also plays an essential role in mammalian embryonic development [3]. Alterations of DNA methylation are known to occur in several diseases [2], especially in cancer [4].

Different methods have been developed for the discrimination of CpG methylation status [5]. Current approaches can be essentially divided in separation techniques [6] and restriction endonuclease-based [7] or bisulfite conversion-based methods [8]. Moreover, DNA microarray technology [9–11] and sequencing-based approaches [12, 13] allow to obtain a complete epigenetic profile. Global DNA methylation levels can also be detected at fluorescence microscopy [14, 15]. Recently, methylation-specific fluorescence in situ hybridization (MeFISH) was developed for the visualization of DNA methylation at specific sequences [16]. Although an electron microscope (EM) determination of DNA methylation was carried out on plant programmed cell death (PCD) process [17], an EM analysis of DNA methylation dynamics and distribution is still lacking.

Several methods for DNA methylation analysis have been adapted to detect modified nucleotides on RNAs [18] and, to our knowledge, no data are available at EM about RNA methylation. The role of RNAs as important factors in different biological processes has become even clearer [19]. About 100 post-transcriptional modifications were found [20] among which RNA methylation is one of

Published online: 08 April 2017

the most commonly, occurring in different types of RNAs [21]. In particular, 5-methylcytosine (5mC) is widely studied: placed in the variable region and in the anticodon loop, it stabilizes tRNA secondary structure affecting $Mg^{2+}$ binding and is involved in codon recognition [22]; in rRNA it seems to be implicated in tRNA identification and peptidyl-transferase activity [23]. 5mC has only been recently suggested to be localized in the untranslated regions of mRNA [22]. Its function is still unknown: due to the proximity of mRNA methylation sites to the binding ones of Argonaute protein (the central component of miRNA/RISC complex), mRNA 5mC could be involved in miRNA degradation pathway [24] but there is no evidence about methylation involvement in mRNA stability [22].

Here, we propose an analysis of nucleic acid methylation at transmission electron microscope (TEM) to visualize DNA methylation status and RNA methylation sites in cell interphase nuclei at the ultrastructural level. This study has been carried out on different tissue and cell models. Particularly, in liver samples the peripheral condensed chromatin regions are generally evident allowing to better analyse DNA 5mC distribution. For the analysis of RNA methylation, proliferating HeLa cells were also chosen for their high transcription level.

## Materials and methods

### Cells, tissues and treatments

*Cells in vitro*

HeLa cells were grown in Dulbecco's Minimal Essential Medium (DMEM) supplemented with 10% foetal bovine serum, 1% glutamine, 100 U/mL penicillin and streptomycin at 37 °C in a 5% $CO_2$ humidified atmosphere.

For electron microscopy, the cells were grown in 25 $cm^2$ plastic flasks, detached by a mild trypsinization and fixed with 4% paraformaldehyde in the culture medium for 2 h at 4 °C to allow for a good preservation of antigen integrity. The cells were then centrifuged at 2000 rpm for 10 min and rinsed thoroughly with phosphate buffered saline (PBS). They were incubated in 0.5 M $NH_4Cl$ in PBS for 30 min at room temperature (RT) to block free aldehyde groups and rinsed again with several changes of PBS. The cell pellets were pre-embedded in 2% Agar in $H_2O$, dehydrated in graded ethanol and embedded in LRWhite resin. Thin sections of 70–80 nm were obtained with a Reichert OM3 ultramicrotome and collected on formvar-carbon-coated nickel grids (200 mesh).

*Tissues*

Samples from rat liver were fixed with 4% paraformaldehyde in Sörensen phosphate buffer pH 7.2 for 2 h at 4 °C and then processed for ultrastructural histochemistry, as described above.

*Treatments*

To label transcribed RNA, some cell samples were incubated with 5 mM Fluoro-Uridine (FU; Sigma-Aldrich) for 15 min at 37 °C [25, 26]. These samples were then processed for ultrastructural cytochemistry, as previously described.

### EM ultrastructural analysis

*EM immunocytochemistry*

The grids were floated on normal goat serum (NGS) diluted 1:50 in PBS for 5 min at RT and incubated with mouse monoclonal or rabbit polyclonal anti-5mC antibody (GeneTex, GT4111; GeneTex, GTX128455) overnight at 4 °C. The primary antibody was diluted 1:500 in PBS containing 0.1% Bovine Serum Albumin (BSA) and 0.05% Tween 20. The samples were rinsed with PBS-Tween two times for 5 min and equally with PBS. After incubation in NGS, the grids were treated with the specific secondary antibody (Jackson ImmunoResearch) coupled with colloidal gold of 12 nm diluted 1:20 in PBS for 30 min at RT. The sections were rinsed with PBS for 5 min twice and then with $H_2O$.

Some sections were double labelled. In addition to anti-5mC labelling, a rat anti-FU antibody (Techno Genetics) and a chicken anti-hnRNPs antibody (courtesy of Dr. T. Martin) binding to hnRNP core proteins [27] were used. The primary antibodies were diluted 1:10 and 1:500, respectively, in PBS/BSA/TWEEN20. Moreover, a mouse anti-7 methylguanosine (7mG; courtesy of Dr. R. Lührmann) [28] was used to recognize the 5′ cap of mRNA: it was diluted 1:200 in PBS/BSA/TWEEN20. For this double labelling a rabbit anti-5mC antibody diluted 1:500 in PBS/BSA/TWEEN20 was used. The anti-5mC was recognized by the specific secondary antibody coupled with colloidal gold of 6 nm (Jackson ImmunoResearch) while other antigens were revealed with 12 nm specific secondary antibodies (Jackson ImmunoResearch).

As a control of the specificity, some grids were incubated in parallel in PBS/BSA/Tween20 mixture from which the primary antibody was excluded and then processed as above.

As a further control, some grids were incubated with both DNase (500 U/mL) and RNase (1 mg/mL) or RNase alone (1 mg/mL) for 2 h at 37 °C and Proteinase K (PK; 1 mg/mL) for 15 min at 37 °C.

*EM in situ hybridization*

Electron microscope in situ hybridization (EMISH) was performed to recognize the poly(A) tail of mRNA. The sections were incubated with a pre-hybridization solution containing 20% baker RNA, 20% dextran and 4× saline sodium citrate (SSC) for 15 min at RT to allow the following hybridization for 3 h at 37 °C. The hybridization mixture was prepared by adding biotin-labelled poly-d(T) probe (Sigma-Aldrich) to the pre-hybridization solution to give a final concentration of 1 μM of the oligonucleotide. The grids were floated onto 4× SSC for 5 min two times at 37 °C; stringency washings were done in 4× SSC, 2× SSC and 1× SSC at RT. The incubation with NGS (1:100 in PBS) for 3 min was followed by the anti-biotin antibody coupled with 10-nm colloidal gold (Aurion) for 30 min at RT (1:10 in PBS). The samples were rinsed with PBS and $H_2O$ several times.

Immuno-labelling using anti-5mC antibody was performed on these samples, as described above, identifying the 5mC by a 6 nm gold secondary antibody.

*Staining procedures*

Sections were stained for ribonucleoproteins (RNPs) or nucleic acids with one of the following procedures:

(a) regressive EDTA technique for RNPs [29]: the grids were incubated in uranyl acetate for 2 min, in EDTA for 30 s to remove uranyl from DNA and finally in lead citrate for other 2 min;
(b) terbium citrate for RNA [30, 31]: the specimens were floated on terbium citrate drops for 30 min and quickly washed in $H_2O$ for 10 and then 5 s—this staining method gives a very low contrast despite its accuracy;
(c) osmium ammine for DNA [32, 33]: the sections were hydrolyzed with 5 N HCl for 30 min, washed with $H_2O$ several times, incubated in osmium ammine (Polysciences, Inc.) for 1 h and rinsed thoroughly with $H_2O$.

After the enzymatic digestion the specimens were stained with uranyl acetate (2 min) and lead citrate (2 min) only.

All the samples were observed on a Zeiss EM900 electron microscope operating at 80 kV.

### Statistical analysis

The statistical analysis was performed to confirm the results of enzymatic digestions. Ten nuclei were selected showing similarities in size and condensed chromatin areas. The operator counted the gold grains on the condensed chromatin regions in hepatocyte nuclei without any treatment and after PK digestion or DNase and RNase digestion.

The data were organized and analyzed in Excel; a *t* test was carried out between the untreated sample and each sample after enzymatic digestion.

## Results

### DNA methylation analysis

EM immuno-gold labelling of thin sections from rat liver showed the localization of 5mC on the condensed chromatin. The areas of condensed chromatin near the nuclear envelope are bleached by the EDTA staining technique. The labelling is mainly present near the surface of chromatin, facing the inner part of the nucleus (Fig. 1a). An abundant 5mC labelling is also detectable on the nucleolus associated chromatin (Fig. 1b). Few gold grains are visible on the nucleolus itself. After specific DNA staining with osmium ammine and 5mC labelling, the signal was more clearly visible on chromatin areas both at the periphery of the nucleus (Fig. 1c) and surrounding the nucleolus (Fig. 1d). The scanty labelling on the nucleolus can be referred to methylated DNA fibres (arrow) or possibly to methylated rRNA, in the cases where no DNA is visible nearby.

To further confirm the localization of the 5mC immunolabelling on DNA, the results of enzymatic digestions were considered. The signal continued to be present after PK digestion (Fig. 2a), thus demonstrating that proteins did not contribute to the labelling but their removal seemed to increase the yield. This could be due to the unmasking of epitopes before covered by proteins. The labelling pattern, however, remained the same, i.e., more present at the chromatin surface. The immunopositivity, on the contrary, drastically decreased from chromatin areas after digestion of both DNA and RNA (Fig. 2b). The statistical analysis confirmed the significant immuno-gold labelling increase after PK digestion and reduction after DNase and RNase treatment (Fig. 3).

When considering the EM feature of a cell nucleus, according to the data in literature [34], one can arbitrarily subdivide the condensed chromatin areas in three regions (Fig. 4): zone 1_peripheral region near the nuclear envelope; zone 2_a central region; zone 3_inner peripheral region toward the interchromatin space. The analysis of hepatocyte nuclei seemed to reveal a particular distribution of 5mC labelling, changing from the surface of condensed chromatin to the nuclear envelope. The 5mC labelling was generally abundant on the zone 3 while its density gradually decreased towards the nuclear envelope (zone 1), where the signal was often absent (Fig. 5).

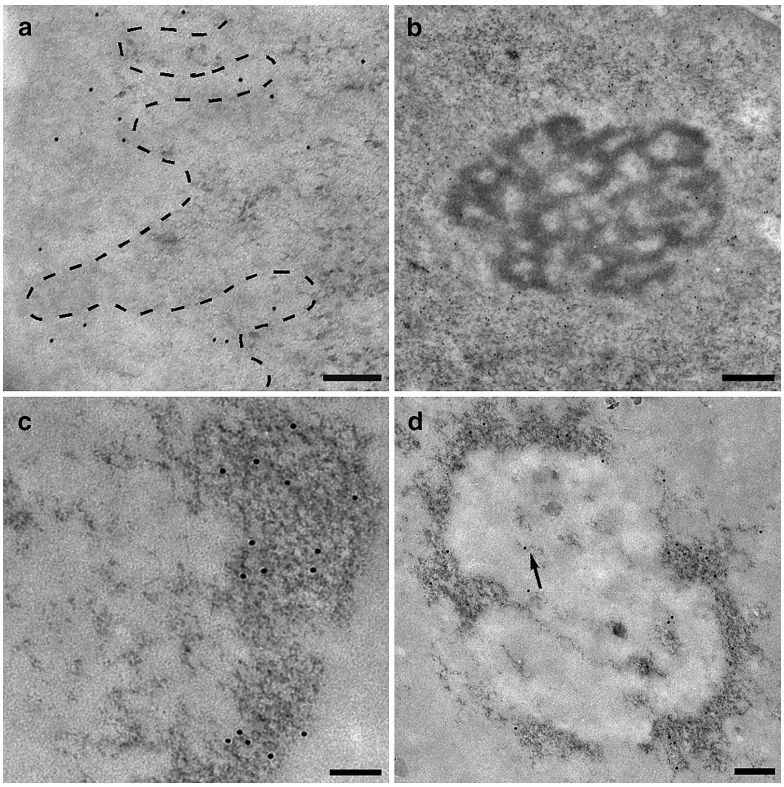


**Fig. 1** **a**, **b** The samples are stained with EDTA regressive technique for RNPs. 5mC labelling is localized on condensed chromatin region, delimited by the hatching, near the nuclear envelope (**a**) and around the nucleolus (**b**). A constant 5mC labelling is also present in the perichromatin region where transcription normally occurs. Rat liver; 150 and 250 nm, respectively. **c**, **d** After the specific DNA staining with osmium ammine, 5mC labelling is observed more clearly on condensed DNA nearby the nuclear envelope (**c**) and around the nucleolus (**d**). In d, some gold grains inside the nucleolus and lying on thin DNA fibres (*arrow*) have been detected. Rat liver; 200 and 150 nm, respectively

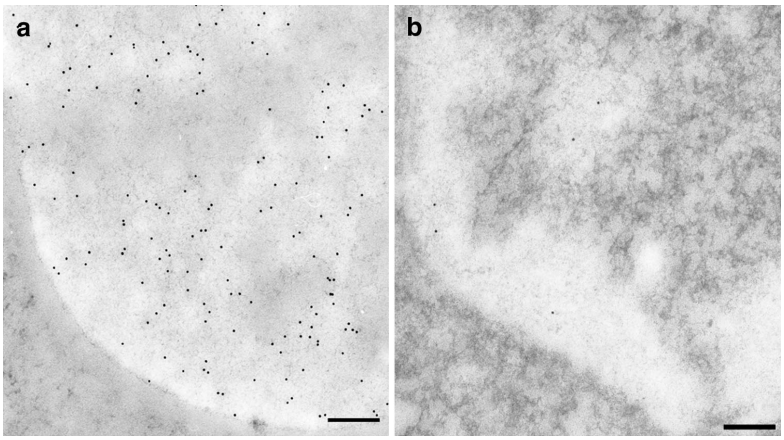


**Fig. 2** **a** Digestion by proteinase K was carried out to demonstrate that proteins did not contribute to the labelling: in fact, the 5mC signal continues to be present after the removal of proteins, reproducing the distribution also in the perichromatin regions. Heterochromatin appears unstained. Rat liver; 200 nm. **b** After removal of both DNA and RNA, the labelling is significantly decreased on chromatin and in the perichromatin region, confirming that the signal depends on DNA but also on nascent RNA molecules confined in the sites of active transcription. Mouse liver; 200 nm

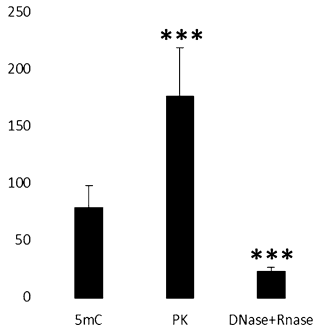


**Fig. 3** The statistical analysis of the number of gold grains of the 5mC immuno-gold labelling on condensed chromatin areas reveals a significant difference in the hepatocyte nuclei before and after the specific enzymatic digestion. The PK digestion significantly increases the immuno-gold labelling thus demonstrating not only that proteins do not contribute to the signal but also that the yield of the immunoreaction could be increased removing chromatin associated proteins ($p < 0.01$). After the removal of both DNA and RNA the gold grains are significantly reduced on the condensed chromatin regions confirming that the signal depends on DNA ($p < 0.01$)

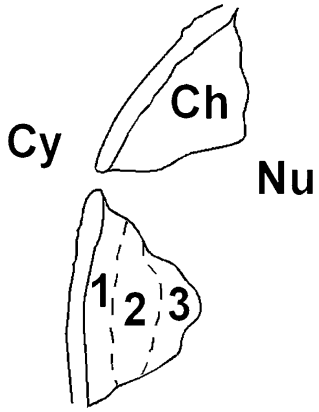


**Fig. 4** The condensed chromatin areas are arbitrarily subdivided in three regions according to EM feature of a cell nucleus. *Zone 1:* it is the peripheral region nearby the nuclear envelope. *Zone 2:* this is the central region of condensed chromatin area, changing the zone 1 in the last region. *Zone 3:* the inner region toward the interchromatin space represents the superficial part of the condensed chromatin area; it is surrounded by the perichromatin region. The artwork was realized by Paint Shop Pro 7

## 5mC detection on RNA fibrils and RNA-containing granules

Interestingly, we found a constant and not negligible 5mC signal at the border of heterochromatin areas (Fig. 1a), in the so called perichromatin region where transcription by RNA polymerase II (Pol II) normally occurs [35]. 5mC

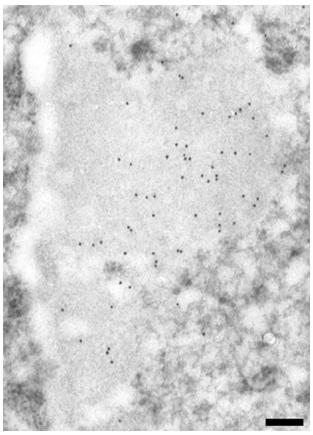

**Fig. 5** 5mC labelling on the condensed chromatin changes moving towards the nuclear envelope. The chromatin appears less stained after EDTA technique. At the surface of the heterochromatin (zone 3), the gold grains (12 nm) are abundant gradually decreasing in the zone 2; nearby the nuclear envelope (zone 1) they are almost absent. Rat liver; 250 nm

labelling in the perichromatin region was difficult to detect after a RNase treatment alone (not shown) and in combination with DNase (Fig. 2b).

After EDTA staining, RNPs were preferentially contrasted. In Fig. 6a, the gold labelling for 5mC was present over RNA fibrils. When terbium staining was used, only RNA is contrasted in the specimen. 5mC can be labelled on the stained RNA fibril (Fig. 6b). To further confirm the presence of 5mC on nascent RNA fibrils, we performed an immunolabelling after an RNA precursor incorporation. In Fig. 6c, a double labelling for 5mC and FU is shown. Several double labelled PF were found, thus showing that RNA methylation can occur precociously. Moreover, double labelling for 5mC and hnRNP core proteins was found to be present on PF (Fig. 6d): hnRNPs are considered markers of PF as in situ forms of nascent transcripts [36]. Despite the presence of 5mC on nascent RNA fibrils, the modified nucleotide was also detected on perichromatin granules (PG; Fig. 6e). To corroborate our finding, double labelled PG for 5mC and hnRNPs were also found several times (Fig. 6f). PG are considered to be a form of stored mRNA leaving the nucleus later [37]. We found labelled PF both near the nuclear pore and in the cytoplasm close to ribosomes (not shown). These data could suggest that this modification is not only an early event, but it remains during the RNA fibril lifespan.

RNA perichromatin fibrils were double labelled for 5mC and 7-methylguanosine (Fig. 6g). Even if this capping is present on other RNA products of Pol II, it is considered specific for mRNA. Finally, the poly(A) tail was

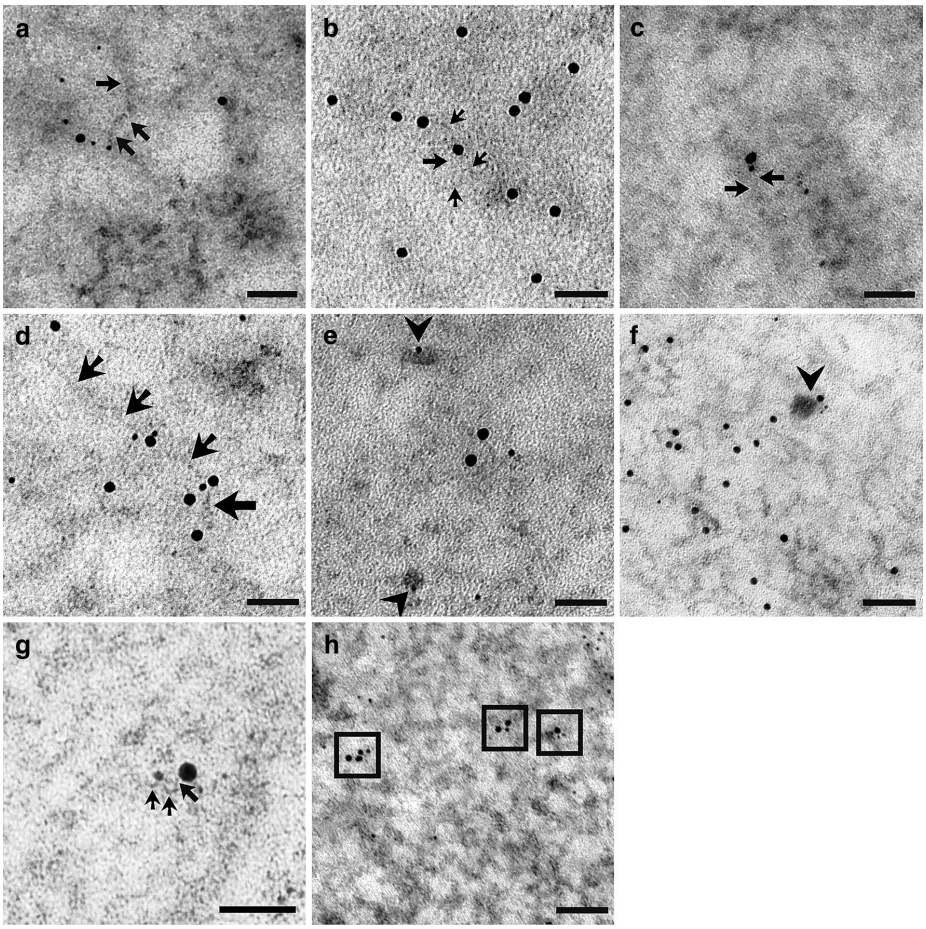


**Fig. 6** **a** 6 nm gold labels 5mC on RNA fibril stained with EDTA technique (12 nm gold grains label FU): PF are indicated by *arrows*. HeLa cell; 50 nm. **b** After terbium staining, 5mC is revealed by a 12 nm secondary antibody on PF (*arrows*). HeLa cell; 50 nm. **c** After EDTA staining, FU (12 nm) and 5mC (6 nm) colocalize on a nascent RNA fibril, indicated by *arrows*, suggesting methylation as an early modification on a nascent transcript. HeLa cell; 50 nm. **d** Terbium stained PF (*arrows*) are labelled both by anti-hnRNPs antibody (12 nm) and anti-5mC antibody (6 nm). HeLa cell; 50 nm. **e** The *arrowheads* show the 6 nm 5mC signal on PG, stained specifically with terbium citrate. As forms of (pre-)mRNA, labelled PG confirm the methylation of this subset of RNA. HeLa cell; 50 nm. **f** PG double labelled for both 5mC and hnRNPs were found. Rat liver; 50 nm. **g** A perichromatin fibril (*arrows*) is detected in the perichromatin region near the nuclear pore by EDTA staining: it is labelled both by anti-5mC (6 nm) and anti-7mG (12 nm) demonstrating that (pre-)mRNA could be methylated. Rat liver; 50 nm. **h** 5mC immunopositivity is detected on poly-adenylated RNA fibrils: in the squares 5mC is labelled by 6 nm gold while poly(A) tail by 12 nm grain. This colocalization seems to confirm mRNA methylation. HeLa cell; 50 nm

recognized by in situ hybridization while 5mC was labelled immunocytochemically: the poly(A) tail and 5mC frequently colocalized (Fig. 6h). As well as 7mG, poly(A) tail is one of mRNA marker despite its presence on other Pol II products. Taken together, 7mG and poly(A) labelling strongly suggest (pre-)mRNA as the target.

## Discussion

This paper describes a different approach for the analysis of nucleic acid methylation. So far, to our knowledge, no data are available on the detection at electron microscope of DNA methylation and especially of RNA modification.

The EM analysis of DNA methylation represents an effective method for characterizing 5mC distribution on DNA. This analysis also allows its localization in the different regions of condensed chromatin. Since the latter are characterized by a different functionality in terms of transcription, 5mC detection could be of interest in correlating DNA modifications, chromatin structure and chromatin functionality. Although until now this modification was considered to directly silence genes involving DNA-binding proteins [38, 39] and to lead to a more compact chromatin structure [40], recent works have revealed that 5mC increases DNA stiffness through the restriction of the conformational fluctuations caused by the methyl group. This fact explains the suppression of DNA looping by 5mC and the consequent loosening of DNA ends around a nucleosome [41]. Moreover, other works have excluded that this modification is the predominant pathway for gene silencing [42]. Here, we showed that the more peripheral condensed regions of chromatin, transcriptionally inactive, are almost unlabelled for 5mC. The more superficial region, on the contrary, is the most labelled. This EM gradient distribution could be the starting point for elucidating the role of 5mC in chromatin condensation/functionality in the new light of what previously cited in the literature.

Finally, EM immunolabelling could be used to detect different level of DNA methylation through a semi-quantitative analysis. In this view, a DNA methylation analysis at TEM could be conducted in tumour cell lines to verify the possible effect of a specific treatment.

As for RNA, we have found 5mC labelled and terbium stained fibrils in the perichromatin region, in close proximity to the condensed chromatin area where transcription occurs [35]. This prompted us to hypothesize that 5mC modification could be an early event. To confirm this, we used FU incorporation to label nascent RNA and hnRNP core proteins labelling as a marker of PF. The identification of double labelled and RNA-specifically stained PF supports that RNA methylation is not only an early event but probably occurs cotranscriptionally.

Since in this thin perichromatin region the RNAs are synthesized by Pol II [35], we decided to verify if it could be possible to detect 5mC presence on (pre-)mRNA by TEM because this modified nucleotide was recently detected on mRNA [24]. Nascent PF were co-labelled for 5mC and 7mG and poly-adenylated RNA fibrils were also methylated. The spatial localization of PF, the double labelling and the relative abundance of each Pol II product strongly suggest that the majority of the 5mC-labelled PF pertain to (pre-)mRNA.

Moreover, we found 5mC labelling on PG which are known as forms of (pre-)mRNA [37] and to contain poly-adenylated RNAs [43]. They are present in all cells and most probably represent a storage form of (pre-)mRNA which will leave the nucleus at a later time [37]. In this view, RNA methylation is also a long-lasting RNA modification. This data is supported by the finding of labelled PF in close proximity of the nuclear pore or ribosomes in the cytoplasm which might indicate that methylated RNAs could be exported from the nucleus whereby this modification remains present during the total RNA lifespan.

In conclusion, this TEM study allows the detailed visualization of a single RNA molecule verifying its possible epigenetic modification via ultrastructural immunocytochemistry. This approach represents an in situ biomolecular characterization of RNA methylation at high resolution level which could have several applications in epigenetic research.

**Acknowledgements** The authors are grateful for the technical assistance of Ms. Francine Flach and Ms. Paola Veneroni and for the critical review of the manuscript of Prof. Carlo Pellicciari and Prof. Antonella Forlino.

**Compliance with ethical standards**

**Funding** This work was supported by Fondi di Ateneo per la Ricerca (F.A.R. 2013–2014) from the University of Pavia.

**Integrity of research** The experiments described in this manuscript comply with the current Italian laws.

**Conflict of interest** The authors declare that no competing interests exist.

## References

1. Hendrich B, Bird A (1998) Identification and characterization of a family of mammalian methyl-CpG binding proteins. Mol Cell Biol 18:6538–6547
2. Robertson KD (2005) DNA methylation and human disease. Nat Rev Genet 6:597–610
3. Li E, Bestor TH, Jaenisch R (1992) Targeted mutation of DNA methyltransferase gene results in embryonic lethality. Cell 69:915–926
4. Bird AP (1996) The relationship of DNA methylation to cancer. Cancer Surv 28:87–101
5. Harrison A, Parle-McDermott A (2011) DNA methylation: a timeline of methods and applications. Front Genet 2:74. doi:10.3389/fgene.2011.00074
6. Gehrke CW, McCune RA, Gama-Sosa MA, Ehrlich M, Kuo KC (1984) Quantitative reversed-phase high-performance liquid chromatography of major and modified nucleosides in DNA. J Chromatogr 301:199–219
7. Bestor TH, Hellewell SB, Ingram VM (1984) Differentiation of two mouse cell lines is associated with hypomethylation of their genomes. Mol Cell Biol 4:1800–1806
8. Frommer M, McDonald LE, Millar DS, Collis CM, Watt F, Grigg GW, Molloy PL, Paul CL (1992) A genomic sequencing protocol that yields a positive display of 5-methylcytosine residues in individual DNA strands. Proc Natl Acad Sci USA 89:1827–1831
9. Huang TH, Perry MR, Laux DE (1999) Methylation profiling of CpG islands in human breast cancer cells. Hum Mol Genet 8:459–470

10. Gitan RS, Shi H, Chen CM, Yan PS, Huang TH (2002) Methylation-specific oligonucleotide microarray: a new potential for high-throughput methylation analysis. Genome Res 12:158–164
11. Weber M, Davies JJ, Wittig D (2005) Chromosome-wide and promoter-specific analyses identify sites of differential DNA methylation in normal and transformed human cells. Nat Genet 37:853–862
12. Cokus SJ, Feng S, Zhang X, Chen Z, Merriman B, Haudenschild CD, Pradhan S, Nelson SF, Pellegrini M, Jacobsen SE (2008) Shotgun bisulfite sequencing of the Arabidopsis genome reveals DNA methylation patterning. Nature 452:215–219. doi:10.1038/nature06745
13. Maunakea AK, Nagarajan RP, Bilenky M, Ballinger TJ, D'Souza C, Fouse SD, Johnson BE, Hong C, Nielsen C, Zhao Y, Turecki G, Delaney A, Varhol R, Thiessen N, Shchors K, Heine VM, Rowitch DH, Xing X, Fiore C, Schillebeeckx M, Jones SJ, Haussler D, Marra MA, Hirst M, Wang T, Costello JF (2010) Conserved role of intragenic DNA methylation in regulating alternative promoters. Nature 466:253–257. doi:10.1038/nature09165
14. Santos F, Hendrich B, Reik W (2002) Dynamic reprogramming of DNA methylation in the early mouse embryo. Dev Biol 241:172–182
15. Kobayakawa S, Miike K, Nakao M, Abe K (2007) Dynamic changes in the epigenomic state and nuclear organization of differentiating mouse embryonic stem cells. Genes Cells 12:447–460
16. Li Y, Miyanari Y, Shirane K, Nitta H, Kubota T, Ohashi H, Okamoto A, Sasaki H (2013) Sequence-specific microscopic visualization of DNA methylation status at satellite repeats in individual cell nuclei and chromosomes. Nucleic Acids Res 41:e186. doi:10.1093/nar/gkt766
17. Solís MT, Chakrabarti N, Corredor E (2014) Epigenetic changes accompany developmental programmed cell death in tapetum cells. Plant Cell Physiol 55:16–29. doi:10.1093/pcp/pct152
18. Hussain S, Aleksic J, Blanco S, Dietmann S, Frye M (2013) Characterizing 5-methylcytosine in the mammalian epitranscriptome. Genome Biol 14:215. doi:10.1186/gb4143
19. Sharp PA (2009) The centrality of RNA. Cell 136:577–580. doi:10.1016/j.cell.2009.02.007
20. Liu N, Pan T (2015) RNA epigenetics. Transl Res 165:28–35. doi:10.1016/j.trsl.2014.04.003
21. Kellner S, Burhenne J, Helm M (2010) Detection of RNA modifications. RNA Biol 7:237–247
22. Liu J, Jia G (2014) Methylation modifications in eukaryotic messenger RNA. J Genet Genomics 41:21–33. doi:10.1016/j.jgg.2013.10.002
23. Motorin Y, Lyko F, Helm M (2010) 5-Methylcytosine in RNA: detection, enzymatic formation and biological functions. Nucleic Acids Res 38:1415–1430. doi:10.1093/nar/gkp1117
24. Squires JE, Patel HR, Nousch M (2012) Widespread occurrence of 5-methylcytosine in human coding and non-coding RNA. Nucleic Acids Res 40:5023–5033. doi:10.1093/nar/gks144
25. Dundr M, Raska I (1993) Nonisotopic ultrastructural mapping of transcription sites within the nucleolus. Exp Cell Res 208:275–281
26. Trentani A, Testillano PS, Risueño MC, Biggiogera M (2003) Visualization of transcription sites at electron microscope. Eur J Histochem 47:195–200
27. Jones RE, Okamura CS, Martin TE (1980) Immunofluorescent localization of the proteins of nuclear ribonucleoprotein complexes. J Cell Biol 86:235–243
28. Bochnig P, Reuter R, Bringmann P, Lührmann R (1987) A monoclonal antibody against 2,2,7-trimethylguanosine that reacts with intact, class U, small nuclear ribonucleoproteins as well as with 7-methylguanosine-capped RNAs. Eur J Biochem 168:461–467
29. Bernhard W (1969) A new staining procedure for electron microscopical cytology. J Ultrastruct Res 27:250–265
30. Biggiogera M, Fakan S (1998) Fine structural specific visualization of RNA on ultrathin sections. J Histochem Cytochem 46:389–395
31. Biggiogera M, Masiello I (2017) Visualizing RNA at electron microscopy by terbium citrate. In: Pellicciari C, Biggiogera M (eds) Histochemistry of single molecules, 1st edn. Springer, Pavia, pp 277–283
32. Vazquez-Nin GH, Biggiogera M, Echeverrìa OM (1995) Activation of osmium ammine by $SO_2$-generating chemicals for EM Feulgen-type staining of DNA. Eur J Histochem 39:101–106
33. Masiello I, Biggiogera M (2017) Osmium ammine for staining DNA in electron microsocopy. In: Pellicciari C, Biggiogera M (eds) Histochemistry of single molecules, 1st edn. Springer, Pavia, pp 261–267
34. Cmarko D, Verschure PJ, Otte AP, van Driel R, Fakan S (2003) Polycomb group gene silencing proteins are concentrated in the perichromatin compartment of the mammalian nucleus. J Cell Sci 116:335–343
35. Cmarko D, Verschure PJ, Martin TE, Dahmus ME, Krause S, Fu XD, Van Driel R, Fakan S (1999) Ultrastructural analysis of transcription and splicing in the cell nucleus after BrUTP-microinjection. Mol Biol Cell 10:211–223
36. Fakan S (1994) Perichromatin fibrils are in situ forms of nascent transcripts. Trends Cell Biol 4:86–90
37. Fakan S (2004) The functional architecture of the nucleus as analysed by ultrastructural cytochemistry. Histochem Cell Biol 122:83–93. doi:10.1007/s00418-004-0681-1
38. Holliday R, Pugh JE (1975) DNA modification mechanisms and gene activity during development. Science 187:226–232
39. Riggs AD (2002) X chromosome inactivation, differentiation, and DNA methylation revisited, with a tribute to Susumu Ohno. Cytogenet Genome Res 99:17–24
40. Geiman TM, Robertson KD (2002) Chromatin remodeling, histone modifications, and DNA methylation-how does it all fit together? J Cell Biochem 87:117–125
41. Ngo TTM, Yoo J, Dai Q, Zhang Q, He C, Aksimentiev A (2016) Effects of cytosine modifications on DNA flexibility and nucleosome mechanical stability. Nat Commun 7:10813. doi:10.1038/ncomms10813
42. Ooi SK, Qiu C, Bernstein E, Li K, Jia D, Yang Z, Erdjument-Bromage H, Tempst P, Lin SP, Allis CD, Cheng X, Bestor TH (2007) DNMT3L connects unmethylated lysine 4 of histone H3 to de novo methylation of DNA. Nature 448:714–717
43. Visa N, Puvion-Dutilleul F, Harper F, Bachellerie JP, Puvion E (1993) Intranuclear distribution of poly(A) RNA determined by electron microscope in situ hybridization. Exp Cell Res 208:19–34